

STRATEGIES FOR LOW-THRUST TRANSFER DESIGN BASED ON DIRECT  
COLLOCATION TECHNIQUES

A Dissertation

Submitted to the Faculty

of

Purdue University

by

Robert E. Pritchett

In Partial Fulfillment of the

Requirements for the Degree

of

Doctor of Philosophy

August 2020

Purdue University

West Lafayette, Indiana

**THE PURDUE UNIVERSITY GRADUATE SCHOOL  
STATEMENT OF DISSERTATION APPROVAL**

Hsu Lo Distinguished Professor of Aeronautics and Astronautics Kathleen C. Howell,  
Chair

School of Aeronautics and Astronautics

Professor James Longuski

School of Aeronautics and Astronautics

Professor Carolin Frueh

School of Aeronautics and Astronautics

Dr. Daniel Grebow

Jet Propulsion Laboratory, California Institute of Technology

**Approved by:**

Professor Gregory Blaisdell

Associate Head of Graduate Program of Aeronautics and Astronautics

For Mom and Dad

Thanks for taking me camping under the stars and teaching me to wonder at them.

## ACKNOWLEDGMENTS

I must begin by thanking Professor Howell, who supported me before I even set foot on Purdue’s campus. Professor Howell, your years of patient guidance and encouragement have not only enabled me to complete this degree, but have shaped me into a better researcher, engineer, and teacher. Thank you for all that you have invested in me. Dan Grebow has also been an exceptional mentor. Dan, you first introduced me to direct collocation in the summer of 2015. My growth as a researcher and engineer over the intervening years is due to your selflessly giving time to provide me with direction and insight. Thank you for your example of curiosity, persistence, and thoughtfulness. My goal in the next phase of my career is to mentor even one student with the same generosity that you have shown me. My other committee members, Professor Frueh and Professor Longuski, have also made valuable contributions to this work through their teaching and thoughtful questioning. Thank you to both of you for giving of your time and knowledge.

I also owe many thanks to my fellow members of the Multibody Dynamics Research Group, both past and present. Your technical advice, encouragement, and — most importantly — friendship, have made it possible for me to not only finish graduate school, but to enjoy the journey as well. There are many other professors and students in the School of Aeronautics and Astronautics at Purdue who have taught me valuable lessons as well as offered friendship. I am grateful for all of you.

This work was supported by a NASA Space Technology Research Fellowship (NSTRF) grant number NXX16AM42H. My graduate student experience has been greatly enhanced by the support of the NSTRF. The NSTRF removed many of the challenging obstacles of graduate school while offering opportunities to learn directly from NASA engineers.

There are many scientists and engineers at Goddard Space Flight Center (GSFC) who I had the privilege of learning from and collaborating with during my summers there. First and foremost, Dave Folta, thank you for taking me under your wing at Goddard and guiding my research efforts. Your enthusiasm, generous mentorship to many, never-ending willingness to learn, and incredible intuition for spacecraft trajectory design are all qualities I will strive to emulate. Thank you as well to the many other engineers at GSFC who taught me the ins and outs of practical mission design while also being incredibly friendly. I am excited to be joining your ranks.

I have also learned a great deal from many engineers at the Jet Propulsion Laboratory (JPL). I was warmly invited into the office of every engineer there regardless of status or seniority, and given free reign to ask and learn. This investigation has benefited substantially from the many engineers there who took the time to work with me when I felt stuck, in particular: Tom Pavlak, Juan Senent, Zubin Olikara, and Jeff Stuart.

My path towards graduate school began in the Texas Spacecraft Laboratory (TSL) run by Professor Glenn Lightsey at The University of Texas at Austin. Thank you to all my peers in the TSL who taught me and made work fun. Thank you especially to Professor Lightsey for creating an environment where we had the freedom to learn and make mistakes, and in particular for your guidance on my senior research project.

Perhaps my first “break” in the space industry came when L-3 STRATIS in Houston offered me an internship with Susan Winnitoy and the rest of the Six Degree-of-Freedom Dynamic Test System (SDTS) team at Johnson Space Center. Thank you Susan for your mentorship, and thank you to the rest of the SDTS team for incorporating me into your projects even when inconvenient. Finally, thank you to the team at L-3 for taking a leap of faith and bringing on an inexperienced college sophomore.

Christian fellowship has been a source of continual love and encouragement at every step in my journey. My friends in Graduate Intersity past and present, you were the first to welcome me to Purdue and the last to say goodbye. Thank you for your constant support and for helping me to grow spiritually during my time at

Purdue. My friends in World Welcome and Covenant Church, thank you for your warm embrace and for keeping me anchored while at Purdue. I did not expect to gain a second family during my time in West Lafayette, but you became that. To the friends and family at NBBC back in Texas, thank you for your unfailing love and support. Your encouragement, prayers, and love have been with me since day one (literally) and have shaped me into the person I am today. You are more family than friends and a constant source of love amidst the changes of life. I am always deeply grateful for you.

Family near and far, new and old, has made me feel known and loved from day one. Aunt Jean, Uncle John, Kate, and Sarah, thank you for giving me a home during my time in Los Angeles. Your generous hospitality made me feel loved and surrounded by family even when far away from home. I treasure the memories I made with you all there. Cupery and Prince families, thank you for welcoming me in with open arms (and the expected teasing). It has been a joy to get to know each one of you and to have experienced both the joy and inevitable zaniness of a house full of relatives. Grandma and Grandpa, thank you for your unwavering love and support over all these years. Your examples of kindness, hard work, and humility are ones I will continually seek to follow. Mom and Dad, this work is dedicated to you because you were there from the start and have supported me every step of the way. Everywhere I look I see how your self-sacrificial love for me enabled me to reach where I am today. Thank you for modeling this love for me. This accomplishment is just as much yours as mine. And Sam, thanks for being the best brother and friend I could ask for. You are always a source of encouragement and know how to make me laugh.

Finally, Maria, the things I gained in graduate school pale in comparison to the blessing I've received by being able to call you my wife in this phase of life and all the ones to come. During these final months you have shouldered many of the burdens of our everyday life, in addition to editing nearly every page of this document and preparing for a big move. Yet, these are a sliver of the ways you love and support

me. Thank you for the walks, the late night talks, the comforting words, the wise advice, the well-timed prayers, the belly laughs, and your multitude of other acts of love towards me. I am eager for our next adventure and at ease knowing that I am going on it with you.

*Soli Deo Gloria*

## TABLE OF CONTENTS

	Page
LIST OF TABLES . . . . .	xii
LIST OF FIGURES . . . . .	xv
ABSTRACT . . . . .	xxii
1 INTRODUCTION . . . . .	1
1.1 Problem Definition . . . . .	3
1.2 Previous Contributions . . . . .	4
1.2.1 Orbit Chain Approach . . . . .	5
1.2.2 Low-Thrust Trajectory Design with Direct Collocation . . . . .	6
1.3 Current Work . . . . .	6
2 DYNAMICAL MODELS . . . . .	10
2.1 N-Body Model . . . . .	11
2.2 Circular Restricted Three-Body Problem . . . . .	13
2.2.1 Assumptions . . . . .	14
2.2.2 Coordinate Frames . . . . .	16
2.2.3 Formulation of the CR3BP Equations of Motion . . . . .	17
2.2.4 Integral of Motion . . . . .	23
2.2.5 Equilibrium Solutions . . . . .	24
2.3 Bicircular Restricted Four-Body Problem . . . . .	26
2.3.1 Assumptions . . . . .	28
2.3.2 Equations of Motion . . . . .	31
2.3.3 System Hamiltonian . . . . .	33
2.3.4 Coordinate Frame Transformation . . . . .	34
2.4 Higher-Fidelity Modeling . . . . .	35
2.5 Low-Thrust Electric Propulsion . . . . .	38

	Page
3 LOW-THRUST TRAJECTORY COMPUTATION AND OPTIMIZATION . . . . .	42
3.1 The Optimal Control Problem . . . . .	43
3.1.1 General Formulation . . . . .	44
3.1.2 Euler-Lagrange Theorem . . . . .	45
3.1.3 General Multi-Phase Formulation . . . . .	46
3.2 Optimization Methods . . . . .	49
3.2.1 Indirect Optimization Methods . . . . .	51
3.2.2 Direct Optimization Methods . . . . .	52
3.2.3 Global Optimization and Other Methods . . . . .	53
3.2.4 Selecting an Optimization Method . . . . .	54
3.3 Newton's Method . . . . .	55
3.3.1 Number of Variables Equals the Number of Constraints . . . . .	56
3.3.2 Number of Variables Greater than the Number of Constraints . . . . .	57
3.4 Nonlinear Programming . . . . .	59
3.5 Transcription Methods . . . . .	61
3.6 Shooting Methods . . . . .	63
3.7 Collocation Methods . . . . .	66
3.7.1 General Formulation . . . . .	67
3.7.2 Mesh Refinement . . . . .	77
3.8 Collocation with Optimization for Low-Thrust (COLT) Implementation . . . . .	85
3.9 Finite Difference Approach for Partial Derivative Computation . . . . .	91
4 ORBIT CHAIN TECHNIQUE FOR LOW-THRUST TRANSFER DESIGN . . . . .	93
4.1 Motivation and Overview . . . . .	93
4.2 Dynamical Structures . . . . .	96
4.2.1 Periodic Orbits . . . . .	97
4.2.2 Invariant Manifolds . . . . .	99
4.3 Orbit Chain Methodology . . . . .	101
4.3.1 Orbit Chain Construction: Analyze and Select . . . . .	102

	Page
4.3.2 Orbit Chain Construction: Clip, Subdivide, and Stack . . . . .	105
4.3.3 Orbit Chain Construction: Define Control History . . . . .	109
4.3.4 Orbit Chain to Optimal Solution . . . . .	112
4.4 Orbit Chain Examples . . . . .	115
4.5 Direct Collocation and Direct Multiple Shooting . . . . .	125
4.6 Orbit Chain and Direct Collocation Parameter Analysis . . . . .	130
5 GATEWAY MISSION DESIGN . . . . .	137
5.1 Background . . . . .	139
5.1.1 Mission Overview . . . . .	139
5.1.2 Previous Contributions . . . . .	142
5.1.3 Missed Thrust Background . . . . .	142
5.2 Gateway Methodology . . . . .	144
5.2.1 Sample Transfer Computation . . . . .	144
5.2.2 Missed Thrust Analysis . . . . .	147
5.3 Sample Transfers . . . . .	151
5.3.1 9:2 NRHO to DRO Transfers . . . . .	153
5.3.2 9:2 NRHO to Low-Amplitude Halo Orbit Transfers . . . . .	162
5.3.3 9:2 NRHO to Northern $L_1$ NRHO Transfers . . . . .	170
5.3.4 Summary of Transfers from the 9:2 NRHO . . . . .	178
5.4 Missed Thrust Analysis . . . . .	181
6 LUNAR ICECUBE MISSION DESIGN . . . . .	190
6.1 Background . . . . .	192
6.1.1 Mission Overview . . . . .	192
6.1.2 Previous Contributions . . . . .	194
6.2 Trajectory Design Framework . . . . .	197
6.2.1 Nearest Neighbor Search Algorithm . . . . .	198
6.2.2 Staging Orbit Selection . . . . .	200
6.2.3 Phase 1 Trajectory Design: Deployment to Staging Orbit . . . . .	203

	Page
6.2.4 Phase 2 Trajectory Design: Staging Orbit to Science Orbit . . .	208
6.2.5 Phase 2 Trajectory Design: Staging Orbit to NRHO . . . . .	214
6.2.6 Design Framework Summary . . . . .	215
6.3 Lunar IceCube Results . . . . .	216
6.3.1 Phase 1 Results: Deployment to a Staging Orbit . . . . .	217
6.3.2 Phase 2 Results: Staging Orbit to Science Orbit . . . . .	223
6.3.3 Phase 2 Results: Staging Orbit to NRHO . . . . .	232
6.3.4 Combined Transfer Trajectory Summaries . . . . .	236
6.4 Concluding Remarks . . . . .	241
7 CONCLUSION . . . . .	246
7.1 Investigation Summary . . . . .	246
7.1.1 Orbit Chain and Direct Collocation Technique . . . . .	247
7.1.2 Gateway Mission Design . . . . .	248
7.1.3 Lunar IceCube Mission Design . . . . .	249
7.2 Recommendations for Future Work . . . . .	250
7.2.1 Orbit Chain and Direct Collocation . . . . .	250
7.2.2 Gateway Mission Design . . . . .	253
7.2.3 Lunar IceCube Mission Design . . . . .	255
REFERENCES . . . . .	257
APPENDICES . . . . .	269
VITA . . . . .	288

## LIST OF TABLES

Table	Page	
2.1	Characteristic quantity and mass ratio values for the Earth-Moon CR3BP	20
2.2	Characteristic quantity and mass ratio values for the Sun- $B_1$ CR3BP . . .	20
2.3	Values of constant Sun parameters in the BCR4BP. . . . .	31
2.4	Spacecraft and engine parameters for real low-thrust spacecraft. . . . .	41
3.1	Node Placement Schemes . . . . .	71
3.2	Constant Values for Odd Degree Polynomial Error Calculation . . . . .	78
5.1	Jacobi constant, period, and initial state values for departure and destination orbits used to compute Gateway transfers. All quantities are presented in nondimensional units. . . . .	153
5.2	Summary of Gateway transfers computed in the CR3BP. . . . .	179
5.3	Summary of Gateway transfers computed in an ephemeris model including the Earth, Moon, and Sun. . . . .	180
5.4	Julian dates of initial epochs used to compute each Gateway transfer in an ephemeris model. . . . .	181
6.1	Lunar IceCube science orbit Keplerian orbital elements defined in a Moon-centered inertial frame. Inclination is measured relative to the Moon's equator and the right ascension of the ascending node (RAAN) is defined with respect to the vernal equinox vector. . . . .	194
6.2	Deployment dates and corresponding Sun angles considered for Lunar IceCube. At the time of writing Lunar IceCube is scheduled to launch in November 2020. . . . .	204
6.3	Summary of sample transfers to the low-altitude lunar orbit for all four deployment dates, computed in the BCR4BP. Given characteristics are time of flight (TOF), change in mass ( $\Delta m$ ), and final mass. . . . .	237
6.4	Summary of sample Phase 1 transfers from deployment to the staging orbit, computed in an ephemeris model. Given characteristics are time of flight (TOF), change in mass ( $\Delta m$ ), and final mass. . . . .	239

Table	Page
6.5 Summary of sample transfers to the 9:2 NRHO for all four deployment dates, computed in the BCR4BP. Given characteristics are time of flight (TOF), change in mass ( $\Delta m$ ), and final mass. . . . .	240
6.6 Summary of sample transfers to the 9:2 NRHO for all four deployment dates, computed in an ephemeris model. Given characteristics are time of flight (TOF), change in mass ( $\Delta m$ ), and final mass. . . . .	241
A.1 Summary of orbit chain example transfers. The initial mass for each transfer is $m_0 = 1000$ kg. . . . .	270
A.2 Orbit chain setup data for DRO to $L_3$ Lyapunov orbit with $L_4$ SPO transfer. All quantities are presented in nondimensional units. . . . .	271
A.3 Orbit chain setup data for $L_1$ to $L_2$ Lyapunov orbit transfer. All quantities are presented in nondimensional units. . . . .	272
A.4 Orbit chain setup data for $L_1$ to $L_2$ halo orbit transfer. All quantities are presented in nondimensional units. . . . .	273
A.5 Orbit chain setup data for DRO to $L_3$ Lyapunov orbit transfer with 2:3 resonant orbit. All quantities are presented in nondimensional units. . . . .	274
A.6 Part 1 of the orbit chain setup data for $L_2$ Lyapunov to $L_2$ vertical orbit transfer. All quantities are presented in nondimensional units. . . . .	275
A.7 Part 2 of the orbit chain setup data for $L_2$ Lyapunov to $L_2$ vertical orbit transfer. All quantities are presented in nondimensional units. . . . .	276
B.1 Orbit chain setup data for 9:2 NRHO to DRO exterior type transfer. All quantities are presented in nondimensional units. . . . .	278
B.2 Part 1 of the orbit chain setup data for 9:2 NRHO to DRO interior type transfer. All quantities are presented in nondimensional units. . . . .	279
B.3 Part 2 of the orbit chain setup data for 9:2 NRHO to DRO interior type transfer. All quantities are presented in nondimensional units. . . . .	280
B.4 Orbit chain setup data for 9:2 NRHO to low-amplitude halo orbit exterior type transfer. All quantities are presented in nondimensional units. . . . .	281
B.5 Part 1 of the orbit chain setup data for 9:2 NRHO to low-amplitude halo orbit interior type transfer. All quantities are presented in nondimensional units. . . . .	282
B.6 Part 2 of the orbit chain setup data for 9:2 NRHO to low-amplitude halo orbit interior type transfer. All quantities are presented in nondimensional units. . . . .	283

Table	Page
B.7 Orbit chain setup data for 9:2 NRHO to northern NRHO exterior type transfer. All quantities are presented in nondimensional units. . . . .	284
B.8 Part 1 of the orbit chain setup data for 9:2 NRHO to northern NRHO interior type transfer. All quantities are presented in nondimensional units.	285
B.9 Part 2 of the orbit chain setup data for 9:2 NRHO to northern NRHO interior type transfer. All quantities are presented in nondimensional units.	286
B.10 Part 3 of the orbit chain setup data for 9:2 NRHO to northern NRHO interior type transfer. All quantities are presented in nondimensional units.	287

## LIST OF FIGURES

Figure	Page
2.1 Vector diagram of an N-Body System . . . . .	12
2.2 Circular-Restricted Three-Body Problem . . . . .	15
2.3 Configuration of the Lagrange points in the Earth-Moon CR3BP as viewed in the rotating frame. . . . .	27
2.4 Definition of the Sun angle in the Bicircular Restricted Four-Body Problem.	29
2.5 Definition of the $P_1$ - $P_2$ angle in the Bicircular Restricted Four-Body Problem.	30
3.1 Multiple (Parallel) Shooting Problem . . . . .	65
3.2 Collocation Using Euler's Rule . . . . .	68
3.3 Collocation Using the Trapezoidal Rule . . . . .	69
3.4 Collocation Using a 7th Degree Polynomial . . . . .	70
3.5 Procedure for Applying Collocation with Newton's Method or Minimum- Norm Equation . . . . .	76
3.6 Procedure for de Boor method of mesh refinement. . . . .	81
3.7 Procedure for CEP mesh refinement. . . . .	83
4.1 Lyapunov orbit about the $L_1$ libration point in the Earth-Moon CR3BP. The period of this orbit is $\mathcal{P} = 15.356$ days and the Jacobi constant value is $\mathfrak{J} = 3.053$ . . . . .	97
4.2 (a) Subset of the family of $L_1$ Lyapunov orbits in the Earth-Moon CR3BP plotted in position space. (b) Subset of the family of $L_1$ Lyapunov orbits plotted in parameter space. Note, a smaller subset of the family is depicted in (a) than in (b). . . . .	98
4.3 Paths on the stable and unstable invariant manifolds corresponding to the $L_1$ Lyapunov orbit shown in Figure 4.1. . . . .	100
4.4 Orbit families included in the orbit chain constructed for a DRO to $L_3$ Lyapunov orbit transfer. An orbit from the $L_4$ SPO family is employed as an intermediate link because it bridges discontinuities in position and energy space between the initial and final orbits. . . . .	103

Figure	Page
4.5 Individual orbits from each orbit family are selected for inclusion in the orbit chain. The initial and final orbits in the chain are the departure and arrival orbits of the resulting low-thrust transfer. The orbits included in the chain are clipped to reduce discontinuities between links and reduce the time of flight of the final transfer. . . . .	105
4.6 An initial mesh along with the desired number of stacked revolutions is determined for the orbit chain initial guess. The orbit chain leads to a feasible solution with a redistributed mesh, but a geometry similar characteristics to that of the initial guess. . . . .	107
4.7 Thrust profiles for the initial guess, feasible solution, and optimal result of the DRO to $L_3$ Lyapunov transfer. As expected, the thrust profile of the optimized solution consists almost exclusively of thrust arcs at the maximum thrust magnitude. . . . .	111
4.8 The feasible solution obtained from the orbit chain initial guess is optimized to maximize the mass delivered to the final orbit. . . . .	113
4.9 Jacobi constant profiles for the initial guess, feasible solution, and optimal result of the DRO to $L_3$ Lyapunov transfer. . . . .	114
4.10 The orbit chain initial guess and final optimal solution for a transfer from an $L_1$ Lyapunov orbit to an $L_2$ Lyapunov orbit. . . . .	116
4.11 The orbit chain initial guess and final optimal solution for a transfer from an $L_1$ halo orbit to an $L_2$ halo orbit. . . . .	117
4.12 The 2:3 resonant orbit family is selected to provide an intermediate link for a transfer from a DRO to an $L_3$ Lyapunov orbit because this family bridges discontinuities in position and energy space between the initial and final orbits. . . . .	119
4.13 An orbit chain that includes a clipped 2:3 resonant orbit is assembled and used to compute an optimal transfer from a DRO to an $L_3$ Lyapunov orbit. Contrast this result with that obtained from the alternate orbit chain displayed in Figure 4.5(b) which includes an $L_4$ SPO. . . . .	120
4.14 An orbit chain that includes multiple members of the $L_2$ axial family as intermediate links is used to compute an optimal transfer from an $L_2$ Lyapunov to an $L_2$ vertical orbit. . . . .	121
4.15 Low-thrust transfer from an $L_4$ SPO to an $L_1$ Lyapunov orbit in the Earth-Moon CR3BP. An orbit chain approach leveraging dynamical structures from the CR3BP+LT is utilized. Unlike its natural CR3BP counterpart, the $L_4$ SPO generated in the CR3BP+LT offers manifolds that are leveraged for trajectory design. . . . .	123

Figure	Page
4.16 Low-thrust transfer from a DRO to an $L_4$ Lyapunov orbit in the Earth-Moon CR3BP. This transfer is computed with a direct multiple shooting algorithm using the orbit chain initial guess depicted in 4.6(a). . . . .	128
5.1 Concept for the Gateway spacecraft [93]. . . . .	140
5.2 Schematic of trajectory design framework for computing optimal Gateway transfers beginning with an orbit chain initial guess. . . . .	145
5.3 Missed thrust analysis schematic. (a) An evenly spaced missed thrust time interval is applied to an existing low-thrust solution and time margin is appended to the end of the trajectory. (b) A thrust outage period is enforced on the newly modified trajectory, and the added margin is utilized to achieve the desired end state. . . . .	149
5.4 Orbits of interest for the Gateway spacecraft. . . . .	152
5.5 Subsets of the orbit families from which intermediate links are selected for the construction of orbit chains that link the chosen NRHO and DRO. . . . .	154
5.6 Jacobi constant values as a function of orbital period for the orbits selected for the construction of orbit chains that link the chosen NRHO and DRO. . . . .	155
5.7 Orbit chain initial guess for an NRHO to DRO exterior type transfer plotted in position space. . . . .	156
5.8 Optimal exterior type transfer from an NRHO to a DRO, computed in the CR3BP and plotted in position space. . . . .	158
5.9 Orbit chain initial guess for an NRHO to DRO interior type transfer plotted in position space. . . . .	159
5.10 Optimal interior type transfer from an NRHO to a DRO, computed in the CR3BP and plotted in position space. . . . .	160
5.11 Optimal exterior and interior type transfers from an NRHO to a DRO, computed in an ephemeris model and plotted in the $xy$ -plane. . . . .	161
5.12 A subset of the southern members of the $L_2$ Halo orbit family colored according to Jacobi constant value. . . . .	163
5.13 Jacobi constant values as a function of orbital period for the orbits employed to construct orbit chains for the exterior and interior NRHO to low-amplitude $L_2$ halo transfers. . . . .	164
5.14 Orbit chain initial guess for an NRHO to low-amplitude $L_2$ halo exterior type transfer plotted in position space. . . . .	165

Figure	Page
5.15 Optimal exterior type transfer from an NRHO to a low-amplitude $L_2$ halo, computed in the CR3BP and plotted in position space. . . . .	166
5.16 Orbit chain initial guess for an NRHO to low-amplitude $L_2$ halo interior type transfer plotted in position space. . . . .	167
5.17 Optimal interior type transfer from an NRHO to a low-amplitude $L_2$ halo, computed in the CR3BP and plotted in position space. . . . .	168
5.18 Optimal exterior and interior type transfers from an NRHO to a low-amplitude halo orbit, computed in an ephemeris model. . . . .	170
5.19 Orbit families from which intermediate links are selected for the construction of orbit chains used to compute exterior and interior NRHO to an $L_1$ northern NRHO transfers. . . . .	171
5.20 Jacobi constant values as a function of orbital period for the orbits employed to construct orbit chains for the exterior and interior NRHO to low-amplitude $L_2$ halo transfers. . . . .	172
5.21 Orbit chain initial guess for an NRHO to an $L_1$ northern NRHO exterior type transfer plotted in position space. . . . .	173
5.22 Optimal exterior type transfer from an NRHO to an $L_1$ northern NRHO, computed in the CR3BP and plotted in position space. . . . .	174
5.23 Orbit chain initial guess for an NRHO to an $L_1$ northern NRHO interior type transfer plotted in position space. . . . .	176
5.24 Optimal interior type transfer from an NRHO to an $L_1$ northern NRHO, computed in the CR3BP and plotted in position space. . . . .	177
5.25 Optimal exterior and interior type transfers from the 9:2 NRHO to a northern $L_1$ NRHO, computed in an ephemeris model. . . . .	178
5.26 Missed thrust analysis results for 5 day thrust outage time. . . . .	183
5.27 Thrust profile and zoomed configuration space plot corresponding to the Gateway transfer from a 9:2 NRHO to a DRO. . . . .	184
5.28 Summaries of missed thrust analysis results when 7 and 14 day thrust outage times are employed. . . . .	187
6.1 Artist rendition of Lunar IceCube in lunar orbit. Credit: Morehead State University . . . . .	193
6.2 Baseline Lunar IceCube trajectory developed for a November 6 <sup>th</sup> , 2020 launch date and computed in an ephemeris model. . . . .	195

Figure	Page
6.3 Schematic of a trajectory design framework for the nominal Lunar IceCube mission profile. . . . .	197
6.4 Two views of a 2:1 synodic resonant halo orbit computed in the Sun-Earth-Moon BCR4BP and displayed in the Earth-Moon rotating frame. This orbit is generated about the Earth-Moon $L_2$ libration point, and is used as a staging orbit in the proposed design framework. . . . .	201
6.5 Comparison of the selected staging orbit in three different models. Significant differences in geometry are apparent between the three orbits, particularly when viewed in the X-Z plane. The CR3BP northern $L_2$ halo orbit possessing a 2:1 synodic resonance is used as an initial guess for the same orbit in the BCR4BP. The BCR4BP result is then employed as an initial guess for an ephemeris orbit with similar motion. . . . .	202
6.6 (a) Sample range for deployment trajectories in the creation of a Phase 1 map, plotted in the Earth-Moon rotating frame. The first coast period is 0.8 days, the thrust segment is 3 days, and the second coast section is 4 days. Thrust vectors span a range of $\alpha$ angle values from 0 to $360^\circ$ in the velocity-normal-binormal frame. Trajectories that impact the Moon are omitted. (b) Stable (blue) and unstable (magenta) manifold trajectories plotted in the Earth-Moon rotating frame and originating from the 2:1 resonant $L_2$ halo orbit displayed in Figure 6.4. . . . .	205
6.7 Illustration of the orientation of the thrust vector, $\mathbf{T}$ , in the velocity-normal-binormal (VNB) frame. The origin of this frame is centered on the spacecraft $S$ . The vector $\mathbf{r}$ is the position vector from the barycenter of the rotating frame to the spacecraft, and $\mathbf{v}$ is the spacecraft velocity expressed in the rotating frame. The cross product of these two vectors, $\mathbf{n} = \mathbf{v} \times \mathbf{r}$ , yields the angular momentum vector of the spacecraft with respect to the barycenter. The vector $\hat{n}$ is defined such that $\hat{v}$ , $\hat{n}$ , and $\hat{b}$ are an orthonormal set. . . . .	206
6.8 Map of $\Sigma_1$ intersections of the forward propagated $D$ and backward propagated $W^S$ trajectory arcs in the BCR4BP plotted in the Earth-Moon and Sun- $B_1$ rotating frames. Intersections are projected in the $xy$ -plane for both frames. This map is generated for the November 2020 deployment and using a $\Sigma_1$ Sun angle of $\theta_{S_1} = 318^\circ$ . . . . .	207
6.9 Backward propagation from the science orbit with a constant maximum thrust anti-velocity thrust vector. . . . .	210

Figure	Page
6.10 Map of $\Sigma_2$ intersections of the forward propagated $W^U$ and backward propagated $C$ trajectory arcs in the BCR4BP. Intersections are projected in the $xy$ -plane of the Earth-Moon rotating frame, and the Sun angle selected for $\Sigma_2$ is $\theta_{S_2} = 66^\circ$ . The zoomed view displays an intersection selected by the NN search algorithm. This map corresponds to the October 2018 deployment date and assumes an SOI epoch of midnight on September 24 <sup>th</sup> , 2019. . . . .	211
6.11 Initial guess for a transfer from the 2:1 synodic resonant E-M $L_2$ northern halo orbit to the 9:2 synodic resonant E-M $L_2$ southern near rectilinear halo orbit in the BCR4BP. . . . .	215
6.12 Initial guess and BCR4BP result for Phase 1 of the Lunar IceCube trajectory given a November 2020 deployment date. The resulting transfer requires 117 days and 0.10 kg of propellant. The initial guess is displayed in the Sun- $B_1$ ( $S-B_1$ ) and Earth-Moon (E-M) rotating (rot.) frames. . . .	217
6.13 Initial guess (a) and BCR4BP (b) solutions for Phase 1 of the Lunar IceCube trajectory given a June 2020 deployment date. The resulting BCR4BP transfer requires 140 days and 0.21 kg of propellant. The BCR4BP transfer is validated in an ephemeris model (c) where it maintains similar characteristics. . . . .	219
6.14 Initial guess (a) and BCR4BP (b) solution for Phase 1 of the Lunar IceCube trajectory given a March 2021 deployment date. The resulting transfer requires 194 days and 0.08 kg of propellant. The BCR4BP transfer is validated in an ephemeris model (c) where it maintains similar characteristics. . . . .	220
6.15 Initial guess (a) and BCR4BP (b) solution for Phase 1 of the Lunar IceCube trajectory given an October 2018 deployment date. The resulting transfer requires 110 days and 0.1 kg of propellant. The BCR4BP transfer is validated in an ephemeris model (c) where it maintains similar characteristics. . . . .	221
6.16 Phase 1 transfers computed in the BCR4BP and displayed in the Sun- $B_1$ rotating frame. For all four transfers the apoapse furthest from the Earth-Moon (E-M) barycenter occurs in the second or fourth quadrants of the Sun- $B_1$ rotating frame. This geometry leverages the tidal forces of the Sun to raise the periaipse of LIC about the E-M barycenter to the orbital radius of the Moon. . . . .	222

Figure	Page
6.17 Initial guess for Phase 2 of the Lunar IceCube trajectory. The endpoints of the unstable manifold and the low-thrust spiral trajectory are indicated with a black circle. This initial guess corresponds to the NN match highlighted in Figure 6.10 which is generated for the October 2018 deployment date. . . . .	224
6.18 Converged result for Phase 2 of the Lunar IceCube trajectory given the initial guess presented in Figure 6.17. The Phase 1 result for the October 2018 deployment is used to initialize this transfer. The resulting transfer requires 229 days and 0.5 kg of propellant. . . . .	226
6.19 Converged result for Phase 2 of the Lunar IceCube trajectory. This transfer is initialized using the Phase 1 result for the June 2020 deployment. . . . .	227
6.20 Converged result for Phase 2 of the Lunar IceCube trajectory. This transfer is initialized using the Phase 1 result for the March 2021 deployment. . . . .	228
6.21 Initial guess for Phase 2 of the Lunar IceCube trajectory generated for the November 2020 deployment date. . . . .	229
6.22 Converged result for Phase 2 of the Lunar IceCube trajectory. This transfer is initialized using the Phase 1 result for the November 2020 deployment. . . . .	230
6.23 Comparison of low-thrust spiral trajectories propagated in the BCR4BP and ephemeris models and displayed in a Moon-centered inertial frame. The ephemeris model includes the Earth, Moon, and Sun. . . . .	231
6.24 Projections of the optimal low-thrust transfer for LIC from the staging orbit to the 9:2 NRHO in the $xy$ -plane and $xz$ -planes. This transfer is initialized using the Phase 1 result for the March 2021 deployment. . . . .	233
6.25 Three-dimensional configuration space view and the thrust profile of the optimal low-thrust transfer for LIC from the staging orbit to the 9:2 NRHO. This transfer is initialized using the Phase 1 result for the March 2021 deployment. . . . .	235
6.26 Projections of the optimal low-thrust transfer for LIC from the staging orbit to the 9:2 NRHO in the $xy$ -plane and $xz$ -planes. This transfer is initialized using the Phase 1 result for the March 2021 deployment. . . . .	235

## ABSTRACT

Pritchett, Robert E. Ph.D., Purdue University, August 2020. Strategies for Low-Thrust Transfer Design Based on Direct Collocation Techniques. Major Professor: Kathleen C. Howell.

In recent decades the revolutionary possibilities of low-thrust electric propulsion have been demonstrated by the success of missions such as Dawn and Hayabusa 1 and 2. The efficiency of low-thrust engines reduces the propellant mass required to achieve mission objectives and this benefit is frequently worth the additional time of flight incurred, particularly for robotic spacecraft. However, low-thrust trajectory design poses a challenging optimal control problem. At each instant in time, spacecraft control parameters that minimize an objective, typically propellant consumption or time of flight, must be determined. The characteristics of low-thrust optimal solutions are often unintuitive, making it difficult to develop an *a priori* estimate for the state and control history of a spacecraft that can be used to initialize an optimization algorithm. This investigation seeks to develop a low-thrust trajectory design framework to address this challenge by combining the existing techniques of orbit chaining and direct collocation. Together, these two methods offer a novel approach for low-thrust trajectory design that is intuitive, flexible, and robust.

This investigation presents a framework for the construction of orbit chains and the convergence of these initial guesses to optimal low-thrust solutions via direct collocation. The general procedure is first demonstrated with simple trajectory design problems which show how dynamical structures, such as periodic orbits and invariant manifolds, are employed to assemble orbits chains. Following this, two practical mission design problems demonstrate the applicability of this framework to real world scenarios. An orbit chain and direct collocation approach is utilized to develop low-

thrust transfers for the planned Gateway spacecraft between a variety of lunar and libration point orbits (LPOs). Additionally, the proposed framework is applied to create a systematic method for the construction of transfers for the Lunar IceCube spacecraft from deployment to insertion upon its destination orbit near the Moon. Three and four-body dynamical models are leveraged for preliminary trajectory design in the first and second mission design applications, respectively, before transfers are transitioned to an ephemeris model for validation. Together, these realistic sample applications, along with the early examples, demonstrate that orbit chaining and direct collocation constitute an intuitive, flexible, and robust framework for low-thrust trajectory design.

## 1. INTRODUCTION

Science fiction has long imagined spacecraft of all shapes and sizes hurtling through space, bound for fantastic destinations. Rarely in these stories does anyone do anything as mundane as check the fuel gauge. While this makes for enthralling fiction it is, unfortunately, not a principle by which present spacecraft can operate. The strictures imposed by the reality of a limited fuel supply are often the driving forces behind spacecraft mission design. However, the recent development of innovative means of spacecraft propulsion have brought humanity's dreams of uninhibited space travel a little closer.

The field of low-thrust propulsion offers a variety of exciting advancements in spacecraft propulsion technology which exchange force for efficiency. Propelling a spacecraft via the explosive mixture of volatile chemicals is spectacular and powerful, but not efficient. A variety of alternatives to this type of chemical engine have been developed that fall under the broad label of low-thrust propulsion. This classification encompasses a variety of technologies from ion engines to solar sails. And, while the implementation of these technologies is recent, their conceptualization is not. Indeed, in correspondence with Galileo Galilei in the early 17<sup>th</sup> century, the astronomer Johannes Kepler postulated, “provide ships or sails adapted to the heavenly breezes, and there will be some who will brave even that void” [1]. Several centuries later, a far-sighted adventurer in Jules Verne's 1865 novel *From the Earth to the Moon* discusses the possibility of lunar travel and predicts that, “there will some day appear velocities far greater than [currently imagined], of which light or electricity will probably be the mechanical agent” [2]. While Kepler and Jules Verne were not the originators of low-thrust spacecraft propulsion, these quotes demonstrate that artists and visionaries were contemplating the concept well before it began to take physical form.

Though the scientific foundations of various low-thrust propulsion concepts were laid in the early 20<sup>th</sup> century, it would be many years before the promise of these technologies was more fully realized [3]. Some of the same visionaries that pioneered early rocket technology, were pivotal in the initial development of electric propulsion (EP), the form of low-thrust propulsion that is the focus of this investigation. Scientists and engineers such as Tsiolkovsky, Oberth, and Goddard recognized the potential of EP to radically transform space travel. The efficiency of low-thrust engines reduces the propellant mass required to achieve mission objectives and this benefit is frequently worth the additional time of flight incurred, particularly for robotic spacecraft. Development and testing of low-thrust engines have been underway since the 1950s [4]; however, the revolutionary possibilities of this technology have only been realized in recent decades with the stunning success of missions such as Deep Space 1, Dawn, and Hayabusa 1 and 2 [5–7]. Given these successes, many forthcoming missions, such as DESTINY+, Psyche, DART, and Gateway, plan to utilize low-thrust propulsion.

The best engine in the world (or out of it) is of little use unless there is some notion of where to point it to arrive at the intended destination. This task of determining a trajectory from point A to point B and how the engine will operate along this path falls to the mission designer. Recognizing the promise of low-thrust propulsion, mission designers have developed improved methods for designing low-thrust trajectories. However, low-thrust trajectory design still poses a challenging optimal control problem. At each instant in time, spacecraft control parameters that optimize an objective must be determined. This objective is frequently minimization of propellant consumption or time of flight. A primary challenge to solving this optimal control problem is the determination of an initial estimate for the state and control history of a spacecraft, i.e., an initial guess.

Whether a chemical or low-thrust engine is employed, the overall process of designing a trajectory is similar and typically begins with the development of an initial guess. Most algorithms employed to compute spacecraft trajectories are iterative. To obtain a final solution that satisfies all the requirements of the given problem, these

algorithms are first supplied with an initial estimate of that solution; then, successive updates are made to the initial guess until all the problem constraints are met, i.e., the algorithm *converges*. When the algorithm employed merely seeks to satisfy a set of constraints it is termed a *corrector*, and if the algorithm has the additional objective of minimizing some parameter it is called an *optimizer*. Given a poor initial guess, i.e., an *a priori* estimate that insufficiently resembles the final solution, a corrector or optimizer may not converge. Thus, the development of an initial guess is a nontrivial endeavor and the creation of improved methods for carrying out this step is a key area of research.

A primary challenge of low-thrust trajectory design is that the characteristics of optimal low-thrust solutions are often unintuitive, making it difficult to develop an adequate initial guess. Initial guess development is especially arduous in unfamiliar dynamical regimes where the natural flow characteristics that could be leveraged for design are unknown. An additional challenge is that many optimization techniques only provide local optimal solutions, and it is computationally expensive to employ methods that search the entire solution space for a global optimal result. This investigation seeks to develop a low-thrust trajectory design framework to address these challenges by combining the existing techniques of orbit chaining and direct collocation. Together, these two methods offer a novel approach for low-thrust trajectory design that is intuitive, flexible, and robust. Ultimately, improved methods for low-thrust trajectory design enable scientists and engineers to fully harness the promise of this revolutionary technology.

## 1.1 Problem Definition

The main goal of this investigation is the development of a framework that combines the strengths of an orbit chain technique and direct collocation method to facilitate versatile and robust low-thrust trajectory design, particularly in unfamiliar dynamical regimes. This strategy addresses two of the primary challenges of low-

thrust trajectory design, namely developing an initial guess and identifying solutions beyond a local optimum. The orbit chain approach offers a flexible scheme for linking dynamical structures to generate an initial guess for a corrections process, and direct collocation is a robust optimization method that is adaptable to many different trajectory design scenarios. The proposed framework is developed via the completion of three research objectives. First, a robust tool that implements a direct collocation scheme and is compatible with multiple dynamical models is created. Second, a framework for low-thrust trajectory design is developed that is based on an orbit chain approach and leverages direct collocation. Finally, the efficacy of the trajectory design framework is verified through application to realistic trajectory design scenarios. The first three chapters of this document present necessary background material and detail the completion of the first objective. Chapter 4 details the orbit chain and direct collocation low-thrust trajectory design framework created in fulfillment of the second objective. Lastly, Chapters 5 and 6 describe the Gateway and Lunar IceCube sample applications utilized to validate the proposed framework. Altogether this work offers a procedure for low-thrust trajectory design that offers solutions to the previously described formidable design challenges.

## 1.2 Previous Contributions

The work of many previous authors contributes to the development of the orbit chain and direct collocation approach and the application of this strategy to the selected design problems. The research that influences the creation of the design framework is discussed in the following sections, while the previous contributions to the Gateway and Lunar IceCube trajectory design problems are examined in the chapters dedicated to these problems.

### 1.2.1 Orbit Chain Approach

A variety of authors have explored techniques for trajectory design similar to the chaining approach leveraged in this investigation. For example, this strategy is employed in the context of the circular restricted three body problem (CR3BP) to link invariant manifolds that facilitate transfers between periodic orbits. Howell, Barden, and Lo demonstrate this approach and its applicability in their exploration of trajectories for what was to become the Genesis mission [8]. Koon et al. [9] further develop this application of dynamical systems theory by linking heteroclinic cycles with homoclinic orbits to form “dynamical chains” that reveal global flow within the CR3BP. These authors also expand their work to three dimensions and demonstrate its application to the design of a tour of the Jovian moons, among other examples [10]. Similarly, Ross and Lo describe the existence of a vast array of invariant manifold tubes emanating from three-body systems throughout the solar system that, when linked together, form an “Interplanetary Superhighway” [11]. The method of chaining together LPOs and their manifolds to form complex new periodic orbits is continued by Lo and Parker [12], as well as Parker et al. [13], who present a generalized approach for prescribing the itineraries of these chains.

More recently, Vaquero and Howell show that resonant orbits offer a wide array of trajectory arcs that may be similarly connected to design transfers between LPOs [14]. A framework for constructing transfers between LPOs using invariant manifolds is detailed by Haapala and Howell, and subsequently employed to generate and catalog a large number of such transfers [15]. Finally, Restrepo and Russell present a method of “Patched Periodic Orbits” that leverages an extensive database of periodic orbits [16] to quickly design low-energy transfers throughout the CR3BP by patching together successive periodic orbits [17]. While these works have many different applications, each employs a chaining strategy to link trajectories embedded within well-known dynamical structures, as this is a straightforward and practical approach to trajectory design. The present investigation builds upon these develop-

ments by assembling chains of various dynamical structures to alleviate the challenge of initial guess generation for low-thrust trajectory design.

### 1.2.2 Low-Thrust Trajectory Design with Direct Collocation

Many authors have leveraged direct collocation to explore solutions to the challenging problem of low-thrust trajectory design. For example, Grebow, Ozimek, and Howell utilize this method to design lunar pole-sitting orbits [18,19]. The robustness and flexibility of collocation techniques enabled the discovery of these orbits despite crude initial guesses. Herman offers various improvements to collocation methods for low-thrust trajectory optimization, and demonstrates a variety of low-thrust transfers within the Earth-Moon system [20]. Similarly, Parrish et al. provide a number of low-thrust transfers within the same regime computed with collocation [21]. Parrish et al. constructs initial guesses for these transfers by stacking ballistic revolutions of periodic orbits generated in the Earth-Moon CR3BP. A straightforward approach to generating low-thrust transfers that leverages a similar initial guess assembly technique involving stacking and chaining orbits is described by Pritchett, Howell, and Grebow [22]. This framework is expanded upon in subsequent work by these authors which demonstrates the wide variety of trajectory segments that can be incorporated into the initial guess generation procedure [23,24]. Overall, these recent applications of direct collocation for low-thrust trajectory design demonstrate that the robustness and adaptability of this method make it a powerful tool.

### 1.3 Current Work

This investigation builds upon the work of the authors cited above to combine an orbit chain technique and direct collocation into a systematic framework that retains the strengths of these individual approaches. This document describes the development and testing of this framework via the fulfillment of the research objectives. It is organized as follows:

- Chapter 2: Dynamical Models

The three dynamical models employed in this investigation are presented, beginning with the Circular Restricted Three-Body Problem (CR3BP). A derivation of the equations of motion for the CR3BP expressed in a rotating frame is presented and several features of this dynamical model are highlighted, including the existence of equilibrium points and an integral of the motion. Following this, the Bicircular Restricted Four-Body Problem (BCR4BP) is presented and its epoch dependence is discussed. Furthermore, a formulation for transforming states between a  $P_1$ - $P_2$  rotating frame and a Sun- $B_1$  rotating frame is offered. Next, the equations of motion are provided for the high-fidelity ephemeris model utilized to validate trajectories generated in the CR3BP and BCR4BP. Finally, the inclusion of an additional low-thrust force in any of the aforementioned models is discussed and realistic values for such a force are offered.

- Chapter 3: Low-Thrust Trajectory Design and Optimization

Low-thrust trajectory design is cast as a continuous optimal control problem, and a general form of this problem is stated. The categories of methods employed to solve this problem are discussed, focusing on direct optimization. Concepts central to the direct optimization approach, e.g., the nonlinear programming problem and Newton's method, are presented. Direct collocation, the direct optimization scheme employed in this investigation, is outlined, along with the specific implementation of this algorithm employed here.

- Chapter 4: Orbit Chain Technique for Low-Thrust Trajectory Design

Examples of the various types of dynamical structures utilized by the orbit chain technique are presented. Then a transfer scenario from a distant retrograde orbit to a Lyapunov near the Earth-Moon  $L_3$  libration point is used to illustrate the essential steps of the orbit chain and direct collocation framework. Following this, more examples of the orbit chain and direct collocation technique are provided that highlight aspects of the robustness and flexibility of the method.

Some of these results are compared to a low-thrust trajectory computed with a direct multiple shooting algorithm, and the differences between these two approaches are discussed. Finally, the role various parameters of the orbit chain and direct collocation technique play in the convergence process is qualitatively examined.

- Chapter 5: Gateway Mission Design

The orbit chain and direct collocation technique is applied to design optimal low-thrust transfers for the Gateway spacecraft from the 9:2 synodic resonant near rectilinear halo orbit (NRHO) to three other libration point orbits near the Moon. Background information on the Gateway spacecraft is followed by a description of the methodology employed to compute low-thrust transfers and conduct missed thrust analysis. Transfers from the 9:2 NRHO to a distant retrograde orbit (DRO), a low-amplitude halo orbit, and a northern  $L_1$  NRHO are computed in the CR3BP and transitioned to an ephemeris model. Exterior and interior type transfer geometries are obtained from the 9:2 NRHO to each destination orbit. A missed thrust analysis is conducted for the exterior transfer to the DRO and insight on sensitive areas of the baseline trajectory is gained.

- Chapter 6: Lunar IceCube Mission Design

The orbit chain and direct collocation technique is utilized within a systematic procedure for designing an end-to-end low-thrust transfer for the Lunar IceCube spacecraft. In total, this transfer takes Lunar IceCube from deployment near the Earth to insertion upon its destination orbit near the Moon. The proposed framework divides the trajectory design challenge into two distinct phases connected by a staging orbit at the Earth-Moon  $L_2$  libration point. The BCR4BP is utilized for trajectory design because this allows the perturbing acceleration of the Sun to be leveraged to achieve the change in energy required to reach the destination orbit. The proposed framework is employed to design transfers to either a low lunar orbit or the 9:2 NRHO. Transfers are computed for multiple

deployment dates and in each case, Lunar IceCube is delivered to the final orbit with significant reserves of propellant. Finally, sections of the transfers developed for each deployment date are successfully transitioned to an ephemeris model.

- Chapter 7: Conclusions

A summary of the results presented in preceding chapters is provided along with recommendations for future work.

## 2. DYNAMICAL MODELS

Every trajectory design problem begins by defining the universe. While this freedom is sadly lacking in everyday life, it is a legitimate choice for the mission designer. In this case, the “universe” is comprised of the set bodies and forces that govern the motion of a spacecraft and, for this reason, it is more aptly termed a dynamical model. The spacecraft that will ultimately utilize the results of the mission designer’s efforts is consigned to abide by the dynamics of the actual universe. However, the set of models employed to design trajectories for this spacecraft need not capture every reality. Indeed, if it were even possible, this choice would lead to an overly complex dynamical model. In reality, a relatively small number of forces deliver the most significant contributions to a spacecraft’s motion at any given time, and the design problem is greatly simplified by incorporating only these forces.

The mission design process often begins with the simplest possible dynamical model that adequately captures the major forces in a problem. For example, the design of an orbit at a Lagrange point must, at least, include the two bodies whose gravitational interactions define this equilibrium point. After a preliminary solution is developed in this simpler dynamical model, it is recomputed in a higher-fidelity one. The process of increasing the model’s fidelity occurs in one step or many, but it always leads to a final result that is validated in one or more highly accurate models that are employed for the actual flight of the spacecraft. The strategy of starting simply and gradually increasing complexity often saves time and frequently leads to superior solutions compared to an approach that conducts the entire design process in a model of the highest possible complexity.

Many different dynamical models are available and each possesses distinct advantages for use in various mission design scenarios. The models in this investigation all originate from the N-body dynamical model first described by Newton and governed

by his well known three laws. From this model, the two, three, and four-body problems and their respective variants are derived. Although other options are available, the increasing complexity of these models typically limits rigorous analytical analysis to these three options.

## 2.1 N-Body Model

Issac Newton's groundbreaking work *Philosophiæ Naturalis Principia Mathematica*, published in 1687, introduced his three laws of motion as well as, the universal law of gravitation [25]. While subsequent discoveries have uncovered more accurate models of gravity and its effects, Newton's classic laws of motion are often sufficient to model the gravitational interactions for the purpose of spacecraft trajectory design. When combined, Newton's second law of motion and universal law of gravitation yield an expression that represents the gravitational interaction of  $\mathbb{N}$  point masses,  $P_i$ . In vector form, this expression is,

$$M_i \tilde{\mathbf{R}}_i'' = -\tilde{G} \sum_{\substack{j=1 \\ j \neq i}}^{\mathbb{N}} \frac{M_i M_j}{\tilde{R}_{ji}^3} \tilde{\mathbf{R}}_{ji}, \quad (2.1)$$

where  $\tilde{G}$  is the universal gravitational constant and  $\tilde{\mathbf{R}}_i''$  is the second derivative of the position vector defined from the inertially fixed origin to the particle  $P_i$  with mass  $M_i$ . Vector and matrix quantities are denoted with a bold typeface, and the tilde symbol above a variable indicates a dimensional quantity. The relative position vector of particle  $P_i$  with respect to particle  $P_j$  with mass  $M_j$  is expressed,  $\tilde{\mathbf{R}}_{ji} = \tilde{R}_i - \tilde{R}_j$ , and the scalar magnitude of this vector is written,  $\tilde{R}_{ji} = \|\tilde{\mathbf{R}}_{ji}\|$ , where the  $l^2$ -norm is used to calculate magnitude. Figure 2.1 offers a schematic that demonstrates these vector relationships between massive bodies. The unit vectors,  $\hat{X}$ ,  $\hat{Y}$ , and  $\hat{Z}$ , define the axes of an inertially fixed frame, and are denoted as unit vectors by the carat symbol above each variable. Collecting differential equations in the form of Equation (2.1) generates an increasingly intractable system as  $\mathbb{N}$  grows larger. Thus, simplifying assumptions

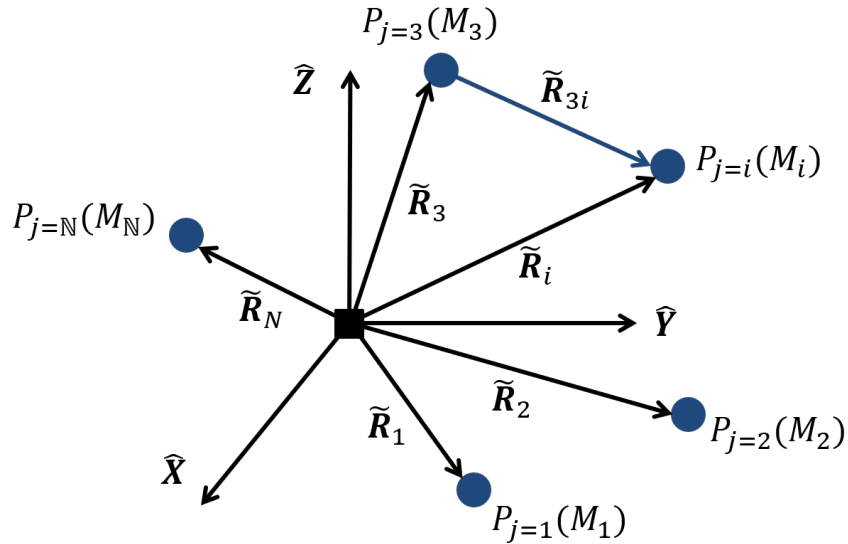


Fig. 2.1. Vector diagram of an  $\mathbb{N}$ -Body System

are applied to systems with low values of  $\mathbb{N}$  for the purpose of preliminary trajectory design.

The least complex systems occurs when  $\mathbb{N} = 2$ . This system is denoted the two-body problem and has been a problem of interest to mathematicians for hundreds of years. By rearranging terms such that one of the bodies in this systems is treated as an inertially fixed base point, and assuming that the other body has a negligible mass compared to the first body, an analytical solution to the two-body system is derived. This analytical solution generates orbits that are conic sections, e.g., circles, ellipses, and hyperbolas. These simple closed-form solutions render reasonably accurate approximations for the motion of many celestial bodies. Indeed, the paths described by these orbits closely match the observations made by Kepler prior to the publication of Newton's work. The solutions of the two-body problem were especially useful when computational capabilities were more limited. However, the rapid advancement of computing power over the last 75 years has enabled feasible examination of motion in more complex dynamical models. As a result, a new and diverse set of tools for understanding gravitational interactions has emerged.

While increasing the value of  $N$  leads to a more complex dynamical model, it also improves the accuracy of solutions generated. In some cases, the two-body problem is wholly sufficient for preliminary mission design. For example, the design of a trajectory for a satellite in low-Earth orbit typically does not need to consider any forces outside those exerted by the Earth until the latter stages of the trajectory design process. However, trajectory design for other missions cannot even begin without the introduction of an additional gravitational body. For example, trajectory design to one of the Sun-Earth libration points must include at least the two bodies whose mutual gravitational interaction generates these points, e.g., the Earth and Sun. Thus, the benefits of increased accuracy must be carefully weighed against the disadvantages of heightened complexity when considering whether to increase the value of  $N$ .

## 2.2 Circular Restricted Three-Body Problem

The limitations of the two-body problem sometimes necessitate the introduction of one or more gravitational bodies. A primary limitation of the two-body model is that it often requires a piecemeal approach to mission design. Furthermore, the effects of additional gravitational fields are typically only included in the two-body problem as perturbations. While this approach is successful in certain dynamical regimes, it obscures the impact of these additional forces when they contribute more than simple perturbations, and prevents them from being more fully leveraged in the mission design process. Admitting one additional gravitational field into the dynamical model yields the three-body problem (3BP), where  $N = 3$ . This expanded model possesses no closed-form analytical solution and even by the year 1900 it was clear that insight into the three-body problem requires a fundamental shift in approach. This new strategy begins by reducing the problem to its most essential elements, a process that yields the circular restricted three-body problem (CR3BP). Analysis in the CR3BP has produced a wealth of dynamical insights that, in turn, have resulted in innovative

approaches to mission design. The CR3BP model is particularly useful for low-thrust trajectory design, and for this reason, it is the primary dynamical model explored in this investigation.

### 2.2.1 Assumptions

Derivation of the CR3BP equations of motion begins by setting  $N = 3$  in Equation (2.1). This choice limits the number of active gravitational fields to three, corresponding to the three particles  $P_1$ - $P_3$ . The motion of  $P_3$  is assumed to be the focus, thus,

$$M_3 \tilde{\mathbf{R}}_3'' = -\frac{\tilde{G}M_3M_1}{\tilde{R}_{13}^3} \tilde{\mathbf{R}}_{13} - \frac{\tilde{G}M_3M_2}{\tilde{R}_{23}^3} \tilde{\mathbf{R}}_{23}, \quad (2.2)$$

represents the vector differential equation that describes the motion of  $P_3$ . Solving for the motion of  $P_3$  from Equation (2.2) requires knowledge of the time histories of  $P_1$  and  $P_2$ ; however, because these particles are themselves influenced by the motion of  $P_3$ , such information is generally not available *a priori*. Therefore, a solution of Equation (2.2) necessitates that the equations of motion of all three particles be solved simultaneously. When Cartesian coordinates are employed, integrating the equations of motion simultaneously requires six scalar integrals per particle, three for position and three for velocity. Thus, a total of 18 constants of integration are needed; but only 10 constants of integration are known to exist in this problem. Six of these constants are obtained from the conservation of linear momentum, three from conservation of angular momentum, and one from conservation of energy. Because an insufficient number of integration constants are available, a time history for the motion of all three bodies is not available analytically. However, several assumptions can transform the problem into a more tractable form.

Three key assumptions reduce the complexity of the three-body problem. First, the mass of the third particle,  $P_3$ , is assumed to be infinitesimal compared to the masses of  $P_1$  and  $P_2$ , e.g.,  $M_3 \ll M_2 < M_1$ . Because the masses of these latter two bodies are assumed to be much larger than that of  $P_3$ , these bodies are termed the “primaries”. The result of this assumption is that the motion of the primaries is not

influenced by  $P_3$ ; this scenario is a reasonable approximation for many applications, for example, the path of a spacecraft under the gravitational influence of the Sun and a planet. Another consequence of this assumption is that the motion of the primaries can be modeled in terms of conics, which leads to the second assumption. From the large set of potential closed conics, the primary system orbit may be assumed to be circular. Again this simplification is reasonable for many celestial systems of interest such as the Earth-Moon or Sun-Jupiter systems, where the relative orbit eccentricity is very small. The final assumption is that the mass of the first primary is greater than the second,  $M_1 > M_2$ . Therefore, the primaries orbit about a common barycenter located near  $P_1$  as shown in Figure 2.2. Depending on the mass ratio of  $M_1$  and  $M_2$ ,

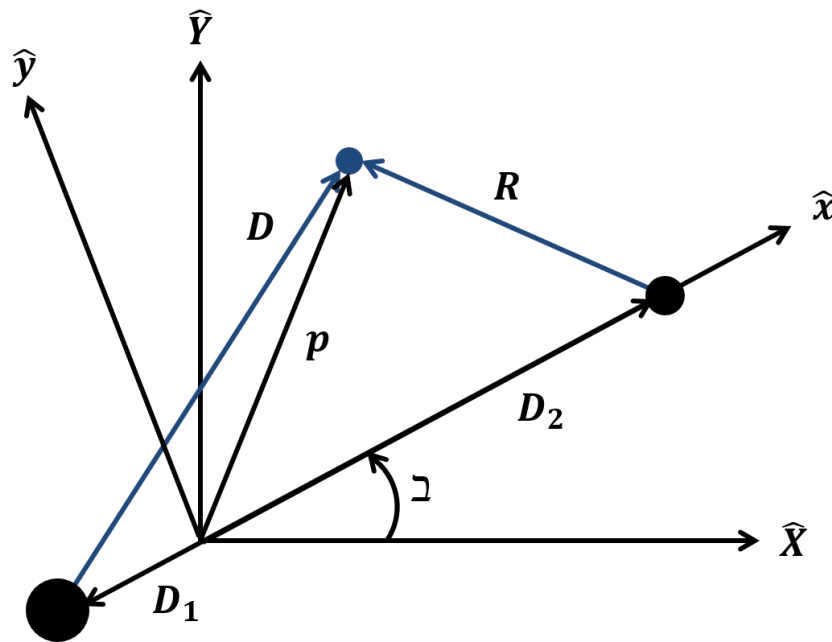


Fig. 2.2. Circular-Restricted Three-Body Problem

the barycenter may even be located beneath the surface of the body corresponding to  $P_1$ . Together, these simplifications reduce the three-body problem to the circular restricted three-body problem (CR3BP) offering a decrease in complexity that still reasonably approximates the motion in a three-body system.

### 2.2.2 Coordinate Frames

Motion in a dynamical model is defined relative to a reference frame, and, as seen with the two-body problem, intelligent selection of this frame can lead to a more manageable and intuitive problem definition. The formulation of many dynamical models begins with the establishment of an inertial reference frame, i.e., a frame that is theoretically at rest or moving at a constant linear velocity. Define an inertial reference frame,  $\mathcal{I}$ , with origin fixed at the barycenter of the primary system and unit vectors  $\hat{X}$  and  $\hat{Y}$  spanning the fixed plane of motion of  $P_1$  and  $P_2$ . A third unit vector,  $\hat{Z}$ , is defined such that  $\mathcal{I}$  is a right-handed coordinate system. The out-of-plane unit vector,  $\hat{Z}$ , is aligned with the orbital angular momentum vector of the primary system.

Viewing motion from a reference frame that rotates with the primary system can improve the understanding and analysis of dynamical behavior. Define a rotating coordinate system,  $\mathcal{R}$ , that is initially aligned with the inertial system,  $\mathcal{I}$ . The frame  $\mathcal{R}$  represents a simple rotation about the out-of-plane direction, i.e.,  $\hat{Z}$ , through the angle  $\beth$ . The frame  $\mathcal{R}$  is defined by the orthonormal triad  $\hat{x}, \hat{y}, \hat{z}$ . The  $\hat{x}$ -axis of  $\mathcal{R}$  is defined along the line passing through the primaries and is directed toward  $P_2$ ;  $\hat{z}$  remains aligned with  $\hat{Z}$ . Finally,  $\hat{y}$  completes the right handed coordinate system; thus, it is perpendicular to  $\hat{x}$  and in the plane of motion of the primaries. The time rate of change  $\dot{\beth}$ , is the magnitude of the angular velocity of the primary system,  ${}^{\mathcal{I}}\boldsymbol{\omega}^{\mathcal{R}} = \dot{\beth}\hat{z}$ . Because the path of the primaries is circular,  $\dot{\beth}$  is a constant value equal to the mean motion,  $\mathcal{N}$ , of the two-body system, thus,  $\beth = \mathcal{N}t$ . The inertial and rotating coordinate frames are related by the angle  $\beth$ , therefore, vectors are transformed between frames using a simple direction cosine matrix (DCM).

$$\begin{Bmatrix} X \\ Y \\ Z \end{Bmatrix} = \begin{bmatrix} \cos(\dot{\mathcal{N}}t) & -\sin(\dot{\mathcal{N}}t) & 0 \\ \sin(\dot{\mathcal{N}}t) & \cos(\dot{\mathcal{N}}t) & 0 \\ 0 & 0 & 1 \end{bmatrix} \begin{Bmatrix} x \\ y \\ z \end{Bmatrix}. \quad (2.3)$$

The DCM in Equation (2.3) permits the straightforward transformation of vectors from the rotating to the inertial frames, and the opposite transformation is enabled by the transpose of this DCM.

### 2.2.3 Formulation of the CR3BP Equations of Motion

Expressing the equations of motion in the rotating frame eliminates explicit dependence on time  $t$ . Thus, Equation (2.2) is rewritten using quantities defined within the rotating frame. Figure 2.2 shows that the barycenter,  $B$ , defined by  $P_1$  and  $P_2$ , is utilized as the inertially fixed basepoint for both the inertial and rotating frames. Uppercase and lowercase variable names are employed to distinguish between quantities expressed in the inertial and rotating frames, respectively. An exception to this rule is mass, which is equivalent in both frames. Therefore, the relative position vectors from  $P_1$  and  $P_2$  to  $P_3$  are,

$$\tilde{\mathbf{r}}_{13} = (\tilde{x} - \tilde{x}_1)\hat{x} + (\tilde{y} - \tilde{y}_1)\hat{y} + (\tilde{z} - \tilde{z}_1)\hat{z} \quad (2.4)$$

$$\tilde{\mathbf{r}}_{23} = (\tilde{x} - \tilde{x}_2)\hat{x} + (\tilde{y} - \tilde{y}_2)\hat{y} + (\tilde{z} - \tilde{z}_2)\hat{z}, \quad (2.5)$$

where the variables  $\tilde{x}$ ,  $\tilde{y}$ , and  $\tilde{z}$  are the components of the position vector  $\tilde{\mathbf{r}}_3$ . The subscripts of the other position components indicate whether they correspond to  $\tilde{\mathbf{r}}_1$  or  $\tilde{\mathbf{r}}_2$ . Subscripts are omitted from the components of  $\tilde{\mathbf{r}}_3$  since the motion of  $P_3$  is the focus of this derivation. These new variable definitions allow Equation (2.2) to be rewritten as,

$$M_3^{\mathcal{I}}\tilde{\mathbf{r}}_3'' = -\frac{\tilde{G}M_3M_1}{\tilde{r}_{13}^3}\tilde{\mathbf{r}}_{13} - \frac{\tilde{G}M_3M_2}{\tilde{r}_{23}^3}\tilde{\mathbf{r}}_{23}, \quad (2.6)$$

where the superscript  $\mathcal{I}$  to the left of  $\tilde{\mathbf{r}}_3''$  indicates that the second derivative is observed from the inertial frame.

Analysis in the CR3BP is simplified by nondimensionalizing the quantities in Equation (2.6). This step transforms dimensional quantities that typically possess very different magnitudes, e.g., position and velocity, into nondimensional quantities with similar orders of magnitude. This trait is particularly useful for numerical

analysis because it reduces numerical error. To enable nondimensionalization, several characteristic quantities are defined, one for each type of fundamental measurement encountered in the differential equations. Distance is nondimensionalized using the characteristic length,  $l^*$ , defined as the constant distance between the primaries:

$$l^* = \tilde{r}_1 + \tilde{r}_2, \quad (2.7)$$

where  $\tilde{r}_1 = \|\tilde{\mathbf{r}}_1\|$  and  $\tilde{r}_2 = \|\tilde{\mathbf{r}}_2\|$ . Likewise, the characteristic mass,  $m^*$ , is defined as the sum of the masses of  $P_1$  and  $P_2$ , i.e.,

$$m^* = M_1 + M_2. \quad (2.8)$$

The characteristic time,  $t^*$ , is evaluated such that the nondimensional value of the universal gravitational constant,  $\tilde{G}$ , is equal to one,

$$t^* = \left[ \frac{(\tilde{r}_1 + \tilde{r}_2)^3}{\tilde{G}(M_1 + M_2)} \right]^{1/2} = \left[ \frac{(l^*)^3}{\tilde{G}m^*} \right]^{1/2}. \quad (2.9)$$

The designation of a characteristic time quantity permits the definition of a nondimensional time,

$$t = \frac{\tilde{t}}{t^*}, \quad (2.10)$$

such that time derivatives of nondimensional quantities are evaluated with respect to nondimensional time.

The choice for the definition of characteristic time also simplifies nondimensional mean motion. Recall that the motion of  $P_2$  with respect to  $P_1$  is assumed to be circular; thus, employing the definition of mean motion in a two-body system we can express the dimensional mean motion,  $\mathcal{N}$ , of the primaries as,

$$\mathcal{N} = \left( \frac{\tilde{G}m^*}{l^{*3}} \right). \quad (2.11)$$

It follows, then, that the nondimensional mean motion,  $n$ , is equal to unity,

$$n = \mathcal{N}t^* = \left( \frac{\tilde{G}m^*}{l^{*3}} \right) \left( \frac{l^{*3}}{\tilde{G}m^*} \right) = 1. \quad (2.12)$$

The period,  $P$ , of a circular orbit is related to mean motion by  $P = 2\pi/n$ , thus, the nondimensional period of the primaries in this formulation of the CR3BP is  $2\pi$ .

The expression for nondimensional mass in the equations of motion is supported by the definition of a mass ratio. The nondimensional mass of  $P_2$  is defined as the mass ratio,  $\mu$ .

$$\mu = \frac{M_2}{m^*} \quad (2.13)$$

By solving Equation (2.13) for  $M_2$ , substituting this expression into Equation (2.8), and rearranging, the nondimensional value of  $M_1$  is also defined using  $\mu$ .

$$1 - \mu = \frac{M_1}{m^*} \quad (2.14)$$

Therefore, only the mass ratio, and not  $M_1$  or  $M_2$ , need appear explicitly in the CR3BP equations of motion.

Another benefit of the mass ratio,  $\mu$ , is that it offers a useful metric for the characterization of a CR3BP system. The Earth-Moon system, the primary focus of this investigation, is represented in terms of a mass ratio  $\mu = .01215$ , which is relatively large compared to other CR3BP systems such as Saturn-Titan, where  $\mu = 0.000237$  or Sun-Jupiter with  $\mu = 0.000954$ . This difference in  $\mu$  implies that dynamical features that appear in the Earth-Moon system may not appear in lower mass ratio systems and vice versa. Tables 2.1 and 2.2 offer the characteristic quantity and  $\mu$  values for the Earth-Moon and Sun- $B_1$  systems, respectively, where  $B_1$  is the barycenter of the Earth-Moon system. These are the values employed for these quantities throughout this investigation.

The characteristic length  $l^*$  is applied to nondimensionalize quantities in Equation (2.6) that include units of length. First, the nondimensional vectors that appear in Figure 2.2 are defined,

$$\mathbf{r}_1 = \frac{\tilde{\mathbf{r}}_1}{l^*} \quad \mathbf{r}_2 = \frac{\tilde{\mathbf{r}}_2}{l^*} \quad \mathbf{r}_3 = \frac{\tilde{\mathbf{r}}_3}{l^*} \quad (2.15)$$

$$\mathbf{r}_{13} = \frac{\tilde{\mathbf{r}}_{13}}{l^*} \quad \mathbf{r}_{23} = \frac{\tilde{\mathbf{r}}_{23}}{l^*}, \quad (2.16)$$

where the absence of the tilde symbol denotes a nondimensional value. These definitions are employed, along with the mass ratio, to express the nondimensional location

Table 2.1.  
Characteristic quantity and mass ratio values for the Earth-Moon CR3BP

Parameter	Value
$l^*$	384747.99198 km
$m^*$	$6.04604 \times 10^{24}$ kg
$t^*$	375699.85904 sec
$\mu$	0.01215

Table 2.2.  
Characteristic quantity and mass ratio values for the Sun- $B_1$  CR3BP

Parameter	Value
$l^*$	149597894.00511 km
$m^*$	$1.98855 \times 10^{30}$ kg
$t^*$	5022636.42910 sec
$\mu$	$3.04042 \times 10^{-6}$

of  $P_1$  and  $P_2$ . To begin, the barycenter,  $B$ , i.e., the center of mass of the  $P_1$ - $P_2$  system, is expressed in the rotating frame as,

$$B\hat{x} = \frac{-M_1 r_1 \hat{x} + M_2 r_2 \hat{x}}{m^*} = \mathbf{0}, \quad (2.17)$$

where  $r_1 = \|\mathbf{r}_1\|$  and  $r_2 = \|\mathbf{r}_2\|$ . Figure 2.2 illustrates that  $\mathbf{r}_1$  and  $\mathbf{r}_2$  lie on the  $\hat{x}$ -axis, thus, these vectors as well as the vector locating the center of mass include only  $\hat{x}$  components. Substituting Equations (2.13) and (2.14) into Equation (2.17) yields,

$$-(1 - \mu)r_1 + \mu r_2 = 0. \quad (2.18)$$

Dividing Equation (2.7) by  $l^*$  generates  $r_1 + r_2 = 1$ , that is rearranged and substituted into Equation (2.18) to produce expressions for  $r_1$  and  $r_2$  in terms of  $\mu$ .

$$r_1 = \mu \quad (2.19)$$

$$r_2 = 1 - \mu \quad (2.20)$$

Thus, because  $\mathbf{r}_1$  and  $\mathbf{r}_2$  only contain components along the  $\hat{x}$ -axis, these vectors are succinctly expressed as  $\mathbf{r}_1 = -\mu\hat{x}$  and  $\mathbf{r}_2 = 1 - \mu\hat{x}$ . Furthermore, these vectors are employed along with the nondimensional counterparts of Equations (2.4) and (2.5) to express the relative position vectors as:

$$\mathbf{r}_{13} = (x + \mu)\hat{x} + y\hat{y} + z\hat{z} \quad (2.21)$$

$$\mathbf{r}_{23} = (x - 1 + \mu)\hat{x} + y\hat{y} + z\hat{z}. \quad (2.22)$$

Finally, the nondimensional quantities developed thus far are leveraged to rewrite Equation (2.6) in nondimensional form,

$$\frac{{}^{\mathcal{I}}d^2\mathbf{r}_3}{dt^2} = {}^{\mathcal{I}}\ddot{\mathbf{r}}_3 = -\frac{(1 - \mu)}{r_{13}^3}\mathbf{r}_{13} - \frac{\mu}{r_{23}^3}\mathbf{r}_{23}, \quad (2.23)$$

where  $\ddot{\mathbf{r}}_3$  denotes the 2<sup>nd</sup> derivative of the position vector  $\mathbf{r}_3$  with respect to nondimensional time observed from the inertial frame. While Equation (2.23) is written entirely with quantities expressed in the rotating frame, the final form of the equations of motion should instead express  $\ddot{\mathbf{r}}_3$  as an acceleration observed from the rotating frame.

The transformation of a derivative observed in one frame to the same derivative observed in another frame is enabled by the Basic Kinematic Equation (BKE). For example, the 1<sup>st</sup> derivative of  $\mathbf{r}_3$  with respect to nondimensional time observed in the inertial frame is related to the same quantity observed in the rotating frame by,

$$\frac{{}^{\mathcal{I}}d\mathbf{r}_3}{dt} = \frac{{}^{\mathcal{R}}d\mathbf{r}_3}{dt} + {}^{\mathcal{I}}\boldsymbol{\omega}^{\mathcal{R}} \times \mathbf{r}_3, \quad (2.24)$$

where  ${}^{\mathcal{I}}\boldsymbol{\omega}^{\mathcal{R}}$  is the angular velocity of the rotating frame relative to the inertial frame. As noted previously, a result of the assumptions of the CR3BP is that this angular

velocity is equivalent to the mean motion of  $P_1$  and  $P_2$ , thus,  ${}^{\mathcal{I}}\boldsymbol{\omega}^{\mathcal{R}} = n\hat{z}$ . Computing the 2<sup>nd</sup> derivative with respect to nondimensional time of Equation (2.24) and applying the BKE in the resulting expression produces an equation that relates the acceleration of  $\mathbf{r}_3$  observed in two different frames:

$$\frac{{}^{\mathcal{I}}d^2\mathbf{r}_3}{dt^2} = \frac{{}^{\mathcal{R}}d^2\mathbf{r}_3}{dt^2} + 2{}^{\mathcal{I}}\boldsymbol{\omega}^{\mathcal{R}} \times \frac{{}^{\mathcal{R}}d\mathbf{r}_3}{dt} + {}^{\mathcal{I}}\boldsymbol{\omega}^{\mathcal{R}} \times {}^{\mathcal{I}}\boldsymbol{\omega}^{\mathcal{R}} \times \mathbf{r}_3. \quad (2.25)$$

The second and third terms in Equation (2.25) are termed Coriolis and centrifugal accelerations, respectively, which contribute to the total acceleration of  $\mathbf{r}_3$  when observed in a rotating frame. The Cartesian components of each vector quantity on the right side of Equation (2.25) are substituted and the resulting expression is evaluated:

$$\frac{{}^{\mathcal{I}}d^2\mathbf{r}_3}{dt^2} = (\ddot{x} - 2n\dot{y} - n^2x)\hat{x} + (\ddot{y} + 2n\dot{x} - n^2y)\hat{y} + \ddot{z}\hat{z}. \quad (2.26)$$

Recall that the nondimensional mean motion,  $n$ , equals one. Thus, Equation (2.26) is simplified by substituting in this value.

A complete expression of the CR3BP equations of motion in the rotating frame offers insight on the individual terms that contribute to the motion of  $P_3$ . To obtain this complete expression, Equation (2.26) is substituted into the left side of Equation (2.23). Additionally, Equations (2.21) and (2.22) are used to replace  $\mathbf{r}_{13}$  and  $\mathbf{r}_{23}$  on the right side of Equation (2.23). The components of the resulting equation are written as three separate scalar equations:

$$\ddot{x} - 2\dot{y} - x = -\frac{(1-\mu)(x+\mu)}{r_{13}^3} - \frac{\mu(x-1+\mu)}{r_{23}^3} \quad (2.27)$$

$$\ddot{y} + 2\dot{x} - y = -\frac{(1-\mu)y}{r_{13}^3} - \frac{\mu y}{r_{23}^3} \quad (2.28)$$

$$\ddot{z} = -\frac{(1-\mu)z}{r_{13}^3} - \frac{\mu z}{r_{23}^3}, \quad (2.29)$$

where the fact that  $n = 1$  is employed to eliminate the appearance of this variable from the equations. Furthermore, the magnitudes of the relative position vectors are:

$$r_{13} = \sqrt{(x+\mu)^2 + y^2 + z^2} \quad (2.30)$$

$$r_{23} = \sqrt{(x+\mu-1)^2 + y^2 + z^2}. \quad (2.31)$$

In summary, Equations (2.27)-(2.29) are expressed in the coordinates of the rotating frame, and the scalar velocity and acceleration terms that appear in these equations are derivatives observed in the rotating frame. This system of second-order differential equations describes the motion of  $P_3$  under the influence of the primary system.

The equations of motion in the CR3BP model are also represented in terms of the gravitational potential function of the CR3BP. Because the equations of motion are expressed in the rotating frame, a pseudo-potential function,  $U^*$ , rather than the true potential  $U$  is utilized:

$$U^* = \frac{(1 - \mu)}{r_{13}} + \frac{\mu}{r_{23}} + \frac{1}{2}n^2(x^2 + y^2), \quad (2.32)$$

where the third term of this expression is introduced to accommodate the rotation of the coordinate frame. In the rotating coordinate frame is what differentiates the pseudo-potential from the true potential,  $U$ , formulated in the inertial frame. The equations of motion are then available in a more succinct form,

$$\ddot{x} - 2\dot{y} = \frac{\partial U^*}{\partial x} \quad (2.33)$$

$$\ddot{y} + 2\dot{x} = \frac{\partial U^*}{\partial y} \quad (2.34)$$

$$\ddot{z} = \frac{\partial U^*}{\partial z}. \quad (2.35)$$

This formulation also lends insight into the existence of an integral of motion and equilibrium solutions.

#### 2.2.4 Integral of Motion

In theory, Equations (2.27)-(2.29), supply all of the necessary information to solve for the motion of  $P_3$ . However, the equations are coupled and nonlinear; no general closed-form solution is currently known. Valuable insight into this challenging problem is supplied by an integral of motion, and the potential for such a quantity is

suggested by the existence of  $U^*$ . To derive such a quantity, use the dot product of acceleration with velocity.

$${}^{\mathcal{R}}\ddot{\mathbf{r}}_3 \cdot {}^{\mathcal{R}}\dot{\mathbf{r}}_3 = \ddot{x}\dot{x} + \ddot{y}\dot{y} + \ddot{z}\dot{z} = \frac{\partial U^*}{\partial x}\dot{x} + \frac{\partial U^*}{\partial y}\dot{y} + \frac{\partial U^*}{\partial z}\dot{z} \quad (2.36)$$

The pseudo-potential,  $U^*$ , is autonomous, i.e., not a function of time, therefore, the right side of Equation (2.36) is equivalent to the scalar derivative  $dU^*/dt$ . Thus, it is straightforward to integrate Equation (2.36) with respect to nondimensional time resulting in,

$$\frac{1}{2}(\dot{x}^2 + \dot{y}^2 + \dot{z}^2) = U^* + \textit{integration const.} \quad (2.37)$$

where the integration constant  $\mathfrak{J}$  is defined with a negative sign by convention. Equation (2.37) is more succinctly expressed as,

$$v^2 = 2U^* - \mathfrak{J}, \quad (2.38)$$

where  $v$  is the scalar magnitude of the velocity of  $P_3$ ,  $v = \|{}^{\mathcal{R}}\dot{\mathbf{r}}_3\|$ , as viewed by a rotating observer. Equation (2.38) is denoted Jacobi's integral and the integration constant  $\mathfrak{J}$  is labeled the Jacobi constant after the mathematician Carl Gustav Jacob Jacobi. This constant represents an energy-like quantity in the CR3BP. The Jacobi constant has various uses, such as approximating the energy change necessary for transfers and as a check on the accuracy of numerical integration. The Jacobi constant yields powerful insights into behavior within the CR3BP, especially when combined with particular solutions to the differential equations.

### 2.2.5 Equilibrium Solutions

Another strategy for gaining insight into the CR3BP is the search for equilibrium solutions. These particular solutions are states for which the first and second order differential equations evaluate to zero. Equilibrium states are located by recognizing

that, at any equilibrium point, the velocity and acceleration of  $P_3$  relative to the rotating frame equals zero. Thus, applied to Equations (2.27)-(2.29), the result is:

$$0 = -\frac{(1-\mu)(x_{eq} + \mu)}{r_{13eq}^3} - \frac{\mu(x_{eq} - 1 + \mu)}{r_{23eq}^3} + x_{eq} \quad (2.39)$$

$$0 = -\frac{(1-\mu)y_{eq}}{r_{13eq}^3} - \frac{\mu y_{eq}}{r_{23eq}^3} + y_{eq} \quad (2.40)$$

$$0 = -\frac{(1-\mu)z_{eq}}{r_{13eq}^3} - \frac{\mu z_{eq}}{r_{23eq}^3}, \quad (2.41)$$

where each equation is rearranged so that all nonzero terms appear on the right side. The subscript  $eq$  on the state variables indicates that these equations are satisfied at the equilibrium points. Equation (2.41) is only satisfied when  $z_{eq} = 0$ , thus all the equilibrium solutions are planar. Similarly, Equation (2.40) is satisfied with  $y_{eq} = 0$ , therefore, at least one or more of the equilibrium solutions are located on the  $x$ -axis of the rotating coordinate frame. To locate these collinear equilibrium solutions, recall that  $n = 1$  and substitute  $z_{eq} = y_{eq} = 0$  into Equation (2.39).

$$0 = -\frac{(1-\mu)(x_{eq} + \mu)}{|x_{eq} + \mu|^3} - \frac{\mu(x_{eq} - 1 + \mu)}{|x_{eq} - 1 + \mu|^3} + x_{eq} \quad (2.42)$$

Equation (2.42) yields five solutions for  $x_{eq}$ , two of which are imaginary and are neglected for the purposes of this evaluation. No closed-form solutions exist for Equation (2.42); therefore, the remaining three values of  $x_{eq}$  are solved for iteratively. This numerical process is aided by reformulating Equation (2.42) in terms of the displacement,  $\gamma_i$ , from the nearest primary. The three possible values of  $x_{eq}$  are defined as follows,

$$x_{eq1} = 1 - \mu - \gamma_1 \quad (2.43)$$

$$x_{eq2} = 1 - \mu + \gamma_2 \quad (2.44)$$

$$x_{eq3} = -\mu - \gamma_3. \quad (2.45)$$

These definitions indicate that one equilibrium point,  $x_{eq1}$ , is located between the two primaries on the  $x$ -axis, while  $x_{eq3}$  and  $x_{eq2}$  are outside  $P_1$  and  $P_2$ , respectively. Such a configuration appears in Figure 2.3, where the equilibrium points are numbered

consistent with the typical NASA convention. Equations (2.43)-(2.45) are substituted into Equation (2.42) yielding three possible scalar equations,

$$0 = -\frac{(1-\mu)}{(1-\gamma_1)^2} + \frac{\mu}{(\gamma_1)^2} + 1 - \mu - \gamma_1 \quad (2.46)$$

$$0 = -\frac{(1-\mu)}{(1+\gamma_2)^2} - \frac{\mu(\gamma_2)}{(\gamma_2)^2} + 1 - \mu + \gamma_2 \quad (2.47)$$

$$0 = \frac{(1-\mu)}{(\gamma_3)^2} + \frac{\mu}{(\gamma_3+1)^2} + -\mu + \gamma_3. \quad (2.48)$$

Newton's method is used, in combination with a reasonably accurate initial guess, to solve for  $\gamma_i$  in Equations (2.46)-(2.48). The resulting values of  $\gamma_i$  are substituted into Equations (2.43)-(2.45) to compute the positions of the collinear equilibrium points,  $L_1$ ,  $L_2$ , and  $L_3$ .

Two additional equilibrium points are located for  $y_{eq} \neq 0$  in Equation (2.40). When the equilibrium points are off the  $x$ -axis, the values of  $r_{13}$  and  $r_{23}$  must be equivalent to satisfy Equations (2.39) and (2.40). When  $r_{13} = r_{23}$ , two possible values for the location of the equilibrium point exist, i.e.,

$$x_{eq4,5} = \frac{1}{2} - \mu \quad (2.49)$$

$$y_{eq4,5} = \pm \frac{\sqrt{3}}{2}. \quad (2.50)$$

The points  $L_4$  and  $L_5$  are located on either side of the  $x$ -axis equidistant from the primaries and, for this reason, they are denoted the equilateral or triangular points. The locations of these points are also depicted in Figure 2.3. Note, when observed in an inertial frame,  $L_4$  appears to lead  $P_2$  by  $60^\circ$  while  $L_5$  lags by  $60^\circ$ .

### 2.3 Bicircular Restricted Four-Body Problem

The bicircular restricted four-body problem (BCR4BP) is a useful dynamical model because it offers some of the simplicity of the CR3BP, while including perturbations from a fourth gravitational body, thus,  $\mathbb{N} = 4$ . For mission scenarios that are not adequately modeled with the assumptions of the CR3BP alone, the BCR4BP

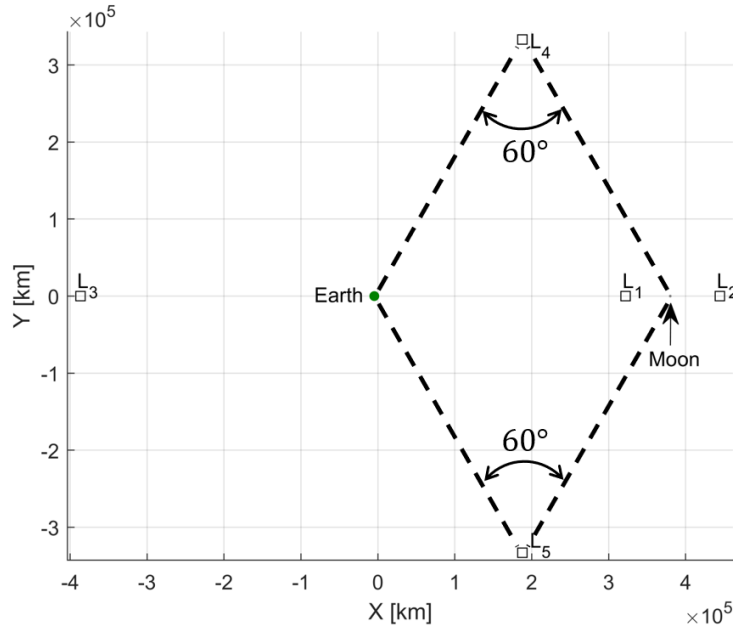


Fig. 2.3. Configuration of the Lagrange points in the Earth-Moon CR3BP as viewed in the rotating frame.

offers an alternative to conducting preliminary design in a full ephemeris model. For example, some missions that operate primarily in the Earth-Moon system are heavily influenced by the gravity of the Sun due to temporary excursions far beyond the radius of the Moon; thus, conducting design in a BCR4B model that includes the Earth, Moon, and Sun yields more accurate preliminary results. This investigation focuses exclusively on a BCR4BP model that includes these three gravitational bodies; however, the BCR4BP can be utilized to model many other collections of gravitational bodies, for example, other Planet-Moon-Sun systems or a binary asteroid system in heliocentric orbit. A more comprehensive analysis of the BCR4BP model utilized in this investigation is presented by Boudad [26, 27].

### 2.3.1 Assumptions

The BCR4BP adds to the assumptions of the CR3BP to supply a model that includes a fourth body without introducing an overwhelming increase in complexity. In this investigation, the Sun is the fourth body that is introduced to the three-body system, which consists of the primaries  $P_1$  and  $P_2$ , and the body of interest  $P_3$ . The first new assumption is that the Sun and the  $P_1$ - $P_2$  barycenter move in circular orbits about their mutual barycenter  $B_2$ . The barycenter of the  $P_1$ - $P_2$  system considered in Section 2.2 is redefined,  $B_1 = B$ , to distinguish it from the new barycenter,  $B_2$ . A second assumption is that the circular orbits of  $P_1$  and  $P_2$  are unaffected by the gravitational force of the Sun. A consequence of this assumption is that the BCR4BP is *not coherent* because the motion of  $P_2$  is not a dynamical result of the influence of  $P_1$  and the Sun. Other formulations of the BCR4BP that implement a coherent dynamical model are available, but are not implemented here [28]. These first two assumptions generate a dynamical model that consists of two nested circular orbits, hence the inclusion of the term *bicircular* in the model's title. Next, the restricted assumption of the CR3BP, namely that the mass of  $P_3$  is infinitesimally smaller than that of the other bodies, remains true in the BCR4BP, except that the mass of the Sun is now included, i.e.,  $m_3 \ll m_2 < m_1 < m_S$ . Finally, the circular orbits of the Sun- $B_1$  system and  $P_1$ - $P_2$  are assumed to be coplanar. Formulations of the BCR4BP that do not include this final assumption are available [26]; however, because the angle of the Earth-Moon orbital plane is only  $5^\circ$  relative to the ecliptic a coplanar assumption is reasonable for the applications considered here.

A new rotating coordinate frame, associated with the circular orbits of the Sun and  $B_1$ , is established to facilitate design and analysis in the BCR4BP. The origin of this new coordinate frame is located at  $B_2$ , and the axes of this coordinate frame are distinguished from those of the  $P_1$ - $P_2$  rotating frame by augmenting the variables with an apostrophe. Thus, the  $\hat{x}'$ -axis of the Sun- $B_1$  rotating frame is oriented along the line passing through  $B_1$  and the Sun and is directed towards the latter of these bodies,

as displayed in Figure 2.4. The  $\hat{z}'$ -axis is aligned with the orbital angular momentum

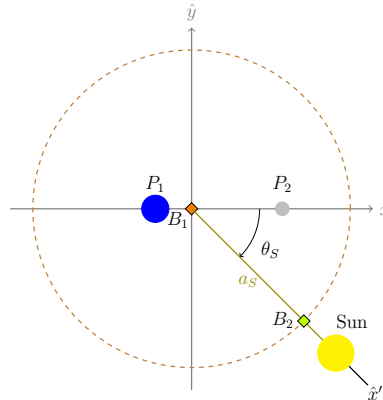


Fig. 2.4. Definition of the Sun angle in the Bicircular Restricted Four-Body Problem.

vector of the Sun- $B_1$  system, which, given the coplanar assumption is parallel to the angular momentum vector of the  $P_1$ - $P_2$  system. Finally, the  $\hat{y}'$ -axis completes the right-handed coordinate system. Another result of the coplanar assumption is that a single angle, the Sun angle,  $\theta_S$ , is relates the Sun- $B_1$  and  $P_1$ - $P_2$  reference frames. The angle between the  $\hat{x}'$  and the  $\hat{x}$  axes defines,  $\theta_S$ , as illustrated in Figure 2.4. The Sun angle orients the Sun within the  $P_1$ - $P_2$  frame, and changes continuously with time. The inclusion of a time-varying angle implies that the BCR4BP is time-dependent, i.e., a nonautonomous model unlike the CR3BP. Fortunately, the BCR4BP is still periodic; one period corresponds to a complete revolution of the Sun about  $B_1$  in the  $P_1$ - $P_2$  rotating frame. For the Earth-Moon-Sun system, this period is equivalent to the synodic period of the Moon, approximately 29.5 days. Because the BCR4BP remains periodic, analogs to some of the dynamical structures available in the CR3BP are available in this higher-fidelity model. However, computation and analysis of these structures is complicated by the fact that every state must be associated with a time or epoch. The Sun angle itself is employed to denote the epoch corresponding to a given state.

An alternative to the Sun angle for tracking the epoch in the BCR4BP is the  $P_1$ - $P_2$  angle,  $\theta_{P_2}$ , which is defined in the Sun- $B_1$  rotating frame. Figure 2.5 illustrates the angle as defined between the  $\hat{x}'$ -axis and the projection of the  $\hat{x}$ -axis in the Sun- $B_1$  rotating frame. From Figure 2.5, it is clear that a value of  $\theta_{P_2} = 0^\circ$  produces

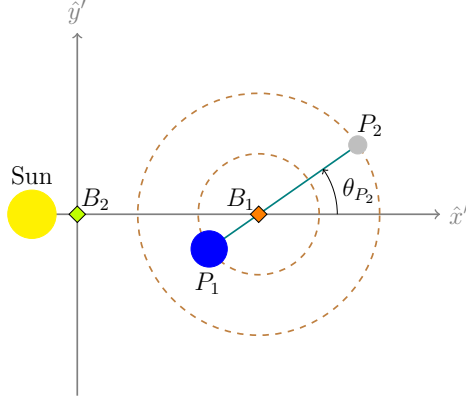


Fig. 2.5. Definition of the  $P_1$ - $P_2$  angle in the Bicircular Restricted Four-Body Problem.

a Sun- $P_1$ - $P_2$  alignment. Similarly, observation of Figure 2.4 reveals that a value of  $\theta_S = 0^\circ$  generates a  $P_1$ - $P_2$ -Sun alignment. Given the difference in the order of the bodies for these two alignments, it is evident that the Sun and  $P_1$ - $P_2$  angles are related by  $\theta_{P_2} = \theta_S - \pi$ . That is, when  $\theta_S = 0^\circ$ , then  $\theta_{P_2} = 180^\circ$ . This alternative epoch angle,  $\theta_{P_2}$ , is useful for computing a rotation matrix that transforms states from one rotating frame to another.

Two additional constant parameters complete the relationship between the Sun- $B_1$  and  $P_1$ - $P_2$  rotating frames. First, the distance from  $B_1$  to the Sun,  $a_S$ , establishes the orbital radii for the Sun and  $B_1$  with respect to  $B_2$ . In reality, this value oscillates with time, but a reasonable average value is selected over the time period of interest for a given problem. The second constant parameter is the mass of the Sun,  $m_S$ . This quantity, along with the location of the Sun, determines the nature of the additional acceleration imparted by the Sun in the BCR4BP. When employed within the BCR4BP equations of motion,  $a_S$  and  $m_S$  are nondimensionalized by the same

characteristic quantities that would be employed for the  $P_1$ - $P_2$  CR3BP. The definition of  $a_S$  and  $m_S$  permits the calculation of the nondimensional mean motion of the Sun in the inertial frame:

$$n_S = \sqrt{\frac{1 + m_S}{a_S^3}}. \quad (2.51)$$

The mean motion of the Sun in the inertial frame is related to the nondimensional angular velocity of the Sun as viewed in the  $P_1$ - $P_2$  frame by,

$$\omega_S = n_S - 1. \quad (2.52)$$

Thus, the angular velocity of the Sun in the BCR4BP is a constant value that is used to calculate the value of the Sun angle at any time as long as the initial value of the Sun angle,  $\theta_{S_0}$ , is known. The Sun angle at time  $t$  is given by,

$$\theta_S = \omega_S t + \theta_{S_0}, \quad (2.53)$$

where  $\theta_{S_0}$  operates as the initial epoch that determines the value of  $\theta_S$  at the current time. Table 2.3 offers the values of  $a_S$  and  $m_S$  employed in this investigation.

Table 2.3.  
Values of constant Sun parameters in the BCR4BP.

Parameter	Value
$\tilde{a}_S = a_S \cdot l^*$	149597894.00511 km
$M_S = m_S \cdot m^*$	$1.98855 \times 10^{30}$ kg

### 2.3.2 Equations of Motion

Motion in the BCR4BP is described by a set of differential equations similar to those of the CR3BP, but modified to accommodate the perturbing acceleration of the Sun. The  $P_1$ - $P_2$  rotating frame together with the Sun- $B_1$  rotating frame are commonly

employed for analysis in the BCR4BP, and the equations of motion for  $P_3$  may be expressed in either of these frames. The equations of motion for  $P_3$  expressed in terms of the  $P_1$ - $P_2$  frame are,

$$\ddot{x} = 2\dot{y} + x - \frac{(1-\mu)(x+\mu)}{r_{13}^3} - \frac{\mu(x-1+\mu)}{r_{23}^3} - \frac{m_S(x-x_S)}{r_{S3}^3} - \frac{m_S}{a_S^3}x_S \quad (2.54)$$

$$\ddot{y} = -2\dot{x} + y - \frac{(1-\mu)y}{r_{13}^3} - \frac{\mu y}{r_{23}^3} - \frac{m_S(y-y_S)}{r_{S3}^3} - \frac{m_S}{a_S^3}y_S \quad (2.55)$$

$$\ddot{z} = -\frac{(1-\mu)z}{r_{13}^3} - \frac{\mu z}{r_{23}^3} - \frac{m_S(z-z_S)}{r_{S3}^3} - \frac{m_S}{a_S^3}z_S, \quad (2.56)$$

where the vector  $\mathbf{r}_{S3}$  is the relative position vector from the Sun to  $P_3$ , and  $r_{S3} = \|\mathbf{r}_{S3}\|$ . This vector is computed by subtracting the position of the Sun relative to  $B_1$  from the position of  $P_3$  with respect to  $B_1$ , i.e.,  $\mathbf{r}_{S3} = \mathbf{r} - \mathbf{r}_S$ . The location of the Sun with respect to  $B_1$  is determined by,

$$\mathbf{r}_S = \begin{bmatrix} x_S \\ y_S \\ z_S \end{bmatrix} = \begin{bmatrix} a_S \cos(\omega_S t + \theta_{S_0}) \\ a_S \sin(\omega_S t + \theta_{S_0}) \\ 0 \end{bmatrix}. \quad (2.57)$$

Thus, the value of  $\mathbf{r}_{S3}$  must be updated at each instant in time when Equations (2.54)-2.56 are integrated.

As in the CR3BP, a pseudo-potential is also defined for the BCR4BP, and is useful for expressing the equations of motion in an abbreviated form. The pseudo-potential can be formulated in either the  $P_1$ - $P_2$  or Sun- $B_1$  rotating frames. In the  $P_1$ - $P_2$  rotating frame it is expressed as,

$$\Psi = \frac{1-\mu}{r_{13}} + \frac{\mu}{r_{23}} + \frac{1}{2}(x^2 + y^2) + \frac{m_S}{r_{S3}} - \frac{m_S}{a_S^3}(x_S x + y_S y + z_S z), \quad (2.58)$$

where the first three terms of the pseudo-potential are identical to those of the CR3BP pseudo-potential in Equation (2.32), and the final two terms incorporate the influence of the Sun. As a result of the Sun's inclusion, the value of the BCR4BP pseudo-potential varies with time in contrast to its CR3BP counterpart. The BCR4BP

equations of motion expressed in the  $P_1$ - $P_2$  rotating frame using the pseudo-potential are:

$$\ddot{x} - 2\dot{y} = \frac{\partial \Psi}{\partial x} \quad (2.59)$$

$$\ddot{y} + 2\dot{x} = \frac{\partial \Psi}{\partial y} \quad (2.60)$$

$$\ddot{z} = \frac{\partial \Psi}{\partial z}. \quad (2.61)$$

The pseudo-potential is also useful for describing the energy of the BCR4BP system in the form of the system Hamiltonian.

The pseudo-potential is also formulated in terms of coordinates and quantities expressed in the Sun- $B_1$  frame. Recall, variables expressed in this frame are augmented with an apostrophe, thus, the pseudo-potential in the Sun- $B_1$  frame is written,

$$\Psi' = \frac{1}{2}(x'^2 + y'^2) + \frac{1 - \mu_{SB_1}}{r'_{S3}} + \frac{\mu_{SB_1}(1 - \mu_{P_1P_2})}{r'_{13}} + \frac{\mu_{SB_1}\mu_{P_1P_2}}{r'_{23}}, \quad (2.62)$$

where  $\mu_{SB_1}$  is the mass ratio of the Sun- $B_1$  system and  $\mu_{P_1P_2}$  is the mass ratio of the  $P_1$ - $P_2$  system. If  $P_1$  and  $P_2$  are the Earth and the Moon, then these two mass ratios are presented in Tables 2.2 and 2.1, respectively. The  $\Psi'$  pseudo-potential is useful for developing equation of motion or the system Hamiltonian in the Sun- $B_1$  frame.

### 2.3.3 System Hamiltonian

The time dependence of the BCR4BP implies that the value of the pseudo-potential  $\Psi$  is not constant, thus,  $d\Psi/dt \neq 0$ , and an integral of the motion does not exist. However, the Hamiltonian, the total energy of the system, serves as a useful metric for analyzing the motion of  $P_3$  in the BCR4BP. The Hamiltonian is evaluated using coordinates expressed in the  $P_1$ - $P_2$  or Sun- $B_1$  rotating frames. The Hamiltonian values calculated in these two frames are similar in magnitude to the Jacobi constant values computed in either of these two frames; that is, the Jacobi

constant of the Sun- $B_1$  CR3BP is similar in magnitude to the BCR4BP Hamiltonian computed in the Sun- $B_1$  rotating frame,  $H_{SB_1}$ .

$$H_{P_1P_2} = 2\Psi - (\dot{x}^2 + \dot{y}^2 + \dot{z}^2) - \aleph \quad (2.63)$$

$$H_{SB_1} = 2\Psi' - (\dot{x}'^2 + \dot{y}'^2 + \dot{z}'^2) \quad (2.64)$$

The value of  $H_{P_1P_2}$  is scaled by a constant parameter  $\aleph$  that is included to offset the high value terms introduced by the Sun and ensure that  $H_{P_1P_2}$  is of a similar magnitude to the Jacobi constant value in the Earth-Moon CR3BP. Throughout this analysis,  $\aleph = 1690$  nondimensional units.

### 2.3.4 Coordinate Frame Transformation

The equations of motion of the BCR4BP are formulated within the  $P_1$ - $P_2$  rotating frame, thus, it is straightforward to plot the results in this same frame. However, it is frequently advantageous to observe trajectories in the Sun- $B_1$  rotating frame as well because analysis in this frame highlights the influence of the Sun on the motion of  $P_3$ . Therefore, a means of transforming states between the  $P_1$ - $P_2$  and Sun- $B_1$  rotating frames is necessary.

States are transformed from the  $P_1$ - $P_2$  rotating frame to the Sun- $B_1$  rotating via a single rotation. This rotation is about the  $\hat{z}$  axis and through the angle  $\pi - \theta_S$ . The DCM for this rotation is,

$$\mathbb{C} = \begin{bmatrix} \cos(\pi - \theta_S) & -\sin(\pi - \theta_S) & 0 \\ \sin(\pi - \theta_S) & \cos(\pi - \theta_S) & 0 \\ 0 & 0 & 1 \end{bmatrix}, \quad (2.65)$$

where the coordinate frame emerging from this rotation is the desired Sun- $B_1$  frame with axes  $\hat{x}'$ ,  $\hat{y}'$ , and  $\hat{z}'$ . Thus, the matrix  $\mathbb{C}$  is applied to a position vector to transform it from the  $P_1$ - $P_2$  to the Sun- $B_1$  rotating frame. The successful transformation of velocity vectors from the  $P_1$ - $P_2$  to the Sun- $B_1$  requires that  $\dot{\mathbb{C}}$ , the time derivative of  $\mathbb{C}$ , be computed. The derivative of each element of  $\mathbb{C}$  with respect to nondimensional

time  $t$  yields  $\dot{\mathbb{C}}$ . While time does not appear explicitly in Equation (2.65), recall that the variable  $\theta_S$  is a function of time,  $\theta_{P_2} = \omega_S t + \theta_{S_0}$ . Therefore, the variable  $\omega_S$  appears in some of the components of the  $\dot{\mathbb{C}}$  matrix, written as,

$$\dot{\mathbb{C}} = \begin{bmatrix} \omega_S \sin(\pi - \theta_S) & \omega_S \cos(\pi - \theta_S) & 0 \\ -\omega_S \cos(\pi - \theta_S) & \omega_S \sin(\pi - \theta_S) & 0 \\ 0 & 0 & 1 \end{bmatrix}. \quad (2.66)$$

Together  $\mathbb{C}$  and  $\dot{\mathbb{C}}$  enable states expressed in the  $P_1$ - $P_2$  rotating frame to be transformed to the Sun- $B_1$  rotating frame.

Once the rotation matrices  $\mathbb{C}$  and  $\dot{\mathbb{C}}$  are assembled, the transformation process from the  $P_1$ - $P_2$  to the Sun- $B_1$  rotating frame is accomplished. The matrices  $\mathbb{C}$  and  $\dot{\mathbb{C}}$  are combined into a single  $6 \times 6$  matrix that is employed to transform a row vector of position and velocity states between frames.

$$\begin{bmatrix} x' & y' & z' & \dot{x}' & \dot{y}' & \dot{z}' \end{bmatrix} = \begin{bmatrix} x & y & z & \dot{x} & \dot{y} & \dot{z} \end{bmatrix} \begin{bmatrix} \mathbb{C} & \dot{\mathbb{C}} \\ \mathbf{0} & \mathbb{C} \end{bmatrix} \quad (2.67)$$

Following the rotation, the result from Equation (2.67) is first dimensionalized using the characteristic quantities of the  $P_1$ - $P_2$  system and then nondimensionalized with the characteristic quantities of the Sun- $B_1$  system. The characteristic quantities and mass ratio employed to plot trajectories in the Sun- $B_1$  frame are the same as for a Sun- $B_1$  CR3B model. Finally, the origin for the position states of the rotated vector are shifted from  $B_1$  to  $B_2$ , by adding the nondimensional quantity  $(1 - \mu_{SB_1})$  to the  $x'$  component. If states in a  $B_1$ -centered Sun- $B_1$  frame are desired, then this final step is omitted.

## 2.4 Higher-Fidelity Modeling

While it is frequently beneficial to conduct preliminary mission analysis in a simplified dynamical model, all trajectory designs must be validated in a high-fidelity dynamical model before they are utilized for an actual mission. The  $\mathbb{N}$ -body ephemeris

model from Section 2.1 is frequently employed for this validation step. This model permits an arbitrary number of gravitational bodies to be included as perturbing influences and draws on highly accurate ephemeris data to update the states of these bodies. The inclusion of  $\mathbb{N}$  bodies in the dynamical model is most straightforward when the equations of motion are expressed in an inertial reference frame. Thus, all computations in the ephemeris model occur in an inertial frame and results are transformed into alternate frames as desired. The J2000 ecliptic frame is employed in this investigation; however, other frames, e.g., the J2000 Equatorial, are available. Furthermore, the DE438 ephemeris file from the Jet Propulsion Laboratory’s Navigation and Ancillary Information Facility is utilized to obtain ephemerides for all bodies included in this analysis.

The ephemeris model employs the  $\mathbb{N}$ -body equations of motion to compute the path of a particle of interest,  $M_i$ , whose mass is assumed to be negligible relative to the  $\mathbb{N} - 1$  other bodies included in the model. The motion of the particle of interest is typically expressed in an inertial reference frame that is fixed at one of the massive bodies, called the central body, with mass,  $M_q$ . The  $\mathbb{N} - 2$  other bodies included in the model are considered perturbing bodies with masses,  $M_j$ , and these exert additional accelerations on the particle of interest with mass,  $M_i$ . All massive bodies included in this model are assumed to be centrobaric point masses and their paths, relative to the central body, are defined at each instant in time with ephemeris data. Equation (2.1) is modified to supply an expression that describes the motion of  $M_i$  with respect to the central body  $M_q$  while under the gravitational influence of  $M_q$  and  $\mathbb{N} - 2$  other bodies. The modification process begins by defining the expression for the relative position vector from  $M_q$  to  $M_i$  and computing the second derivative of each term:

$$\tilde{\mathbf{R}}_{qi} = \tilde{\mathbf{R}}_i - \tilde{\mathbf{R}}_q \quad (2.68)$$

$$\frac{{}^I d^2 \tilde{\mathbf{R}}_{qi}}{dt^2} = \frac{{}^I d^2 \tilde{\mathbf{R}}_i}{dt^2} - \frac{{}^I d^2 \tilde{\mathbf{R}}_q}{dt^2} \quad (2.69)$$

This step yields an expression for the desired quantity, i.e., the acceleration of the relative position vector from  $M_q$  to  $M_i$  as observed from the inertial frame. Next, the

two terms on the right side in Equation (2.69) are expanded to produce an expression comprised solely of masses and position vectors. Equation (2.1) in Section 2.1 provides an expression for one of these two terms, that is,

$$M_i \frac{{}^I d^2 \tilde{\mathbf{R}}_i}{dt^2} = -\tilde{G} \sum_{\substack{j=1 \\ j \neq i}}^N \frac{M_i M_j}{\tilde{R}_{ji}^3} \tilde{\mathbf{R}}_{ji}, \quad (2.70)$$

where the second derivative is now written in Leibniz form for consistency with Equation (2.69). Recall that  $R_{ji} = \|\tilde{\mathbf{R}}_{ji}\|$ . An expression for the second term in Equation (2.69) is obtained in a similar manner, by replacing  $i$  with  $q$  in Equation (2.70) to represent the particle of interest:

$$M_q \frac{{}^I d^2 \tilde{\mathbf{R}}_q}{dt^2} = -\tilde{G} \sum_{\substack{j=1 \\ j \neq q}}^N \frac{M_q M_j}{\tilde{R}_{jq}^3} \tilde{\mathbf{R}}_{jq}. \quad (2.71)$$

Following these definitions, both sides of Equations (2.70) and (2.71) are divided by the mass terms  $M_i$  and  $M_q$ , respectively, to remove these variables from each equation. Then, the results of this operation are substituted into the appropriate terms in Equation (2.69) that yields,

$$\frac{{}^I d^2 \tilde{\mathbf{R}}_{qi}}{dt^2} = -\tilde{G} \sum_{\substack{j=1 \\ j \neq i}}^N \frac{M_j}{\tilde{R}_{ji}^3} \tilde{\mathbf{R}}_{ji} + \tilde{G} \sum_{\substack{j=1 \\ j \neq q}}^N \frac{M_j}{\tilde{R}_{jq}^3} \tilde{\mathbf{R}}_{jq}. \quad (2.72)$$

Next, the direction of the relative position vectors on the right side of Equation (2.72) are reversed, which effects a sign change on both terms, thus,

$$\frac{{}^I d^2 \tilde{\mathbf{R}}_{qi}}{dt^2} = \tilde{G} \sum_{\substack{j=1 \\ j \neq i}}^N \frac{M_j}{\tilde{R}_{ij}^3} \tilde{\mathbf{R}}_{ij} - \tilde{G} \sum_{\substack{j=1 \\ j \neq q}}^N \frac{M_j}{\tilde{R}_{qj}^3} \tilde{\mathbf{R}}_{qj}, \quad (2.73)$$

where this reversal in direction is conducted for consistency with the literature. The final form of the desired expression is generated by extracting the  $j = i$  iterate from the second term in Equation (2.73) and combining the remaining sums to yield,

$${}^I \ddot{\mathbf{R}}_{qi} = -G \frac{m_q}{R_{qi}^3} \mathbf{R}_{qi} + G \sum_{\substack{j=1 \\ j \neq i, q}}^N m_j \left( \frac{\mathbf{R}_{ij}}{R_{ij}^3} - \frac{\mathbf{R}_{qj}}{R_{qj}^3} \right). \quad (2.74)$$

As in the previous two models, the mass of the particle of interest in the  $\mathbb{N}$ -body ephemeris model is regarded as negligible and, therefore, does not appear in Equation (2.74). Furthermore, the quantities in Equation (2.74) are nondimensionalized with the characteristic quantities described in Section 2.2.3. The exact values of these quantities are a choice for the user and should be selected based upon the gravitational bodies included in the system.

Though an inertial reference frame is employed to compute trajectories in an ephemeris model, solutions are transformed into alternate frames for further analysis. The applications in this investigation include trajectories in the Earth-Moon system, thus, one of these two bodies is typically employed as the central body in the inertial frame while the other body, along with the Sun, are included as additional perturbing bodies. More than one approach for transforming trajectories from an Earth or Moon centered inertial frame to a barycentered rotating frame are available. Thorough details for the steps required to transform the states computed in an ephemeris model between the inertial and rotating frames are presented by Pavlak [29] and Das-Stuart [30]. The explanations offered by Das-Stuart are notable to illustrate two versions of the transformation process that yield different results each offering distinct advantages.

## 2.5 Low-Thrust Electric Propulsion

The dynamical models previously introduced all assume ballistic motion; that is, motion influenced solely by the naturally occurring forces within a model, e.g., those forces exerted by gravitational bodies. However, if the particle of interest in these simulations is a spacecraft, it is likely equipped with the means to introduce a force of its own. Low-thrust spacecraft, in particular, those propelled via solar electric propulsion, are the focus of this investigation; this type of spacecraft imparts a relatively small force over a long period of time to affect changes in the motion of a spacecraft. The gradual nature of low-thrust spacecraft requires that the accelerations

they introduce be included in the equations of motion of the dynamical model and integrated along with the naturally occurring accelerations.

Many options, over a wide range of fidelity, are available for modeling the force imparted by a low-thrust engine; a relatively simple model is employed in this investigation. The acceleration imparted by a low-thrust force,  $\mathbf{a}_T$ , is defined as,

$$\mathbf{a}_T = \frac{\mathbf{T}}{m_s}, \quad (2.75)$$

where  $\mathbf{T} = [T_x, T_y, T_z]$  and  $m_s$  is the spacecraft mass. Moreover, the magnitude of the thrust vector is determined by the  $l^2$ -norm,  $T = \|\mathbf{T}\|$ . The thrust vector indicates the direction of the force imparted by the low-thrust engine. This vector is expressed in any number of frames and rotated between them as illustrated for a position vector. Thus, Equation (2.3) is employed to transform the thrust vector from the rotating to an arbitrary inertial frame in the CR3BP and BCR4BP. Similarly, transformations in an ephemeris model that are typically applied to position vectors are also utilized for thrust vectors, although ensuring that the dimensionalization and nondimensionalization steps employ the appropriate characteristic quantities is a key step.

Many options for parameterizing the spacecraft mass and thrust vector are available; however, they all ultimately generate an acceleration vector of the form in Equation (2.75). The vector  $\mathbf{a}_T$  is split into its component parts and added to any of the equations of motion. It is essential to ensure that  $\mathbf{a}_T$  and the associated equations of motion are expressed in the same frame. Thus, while the thrust vector may be initially defined in a different frame, it is transformed to the frame consistent with the equations of motion before  $\mathbf{a}_T$  is calculated. In contrast, the value of the spacecraft mass is independent of the selected frame. Together, the thrust vector and the mass of a low-thrust spacecraft determine the acceleration added to the equations of motion at a given instant in time.

The spacecraft mass,  $m_s$ , evolves with time as the thrust maneuvers are executed. The mass flow rate,  $\dot{m}_s$ , governs the rate at which spacecraft propellant is consumed and is expressed as,

$$\dot{m}_s = \frac{T}{v_e}, \quad (2.76)$$

where  $v_e$  is the exhaust velocity evaluated as,  $v_e = I_{sp}g_0$ . A value of  $g_0 = 9.80665 \text{ m/s}^2$  is employed for the acceleration due to gravity on the surface of the Earth. Specific impulse,  $I_{sp}$ , is a measure of engine efficiency. It is clear from Equation (2.76) that, if the thrust magnitude remains fixed, then an increase in  $I_{sp}$  decreases  $\dot{m}_s$ , thus, decreasing propellant consumption for the same thrust magnitude. Low-thrust engines possess far higher  $I_{sp}$  values than their high-thrust chemical counterparts, which is the primary motivation for employing this engine type. The manner in which the thrust vector and spacecraft mass are parameterized determines whether Equation (2.76) is integrated along with the other equations of motion in the dynamical model. When the thrust magnitude is constant, it is straightforward to analytically compute the resulting change in spacecraft mass given Equation (2.76) and the duration of the thrust arc. Indeed, this approach is used for the direct collocation scheme introduced later in the document. However, if the selected parameterization permits the thrust magnitude to change at every instant in time, then Equation (2.76) must be numerically integrated along with the equations of motion in the dynamical model.

The scheme for incorporating a low-thrust force into the equations of motion is adaptable to many types of low-thrust spacecraft. Three key parameters differentiate one low-thrust spacecraft from another in the selected thruster model: maximum thrust ( $T_{max}$ ), specific impulse ( $I_{sp}$ ), and initial spacecraft mass ( $m_{s_0}$ ). Together  $T_{max}$  and  $m_{s_0}$  are used to evaluate a spacecraft's maximum acceleration,  $a_{T_{max}}$ . This quantity is the maximum low-thrust acceleration a spacecraft can impart at the beginning of its lifetime. The maximum acceleration for a low-thrust spacecraft dictates its *control authority*, that is, its ability to alter its natural motion. The larger the value of  $a_{T_{max}}$  for a spacecraft, the more quickly it can affect its velocity and ultimately the position. A spacecraft with low control authority often requires more time than

a spacecraft with a higher control authority to achieve the same transfer, and sometimes a transfer may not be possible for a given level of control authority. Of course, as the mass of a spacecraft decreases through the consumption of propellant, the acceleration it imparts increase, however, this change is often gradual and relatively small. Finally, note that a higher-fidelity model of the low-thrust engine introduces additional characteristics that distinguish one spacecraft from another, e.g., available spacecraft power and thruster performance curves. However, these more complex considerations are omitted in the present investigation.

It is essential to examine  $a_{T_{max}}$ , not solely  $T_{max}$ , when comparing the capabilities of multiple spacecraft. This necessity is illustrated by Table 2.4, which displays the key spacecraft and engine parameters from a range of real low-thrust spacecraft. Table

Table 2.4.  
Spacecraft and engine parameters for real low-thrust spacecraft.

Spacecraft	$m_{s_0}$ [kg]	$T_{max}$ [mN]	Max $I_{sp}$ [sec]	$a_{T_{max}}$ [m/s <sup>2</sup> ]
Deep Space 1 [31]	486.3	92.7	3127	$1.91 \times 10^{-4}$
Lunar IceCube [32]	14	1.24	2640	$8.86 \times 10^{-5}$
Dawn [6]	1217.8	91	3127	$7.47 \times 10^{-5}$
Hayabusa 2 [33]	608.6	27	2890	$4.44 \times 10^{-5}$
Gateway [34]	39000	1132.6	2323	$2.90 \times 10^{-5}$

2.4 illustrates that Gateway, the spacecraft with, by far, the highest  $T_{max}$ , actually possesses the lowest value of  $a_{T_{max}}$  as a result of its extremely large mass. Thus, despite its powerful low-thrust engines, Gateway exhibits the least control authority of all the spacecraft listed. In contrast, Lunar IceCube, a very small spacecraft with a comparably tiny engine, actually possesses substantially more control authority than Gateway. Other spacecraft operate above and between Lunar IceCube and Gateway in Table 2.4, thus, demonstrating the wide range of capabilities.

### 3. LOW-THRUST TRAJECTORY COMPUTATION AND OPTIMIZATION

Selection of a dynamical model for simulating the motion of a spacecraft serves as the foundation for trajectory design. Trajectory design encompasses many different objectives, from creating a stable orbit around a planet to constructing a transfer between two different orbits. In this investigation, transfer design for low-thrust spacecraft is the goal. For low-thrust spacecraft, trajectory design is markedly different than the process required for chemical spacecraft because it requires solving a continuous optimal control problem. The nature of this problem is discussed prior to presenting several approaches for solution. This development follows the work from Betts [35] from Longuski, Guzmán, and Prussing [36], as well as from other authors. One particular method, direct collocation, is utilized to solve low-thrust trajectory design problems in this investigation and a specific direct collocation formulation is implemented.

Mathematically, the dynamical models are characterized by the equations of motion that describe the motion of a spacecraft. The equations of motion for the three models examined previously are all represented as sets of three scalar second-order differential equations. However, it is straightforward to transform these equations into a system of six first-order differential equations via a change of variables approach. A general format for representing these equations is,

$$\dot{\mathbf{x}} = \begin{bmatrix} \dot{x}_1 \\ \dot{x}_2 \\ \vdots \\ \dot{x}_{n_x} \end{bmatrix} = \begin{bmatrix} f_1[x_1(t), \dots, x_{n_x}(t)] \\ f_2[x_1(t), \dots, x_{n_x}(t)] \\ \vdots \\ f_{n_x}[x_1(t), \dots, x_{n_x}(t)] \end{bmatrix} = \mathbf{f}[\mathbf{x}(t), t], \quad (3.1)$$

where  $n_x$  denotes the number of state variables and, therefore, the number of first-order ODEs included in the dynamical system. For the problems considered here, the state variables are expressed in Cartesian coordinates, thus,  $n_x = 6$  where  $\mathbf{x}$  consists of three position states  $\mathbf{r}$  and three velocity states  $\dot{\mathbf{r}}$ , thus  $\mathbf{x} = \{\mathbf{r}, \dot{\mathbf{r}}\}^T$ . Equation (3.1) represents a dynamical system that is only a function of states and time; however, some systems also include control variables,  $\mathbf{u}(t)$ , and various parameters that are constant over time,  $\boldsymbol{\rho}$ . When these additional variables and parameters are included the system of equations is represented as,

$$\dot{\mathbf{x}} = \mathbf{f}[\mathbf{x}(t), \mathbf{u}(t), \boldsymbol{\rho}, t], \quad (3.2)$$

where  $\boldsymbol{\rho}$  is not a function of time. The dynamical system provided by the selected model and expressed in Equation (3.2) supplies the foundation for the general optimal control problem.

### 3.1 The Optimal Control Problem

Fundamentally, an optimal control problem concerns the determination of a set of inputs to a system to extremize a desired parameter. The problem of low-thrust trajectory design perfectly fits this description. At each instant in time, the thrust vector of a low-thrust spacecraft, the input, must be selected to minimize a cost, typically propellant consumption or time of flight. The world is filled with optimization problems, both naturally occurring, such as light refracting through water, and human-made. Thus, significant effort has been invested in solving these problems. The modern field of optimal control theory originated in the 1690s when Johann Bernoulli challenged his fellow mathematicians to solve the brachistochrone problem. This prompting led to several solution methods, including ones by Issac Newton and Bernoulli himself, whose concepts are utilized to this day. The advent of computers in the 20<sup>th</sup> century spurred rapid advancement in the field of optimal control, leading to many new approaches for solving such problems. However, regardless of the method

selected, all approaches require an initial mathematical formulation of the optimal control problem.

### 3.1.1 General Formulation

A simple optimal control problem that omits inequality constraints is examined first to facilitate introduction of the Euler-Lagrange Theorem. This problem states that the control values  $\mathbf{u}(t)$  must be selected to minimize the function,

$$J = \phi[\mathbf{x}(t_F), \mathbf{u}(t_F), \boldsymbol{\rho}, t_F] + \int_{t_I}^{t_F} L[\mathbf{x}(t), \mathbf{u}(t), \boldsymbol{\rho}, t] dt, \quad (3.3)$$

where the first and second terms in the total cost,  $J$ , represent *terminal* and *path* costs, respectively. The terminal cost is evaluated at the final time,  $t_F$ , and the final state  $\mathbf{x}_F = \mathbf{x}(t_F)$ . While the path cost is accumulated over the entire duration of the path, and is equal to the integral of the Lagrangian,  $L[\mathbf{x}(t), \mathbf{u}(t), \boldsymbol{\rho}, t]$ , from the initial to the final time. Equation (3.3) is described under a variety of names including cost function, objective function, and performance index. Minimization of Equation (3.3) is subject to the state equations,

$$\dot{\mathbf{x}} = \mathbf{f}[\mathbf{x}(t), \mathbf{u}(t), \boldsymbol{\rho}, t], \quad (3.4)$$

and the boundary constraints,

$$\boldsymbol{\psi}[\mathbf{x}(t_F), \mathbf{u}(t_F), \boldsymbol{\rho}, t_F] = \mathbf{0}, \quad (3.5)$$

where  $\mathbf{u}(t)$  is restricted to the set of admissible controls  $\mathbf{u}(t) \in \mathcal{U}$ . Furthermore, the initial conditions  $\mathbf{x}_I = \mathbf{x}(t_I)$  are given at the initial time  $t_I$  and the final time  $t_F$  is free. Two types of equality constraints are imposed in this optimal control problem. The constraints in Equation (3.4) are continuous, because they apply over the entire time interval,  $t_I \leq t \leq t_F$ . In contrast, Equation (3.5) represents discrete constraints that are only evaluated at the final time,  $t_F$ .

### 3.1.2 Euler-Lagrange Theorem

The solution of the brachistochrone problem spurred the development of a new field of mathematical analysis, the calculus of variations. The mathematicians Euler and Lagrange furthered this area of research in the 1700s with their development of the aptly named Euler-Lagrange Theorem. As this theorem is the basis for an entire branch of optimization methods called indirect methods, it merits examination here. The development of the Euler-Lagrange theorem is aided by reformulating the general optimal control problem as introduced in the previous section. First, the cost function, Equation (3.3), is augmented with the constraints,

$$\hat{J} = (\phi + \boldsymbol{\nu}^T \boldsymbol{\psi})_{t_F} + \int_{t_i}^{t_F} L[\mathbf{x}(t), \mathbf{u}(t), \boldsymbol{\rho}, t] + \boldsymbol{\lambda}^T \left\{ \dot{\mathbf{x}} - \mathbf{f}[\mathbf{x}(t), \mathbf{u}(t), \boldsymbol{\rho}, t] \right\} dt, \quad (3.6)$$

where the *Lagrange multipliers*,  $\boldsymbol{\nu}$ , are included with the discrete constraints and the *costate* or *adjoint variables*,  $\boldsymbol{\lambda}(t)$ , are multiplied by the continuous constraints. This modification ensures that minimization of the cost function does not ignore enforcement of the constraints. Next, the expression for the augmented cost function is simplified with the definition of several additional variables, i.e., the *Hamiltonian*,

$$H = L[\mathbf{x}(t), \mathbf{u}(t), \boldsymbol{\rho}, t] + \boldsymbol{\lambda}(t)^T \mathbf{f}[\mathbf{x}(t), \mathbf{u}(t), \boldsymbol{\rho}, t], \quad (3.7)$$

and the auxiliary function,

$$\Phi = \phi + \boldsymbol{\nu}^T \boldsymbol{\psi}. \quad (3.8)$$

The necessary conditions of the Euler-Lagrange theorem are derived by setting the first variation of the augmented cost function to zero,  $\hat{J} = \delta 0$ . A detailed explanation of this derivation is presented by Longuski, Guzmán, and Prussing [36]. The results of this process are four necessary conditions that must be met to obtain a constrained optimum that satisfies the optimal control problem presented in Equations (3.3)-(3.5). These necessary conditions are,

$$\dot{\boldsymbol{\lambda}} = -\mathbf{H}_x^T, \quad (3.9)$$

called the costate or adjoint equations,

$$\mathbf{0} = -\mathbf{H}_u^T, \quad (3.10)$$

called the control equations, and

$$\boldsymbol{\lambda}(t_F) = \frac{\partial \Phi^T}{\partial \mathbf{x}_F} \quad (3.11)$$

$$0 = \left( \frac{d\Phi}{dt} + H \right) \Big|_{t=t_F}, \quad (3.12)$$

denoted the transversality conditions. The variables  $\mathbf{H}_x$  and  $\mathbf{H}_u$  denote the partial derivatives of the Hamiltonian with respect to the state and control variables, respectively. These partial derivatives are considered column vectors, thus,  $\mathbf{H}_x = [\partial H / \partial x_1, \dots, \partial H / \partial x_n]^T$ . Together Equations (3.9)-(3.12) are termed the Euler-Lagrange equations. Note that Equation (3.12) only applies if the final time  $t_F$  is free.

The Euler-Lagrange equations provide a set of necessary conditions that must be met to minimize  $J$  while satisfying the given constraints. These necessary conditions consist of the system of differential algebraic equations formed by Equations (3.4), (3.9), and (3.10), whose boundary conditions at  $t_I$  and  $t_F$  are given by Equations (3.5), (3.11), and (3.12). Collectively, these equations form a two-point boundary value problem (TPBVP) whose solution yields an answer to the optimal control problem posed in Section 3.1.1. A variety of solution methods for TPBVPs are available, several of which are discussed in subsequent sections. Finally, note that the simple optimal control problem addressed in this section omits inequality constraints; however, strategies for applying the Euler-Lagrange Theorem to a problem that includes these types of constraints are available [36].

### 3.1.3 General Multi-Phase Formulation

A more general presentation of the optimal control problem highlights other constraints that can appear, and to offer a framework for problems that consist of multiple phases. A phase is defined by Betts [35] as a section of an optimal control problem where the differential equations that define the dynamical system remain unchanged. Time,  $t$ , is typically the independent variable in low-thrust optimal control problems, thus, each phase is denoted by its start and end times,  $t_I^s < t < t_F^s$ . Phases are

typically ordered sequentially such that  $t_I^{\kappa+1} = t_F^\kappa$  and constraints may be enforced that require state and control variables to remain continuous between phases, though this constraint is not required. In this investigation, all problems have one phase, thus  $Q = 1$ ; however, a multi-phase scheme is presented to demonstrate potential extensions for the current framework. State and control variables are the dynamic variables,  $\mathfrak{z}$ , of the optimal control problem, i.e.,

$$\mathfrak{z} = \begin{bmatrix} \mathbf{x}^{(\kappa)}(t) \\ \mathbf{u}^{(\kappa)}(t) \end{bmatrix}. \quad (3.13)$$

The goal of the optimal control problem is determination of the histories of these time-dependent dynamic variables that satisfy the problem dynamics and constraints while minimizing the objective function. The dynamic variables are constrained to abide by the dynamical equations of the current phase at all times,

$$\dot{\mathbf{x}}^{(\kappa)} = \mathbf{f}^{(\kappa)}[\mathbf{x}^{(\kappa)}(t), \mathbf{u}^{(\kappa)}(t), \boldsymbol{\rho}^{(\kappa)}, t], \quad (3.14)$$

and are also restricted by additional path constraints that are applicable over the duration of a phase,

$$\mathbf{g}_L^{(\kappa)} \leq \mathbf{g}^{(\kappa)}(\mathbf{x}^{(\kappa)}(t), \mathbf{u}^{(\kappa)}(t), \boldsymbol{\rho}^{(\kappa)}, t) \leq \mathbf{g}_U^{(\kappa)}. \quad (3.15)$$

Furthermore, the state and control variables themselves are bounded to remain within set upper and lower limits,

$$\mathbf{x}_L^{(\kappa)} \leq \mathbf{x}^{(\kappa)}(t) \leq \mathbf{x}_U^{(\kappa)} \quad (3.16)$$

$$\mathbf{u}_L^{(\kappa)} \leq \mathbf{u}^{(\kappa)}(t) \leq \mathbf{u}_U^{(\kappa)}. \quad (3.17)$$

Boundary constraints are evaluated at the initial and final times of each phase. The simplest forms of these constraints fix the initial and final values of the dynamic vari-

ables themselves, but other boundary constraints may apply to quantities evaluated with the initial or final values of these variables.

$$\begin{aligned}
\psi_L \leq \psi & \left[ \mathbf{x}^{(1)}(t_I^{(1)}), \mathbf{u}^{(1)}(t_I^{(1)}), \boldsymbol{\rho}^{(1)}, t_I^{(1)}, \right. \\
& \mathbf{x}^{(1)}(t_F^{(1)}), \mathbf{u}^{(1)}(t_F^{(1)}), \boldsymbol{\rho}^{(1)}, t_F^{(1)}, \\
& \mathbf{x}^{(2)}(t_I^{(2)}), \mathbf{u}^{(2)}(t_I^{(2)}), \boldsymbol{\rho}^{(2)}, t_I^{(2)}, \\
& \mathbf{x}^{(2)}(t_F^{(2)}), \mathbf{u}^{(2)}(t_F^{(2)}), \boldsymbol{\rho}^{(2)}, t_F^{(2)}, \\
& \dots \\
& \left. \mathbf{x}^{(Q)}(t_I^{(Q)}), \mathbf{u}^{(Q)}(t_I^{(Q)}), \boldsymbol{\rho}^{(Q)}, t_I^{(Q)}, \right. \\
& \left. \mathbf{x}^{(Q)}(t_F^{(Q)}), \mathbf{u}^{(Q)}(t_F^{(Q)}), \boldsymbol{\rho}^{(Q)}, t_F^{(Q)} \right] \leq \psi_U
\end{aligned} \tag{3.18}$$

An additional type of constraint is enforced via *quadrature functions*. These are expressed as,

$$\int_{t_F^{(\kappa)}}^{t_I^{(\kappa)}} \mathbf{w}^{(\kappa)}(\mathbf{x}^{(\kappa)}(t), \mathbf{u}^{(\kappa)}(t), \boldsymbol{\rho}^{(\kappa)}, t) dt, \tag{3.19}$$

and these functions are required to evaluate to certain quantities when integrated over the time span of a given phase. The constraints presented in Equations (3.14), (3.15), (3.19) are all *continuous functions* and apply at all times within a phase. Alternatively, constraints evaluated at specific times, such as boundary constraints, are termed *point functions*. This differentiation between constraint types is similar to the distinction between the terms of the cost function  $J$ . The cost function in the multi-phase optimal control problem also consists of terminal and path terms and

is evaluated with variables and parameters from all  $Q$  phases. The complete cost function is expressed as,

$$\begin{aligned}
J = \phi & \left[ \mathbf{x}^{(1)}(t_I^{(1)}), \mathbf{u}^{(1)}(t_I^{(1)}), \boldsymbol{\rho}^{(1)}, t_I^{(1)}, \right. \\
& \mathbf{x}^{(1)}(t_F^{(1)}), \mathbf{u}^{(1)}(t_F^{(1)}), \boldsymbol{\rho}^{(1)}, t_F^{(1)}, \\
& \mathbf{x}^{(2)}(t_I^{(2)}), \mathbf{u}^{(2)}(t_I^{(2)}), \boldsymbol{\rho}^{(2)}, t_I^{(2)}, \\
& \mathbf{x}^{(2)}(t_F^{(2)}), \mathbf{u}^{(2)}(t_F^{(2)}), \boldsymbol{\rho}^{(2)}, t_F^{(2)}, \\
& \dots \\
& \left. \mathbf{x}^{(Q)}(t_I^{(Q)}), \mathbf{u}^{(Q)}(t_I^{(Q)}), \boldsymbol{\rho}^{(Q)}, t_I^{(Q)}, \right. \\
& \left. \mathbf{x}^{(Q)}(t_F^{(Q)}), \mathbf{u}^{(Q)}(t_F^{(Q)}), \boldsymbol{\rho}^{(Q)}, t_F^{(Q)} \right] \\
& + \sum_{j=1}^Q \left\{ \int_{t_F^{(j)}}^{t_I^{(j)}} \mathbf{w}^{(j)}(\mathbf{x}^{(j)}(t), \mathbf{u}^{(j)}(t), \boldsymbol{\rho}^{(j)}, t) dt \right\}, \tag{3.20}
\end{aligned}$$

where the sum in the second term is included to ensure that the path cost is evaluated for each phase. The objective function expressed in Equation (3.20) includes both terminal and path costs, and is termed a *problem of Bolza*. When no path terminal constraints are included in the cost function, the optimal control problem is called a *problem of Lagrange* and, in the opposite case, the result is denoted a *problem of Mayer*. Together, Equations (3.13)-(3.20) represent the variables, constraints, and objective functions that compose a standard multi-phase optimal control problem. From this very general form, the smaller single-phase optimal control problems explored in this investigation can be derived. Correctly stating the optimal control problem in mathematical form is the first step towards determining an optimal solution.

### 3.2 Optimization Methods

Once the optimal control problem is stated mathematically, many different optimization methods are potentially utilized to determine a solution. Generally, these approaches are sorted into two broad categories: indirect and direct methods. Indirect methods apply the Euler-Lagrange theorem to the continuous optimal control

problem to transform it into a TPBVP. The proof of the Euler-Lagrange theorem demonstrates that solving this TPBVP supplies an extremal (optimal) solution to the original optimal control problem. In contrast, direct methods operate *directly* on the cost function, employing the gradient of this function with respect to the problem variables to compute a minimum cost. This minimum is obtained in an iterative fashion by assessing the value of the cost function as well as the constraints from one step to the next. While a diversity of approaches for solving the optimal control problem exists within the indirect and direct categories, these labels capture the most significant distinctions between methods.

Despite their differences, both categories of optimization methods require discretization and optimization, and Betts notes [35] that the order in which these two steps are performed offers a convenient means of distinguishing between indirect and direct optimization methods. Due to their complexity, most real-world optimization problems necessitate the use of a computer to produce a solution, and the continuous optimal control problem must be discretized to pose the problem in a format amenable to this approach. Direct optimization approaches are discretized first; the continuous optimization problem is transcribed into a Nonlinear Programming (NLP) problem. Shooting and collocation methods are often employed to offer a framework for the discretization process and to serve as function generators that translate state and control variables into an evaluated objective function and a set of constraints. Following the discretization step, direct methods implement the optimization step by utilizing any one of the many solution methods available for solving the NLP. Due to the importance of the discretization step, direct optimization is alternately denoted as parameter optimization. Conversely, indirect methods implement the optimization step first by applying the Euler-Lagrange theorem to the continuous optimal control problem to generate a TPBVP. While this reformulation does not itself provide an optimal solution, it sets up a problem whose solution is guaranteed to be locally optimal. Next, the TPBVP is discretized and solved using one of the strategies available for solving this type of problem, such as shooting and collocation techniques. The

order of the discretization and optimization steps is a simple means of distinguishing between the indirect and direct optimization approaches.

Greater detail on indirect and direct methods is offered in the following subsections. The advantages and disadvantages of these two techniques are highlighted, as well as the process for the selection of a technique in this investigation. Additionally, several other optimization approaches are briefly introduced. This overview of various optimization approaches is aided by several helpful survey papers, including those by Betts [35, 37], Conway [38], Rao [39], and Topputo and Zhang [40].

### 3.2.1 Indirect Optimization Methods

Indirect methods are as old as the field of optimal control itself, yet they are still successfully employed today for a variety of problems, including low-thrust trajectory optimization. These methods offer an advantage, i.e., the necessary conditions guarantee that a solution to the TPBVP is a local optimal. Additionally, application of the Euler-Lagrange theorem provides a convenient control law. Another benefit of this approach is the costates provide information on the sensitivity of the objective. A sometimes underappreciated aspect of the indirect optimization technique is the beauty of its elegance and mathematical rigor. However, indirect optimization approaches also possess a number of challenges that have, perhaps, caused their popularity to wane in the field of spacecraft trajectory optimization.

The drawbacks of the indirect optimization approach center around the rigidity of the problem formulation and the difficulty in producing a satisfactory initial guess. First, application of the Euler-Lagrange theorem is non-trivial and the computation of the required partial derivatives can be quite challenging for some problems. Moreover, changes to the original optimal control problem, such as the addition of new variables or constraints, require reapplication of the Euler-Lagrange Theorem to formulate a new TPBVP. Furthermore, Betts notes that if a problem contains path inequalities, then an a priori guess for the constrained arc sequence is required. In low-thrust

trajectory optimization problems, this situation manifests as the requirement to provide an initial estimate for the sequence of thrust and coast arcs along a trajectory. Similarly, it is difficult to formulate an initial guess for the costate variables that appear in the TPBVP, particularly because these variables do not directly relate to any physical quantity. Compounding this difficulty is the fact that the TPBVP can be quite sensitive to the values of the costates. Thus, a poor initial guess greatly hinders or often prevents convergence. These challenges, along with drastic increases in computing power, have contributed to increased interest in direct optimization methods.

### 3.2.2 Direct Optimization Methods

In the latter half of the 20<sup>th</sup> century, the application of direct optimization methods to the continuous optimal control problem garnered increased attention, as advances in computer technology made these methods increasingly practical. The initial discretization of the continuous optimal control problem that direct methods require can produce very large optimization problems whose solution demands significant computational resources. Recent increases in computational capability have made the size of many direct optimization problems less prohibitive, enabling the benefits of direct optimization to be fully leveraged.

The benefits of direct optimization methods center on the flexibility and robustness of these methods. Transcribing the continuous optimal control problem into an NLP does not require detailed knowledge of optimal control theory or even extensive analytical derivations (unless analytical derivatives are desired). Thus, it is more straightforward to implement a direct optimization method in comparison to an indirect strategy. This trait also influences the adaptability of direct approaches to changes in an optimization problem. It is again comparatively easy to add or remove constraints; moreover, direct methods render the inclusion of path constraints

simpler. In general, direct optimization techniques are also more robust than indirect ones, that is, a direct method is more likely to converge a poor initial guess.

Despite the advantages, direct methods are not the obvious choice for every problem; there are disadvantages beyond simply the large problem size. A second drawback is that the solution supplied by a direct optimization technique is frequently a local optimal in the neighborhood of the initial guess and offers no information on potential improvements. This result is in contrast to the indirect approach which, though it also only offers local optimal solutions, includes costate values that offer helpful information regarding potential improvements. Therefore, it can be challenging to determine how close the result is to the true local optimal of the continuous optimal control problem. As Conway indicates, the provided solution is the best available for the problem structure supplied to the optimizer [38].

### 3.2.3 Global Optimization and Other Methods

The propensity of indirect and direct optimization methods to yield local optimal solutions within the neighborhood of the initial guess motivates the development of a distinct set of optimization techniques, termed evolutionary algorithms and metaheuristics by Conway [38]. These algorithms exploit heuristic methods, often based conceptually upon processes observed in nature, to compute globally optimal solutions. Examples include ant-colony optimization, simulated annealing, and monotonic basin hopping. For real-world problems, it is rarely possible to verify that the solutions obtained by these methods are true global optimals, though these approaches can produce very good solutions given sufficient time. Moreover, they can obtain solutions even when provided with a random initial guess, thus circumventing this challenge in the trajectory design process. However, an additional drawback is that the number of variables must be relatively small or the process becomes computationally prohibitive. This requirement reflects the fact that explicit propagation is likely required to accurately represent a trajectory, thereby further increasing the

computation time. Despite these drawbacks, evolutionary algorithms are successfully employed for trajectory design by a number of authors [41–44]. Furthermore, other authors pair global optimization techniques with indirect or direct methods to offer approaches that possess the strengths of both strategies [30, 45, 46].

Another optimization approach that does not neatly fit into either the indirect or direct optimization categories is Differential Dynamic Programming (DDP). A version of this method is utilized within the low-thrust trajectory design tool Mystic, developed by Gregory Whiffen [47–49], which is employed to conduct trajectory design for the Dawn and Psyche missions. In recent decades applications of the DDP technique for low-thrust trajectory design have received increased study. A variety of authors have successfully utilized this technique to optimize low-thrust transfers [50–54]. The success of these efforts suggests that the application of DP to low-thrust trajectory design merits further investigation to improve understanding of the comparisons to the approaches in this investigation.

### 3.2.4 Selecting an Optimization Method

Clearly, there is no one best optimization method. The many approaches available have been developed over time to address the needs of many different types of problems. Each approach possesses strengths and weaknesses that make it the ideal solution to one problem and a poor choice for another. It is the role of the engineer to apply their knowledge and experience to the selection of an optimization technique best suited for the problem at hand. Thus, the available optimization techniques are considered and a direct optimization approach is selected for use in this investigation.

The motivation for selecting a direct optimization technique follows from the central goals of this investigation. A robust and adaptable approach for low-thrust trajectory design over a range of dynamical environments is desired, and direct optimization best meets these needs. Direct optimization techniques are generally more robust than indirect optimization formulations and faster than global optimization

approaches. As a consequence, direct optimization is potentially less precise than indirect optimization, nor does it offer any guarantee of global optimality. Direct optimization is selected as the best approach for solving the type of optimal control problems encountered in this analysis due to its balance of robustness and efficiency.

### 3.3 Newton's Method

When solving an NLP problem or a TPBVP, many of the strategies are iterative and fundamentally rely upon Newton's method. Also labelled the Newton-Raphson method, it is a strategy for determining the root of one or more equations, and is generalized for a problem of multiple variables. The goal of this scheme is to determine the  $n_z \times 1$  vector  $\mathbf{z}^T = \{z_1, \dots, z_{n_z}\}$  such that,

$$\mathbf{c}(\mathbf{z}) = \begin{Bmatrix} c_1(\mathbf{z}) \\ c_2(\mathbf{z}) \\ \vdots \\ c_m(\mathbf{z}) \end{Bmatrix} = \mathbf{0}, \quad (3.21)$$

where  $\mathbf{c}(\mathbf{z})$  is an  $m_{eq} \times 1$  vector of nonlinear equality constraints and  $m_{eq}$  denotes the number of equality constraints. The column vector  $\mathbf{z}$  is also termed the design variable vector, and  $n_z$  designates the total number of design variables. The root of Equation (3.21) is denoted  $\mathbf{z}^*$ , such that  $\mathbf{c}(\mathbf{z}^*) = \mathbf{0}$ . If the number of variables is greater than or equal to the number of constraints, that is  $n_z \geq m_{eq}$ , then a value of  $\mathbf{z}^*$  is typically available. When  $n_z < m_{eq}$ , the problem is overconstrained and the system of equations in Equation (3.21) is overdetermined, thus, no solutions are available unless some of the constraints are redundant. An approach for determining  $\mathbf{z}^*$  is supplied by approximating the nonlinear constraint equations via the first two terms of a Taylor series expansion about an initial guess,  $\mathbf{z}^0$ , that is,

$$\mathbf{c}(\mathbf{z}) \approx \mathbf{c}(\mathbf{z}^0) + \frac{\partial \mathbf{c}}{\partial \mathbf{z}^0}(\mathbf{z} - \mathbf{z}^0). \quad (3.22)$$

Because the abbreviated Taylor Series offers only an approximation of  $\mathbf{c}(\mathbf{z})$ , an iterative process is required to converge upon a value of  $\mathbf{z}$  that sufficiently satisfies

Equation (3.21). Thus, Equation (3.22) is rewritten such that the zero superscript is replaced with  $k$  to indicate an iterative procedure,

$$0 \approx \mathbf{c}(\mathbf{z}^k) + \frac{\partial \mathbf{c}}{\partial \mathbf{z}^k} \delta \mathbf{z}^k, \quad (3.23)$$

where  $\delta \mathbf{z}^k = (\mathbf{z}^{k+1} - \mathbf{z}^k)$  and Equation (3.23) is set equal to zero for consistency with Equation (3.21). For simplicity, the partial derivative in Equation (3.23) is defined such that,

$$\mathbf{G}^k = \frac{\partial \mathbf{c}}{\partial \mathbf{z}^k} = \begin{bmatrix} \frac{\partial c_1}{\partial z_1^k} & \frac{\partial c_1}{\partial z_2^k} & \cdots & \frac{\partial c_1}{\partial z_{n_z}^k} \\ \frac{\partial c_2}{\partial z_1^k} & \frac{\partial c_2}{\partial z_2^k} & \cdots & \frac{\partial c_2}{\partial z_{n_z}^k} \\ \vdots & \vdots & \ddots & \\ \frac{\partial c_{m_{eq}}}{\partial z_1^k} & \frac{\partial c_{m_{eq}}}{\partial z_2^k} & \cdots & \frac{\partial c_{m_{eq}}}{\partial z_{n_z}^k} \end{bmatrix}, \quad (3.24)$$

where  $\mathbf{G}^k$  is an  $m_{eq} \times n_z$  matrix, termed the *Jacobian* matrix. Equation (3.23) is solved for  $\delta \mathbf{z}^k$  which is employed to update  $\mathbf{z}^k$ . The update step is written,

$$\mathbf{z}^{k+1} = \mathbf{z}^k + \eta_a \delta \mathbf{z}^k, \quad (3.25)$$

where  $\eta_a$  is a scalar value used to attenuate the magnitude of the update step; however,  $\eta_a = 1$  unless otherwise indicated. In general, each step of the iterative process offered by Equation (3.23) satisfies  $\|\mathbf{c}(\mathbf{z}^{k+1})\| \equiv \|\mathbf{c}(\mathbf{z}^k + \delta \mathbf{z}^k)\| \leq \|\mathbf{c}(\mathbf{z}^k)\|$ . This procedure is continued until  $\mathbf{z}^{k+1} = \mathbf{z}^*$ , or, more practically, until  $\|\mathbf{c}(\mathbf{z}^{k+1})\| \leq \epsilon$  where  $\epsilon$  is a tolerance. When the value of  $\mathbf{z}^k$  satisfies this tolerance, the iterative procedure is said to *converge*. Solving Equation (3.23) for  $\delta \mathbf{z}^k$  can be challenging and the approach is dependent on the relationship between  $n_z$  and  $m_{eq}$ , that is, the number of variables and constraints.

### 3.3.1 Number of Variables Equals the Number of Constraints

When  $n_z = m_{eq}$ , the Jacobian,  $\mathbf{G}^k$ , is square and it is straightforward to solve Equation (3.23) for  $\delta \mathbf{z}^k$ . Rearranging Equation (3.23) provides a multidimensional form of the familiar *Newton's method* equation,

$$\delta \mathbf{z}^k = -(\mathbf{G}^k)^{-1} \mathbf{c}(\mathbf{z}^k), \quad (3.26)$$

where  $(\mathbf{G}^k)^{-1}$  is the matrix inverse of  $\mathbf{G}^k$ . Newton's method is quadratically convergent provided  $\mathbf{z}^k$  is within a region of convergence. This extremely advantageous trait implies that  $\mathbf{z}^k$  is two significant digits closer to  $\mathbf{z}^*$  with each iteration. Practically speaking, the initial guesses,  $\mathbf{z}^0$ , employed in this analysis rarely initiate quadratic convergence from the first iteration; however, quadratic convergence is observed as the algorithm hones in upon a solution,  $\mathbf{z}^*$ . Finally, while Equation (3.26) appears simple, the process of computing  $(\mathbf{G}^k)^{-1}$  numerically is sometimes computationally expensive, thus, implementation proceeds cautiously.

### 3.3.2 Number of Variables Greater than the Number of Constraints

When  $n_z > m_{eq}$ , the root-finding problem is underconstrained and the system of equations in Equation (3.21) is underdetermined. In this scenario, an infinite number of solutions are available that satisfy Equation (3.23). A beneficial strategy for isolating one of these solutions is to select the update  $\mathbf{z}^{k+1}$  that is closest to  $\mathbf{z}^k$ . Selecting the nearby solution leverages the fact that gradient searches are more successful when the updated solution is close to the reference, i.e., when  $\|\delta\mathbf{z}^k\|^2$  is minimized. Furthermore, seeking a solution nearby  $\mathbf{z}^k$  biases the convergence process towards  $\mathbf{z}^{k+1}$  that inherit some of the characteristics of the previous step. This tendency is typically beneficial within the trajectory design procedure because the initial guess is selected to possess advantageous characteristics that are also desired in the final solution. The unique solution  $\mathbf{z}^{k+1}$  closest to  $\mathbf{z}^k$  is labelled the minimum-norm and the equation that yields this solution is derived by first posing the optimization problem,

$$\min F = \|\delta\mathbf{z}^k\|^2 = (\delta\mathbf{z}^k)^T \delta\mathbf{z}^k, \quad (3.27)$$

subject to Equation 3.23. The derivation of the solution to this problem presented here follows that offered by Grebow [55]. Next, an expression equivalent to Equation (3.27) where the cost function is augmented with the problem constraints is formulated,

$$\min F^* = (\delta\mathbf{z}^k)^T \delta\mathbf{z}^k + \boldsymbol{\Lambda}^T [\mathbf{c}(\mathbf{z}^k) + \mathbf{G}^k \delta\mathbf{z}^k], \quad (3.28)$$

where  $\mathbf{\Lambda}$  is an  $n_z \times 1$  vector of Lagrange multipliers. Note, this set of multipliers is introduced to solve the NLP problem and is not necessarily equivalent to the Lagrange multipliers first presented in Equation (3.6) that are employed to reformulate the continuous optimal control problem. Observe that at  $\mathbf{z}^*$ , the augmented cost function is equivalent to Equation (3.27) because, when this condition is met, the constraints are satisfied and thus equal to zero. The necessary conditions for a minimum solution to the optimization problem are computed by calculating the partial derivatives of Equation (3.28) with respect to  $\mathbf{z}$  and  $\mathbf{\Lambda}$ .

$$\nabla_{\delta\mathbf{z}} F^* = 2(\delta\mathbf{z}^k)^T + \mathbf{\Lambda}^T \mathbf{G}^k = \mathbf{0} \quad (3.29)$$

$$\nabla_{\mathbf{\Lambda}} F^* = \mathbf{c}(\mathbf{z}^k)^T + (\delta\mathbf{z}^k)^T (\mathbf{G}^k)^T = \mathbf{0} \quad (3.30)$$

Following this step, the system of equations formed by Equations (3.29) and (3.30) is manipulated to eliminate  $\mathbf{\Lambda}$ . This process begins with the multiplication of Equation (3.29) on the right by  $(\mathbf{G}^k)^T$ . The result of this operation is,

$$2(\delta\mathbf{z}^k)^T (\mathbf{G}^k)^T + \mathbf{\Lambda}^T \mathbf{G}^k (\mathbf{G}^k)^T = \mathbf{0}. \quad (3.31)$$

Next, rewrite Equation (3.30) as,

$$-\mathbf{c}(\mathbf{z}^k)^T = (\delta\mathbf{z}^k)^T (\mathbf{G}^k)^T, \quad (3.32)$$

and substitute this expression into Equation (3.31) to produce,

$$-2\mathbf{c}(\mathbf{z}^k)^T + \mathbf{\Lambda}^T \mathbf{G}^k (\mathbf{G}^k)^T = \mathbf{0}. \quad (3.33)$$

Equation (3.33) is then solved for  $\mathbf{\Lambda}$ ,

$$\mathbf{\Lambda}^T = 2\mathbf{c}(\mathbf{z}^k)^T [\mathbf{G}^k (\mathbf{G}^k)^T]^{-1}. \quad (3.34)$$

Substituting this expression into Equation (3.29) and computing the transpose results in,

$$2(\delta\mathbf{z}^k) + 2(\mathbf{G}^k)^T [\mathbf{G}^k (\mathbf{G}^k)^T]^{-1} \mathbf{c}(\mathbf{z}^k) = \mathbf{0}. \quad (3.35)$$

Thus, Equation (3.35) presents an expression where  $\mathbf{\Lambda}$  no longer appears explicitly. Finally, Equation (3.35) is solved for  $\delta\mathbf{z}^k$  which yields,

$$\delta\mathbf{z}^k = -(\mathbf{G}^k)^T [\mathbf{G}^k (\mathbf{G}^k)^T]^{-1} \mathbf{c}(\mathbf{z}^k), \quad (3.36)$$

where Equation (3.36) is the well known *Minimum-Norm Equation*. To ensure that a solution to Equation (3.36) is truly a local minimum of the optimization problem posed in Equation (3.27), the second-derivative test is applied by taking the second partial derivative of Equation (3.28) with respect to  $\delta\mathbf{z}$ . The result of this step is,

$$\frac{\partial}{\partial\delta\mathbf{z}} \left( \frac{\partial J}{\partial\delta\mathbf{z}} \right)^T = 2\mathbf{I} > \mathbf{0}, \quad (3.37)$$

where  $\mathbf{I}$  is an  $n_z \times n_z$  identity matrix. Thus, the second-derivative test is satisfied and the solution of the minimum-norm equation is indeed always a local minimum of Equation (3.27). Equation (3.36) is utilized along with Equation (3.25) to iteratively converge upon  $\mathbf{z}$ . Like Newton's Method, Equation (3.36) also offers quadratic convergence when  $\mathbf{z}^k$  is within a region of convergence. Newton's method or the minimum-norm equation solve shooting and collocation problems in this investigation when no objective function is included in a problem statement; i.e., when a feasible solution alone is desired.

### 3.4 Nonlinear Programming

Today the word "programming" is automatically associated with the task of writing computer code. However, when the term nonlinear programming (NLP) was conceived, this word included the work of algorithm development. Thus, nonlinear programming is the field of mathematics concerned with developing schemes for optimizing an objective function subject to a set of constraints. The general NLP problem appears similar in form to the root-finding problem solved with Newton's Method. The primary difference is that the NLP problem is concerned with determining the  $n_z \times 1$  vector  $\mathbf{z}^T = \{z_1, \dots, z_{n_z}\}$  that minimizes the scalar objective function,

$$F(\mathbf{z}), \quad (3.38)$$

subject to the  $m$  constraints,

$$\mathbf{c}_L \leq \mathbf{c}(\mathbf{z}) \leq \mathbf{c}_U, \quad (3.39)$$

with bounds,

$$\mathbf{z}_L \leq \mathbf{z} \leq \mathbf{z}_U, \quad (3.40)$$

where the subscripts  $L$  and  $U$  denote lower and upper constraints or bounds, respectively. Equality constraints are enforced by setting  $\mathbf{c}_L = \mathbf{c}_U$ . In the special case where the objective function and constraints are all linear, the resulting problem is termed *linear programming* (LP) and is a special case of the NLP problem. Similarly, if the constraints remain linear, but the objective function is instead quadratic, this special case is called a *quadratic programming* (QP) problem. These simpler special cases are important because they often provide the basis for methods to solve more complex NLP problems.

One category of approaches for solving the NLP involves satisfying the Karush-Kuhn-Tucker (KKT) necessary conditions. A derivation of the KKT system and resulting necessary conditions is offered by Betts [35]. Two methods for solving the NLP that rely upon satisfying the KKT necessary conditions are sequential quadratic programming (SQP) and interior-point (IP) methods. The fundamental approach for an SQP algorithm is to approximate the NLP problem as a QP problem, and by successive applications of this approximation, to iteratively approach an optimal solution to the true NLP problem. The popular optimizer SNOPT (Sparse Nonlinear OPTimizer) leverages an SQP algorithm and is particularly well-suited for the large highly sparse NLP problems encountered when solving low-thrust trajectory design problems via direct optimization [56, 57]. Alternatively, IP methods (also termed barrier methods) recast the NLP problem as an optimization problem whose unconstrained minimum is equal to the minimum of the original problem. Then, a penalty function approach is utilized to guide this new problem towards a solution that satisfies all the constraints of the initial NLP problem. The open-source optimizer IPOPT (Interior Point OPTimizer) leverages this approach and is also implemented in an efficient manner that is well-suited for large sparse problems [58]. Finally, note that solving

the NLP via the KKT conditions is one of a variety of approaches for solving a mathematical optimization problem. Other solution strategies fall under the categories of feasible direction methods, Lagrangian methods, and penalty function methods. However, not all of these methods are well-suited for solving the NLP, especially the NLP formulated from the low-thrust trajectory optimization problem.

### 3.5 Transcription Methods

The process of discretizing a continuous optimal control problem to pose it as an NLP problem is called transcription. The optimal control problem in Section 3.1.1 consists of functions that are continuous with time, e.g.,  $\dot{\mathbf{x}}(t)$  and  $\mathbf{u}(t)$ . In contrast, the NLP problem in Section 3.4 includes a finite set of discrete variables and constraints,  $\mathbf{x}$  and  $\mathbf{c}$ . Thus, the process of transcription involves converting the first type of problem into the second. Naturally, representing a continuous time system with a finite set of variables and constraints entails a loss of accuracy. Thus, if the result of the NLP problem does not adequately approximate the original continuous optimal control problem, then the transcription process is modified and repeated.

The manner in which a continuous optimal control problem is transcribed is independent of the chosen optimization method. The algorithms described here as shooting and collocation, may be utilized in either an indirect or direct optimization scheme. In the former case, these methods are employed to numerically solve the TPBVP generated via application of the Euler-Lagrange Theorem. In direct optimization schemes, shooting and collocation methods guide the discretization process and act as function generators that compute the objective and constraints of the NLP problem when supplied with the problem variables.

Both shooting and collocation schemes offer a framework for conducting the transcription step, and each approach has unique benefits. Historically, collocation has more often been employed to complete the transcription step, therefore, the term transcription is sometimes used interchangeably with the word collocation. Thus, a

direct optimization method that utilizes collocation for the transcription step may either be labeled direct collocation or direct transcription. However, in this work, only the title *direct collocation* is employed. Likewise, a direct optimization method that instead leverages a shooting method for the transcription step is denoted *direct shooting*.

Shooting and collocation techniques begin with the same discretization approach. For astrodynamics applications, a trajectory is typically discretized with respect to time. The points along a trajectory associated with these times are termed boundary points or patch points. Cumulatively, this set of boundary points is termed a mesh. The mesh is represented as,

$$\Pi : t_I < t_1 < \dots < t_{s+1} = t_F, \quad (3.41)$$

where  $\Pi$  is comprised of  $s+1$  mesh points, and these points define  $s$  segments. Motion along each segment of a trajectory is defined by the dynamical system, Equation (3.2), associated with the selected model. An accurate representation of this motion is obtained by integrating Equation (3.2), and both shooting and collocation methods offer a means to complete this task.

The fundamental difference between shooting and collocation techniques is the number of segments and integration steps each employs. A single shooting formulation, the most rudimentary shooting technique, utilizes a single segment and many integration steps to represent a trajectory. A multiple shooting scheme expands upon this approach by subdividing a trajectory into multiple segments; over each segment, many integration steps are implemented. A collocation method also employs many segments to represent a trajectory, but the number of integration steps equals the number of segments. Thus, a single integration step is occurs for each segment in a collocation scheme. In sum, shooting and collocation techniques are the means of solving boundary value problems, and their primary difference is the spacing in time over which they perform the integration step.

Shooting and collocation schemes are a means of transcribing the general optimal control problem, as outlined in Section 3.1.1, into the NLP problem described in

Section 3.4. However, these algorithms are also paired with the simple root finding schemes discussed in Section 3.3. In the latter case, shooting and collocation techniques generate feasible solutions to the trajectory design problem. Feasible solutions satisfy the problem constraints but do not optimize a cost function.

### 3.6 Shooting Methods

Shooting methods offer an approach for solving boundary value problems and are also employed to transcribe continuous optimal control problems into NLP problems. Shooting techniques leverage explicit integration to determine the design variable values that satisfy a given set of problem constraints. Single shooting is the simplest type of shooting approach and conveniently illustrates the principles that underlie all shooting methods. A single shooting scheme represents an entire trajectory via a single segment, thus,  $s = 1$  and the entirety of the mesh is  $[t_I, t_F]$ . Following definition of the mesh, single shooting schemes proceed in four basic steps:

1. Estimate the initial conditions  $\mathbf{z}^0$ .
2. Explicitly propagate the differential equations in Equation (3.2) from  $t_I$  to  $t_F$ . This propagation is the “shooting” step.
3. Evaluate the boundary constraints  $\mathbf{c}(\mathbf{z}) = \boldsymbol{\psi}[\mathbf{x}(t_F), \mathbf{u}(t_F), \boldsymbol{\rho}, t_F]$ .
4. Employ an NLP technique to satisfy the constraints  $\mathbf{c}(\mathbf{z}) = \mathbf{0}$ , i.e., repeat the first three steps.

The NLP solution technique described in Step 4 can be as straightforward as Newton’s method or the minimum-norm equation, or one of the optimizers discussed in Section 3.4 can be employed. One advantage of the single shooting technique is the relative simplicity of implementing it, and that it discretizes a problem into a small number of variables. Step 1 above illustrates that the number of variables need only equal the number of first-order equations in the dynamical system,  $\mathbf{f}[\mathbf{x}(t), \mathbf{u}(t), \boldsymbol{\rho}, t]$ . The

small number of variables that is required enables the single shooting approach to be quite computationally efficient, provided a good initial guess. One disadvantage of the single shooting method is the sensitivity (sometimes extreme) to the quality of the initial guess,  $\mathbf{z}^0$ . Because a single explicit propagation is employed across the entire segment, small changes in the initial conditions potentially generate large changes in the states at the end of the propagation, particularly if the dynamical system is nonlinear or the segment time span is quite long. This sensitivity leads to difficulty in determining a vector  $\mathbf{z}$  that satisfies the problem constraints because every update of this vector causes significant changes to the end states of the subsequent propagation step, thus, the algorithm can iterate endlessly with very little, if any, improvement in the satisfaction of the constraints.

To mitigate the sensitivity of the single shooting approach, employing a greater number of segments to represent the trajectory is beneficial. This strategy distributes the problem sensitivity by defining a mesh consisting of  $s$  segments, as seen in Equation (3.41). These segments represent  $s$  shooting subproblems that complete each of steps 1-3 over a shorter timespan. The nonlinearity of the shooting problem across any individual segment is significantly less than in the single shooting scenario, thereby, each subproblem is easier to solve. This approach is termed multiple or parallel shooting because it leverages numerous independent shooting problems. To ensure that these subproblems collectively produce a coherent result, continuity constraints are enforced that ensure the final result from one propagation equals the boundary point at the corresponding time. These constraints are illustrated in Figure 3.1 and are represented in mathematical form as,

$$\mathbf{c} = \left\{ \begin{array}{c} \mathbf{x}_2 - \mathbf{x}_2^t(\mathbf{x}_1) \\ \mathbf{x}_3 - \mathbf{x}_3^t(\mathbf{x}_2) \\ \vdots \\ \mathbf{x}_{s+1} - \mathbf{x}_{s+1}^t(\mathbf{x}_s) \end{array} \right\} = \mathbf{0}, \quad (3.42)$$

where  $\mathbf{x}_2^t(\mathbf{x}_1)$  is the state vector at the end of the explicit propagation from  $\mathbf{x}_1$  for time  $T_1$ . By subdividing a problem into  $s$  segments, the multiple shooting approach

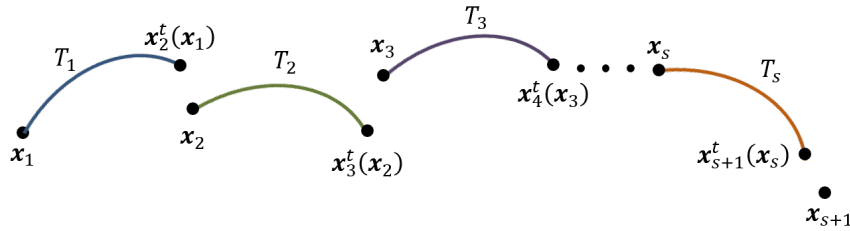


Fig. 3.1. Multiple (Parallel) Shooting Problem

introduces more design variables, thereby, increasing the size of the NLP problem. However, this drawback is mitigated by the fact that the  $s$  subproblems formed by the multiple shooting technique are independent and, therefore, the Jacobian matrix utilized to solve the NLP problem is quite sparse. When only continuity constraints are included in the multiple shooting problem, the Jacobian matrix is banded with  $n_x \times n_x$  blocks of partial derivatives where each block pertains to a shooting subproblem. The multiple shooting approach is a powerful technique for solving boundary value problems that generates highly accurate explicitly integrated results.

Shooting methods typically exploit efficient third-party integration algorithms to propagate the equations of motion for a given dynamical model. Many such algorithms are available and possess varying traits with regard to accuracy and computational efficiency. The primary explicit integration algorithm employed in this investigation is an explicit embedded Runge-Kutta Prince-Dormand (8,9) scheme implemented in C++ and available within the GNU scientific library (GSL). This algorithm is both computationally efficient and highly accurate. Alternately, Matlab's `ode113` explicit integrator is occasionally employed. This tool utilizes a variable-step, variable-order (VSVO) Adams-Bashforth-Moulton PECE solver of orders 1 to 13 and, while it is very accurate, its implementation in Matlab means that it is generally slower than the GSL propagator. Regardless of the explicit integration method, the integration tolerances are defined to equal at least  $1 \times 10^{-12}$  or less. These tools

implement complex explicit integration schemes in a software package that offers a straightforward interface for shooting methods or other explicit integration needs.

### 3.7 Collocation Methods

Collocation is a method for implicitly integrating differential equations, and is frequently utilized to transcribe continuous optimal control problems into NLP problems. This technique approximates motion along a trajectory by fitting piecewise polynomials to a discretization in time. When paired with a direct optimization algorithm, the resulting scheme is denoted as *direct collocation* or *direct transcription* [59]. Descriptions of collocation methods date at least to the first half of the 20<sup>th</sup> century and references to the early work on this subject appear in “The Numerical Treatment of Differential Equations” by Collatz [60]. This text, along with those by de Boor [61] as well as Russell and Shampine [62], mention that Russian researchers performed some of the earliest work on collocation techniques. In the 1960s and 70s, a number of authors applied collocation methods to solve two-point boundary value problems; Russell and Shampine, in particular, generalized a collocation approach to this type of problem [61–63]. By the late 1980s, authors such as Hargraves and Paris began applying collocation methods in the field of trajectory design and optimization [64]. Interest in the utilization of collocation methods for trajectory design has only grown since then, due to its robustness and relative simplicity. Subsequent research has delivered an increase in the order of the polynomials to be leveraged in a collocation scheme [65, 66], and introduced mesh refinement strategies for improving the solution accuracy [37]. Along with the development of enhanced collocation strategies, many researchers implement and distribute these strategies as software packages. Such options include COLSYS [67], OTIS [64], AUTO [68], SOCS [69], MColl [70], and CSALT [71] as examples of the many tools that have been developed for this purpose. Finally, direct transcription is discussed within the broad context of trajectory optimization techniques in several excellent survey papers on the topic [38, 40, 72].

### 3.7.1 General Formulation

A general formulation of the collocation problem is presented here that is applicable to any dynamical system. This scheme computes a result with state continuity and that abides by the equations of motion of the dynamical system. The general formulation begins by considering the mesh in Equation 3.41 that is discretized with respect to time. For numerical convenience, the time along each segment of a collocation problem is typically normalized to the span  $[-1, 1]$ . The mesh defined in Equation (3.41) consists of  $s + 1$  boundary points and  $s$  segments where the time step along each segment is  $\Delta t_i = t_{i+1} - t_i$ . The conversion from nondimensional time  $t$  to normalized time  $\tau$  is then,

$$\tau = \frac{2}{t_{i+1} - t_i}(t - t_i) - 1, \quad (3.43)$$

where  $t_i$  and  $t_{i+1}$  are the times at the boundary points at the beginning and end of the  $i^{\text{th}}$  segment, respectively. Computations on a normalized time scale improves scaling and, thus, computational efficiency. This normalization practice, and the remainder of the collocation framework, follow the approach utilized by Ozimek, Grebow, and Howell [19] and refined by Grebow and Pavlak [70, 73].

Each segment in a collocation problem approximates the solution to Equation (3.2) along the timespan,  $[t_i, t_{i+1}]$ , over that segment. The fidelity of these approximations is governed both by the duration of each segment and the scheme employed to solve Equation (3.2). The simplest approach to solving this dynamical system utilizes Euler's integration rule, i.e.,

$$\mathbf{x}_{i+1} = \mathbf{x}_i + \Delta t_i \mathbf{f}[\mathbf{x}(t_i), \mathbf{u}(t_i), \boldsymbol{\rho}, t_i], \quad (3.44)$$

where  $\mathbf{x}_i = \mathbf{x}(t_i)$  and  $\mathbf{x}_{i+1} = \mathbf{x}(t_{i+1})$ . Equation (3.44) utilizes the vector field information, or "slope", at  $t_i$  to predict the states at  $t_{i+1}$ . The discrepancy between the states predicted by Euler's rule and the actual states at  $t_{i+1}$  is termed the *defect*, and defined,

$$\boldsymbol{\Delta}_i = \mathbf{x}_i - \mathbf{x}_{i+1} + \Delta t_i \mathbf{f}[\mathbf{x}(t_i), \mathbf{u}(t_i), \boldsymbol{\rho}, t_i] = \mathbf{0}. \quad (3.45)$$

The collocation problem is solved when all defects equal zero within a desired tolerance, thus ensuring state continuity between adjacent segments and a mesh that approximates the system dynamics. The Euler rule method of collocation is depicted in Figure 3.2. Euler's rule supplies a simple demonstration of the collocation approach;

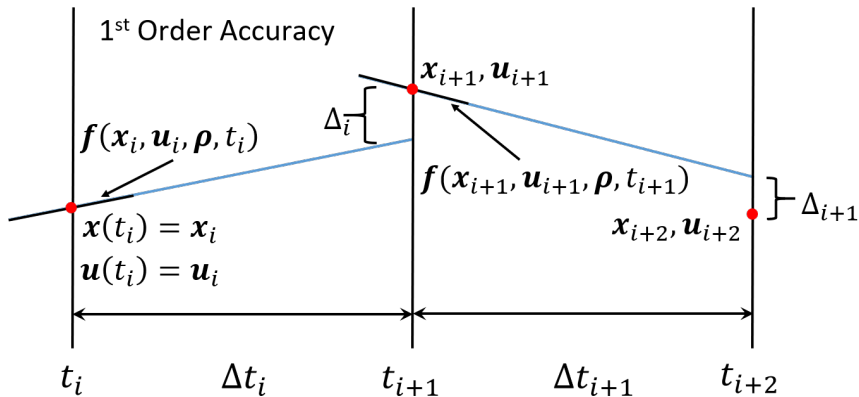


Fig. 3.2. Collocation Using Euler's Rule

however, it only approximates a solution to a set of differential equations with first order accuracy,  $O(h)$ . While the low accuracy associated with Euler's method is mitigated by employing segments with shorter time duration, this approach requires an extremely large number of segments to produce an accurate solution. Alternatively, employing higher order methods to approximate the dynamics along each segment allows a reduction in the number of segments necessary to accurately solve a collocation problem. A method based on the trapezoidal rule, illustrated in Figure 3.3, supplies an additional order of accuracy over Euler's rule,  $O(h^2)$ . The defect equation based on the trapezoidal rule is,

$$\Delta_i = \mathbf{x}_i - \mathbf{x}_{i+1} + \frac{\Delta t_i}{2} \{ \mathbf{f}[\mathbf{x}(t_i), \mathbf{u}(t_i), \boldsymbol{\rho}, t_i] + \mathbf{f}[\mathbf{x}(t_{i+1}), \mathbf{u}(t_{i+1}), \boldsymbol{\rho}, t_{i+1}] \} = \mathbf{0}. \quad (3.46)$$

Low order of accuracy integration schemes, such as Euler's rule, and the trapezoidal rule conveniently demonstrate the fundamental collocation strategy; however, both approaches are generally too coarse for practical application in the dynamical systems encountered in trajectory design problems.

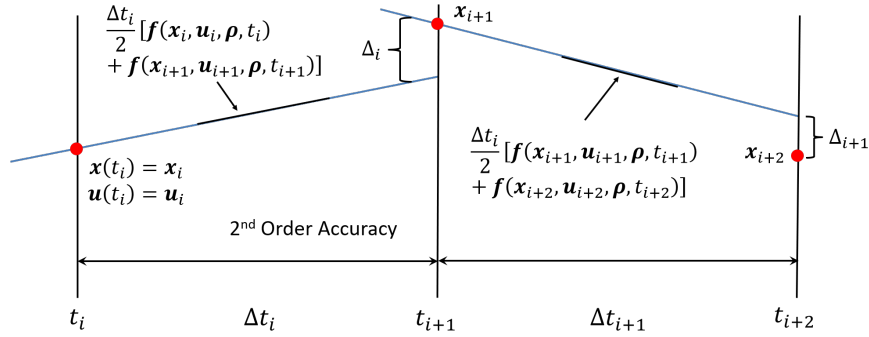


Fig. 3.3. Collocation Using the Trapezoidal Rule

The accuracy of a collocation scheme is determined by the number of segments and the order of the integration method employed to approximate the dynamical system. Most collocation algorithms utilize polynomials to implicitly integrate the differential equations in the dynamical system. Higher degree polynomials typically perform this integration with greater accuracy; although there are diminishing returns after a certain degree is reached. Similar orders of accuracy are achieved either by fitting a coarse discretization with high degree polynomials or by using lower degree polynomials in a discretization with a larger number of segments. The particular approach that is best-suited for implementation to attain the desired solution accuracy is determined by the problem objectives and available computational power.

Given that the benefits of varying the polynomial degree or the segment number are problem dependent, it is advantageous to implement a flexible collocation scheme that can leverage either approach by adjusting the polynomial degree  $N$ . Such a scheme is developed by Williams [66] and refined by Grebow and Pavlak [70, 73]. The method supplied by these latter two authors is represented here. Grebow and Pavlak demonstrate that odd and even degree polynomials whose degrees are adjacent, i.e., 4<sup>th</sup> and 5<sup>th</sup> degree, yield the same accuracy while the odd degree polynomials require

a less complex formulation. Thus, only odd degree polynomials are employed in this investigation. Consider an  $N^{\text{th}}$  degree polynomial for the  $i^{\text{th}}$  segment,

$$\mathbf{p}_i(\tau) = \mathbf{C}_i \{1 \ \tau \ \tau^2 \ \dots \ \tau^N\}^T, \quad (3.47)$$

where  $\mathbf{C}_i$  is a matrix of polynomial coefficients for the  $i^{\text{th}}$  segment with dimensions  $n_x \times (N + 1)$ . The polynomial defining the  $i^{\text{th}}$  segment is then an  $n_x \times 1$  vector that approximates the states at the normalized time,  $\tau$ . This general formulation for representing the polynomials of a collocation scheme accommodates any degree polynomial and an arbitrary number of state variables,  $n_x$ .

A variety of schemes are available for constructing the polynomials along each segment. The matrix of polynomial coefficients,  $\mathbf{C}_i$ , is constructed using states at one or more nodes on the  $i^{\text{th}}$  segment. Each segment is subdivided into  $(N + 1)/2$  *variable nodes* and  $(N - 1)/2$  *defect points*. The index of a variable node or defect point is indicated by the subscript  $j = 1, 2, \dots, N$ ; moreover, the variable nodes and defect points occur at odd and even numbered  $j$ , respectively, as demonstrated in Figure 3.4. A node placement scheme determines the normalized times  $\tau_j$  at which

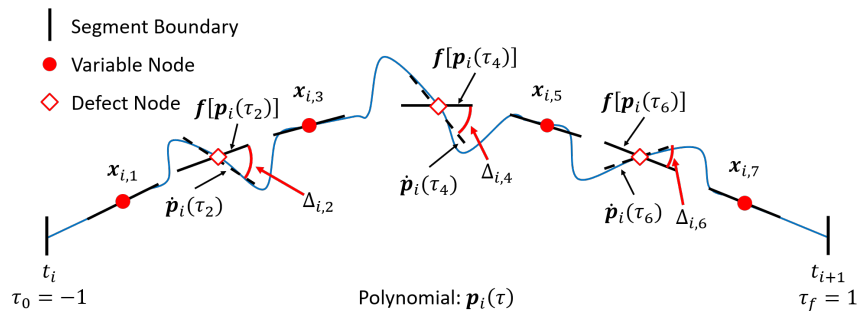


Fig. 3.4. Collocation Using a 7th Degree Polynomial

the variable nodes and boundary points are placed. Though equally distributing the variable nodes in normalized time is the simplest scheme, higher orders of accuracy are delivered by placing the nodes at the roots of Legendre or Chebyshev polynomials. Several node placement schemes prevalent in the literature are listed in Table 3.1,

where  $P_N(\tau)$  are degree  $N$  Legendre polynomials. In this investigation, a collocation

Table 3.1.

Node Placement Schemes		
Method	Description	Order of Accuracy
Legendre-Gauss-Lobatto (LGL)	$\tau_j$ at -1 and 1 and at the roots of $\dot{P}_{N-1}(\tau)$	$2N - 2$
Legendre-Gauss-Radau (LG)	$\tau_j$ at the roots of $P_{N-1}(\tau)$ and $P_N(\tau)$	$2N - 1$
Legendre-Gauss (LG)	$\tau_j$ at the roots of $P_N(\tau)$	$2N$

scheme that utilizes Legendre-Gauss (LG) points is employed due to its high order of accuracy. However, the other methods in Table 3.1 possess similar orders of accuracy and are somewhat less complicated to implement because they include at least one of the segment endpoints. All three schemes lend themselves to highly efficient numerical implementation.

The piecewise polynomials that comprise a collocation problem are constructed with state and gradient information from each segment. A polynomial  $\mathbf{p}_i$  approximates states and derivatives at times  $\tau_j$  along the  $i^{\text{th}}$  segment. The states and derivatives, as evaluated by the polynomial for the  $i^{\text{th}}$  segment at each  $\tau_j$ , are represented as  $\mathbf{p}_{i,j} = \mathbf{p}_i(\tau_j)$  and  $\dot{\mathbf{p}}_{i,j} = d\mathbf{p}_i(\tau_j)/d\tau$ , respectively. The goal of the collocation problem is, for every segment  $i = 1, \dots, s$ , and time,  $j = 1, \dots, N$ , to satisfy the following expressions,

$$\mathbf{p}_{i,j} = \mathbf{x}_{i,j}, \quad i = 1, \dots, s \quad (3.48)$$

$$\dot{\mathbf{p}}_{i,j} = \dot{\mathbf{x}}_{i,j}, \quad j = 1, \dots, N, \quad (3.49)$$

where  $\mathbf{x}_{i,j}$  and  $\dot{\mathbf{x}}_{i,j}$  are the states and derivatives of the dynamical system. The derivatives of the dynamical system are converted to normalized time by,

$$\dot{\mathbf{x}}_{i,j} = \frac{\Delta t_i}{2} \mathbf{f} [\tau_j, \mathbf{x}_{i,j}, \mathbf{u}_{i,j}], \quad (3.50)$$

where  $\Delta t_i$  is the non-normalized time interval of the  $i^{\text{th}}$  segment. Equations (3.48) and (3.49) are first satisfied at the variable nodes by using  $\mathbf{x}_{i,j}$  and  $\dot{\mathbf{x}}_{i,j}$  at the variable node times to construct the polynomial  $\mathbf{p}_{i,j}$ . Substituting Equation (3.47) into Equations (3.48) and (3.49) yields a matrix representation of the variable node constraints along a segment,

$$\mathbf{C}_i [\boldsymbol{\tau} \ \dot{\boldsymbol{\tau}}] = [\mathbf{x}_{i,1}, \mathbf{x}_{i,3}, \dots, \mathbf{x}_{i,N} | \dot{\mathbf{x}}_{i,1} \dot{\mathbf{x}}_{i,3} \dots \dot{\mathbf{x}}_{i,N}], \quad (3.51)$$

where  $\boldsymbol{\tau}$  and  $\dot{\boldsymbol{\tau}}$  represent the matrices,

$$\boldsymbol{\tau} = \begin{bmatrix} 1 & 1 & \dots & 1 \\ \tau_1 & \tau_3 & \dots & \tau_N \\ \tau_1^2 & \tau_3^2 & \dots & \tau_N^2 \\ \vdots & \vdots & \dots & \vdots \\ \tau_1^N & \tau_3^N & \dots & \tau_N^N \end{bmatrix} \quad (3.52)$$

$$\dot{\boldsymbol{\tau}} = \begin{bmatrix} 0 & 0 & \dots & 0 \\ 1 & 1 & \dots & 1 \\ 2\tau_1 & 2\tau_3 & \dots & 2\tau_N \\ \vdots & \vdots & \dots & \vdots \\ N\tau_1^{N-1} & N\tau_3^{N-1} & \dots & N\tau_N^{N-1} \end{bmatrix}. \quad (3.53)$$

Recall that the variable nodes occur at odd values of the subscript  $j$ . The system of equations in Equation (3.51) contains  $2N \times n_x$  constraints and  $n_x \times N + 1$  unknown coefficient values. The constraint represented by Equation (3.51) is implicitly enforced within the collocation scheme by using the states at the variable nodes to construct the segment polynomials. Thus, the states at the variable nodes are supplied as part of the initial guess for the collocation problem, and Equation (3.51) is solved for  $\mathbf{C}_i$  to facilitate polynomial construction. The resulting expression is,

$$\mathbf{C}_i = [\mathbf{x}_{i,1}, \mathbf{x}_{i,3}, \dots, \mathbf{x}_{i,N} | \dot{\mathbf{x}}_{i,1}, \dot{\mathbf{x}}_{i,3}, \dots, \dot{\mathbf{x}}_{i,N}] \mathbf{A}^{-1}, \quad (3.54)$$

where the matrices  $\boldsymbol{\tau}$  and  $\dot{\boldsymbol{\tau}}$  are combined into a single matrix  $\mathbf{A}$  that is square and nonsingular,

$$\mathbf{A} = \left[ \begin{array}{cccc|cccc} 1 & 1 & \cdots & 1 & 0 & 0 & \cdots & 0 \\ \tau_1 & \tau_3 & \cdots & \tau_N & 1 & 1 & \cdots & 1 \\ \tau_1^2 & \tau_3^2 & \cdots & \tau_N^2 & 2\tau_1 & 2\tau_3 & \cdots & 2\tau_N \\ \vdots & \vdots & \cdots & \vdots & \vdots & \vdots & \cdots & \vdots \\ \tau_1^N & \tau_3^N & \cdots & \tau_N^N & N\tau_1^{N-1} & N\tau_3^{N-1} & \cdots & N\tau_N^{N-1} \end{array} \right], \quad (3.55)$$

where a subscript  $i$  is omitted from  $\mathbf{A}$  because this matrix is the same for all segments. The states included in the initial guess are used in Equation (3.54) to compute the unknown polynomial coefficients. Note, if first order differential equations are available for any of the control variables,  $\mathbf{u}_{i,j}$ , then polynomials are constructed for these variables in a similar manner. However, this approach is not employed in this investigation.

Next, the constructed polynomials are leveraged to approximate the states at the defect points. Recall that the normalized times,  $\tau_j$ , at which the defect points are located are determined by the LG node placement scheme and that these points occur at even values of  $j$ . These normalized times are used to create the matrices  $\mathbf{B}$  and  $\mathbf{D}$ ,

$$\mathbf{B} = \left[ \begin{array}{cccccc} 1 & 1 & 1 & \cdots & 1 & 1 \\ -1 & \tau_2 & \tau_4 & \cdots & \tau_{N-1} & 1 \\ -1 & \tau_2^2 & \tau_4^2 & \cdots & \tau_{N-1}^2 & 1 \\ \vdots & \vdots & \vdots & \cdots & \vdots & \vdots \\ -1 & \tau_2^N & \tau_4^N & \cdots & \tau_{N-1}^N & 1 \end{array} \right] \quad (3.56)$$

$$\mathbf{D} = \left[ \begin{array}{cccc} 0 & 0 & \cdots & 0 \\ 1 & 1 & \cdots & 1 \\ 2\tau_2 & 2\tau_4 & \cdots & 2\tau_{N-1} \\ \vdots & \vdots & \cdots & \vdots \\ N\tau_2^{N-1} & N\tau_4^{N-1} & \cdots & N\tau_{N-1}^{N-1} \end{array} \right], \quad (3.57)$$

where, once again, subscripts are omitted from  $\mathbf{B}$  and  $\mathbf{D}$  because these matrices are identical for all segments. The first and last columns of  $\mathbf{B}$  are included to compute the states at the segment boundary points, i.e.,  $\tau = -1$  and  $1$ . While these points are not a part of the LG node placement scheme, they are included here because states at these points are used elsewhere in the collocation framework to ensure segment continuity and enforce boundary constraints. The matrices  $\mathbf{A}$ ,  $\mathbf{B}$ , and  $\mathbf{D}$  demonstrate the utility of normalizing time along each segment. This normalization ensures these matrices as identical for all segments, therefore, they are computed only once, at the beginning of a collocation problem and stored in memory. The matrix  $\mathbf{B}$  and the polynomial coefficients are then employed to evaluate the states at the defect and boundary points,

$$[\mathbf{x}_{i,I}^p \ \mathbf{x}_{i,2}^p \ \mathbf{x}_{i,4}^p \ \cdots \ \mathbf{x}_{i,N-1}^p \ \mathbf{x}_{i,F}^p] = \mathbf{C}_i \mathbf{B}, \quad (3.58)$$

where  $\mathbf{x}_{i,I}^p$  and  $\mathbf{x}_{i,F}^p$  are the states at the initial and final boundary points along the  $i^{\text{th}}$  segment, and the superscript  $p$  denotes that these states are computed with the polynomial,  $\mathbf{p}_i$ . If a polynomial representation of the control history is employed, then control values at the defect points are also computed as demonstrated in Equation (3.58). The polynomial coefficients computed with Equation (3.54) are also used to compute the derivatives of the states at the defect points,

$$[\dot{\mathbf{x}}_{i,2}^p \ \dot{\mathbf{x}}_{i,4}^p \ \cdots \ \dot{\mathbf{x}}_{i,N-1}^p] = \mathbf{C}_i \mathbf{D}, \quad (3.59)$$

where the superscript  $p$  again denotes that these derivatives are computed with the polynomial,  $\mathbf{p}_i$ . The derivatives at the defect points are also calculated with the dynamical system equations and the states at the defect points given by the polynomials, i.e.,

$$[\dot{\mathbf{x}}_{i,2} \ \dot{\mathbf{x}}_{i,4} \ \cdots \ \dot{\mathbf{x}}_{i,N-1}] = [\mathbf{f}(\mathbf{p}_i(\tau_2)) \ \mathbf{f}(\mathbf{p}_i(\tau_4)) \ \cdots \ \mathbf{f}(\mathbf{p}_i(\tau_{N-1}))]. \quad (3.60)$$

Then, the defect equations are defined by the difference between the two approaches for constructing the derivatives at the defect points demonstrated by Equations (3.59) and (3.60), that is,

$$\Delta_i = [\mathbf{C}_i \mathbf{D} - [\dot{\mathbf{x}}_{i,2} \ \dot{\mathbf{x}}_{i,4} \ \cdots \ \dot{\mathbf{x}}_{i,N-1}]] \mathbf{W} = \mathbf{0}, \quad (3.61)$$

where the diagonal matrix  $\mathbf{W}$  incorporates quadrature weights for the even nodes that enable the selected node placement scheme to supply a higher order of accuracy than the same number of unweighted nodes. Driving the defect constraints, Equation (3.61), to zero, or some acceptable tolerance, ensures that the polynomials constructed for each segment sufficiently approximate the system dynamics. When convergence is obtained, the solution for the collocation problem yields piecewise polynomials that approximate the state at any point along a solution arc. The variable node states that result in defect constraints that evaluate to zero are determined by posing the collocation problem as an NLP problem which is implemented as described in Section 3.4. The design variables in this framework are the position and velocity states at the variable nodes, i.e.,

$$\mathbf{X} = \begin{bmatrix} \mathbf{x}_{1,1} & \mathbf{x}_{1,3} & \cdots & \mathbf{x}_{1,N} \\ \mathbf{x}_{2,1} & \mathbf{x}_{2,3} & \cdots & \mathbf{x}_{2,N} \\ \vdots & \vdots & \ddots & \vdots \\ \mathbf{x}_{s,1} & \mathbf{x}_{s,3} & \cdots & \mathbf{x}_{s,N} \end{bmatrix}, \quad (3.62)$$

where the  $\mathbf{X}$  matrix in Equation (3.62) is reshaped into a single column vector and included in  $\mathbf{z}$ , the column vector of design variables for NLP problem. The defect constraints along each segment are included in the constraint vector of the NLP problem, as are continuity constraints that ensure that the segments comprising the final trajectory are continuous in position and velocity,

$$\mathbf{c} = \begin{bmatrix} \mathbf{x}_{2,I}^p - \mathbf{x}_{1,F}^p \\ \mathbf{x}_{3,I}^p - \mathbf{x}_{2,F}^p \\ \vdots \\ \mathbf{x}_{s,I}^p - \mathbf{x}_{s,F}^p \\ [\mathbf{C}_1 \mathbf{D} - [\dot{\mathbf{x}}_{1,2} \ \dot{\mathbf{x}}_{1,4} \ \cdots \ \dot{\mathbf{x}}_{1,N-1}]] \mathbf{W} \\ [\mathbf{C}_2 \mathbf{D} - [\dot{\mathbf{x}}_{2,2} \ \dot{\mathbf{x}}_{2,4} \ \cdots \ \dot{\mathbf{x}}_{2,N-1}]] \mathbf{W} \\ \vdots \\ [\mathbf{C}_s \mathbf{D} - [\dot{\mathbf{x}}_{s,2} \ \dot{\mathbf{x}}_{s,4} \ \cdots \ \dot{\mathbf{x}}_{s,N-1}]] \mathbf{W} \end{bmatrix} = \mathbf{0}. \quad (3.63)$$

The constraints that define the collocation problem are formulated such that computations along each segment are independent. Therefore, the Jacobian matrix that results from the partial derivatives of  $\mathbf{c}$  with respect to  $\mathbf{z}$  is quite sparse. The sparsity of the Jacobian matrix is leveraged to implement strategies that reduce the computational times for general collocation algorithms. These strategies are especially essential when the collocation problem becomes very large. The procedure for solving a NLP problem by collocation is illustrated in the flowchart in Figure 3.5. A converged result to a collocation problem yields the approximation of a solution to a system of differential equations, and this approximation is dependent upon the parameters of the discretization technique and the implicit integration method. The accuracy of the final solution is improved by refining the discretization mesh.

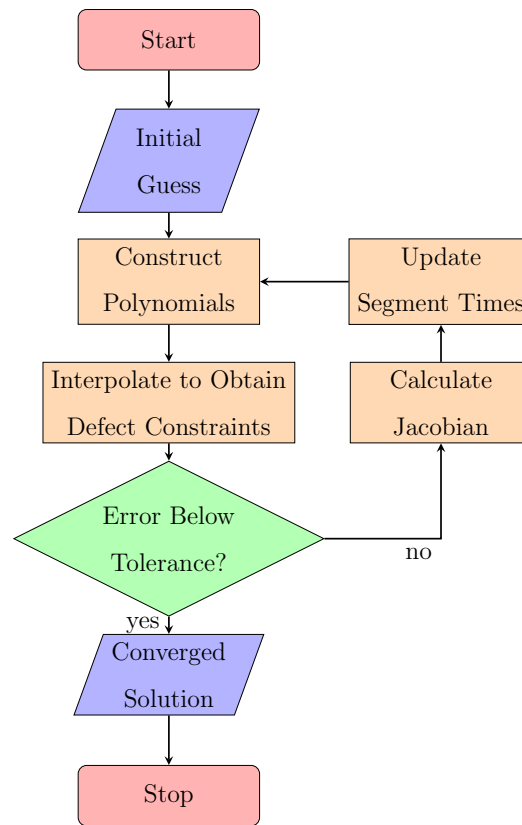


Fig. 3.5. Procedure for Applying Collocation with Newton's Method or Minimum-Norm Equation

### 3.7.2 Mesh Refinement

Collocation is typically paired with a mesh refinement scheme to generate a solution that solves the given differential equations with a sufficient level of accuracy. Because each segment in a collocation problem utilizes a single integration step to solve the equations of motion, the initial solution of this problem may poorly approximate the dynamical system. Mesh refinement schemes update the mesh,  $\Pi$ , by adjusting the boundary point times displayed in Equation (3.41) to evenly distribute and ultimately reduce error. Together, collocation and mesh refinement schemes generate solutions equal in accuracy to those supplied by a multiple shooting strategy.

Several mesh refinement schemes are available and each possesses distinct advantages and disadvantages that inform their use. Russell and Christiansen compare several mesh refinement schemes [74], including the de Boor mesh refinement technique. Originally developed by Carl de Boor [75], this approach reduces and equally distributes the error among the segments in the collocation problem. An alternate mesh refinement approach termed Control with Explicit Propagation (CEP) is proposed by Grebow and Pavlak [70, 76]. This strategy employs explicit propagation to add and remove segments from the mesh and ensure the accuracy of the final collocation solution. Finally, Grebow and Pavlak also propose a hybrid mesh refinement approach that combines the method from de Boor and the CEP technique to yield an approach that leverages the advantages of both strategies.

#### Method from de Boor

The mesh refinement method from de Boor relies on an analytical estimation of the error for each segment to determine the redistribution of the boundary points as well as additions and removals. This entirely analytical approach to mesh refinement implies that the de Boor method typically requires the least computational time of any of the mesh refinement schemes in this investigation. The de Boor mesh refinement method, as outlined here, follows from a framework employed by Ozimek et al. [19]

and further developed by Grebow and Pavlak [73]. The de Boor method estimates the error in a polynomial approximation of order  $N$  for the  $i^{\text{th}}$  segment as,

$$e_i = K\Delta t_i^{N+1}\xi_i + O(\Delta t_i^{N+2}), \quad (3.64)$$

where the scalar error due to the omission of higher order terms,  $O(\Delta t_i^{N+2})$ , is determined by the time interval along a given segment. The  $N^{\text{th}+1}$  derivative of the constructed polynomial is represented by  $\xi$  and the constant  $K$  is a dimensionless scalar value that is dependent on the degree of the polynomial. A method for computing  $K$  appears in Russell and Christiansen (Appendix) [74] and several pre-computed values are listed in Table 3.2. De Boor states that the variable  $\xi_i$  is estimated by the  $N^{\text{th}+1}$

Table 3.2.  
Constant Values for Odd Degree Polynomial Error Calculation

Degree	$K$ Value
1	1.25
2	$8.01875373874480 \times 10^{-3}$
3	$5.208333333333334 \times 10^{-4}$
4	$2.45076190281488 \times 10^{-5}$
5	$1.03339947089947 \times 10^{-6}$
6	$3.59267656090070 \times 10^{-8}$
7	$1.12915151977652 \times 10^{-9}$
8	$3.08927792667408 \times 10^{-11}$
9	$7.74907905728965 \times 10^{-13}$
10	$1.74408359272640 \times 10^{-14}$
11	$3.64148451940432 \times 10^{-16}$

derivative of the solution [75]; however, this value cannot be determined directly from

the polynomial in the collocation solution. As an alternative, the polynomial and time intervals on the converged collocation solution are used to approximate  $\xi_i$ ,

$$\xi_i \approx \begin{cases} 2\max \left[ \frac{|\mathbf{p}_1^{(N)} - \mathbf{p}_2^{(N)}|}{\Delta t_1 + \Delta t_2} \right], & \text{on } (t_1, t_2) \\ \max \left[ \frac{|\mathbf{p}_{i-1}^{(N)} - \mathbf{p}_i^{(N)}|}{\Delta t_{i-1} + \Delta t_i} \right] + \max \left[ \frac{|\mathbf{p}_{i+1}^{(N)} - \mathbf{p}_i^{(N)}|}{\Delta t_{i+1} + \Delta t_i} \right], & \text{on } (t_i, t_{i+1}), \quad i = 2, \dots, s-1. \\ 2\max \left[ \frac{|\mathbf{p}_{s+1}^{(N)} - \mathbf{p}_s^{(N)}|}{\Delta t_{s+1} + \Delta t_s} \right], & \text{on } (t_s, t_{s+1}) \end{cases} \quad (3.65)$$

The error calculated with Equations (3.64) and (3.65) is an approximation of the error in the polynomial fit to the dynamical system differential equations for the  $i^{\text{th}}$  segment. This error approximation is not equivalent to the error determined by comparing the polynomial to an explicit propagation of the same segment.

Following the initial solution of the NLP problem, the error associated with each segment of a collocation scheme may vary significantly along a path. Equally distributing this error along a trajectory is desirable because it promotes efficient node placement. When error is evenly distributed more boundary points are placed in regions of the trajectory where states are changing rapidly and vice versa. The de Boor method offers a strategy of updating the times at the boundary points to achieve error equidistribution; these times are identified by,

$$t_{i+1} = I^{-1} \left[ \frac{iI(t_{s+1})}{s} \right], \quad i = 1, \dots, s-1, \quad (3.66)$$

where  $I$  is determined from the integral,

$$I(t) = \int_{t_1}^t \xi_i(s)^{\frac{1}{s+2}} ds. \quad (3.67)$$

Calculation of the integral in Equation (3.67) is simplified by the fact that  $\xi_i(s)$  is approximated by a piecewise constant method. Therefore, Equation (3.67) is precisely constructed by the rectangle rule of integration. Note, Equation (3.67) is the inverse integral of  $I$ , computed at the value indicated by the expression within the brackets. State and control values at the new boundary point node times, computed via Equation (3.67), are interpolated from the mesh nodes that support the previously converged collocation solution; the NLP problem is then resolved with these

new values. The process of computing the quantities in Equations (3.64)-(3.67) and re-solving the NLP problem is iterated until the maximum difference between the segment errors is less than a predefined tolerance.

After the error in the polynomial approximations is equally distributed along each segment of the mesh, the number of segments is updated as well. The updated number of segments in the mesh is calculated as,

$$s_{r+1} = \text{round} \left[ s_r \left( \frac{10e_i}{tol} \right)^{\frac{1}{N+1}} + 5 \right], \quad (3.68)$$

where  $s_r$  is the number of segments employed for the  $r^{\text{th}}$  solution of the NLP. Then the new times for the boundary points are calculated using Equation (3.66) and the NLP problem is solved again. The procedure for equally distributing and reducing the total error by updating the mesh is repeated until the tolerances governing both these processes are satisfied. A schematic of the de Boor mesh refinement method is illustrated in Figure 3.6.

The two strengths of the de Boor mesh refinement method are its computational speed and the even distribution of error across segments. Equations (3.64)-(3.68) are implemented in an efficient form that enables rapid computation of all necessary quantities. Additionally, the error distribution step included in the de Boor method reduces the total number of segments that must be added to a problem because existing segments are moved to regions of the trajectory where they are needed most rather than always simply adding more segments in problematic areas. A drawback of the de Boor approach is that the computation of the segment error is based on approximations, thus, the solution generated by this procedure likely must still be verified with an explicit propagation technique. Additionally, experience indicates that the segment addition step of the de Boor method typically adds more segments than other approaches. Despite these downsides, the de Boor method is still an effective means of performing mesh refinement for a solution to the NLP problem computed via collocation.

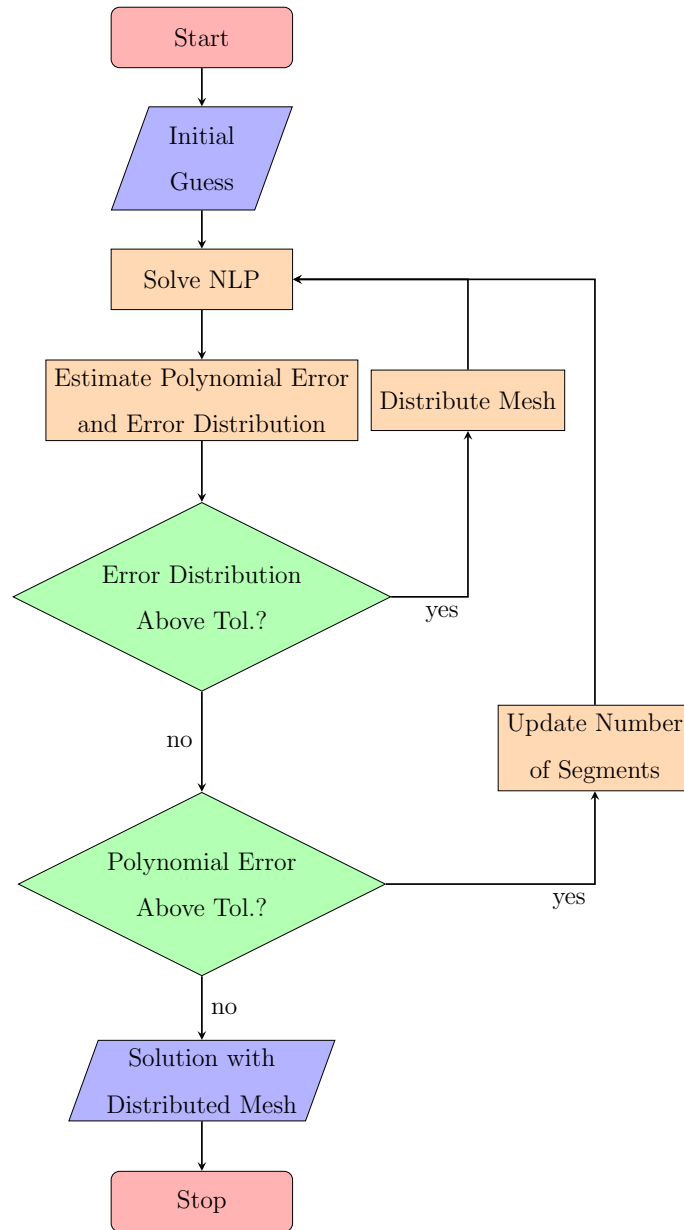


Fig. 3.6. Procedure for de Boor method of mesh refinement.

## Control with Explicit Propagation (CEP)

An alternate approach to the mesh refinement process is offered by the CEP method. This straightforward technique leverages explicit propagation to validate the accuracy of the solution in the NLP problem computed via collocation. A flowchart depicting the essential steps of the CEP approach is offered in Figure 3.7. This diagram illustrates that the CEP mesh refinement method involves two separate phases: segment removal and segment addition. In the segment removal phase, an explicit propagation is performed for every pair of segments, i.e., for the timespan  $[t_i t_{i+2}]$ . Following propagation, the errors between the states at the end of the propagation and the states at the boundary point for the corresponding time are computed. If the  $l^2$ -norm of these errors is below a user-defined tolerance, i.e.,  $\epsilon_{rem} = 1 \times 10^{-12}$ , then the shared boundary point of the segment pair is removed, that is, the two segments are merged into one. The segment removal phase of the CEP method is continued until a comparison with no segments removed.

After extraneous segments are removed from the collocation problem, segments are added where the desired solution accuracy is not satisfied. The steps for the segment addition phase are nearly identical to the removal process except that an explicit propagation is conducted between every segment as opposed to pairs, i.e., for the timespan  $[t_i t_{i+1}]$ . The errors between the states at the terminus of every explicit propagation and the states at the time corresponding to the boundary point are once again assessed. If the  $l^2$ -norm of this error is greater than a user-defined tolerance,  $\epsilon_{add} = 1 \times 10^{-12}$ , then the segment is split in two where the time at the new segment boundary point is,  $t_{new} = t_i + (t_{i+1} - t_i)/2$ . The segment addition phase of the CEP method is continued until no segments are added. The final result from the CEP mesh refinement procedure is a solution to the NLP problem solved via collocation where the accuracy of every segment is verified by a third-party explicit integration tool.

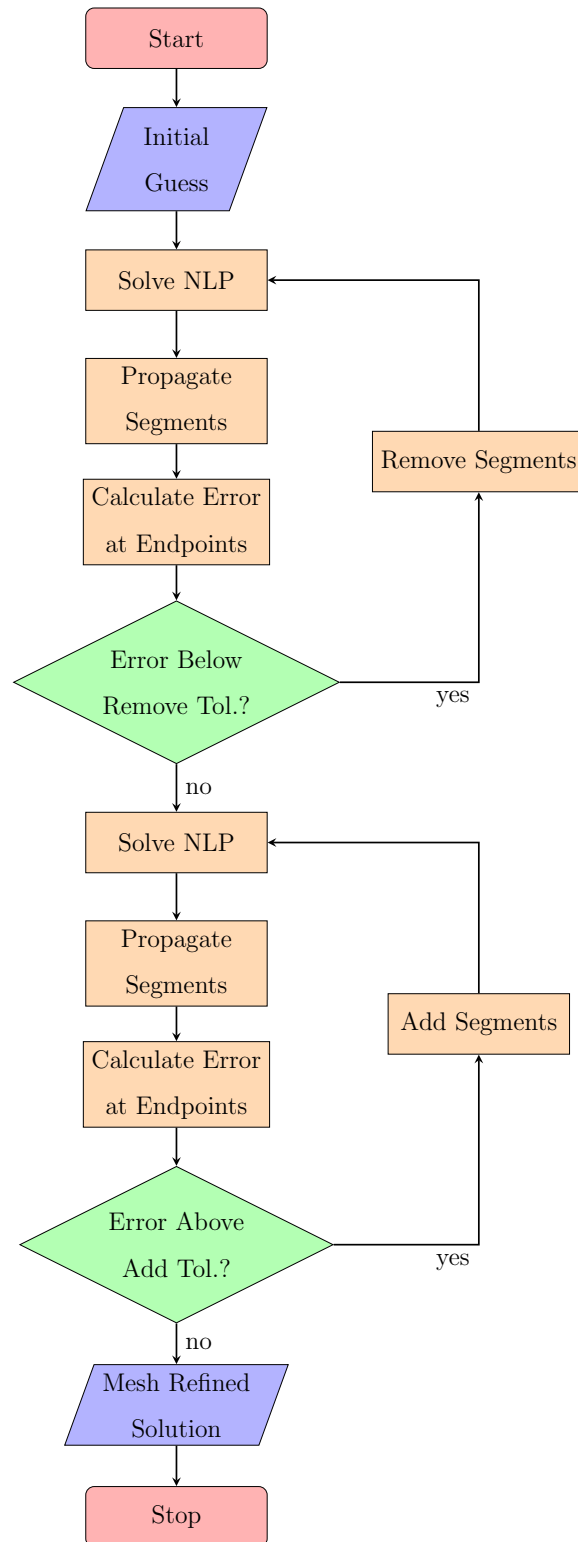


Fig. 3.7. Procedure for CEP mesh refinement.

The external validation offered by the CEP mesh refinement approach is the primary benefit of this method. When this mesh refinement strategy is employed, the end result is a solution with a high level of accuracy verified by an outside tool. An additional benefit is that the error associated with each segment is not an approximation and is more easily understood. More accurate knowledge of the segment errors prevents extraneous segments from being included, thus frequently, fewer segments are added than in the de Boor method. A drawback of the CEP approach is the explicit propagation of every segment that is computationally expensive relative to the analytical segment error estimation in the de Boor technique. However, the mesh refinement step is only performed between successive solutions of the NLP problem and, thus, comprises a relatively small portion of the total computational process. Therefore, the explicit propagation required by the CEP method is usually not prohibitive with regard to computational time. However, if the mesh refinement process becomes a “choke point” in the overall solution process in a given optimal control problem, then it may be beneficial to switch to the de Boor approach. Finally, as the CEP method also does not directly attempt to distribute error across a trajectory, it may require more iterations for segment addition and subtraction than the de Boor process.

### **Hybrid Mesh Refinement**

The hybrid mesh refinement approach combines the strengths of the de Boor and CEP mesh refinement techniques to offer a powerful mesh refinement method that is employed as the default approach for the trajectory design problems in this current investigation. The hybrid method performs the error distribution step of the de Boor method before executing the segment removal and addition phases of the CEP mesh refinement process. Thus, the equations presented in Section 3.7.2 are utilized to determine the error distribution along the trajectory and, once the tolerance for this distribution is satisfied, the CEP mesh refinement process begins. No additional

error distribution steps are introduced once the CEP method commences. Combining these two approaches offers the error distribution of the de Boor method as well as the accuracy and validation of the CEP technique. Completing the error distribution step before the CEP phases reduces the number of segments that are added or removed and, therefore, the total computational time. Because the hybrid mesh refinement technique possesses the strength of the two previously described methods without adding significant computational time, it is typically the default mesh refinement technique employed in this investigation.

### 3.8 Collocation with Optimization for Low-Thrust (COLT) Implementation

The collocation scheme in the preceding section is adapted to generate optimal low-thrust trajectories, a transformation that introduces additional variables and constraints. The set of algorithms produced by this process is collectively termed COLT (Collocation with Optimization for Low-Thrust). This tool, developed in collaboration with Daniel Grebow at the Jet Propulsion Laboratory, serves as a prototype for MColl [70]. MColl is the direct collocation tool, developed by Grebow and Pavlak, included in the MONTE (Mission Analysis, Operations, and Navigation Toolkit) software package. The COLT algorithm computes optimal low-thrust solutions in any of the dynamical models described in Chapter 2, and serves to generate all low-thrust solutions in this document.

Several additional design variables are added to the collocation scheme detailed in Section 3.7 to adapt it for the purpose of low-thrust trajectory optimization. Numerous options are available for parameterizing control, that is,  $\mathbf{u}$  in a low-thrust trajectory optimization problem, and some schemes offer favorable numerical properties. In COLT, the control variables are the three components of the thrust unit vector, i.e.,  $\mathbf{u} = \mathbf{T} = [T_x, T_y, T_z]$ . The thrust vector is defined in an inertial frame and transformed into the frame of the selected equations of motion at the necessary times.

The components of the thrust unit vector are constrained such that  $\|\mathbf{u}\| = 1$ . The magnitude of the thrust vector,  $T$ , is computed using the initial,  $m_{i,I}$ , and final,  $m_{i,F}$ , mass of each segment. These two quantities are employed to calculate a throttling value,  $\sigma_i$ , for each segment that is constrained to the range  $0 \leq \sigma_i \leq 1$ .

$$\sigma_i = \frac{m_{i,I} - m_{i,F}}{\dot{m}_{max,i} \Delta t_i} \quad (3.69)$$

The throttling value from Equation (3.69) produces the thrust magnitude,  $T_i = \sigma_i T_{max,i}$ , and the mass flow rate,  $\dot{m}_i = \sigma_i \dot{m}_{max,i}$ , for a given segment. The maximum mass flow rate,  $\dot{m}_{max,i}$ , and maximum thrust magnitude,  $T_{max,i}$ , are defined by the selected low-thrust engine model. In this investigation  $\dot{m}_{max,i}$  and  $T_{max,i}$  are constant values; however, they can also be formulated as functions of other quantities such as power and distance from the Sun.

The design variables for the collocation scheme implemented in COLT are included in a single column vector,  $\mathbf{x}$ , that includes all of the design variables of the NLP problem as described in Section 3.4. The same types of design variables define each segment along the low-thrust trajectory. The design variables for the  $i^{\text{th}}$  segment are collected into the vector,  $\mathbf{S}_i$ , and these vectors are consolidated in the design variables vector  $\mathbf{z}$ , i.e.,

$$\mathbf{S}_i = \left\{ \mathbf{u}_i \quad m_{i,I} \quad m_{i,F} \quad \mathbf{x}_{i,1} \quad \mathbf{x}_{i,3} \quad \cdots \quad \mathbf{x}_{i,N} \right\}^T \quad (3.70)$$

$$\mathbf{z} = \left\{ \mathbf{S}_1 \quad \mathbf{S}_2 \quad \cdots \quad \mathbf{S}_s \right\}^T. \quad (3.71)$$

The total vector of design variable values for the NLP problem is then comprised of  $s$  of these smaller column vectors. Equations (3.70) and (3.71) illustrate that the control variables and thrust magnitude are constant over each segment. The elements of the design variable vector are updated throughout the optimization process and, at each iteration, these variables are used to evaluate the problem constraints.

A variety of problem constraints are available in COLT. While some are enforced to obtain a solution to the low-thrust trajectory optimization problem, others are

only included for certain scenarios. Within COLT, these constraints are arranged into equality constraints,  $\mathbf{c}_{eq}$ , and inequality constraints,  $\mathbf{c}_{ineq}$ .

$$\mathbf{c}_{eq} = \left[ \mathbf{g}_{defect} \quad \mathbf{g}_{continuity} \quad \mathbf{g}_{\hat{T}} \quad \boldsymbol{\psi}_I \quad \boldsymbol{\psi}_F \right]^T = 0 \quad (3.72)$$

$$\mathbf{c}_{ineq} = \left[ \mathbf{g}_{\sigma} \quad \mathbf{g}_{rad} \right]^T \leq 0 \quad (3.73)$$

Equations (3.72) and (3.73) illustrate, at a high level, the organization of common constraints in COLT. A collocation scheme always enforces defect constraints,  $\mathbf{g}_{defect}$ , to obtain a valid solution. Because of the selected node spacing scheme, COLT also requires the enforcement of continuity constraints between segments,  $\mathbf{g}_{continuity}$ , as do some other collocation implementations. Both of these constraints are incorporated in Equation (3.63) in Section 3.7.1. When control variables are included, additional constraints are required to ensure that these variables maintain realistic values. The three components of the thrust unit vector are constrained to possess unit magnitude, that is,

$$\|\mathbf{u}_i\| = \sqrt{T_{i,x}^2 + T_{i,y}^2 + T_{i,z}^2} = 1, \quad (3.74)$$

where Equation (3.74) is the equality constraint,  $\mathbf{g}_{\hat{T}}$ , included in Equation (3.72). Furthermore, the throttle value,  $\sigma_i$  is bounded to be between 0 and 1 via a set of inequality constraints denoted in Equation (3.73) as  $\mathbf{g}_{\sigma}$ .

All other constraints included in Equations (3.72) and (3.73) are optional and problem specific. Frequently, boundary constraints are applied at the initial,  $\boldsymbol{\psi}_I$ , and final,  $\boldsymbol{\psi}_F$ , boundary points along the trajectory to fix the values of the states, energy, and/or orbital elements at these times. This type of constraint is employed in this investigation to ensure trajectories depart from and insert onto specific orbits. Furthermore, it is often beneficial to include minimum radius constraints with respect to gravitational bodies, i.e.,  $\mathbf{g}_{rad}$ . These constraints enforce a “keep-out” zone around these bodies such that the trajectory cannot pass within the zone. This type of constraint is particularly necessary when a trajectory includes, or is likely to include, a flyby of a primary body. Specific low-thrust trajectory design scenarios may require other constraints, and these are straightforward to incorporate in a collocation

framework. Depending on their nature, additional constraints are appended to either Equation (3.72) or Equation (3.73).

The minimum radius constraints included in COLT enable low-thrust trajectories to converge that would otherwise remain “stuck” near primary bodies. These constraints require each variable node along a trajectory to include a radius value with respect to a chosen body that is greater than or equal to a user-defined value,  $r_{P_{min}}$ . For example, a trajectory that passes close to the Moon may require all variable nodes to have a distance from the center of the Moon equal to, at least, 2 lunar radii, i.e., 3474.8 km. For a single variable node the minimum radius constraint is written,

$$\sqrt{(x_{i,j} - x_P)^2 + (y_{i,j} - y_P)^2 + (z_{i,j} - z_P)^2} \geq r_{P_{min}} \quad (3.75)$$

where the variable node position is  $\mathbf{r}_{i,j} = \{x_{i,j} \ y_{i,j} \ z_{i,j}\}^T$  and the location of the primary body is  $\mathbf{r}_P = \{x_P \ y_P \ z_P\}^T$ . This constraint is intended to prevent any arcs of a trajectory from passing beneath the surface of the primary body and producing an impractical result. Moreover, the nonlinear dynamics near primary bodies significantly challenge convergence of a trajectory that passes close to these bodies. Compounding this difficulty is the fact that optimization algorithms often shift trajectories closer to primary bodies to leverage the effective adjustments in energy that close flybys of them offer. Convergence challenges that result from close flybys of primary bodies are mitigated by preventing a trajectory from passing too close to the Moon. Unfortunately, while this constraint is helpful for obtaining convergence, it is only enforced at the variable nodes, thus, it is still possible for a trajectory to sometimes pass below the minimum radius value. The development of alternative approaches to enforcing a minimum radius constraint may offer more effective strategies (see Chapter 7).

The objective of a low-thrust optimal control problem is typically the minimization of propellant consumption or time of flight. In this investigation, the objective is always the minimization of propellant consumption. Thus, the objective function is,

$$F = \sum_{i=1}^s (m_{i,I} - m_{i,F}), \quad (3.76)$$

one that sums the change in mass over all segments to compute the total change in mass for the trajectory. An alternate formulation of the objective function is  $F = -m_{s,F}$  that maximizes the final mass of the trajectory. While both formulations promote the same objective, their different numerical implementations potentially produce disparate convergence behavior. The expression in Equation (3.76) is utilized in this investigation; however, a rigorous analysis of the effect on convergence behavior of the alternate formulations would be beneficial.

The design variables, constraints, and objective in the collocation scheme implemented in COLT form an NLP problem and several approaches for solving this problem are available. If a merely feasible solution is desired, the objective function is ignored and Equations (3.71), (3.72), and (3.73) are utilized in a Newton’s method or minimum-norm scheme to compute a value of  $\mathbf{z}$  that satisfies the problem constraints. In this scenario, slack variables are added to the design variable vector to enforce the inequality constraints in Equation (3.73). An approach for implementing slack variables is presented by Pavlak [29]. If optimization is desired, then one of several third-party optimizers is employed. The optimizers, `fmincon`, SNOPT [56, 57], and IPOPT [58], are available within COLT to pair with the collocation algorithms, and IPOPT is used for all optimal solutions in this investigation.

Whether a feasible or optimal solution of the NLP problem is sought, the Jacobian, the matrix of partial derivatives of the constraints with respect to the design variables, is necessary to compute a solution. Within COLT, this matrix is computed via a mixture of finite difference approximations and analytical expressions. The partials of the defect and continuity constraints are computed with complex-step differentiation, while the partial derivatives of most other constraints are calculated via analytical expressions. Analytical expressions are typically the most computationally efficient approaches for computing the required partial derivatives. However, evaluation of these expressions must be implemented in a computationally efficient manner or, else, they can be as computationally cumbersome as a finite difference approximation.

Bounding the design variables is an additional step taken within the COLT framework to make large NLP problems more tractable. This step limits the range of the design variable values that the optimizer searches over that, ideally, facilitates convergence towards an optimal solution. The standard design variables included in COLT are bounded as follows,

$$\mathbf{z}_U = \left[ \mathbf{u}_{1U} \quad m_{I,1U} \quad m_{F,1U} \quad \mathbf{r}_{1,1U} \quad \dot{\mathbf{r}}_{1,1U} \quad \cdots \right]^T = \left[ \mathbf{1} \quad m_I \quad m_I \quad \mathbf{r}_{1,1_0} + \boldsymbol{\nu}_r \quad \dot{\mathbf{r}}_{1,1_0} + \boldsymbol{\nu}_{\dot{r}} \quad \cdots \right]^T \quad (3.77)$$

$$\mathbf{z}_L = \left[ \mathbf{u}_{1L} \quad m_{I,1L} \quad m_{F,1L} \quad \mathbf{r}_{1,1L} \quad \dot{\mathbf{r}}_{1,1L} \quad \cdots \right]^T = \left[ -\mathbf{1} \quad 0 \quad 0 \quad \mathbf{r}_{1,1_0} - \boldsymbol{\nu}_r \quad \dot{\mathbf{r}}_{1,1_0} - \boldsymbol{\nu}_{\dot{r}} \quad \cdots \right]^T. \quad (3.78)$$

Some design variables possess obvious upper and lower bounds; for example, necessary constraints on the control and mass variables can be enforced simply by applying bounds, as apparent in Equations (3.77) and (3.78). Bounds on other variables, such as the position and velocity states, are left as user inputs. Position and velocity states are bounded to remain within a certain range of their initial values, and the maximum deviations from these values are labelled  $\nu_r$  for position states and  $\nu_{\dot{r}}$  for velocity states. While applying bounds to the design variables aids the optimization algorithm in identifying an optimal solution, it is undesirable for the final solution, delivered from the optimizer, to be in contact with any of the bounds unless these bounds define an actual physical limitation such as the minimum spacecraft mass. A solution with design variables that equal their bounds typically indicates that the bounds prevented the optimizer from reaching the values of these design variables that generate the true local optimal solution. Therefore, if this scenario is encountered, then the computed solution should be employed as an initial guess for an optimization problem with larger bounds on the design variables.

The COLT software package offers an implementation of a direct collocation scheme developed specifically to solve low-thrust optimization problems. When combined with the orbit chain methodology introduced in the following chapter, the COLT tool supplies an approach for computing optimal low-thrust trajectories even

in unfamiliar dynamical regimes. The variety of dynamical models, constraints, and third-party optimizers that COLT is able to leverage enhances the utility of this tool, enabling real-world trajectory design scenarios. Despite its efficiency and robustness, there are several potential upgrades that could increase the capability of COLT and these are discussed in the final recommendations.

### 3.9 Finite Difference Approach for Partial Derivative Computation

Analytically determining the partial derivatives necessary to construct the Jacobian matrix for the NLP problem posed within the COLT algorithm is challenging, moreover, any modifications of the dynamical force models necessitate an update to the derivation of the partials. Therefore, it is sometimes advantageous to numerically approximate partial derivatives for the STM because such approximations are typically straightforward and easily implemented. Even if analytical derivatives are ultimately employed, possessing a means of validating the analytically-derived partial derivatives is beneficial. However, such an approach warrants caution because the Jacobian is approximated with varying degrees of accuracy. Additionally, this technique can be computationally expensive, increasing the time required to produce a solution. Nonetheless, when used appropriately, numerical approximation methods for partial derivatives provide a powerful approach.

The first-order central difference approximation is a finite difference method commonly employed to numerically approximate partial derivatives. This strategy is based on differencing two first order Taylor-series expansions, resulting in

$$\frac{\partial f_j}{\partial x_i} = \frac{f_j[x_i + h] - f_j[x_i - h]}{2h} + O(h^2), \quad (3.79)$$

where  $h$  is the step size and  $O(h^2)$  indicates a truncation error on the order of  $h^2$ . A small step size,  $h$ , is selected for a low truncation error. However, if  $h$  is too small, excessive round off error occurs due to the subtraction step in the numerator. Strategies for selecting a value of  $h$  that mitigates these two sources of error are available [77].

Complex step differentiation affords an even more powerful method for numerical approximation of partial derivatives. This approach is also derived from a Taylor-series expansion but, in this case, a step occurs along the imaginary axis [78].

$$f(x + ih) = f[x] + ihf'[x] - h^2 f''[x]/2! - ih^3 f^{(3)}/3! + \dots \quad (3.80)$$

Focus on the imaginary part of both sides of Equation (3.80) and solve for  $f'(x)$ , i.e.,

$$\begin{aligned} \text{Im}(f[x + ih]) &= hf'[x] - h^3 f^{(3)}/3! + \dots \\ f'[x] &= \text{Im}(f[x + ih])/h + O(h^2) \end{aligned} \quad (3.81)$$

The division required in Equation (3.81) does not induce round-off error, therefore,  $h$  can be set to be arbitrarily small. The step size,  $h$ , is typically selected such that the truncation error  $O(h^2)$  is below the numerical precision of the computational tool in use, i.e. Matlab, rendering the resulting approximation equal in accuracy to a numerically implemented analytical method.

A third approach to numerically computing partial derivatives is automatic (algorithmic) differentiation (AD). While not implemented in this investigation, such a technique is increasingly applied to trajectory design and optimization problems [79]. The term AD describes a variety of techniques for computing derivatives by implementing basic differentiation rules within the source code of a numerical method. Its primary advantages include the avoidance of truncation errors and automatic computation of the derivatives of a function in parallel with the computation of the function itself [80]. While this procedure is more complex to implement than finite differencing approaches, it is less computationally expensive. Automatic differentiation is facilitated by object-oriented programming and is implemented in many languages with this capability, including Matlab [81].

## 4. ORBIT CHAIN TECHNIQUE FOR LOW-THRUST TRANSFER DESIGN

Powerful tools alone are not sufficient to meet the challenge of low-thrust trajectory design; a methodology with which to employ these tools is also required. This chapter describes such a methodology and demonstrates its efficacy with several low-thrust trajectory design scenarios. The framework developed in this chapter utilizes direct collocation along with orbit chaining to generate optimal low-thrust transfers. Orbit chaining, in this context, refers to the linking together of various dynamical structures, e.g., periodic orbits and their invariant manifolds, to form an initial guess for a low-thrust transfer. This approach leverages the strengths of direct collocation to produce a methodology capable of obtaining optimal low-thrust transfers in an intuitive, flexible, and robust manner. The procedures developed in this chapter are applied in subsequent chapters to generate low-thrust transfers for two upcoming NASA missions.

### 4.1 Motivation and Overview

Linking together orbits or other dynamical structures to design trajectories is a strategy as old as the space age. Missions to the Moon in the 1960s employed one version of this approach, the patched conics approximation, to design successful trajectories from Earth to the Moon and back. The same strategy was used in the next decade to develop the elegant sequence of flybys that compose the trajectories of Voyager 1 and 2. Exploration of the CR3BP and other multi-body dynamical models in recent decades yielded new dynamical structures which were linked together to design a variety of successful missions within the Earth-Moon system and beyond. As the orbit chain approach described in this chapter is based on the same principles

employed in these earlier missions, the strategy is not a new one. However, in this case, its close pairing with a direct collocation algorithm yields a novel approach that is intuitive, flexible, and robust. Thus, the primary contribution of this investigation is to pair the two familiar strategies of orbit chaining and direct collocation in a unified framework for low-thrust trajectory design.

The orbit chain and direct collocation framework presented in this investigation is developed to directly address some of the main challenges of low-thrust trajectory design. The greatest of these challenges is the formulation of an initial guess for the complex and frequently unintuitive state and control histories of many low-thrust trajectories. The proposed framework meets this challenge by utilizing periodic orbits and other dynamical structures to provide the necessary position and velocity states for an initial guess. This approach is beneficial because it biases the resulting transfer to leverage the natural dynamics of the orbits or manifold paths included in the initial guess; generally, the more a transfer exploits the natural dynamical flow of a model, the less propellant it will require. Constructing an initial guess from existing dynamical structures has the added benefit of being relatively straightforward. A designer can “mix and match” known dynamical structures in a manner that best serves the desired transfer. The robust nature of the direct collocation algorithm permits great freedom of choice in this approach because often even initial guesses with large state discontinuities can still lead to optimal solutions. The direct collocation algorithm determines the control profile necessary to eliminate the state space discontinuities and maximize the mass delivered to the final orbit. This simplicity makes the orbit chain and direct collocation approach available to mission designers of all experience levels. Regardless of familiarity, the orbit chain and direct collocation technique offers a methodical approach for the creation of effective initial guesses for low-thrust transfers.

The freedom that the orbit chain approach offers to quickly test a variety of initial guess configurations addresses one of the other key challenges of low-thrust trajectory design: the exploration of a solution space. Unless a global optimization algorithm

is also employed, optimization methods such as direct collocation only produce local optimal solutions whose optimal value in relation to other solutions is unknown. Unfortunately, global optimization algorithms are frequently time intensive when applied to mission design problems, particularly in multi-body dynamical models. The ease with which the orbit chain approach allows a variety of initial guesses to be assembled and tested enables the exploration of a solution space without employing a cumbersome global optimization technique. Multiple solutions for the same trajectory design scenario can be obtained using different orbit chain formulations, as is demonstrated later in this chapter. Therefore, the solution space for a given problem can be explored by constructing orbit chains that utilize different types of intermediate orbits. This technique offers insight on the characteristics of various families of solutions available to address a given trajectory design problem. While experimenting with different orbit chain configurations is unlikely to yield a global optimal solution, it is often sufficient to generate results that satisfy the requirements of a given mission design problem.

The flexibility of the orbit chain and direct collocation framework is reflected not only in the multiple solutions it provides for a single problem, but in that this strategy can be adapted to a variety of dynamical models. Within this investigation, the approach is employed in the CR3BP and BCR4BP models; moreover, structures from the CR3BP+LT model are included in an orbit chain. These results demonstrate that the orbit chain and direct collocation method can be implemented in different dynamical models and can use structures from multiple dynamical models as links in an orbit chain. This methodology is valid for many other dynamical models not examined in this investigation. Ideally, the model employed possesses dynamical structures that can be leveraged for trajectory design; however, if this is not the case, then structures from other models can be imported. The adaptability of the orbit chain approach heightens its appeal because it broadens the range of trajectory design problems this method can be applied to.

This chapter offers a detailed description of the proposed orbit chain and direct collocation framework and multiple demonstrations of its application. A sample transfer design scenario is employed to illustrate the six step procedure for orbit chain construction and how the direct collocation algorithm transforms this initial guess to an optimal solution. Following this, multiple sample problems that highlight the broad applicability and versatile nature of the orbit chain and direct collocation approach are presented. The effectiveness of direct collocation compared to direct multiple shooting is then contrasted based on a literature review and brief example problem. Finally, the various parameters in the proposed framework whose values have the most significant impact on convergence behavior are detailed. In subsequent chapters, the orbit chain and direct collocation framework presented here is applied to compute low-thrust transfers for two upcoming NASA missions.

## 4.2 Dynamical Structures

A benefit of employing one of the simplified dynamical models discussed in Chapter 2 is that these models are amenable to the application of a variety of mathematical tools that yield insights useful for trajectory design. The field of mathematics that encompasses these tools is sometimes called dynamical systems theory (DST). Application of DST to models such as the CR3BP and BCR4BP reveals patterns of dynamical flow resulting from the interaction of the gravitational bodies included in each model. Cumulatively, these patterns comprise a dynamical “topography”, that is leveraged to design trajectories which exploit the natural flow of a dynamical system to achieve mission objectives, in the same way a boat might employ natural currents in the ocean. Individual elements of this overall topography, such as periodic orbits or invariant manifolds, are termed *dynamical structures*. Thus, utilizing these structures in an orbit chain technique enables information on the natural flow within a dynamical model to be included within an initial guess. Periodic orbits and invari-

ant manifolds are discussed here before their use within the orbit chain framework is demonstrated.

### 4.2.1 Periodic Orbits

Periodic orbits are solutions to the equations of motion for a given dynamical model that repeat exactly. These orbits are extremely useful because they supply information on dynamical motion over infinite time but require only finite time to compute. Figure 4.1 displays a Lyapunov orbit, one type of periodic orbit available in the CR3BP, about the Earth-Moon  $L_1$  libration point. The period,  $\mathcal{P}$ , of a periodic

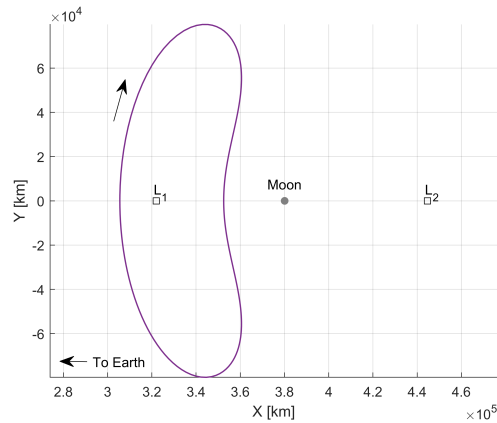


Fig. 4.1. Lyapunov orbit about the  $L_1$  libration point in the Earth-Moon CR3BP. The period of this orbit is  $\mathcal{P} = 15.356$  days and the Jacobi constant value is  $\mathfrak{J} = 3.053$ .

orbit is the length of time required to complete one full revolution and, in the case of the  $L_1$  Lyapunov orbit depicted in Figure 4.1, is equal to  $\mathcal{P} = 15.356$  days. This orbit is one of many orbits in the CR3BP that exhibit symmetry about one or more of the axes of the rotating frame. This symmetry is a product of the Mirror Theorem and assists the generation of periodic orbits because only half the orbit need be computed to obtain the whole orbit [82]. Whether this symmetry is exploited or not, the shooting and collocation techniques discussed in Chapter 3, offer strategies for

computing periodic orbits. Pavlak discusses methods for computing these orbits [29], and McCarthy offers strategies for the generation of quasi-periodic orbits for which motion is bound to a surface, but does not exactly repeat [83].

A limitless number of periodic orbits exist in the CR3BP, and these solutions are organized into distinct categories, denoted families, based on common characteristics. Each orbit along a family is characterized by some parameter (for example  $\mathcal{P}$ ,  $\mathfrak{J}$ ) that evolves along the family. These families are evolved from a single initial orbit using a continuation method e.g., natural parameter or pseudo-arclength continuation [84]. Figure 4.2(a) displays the family of  $L_1$  Lyapunov orbits of which the single periodic orbit displayed in Figure 4.1 is a part.

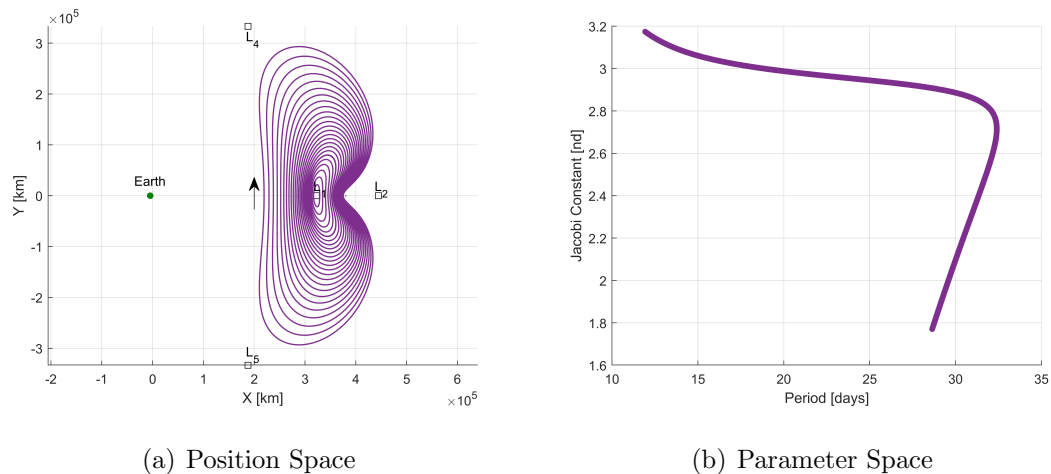


Fig. 4.2. (a) Subset of the family of  $L_1$  Lyapunov orbits in the Earth-Moon CR3BP plotted in position space. (b) Subset of the family of  $L_1$  Lyapunov orbits plotted in parameter space. Note, a smaller subset of the family is depicted in (a) than in (b).

Clearly several parameters are available to characterize the family of  $L_1$  Lyapunov orbits. Not only does the  $x$ -axis crossing location of each Lyapunov orbit differ for each orbit in the family but also the period and Jacobi constant of each member. Plotting the  $L_1$  Lyapunov family in parameter space offers another perspective on these orbits. Figure 4.2(b) shows the Jacobi constant value of each orbit in the  $L_1$

Lyapunov orbit family plotted as a function of its period. Viewing an orbit family in parameter space is advantageous if an orbit at a particular energy level or which possesses a specific period is desired.

Equilibrium points and periodic orbits are solutions to the equations of motion in the CR3BP and BCR4BP with stability characteristics that are analyzed via a linearization about each solution. Simply put, the stability of these solutions describes the tendency of a particle to return to, or remain in the vicinity of, the solution following a perturbation. A simple conceptualization of stability is furnished by imagining a ball at the bottom of a basin or the peak of a hill subject to a uniform gravitational field on the surface of the Earth. Following a slight perturbation away from the lowest point of a basin, the ball will oscillate about and ultimately return to the bottom of the basin. In contrast, after a perturbation the ball at the peak of the hill is likely to roll away never to return. This latter configuration is analogous to an unstable solution while the former is a stable one. Thus, by extension, a spacecraft positioned in a stable periodic orbit is more likely to remain in or stay near that orbit following a perturbation, than a spacecraft in an unstable orbit. A more detailed and mathematical discussion of stability is offered by Vaquero [84]. The natural flow into or out of orbits that are characterized as unstable is indicated by its invariant manifolds and these offer another set of useful dynamical structures.

#### 4.2.2 Invariant Manifolds

Invariant manifolds indicate the natural flow towards or away from an unstable equilibrium point or periodic orbit in the CR3BP and BCR4BP. The invariant manifolds of periodic orbits are leveraged in this investigation, and these dynamical structures are useful because they can be used to design efficient paths into or out of a given orbit. The same linearization process employed to determine the stability of a periodic orbit is also used to compute its stable and unstable invariant manifolds. However, these manifolds are only available if the solution is characterized as unsta-

ble. The linearization provides states on the manifold nearby the solution, then the manifolds are globalized by propagating from these states forward in time along the unstable manifolds and backward in time along the stable manifold. Figure 4.3 displays paths on the stable and unstable manifolds of the  $L_1$  Lyapunov orbit projected in the  $x$ - $y$  plane. Paths on the unstable manifold, plotted in magenta, asymptotically

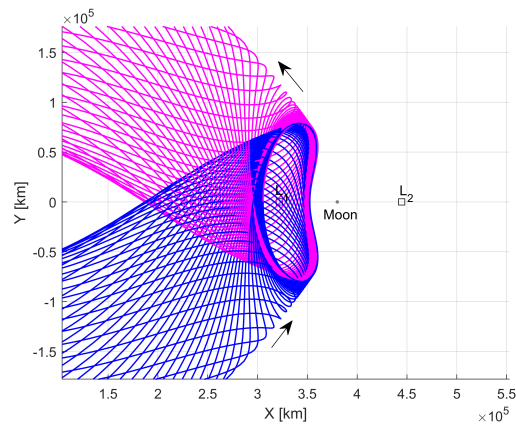


Fig. 4.3. Paths on the stable and unstable invariant manifolds corresponding to the  $L_1$  Lyapunov orbit shown in Figure 4.1.

depart the periodic orbit in forward time, while paths on the stable manifold, plotted in blue, asymptotically approach the orbit in forward time. Because the periodic orbit is a six-dimensional dynamical structure, with three position and three velocity states, the invariant manifolds of the orbit are also six-dimensional. However, only two dimensions are depicted in Figure 4.3. Moreover, the individual trajectories visible in this Figure are distinct paths on the invariant manifold; the manifold itself is a six-dimensional surface. More in-depth discussion of the computation and utilization of invariant manifolds is provided by Haapala [82] and Vaquero [84].

### 4.3 Orbit Chain Methodology

Orbit chaining offers a flexible and relatively simple approach to initial guess construction for low-thrust trajectory design. The orbit chain strategy is not tied to a specific dynamical model; thus, it can be applied within whatever model best meets the needs of a given design problem. This methodology can also employ any type of dynamical structure whether these structures are generated in the working dynamical model or taken from a different one. The use of existing dynamical structures also lends the orbit chain approach its simplicity. At its core, it merely identifies dynamical structures that help traverse gaps in position and velocity space between an initial and final location. This relative simplicity makes the orbit chain approach accessible to mission designers with a range of experience levels. The adaptable and straightforward nature of the orbit chain approach is captured in the six step procedure employed to construct an orbit chain.

1. Analyze
2. Select
3. Clip
4. Subdivide
5. Stack
6. Define Control History

The six steps of the orbit chain procedure are demonstrated via a sample scenario in the CR3BP that requires the design of a low-thrust transfer from a DRO near the Moon to an  $L_3$  Lyapunov orbit. Once the orbit chain is constructed, it is passed to the direct collocation algorithm which ultimately computes an optimal solution. This example problem aptly highlights the flexibility and straightforward nature of the orbit chain process.

### 4.3.1 Orbit Chain Construction: Analyze and Select

The initial step of the orbit chain process, analysis, entails the identification of the types of dynamical structures that will provide links for the orbit chain. The open ended nature of this step means it is often the most time consuming part of the entire assembly procedure. In this investigation, an orbit chain is typically constructed to facilitate a transfer from one periodic orbit to another. When this is the case, the desired departure and destination orbits are automatically designated as the initial and final links in the orbit chain. It is not always necessary to include additional links beyond these two; however, the addition of intermediate links to an orbit chain can help reduce state and energy discontinuities between successive links. The challenge of this step of the orbit chain construction process is the sheer number of options that exist. Many types of dynamical structures are available for use in an orbit chain and this is especially the case in the CR3BP, which is employed for the majority of the examples in this chapter. Fortunately, in many cases a large number of the available options can be quickly eliminated for any given scenario because they do not beneficially reduce discontinuities between the initial and final orbit chain links.

The reduction of state space discontinuities is the first quality sought after when searching for useful intermediate orbit families. The example trajectory design scenario requires a transfer from a DRO to an  $L_3$  Lyapunov orbit. Many orbit families are clearly of little use for facilitating this type of transfer; for example, the axial or vertical orbit families would introduce undesirable out-of-plane components if included. In contrast, several other families offer obviously useful candidates for orbit chain construction, e.g., the  $L_{4/5}$  SPOs or 3:4 resonant orbits, because of their substantial state space overlap with the initial and final orbit families. Figure 4.4(a) displays how the  $L_4$  SPO family intersects numerous members of both the DRO and  $L_3$  Lyapunov family. Not only does the  $L_4$  SPO family overlap in position space, but the direction of motion around each orbit is in the same clockwise direction as members of the other two families. A similar direction of velocity is often as im-

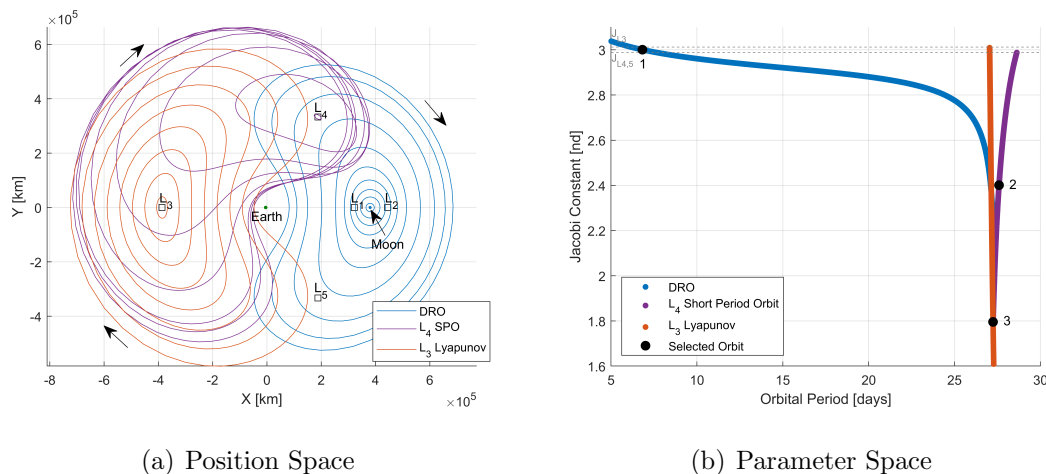


Fig. 4.4. Orbit families included in the orbit chain constructed for a DRO to  $L_3$  Lyapunov orbit transfer. An orbit from the  $L_4$  SPO family is employed as an intermediate link because it bridges discontinuities in position and energy space between the initial and final orbits.

portant as intersections in position space. Adjacent orbit chain links that exhibit small discontinuities in position space but possess opposite directions of motion can hinder rather than help convergence. It is also possible to examine discontinuities in velocity between potential orbit chain links by plotting families of interest in velocity rather than position space. Whichever combination of visualizations is utilized, the analysis of potential orbit chain components in state space is often the first step in the assembly process.

A reduction of discontinuities in energy is another desirable quality of intermediate orbit chain links. Energy parameters, e.g., the Jacobi constant in the CR3BP, are functions of position and velocity, and assessing the energy values of potential members of an orbit chain yields insights not easily ascertained from direct examination of state space discontinuities. Transferring between orbits in the CR3BP at two different energy levels requires expending propellant to change the Jacobi constant value of the spacecraft. Ideally a transfer between two orbits is achieved by consuming only the amount of propellant required to monotonically change the energy level of the

spacecraft. In practice, this ideal is not always achievable, because equivalences in energy do not necessarily entail equivalences in position. Thus, two orbits at similar Jacobi constant values but very different positions will require more propellant to transit between than their energy levels alone imply. Nonetheless, there are transfer scenarios where it is possible and preferable to achieve a monotonic change in energy between the initial and final orbit. Given that this monotonic behavior is the ideal scenario, it is often better to select intermediate orbit chain links that promote this type of energy trend. This preference means choosing links with energy values equal to or between the energy values of the initial and final orbit. This  $L_4$  SPO family is chosen to provide intermediate orbit chain links not only because of its favorable qualities in state space, but also because members of this family span the same range of energy values covered by the DRO and  $L_3$  Lyapunov orbit families as shown in Figure 4.4(b). The overlap in energy space between the three orbit families included in the example scenario ensures that an orbit chain with a monotonic trend in energy can be constructed.

After determining the types of dynamical structures to be used in an orbit chain, it is necessary to select the individual structures that will be included in the chain. The selection step is closely tied to the analysis step because it involves examination of the configuration and parameter space plots composed in the previous step. Typically, the initial and final orbits of a transfer are determined by mission requirements, so only the intermediate orbits to be included in an orbit chain need be selected. The energy levels of the initial DRO and final  $L_3$  Lyapunov orbits included in the example transfer scenario are marked in Figure 4.4(b), and the same orbits are plotted in position space in Figure 4.5(a). Following definition of the departure and arrival orbits in the transfer scenario, intermediate orbit chain links are selected. In this case, only one orbit chain link is employed. The intermediate link chosen from the  $L_4$  SPO family possesses an energy value almost directly between the Jacobi constant values of the initial and final orbits and intersects the final orbit in position space, as shown in Figures 4.4(b) and 4.5(a), respectively. If desired, additional members

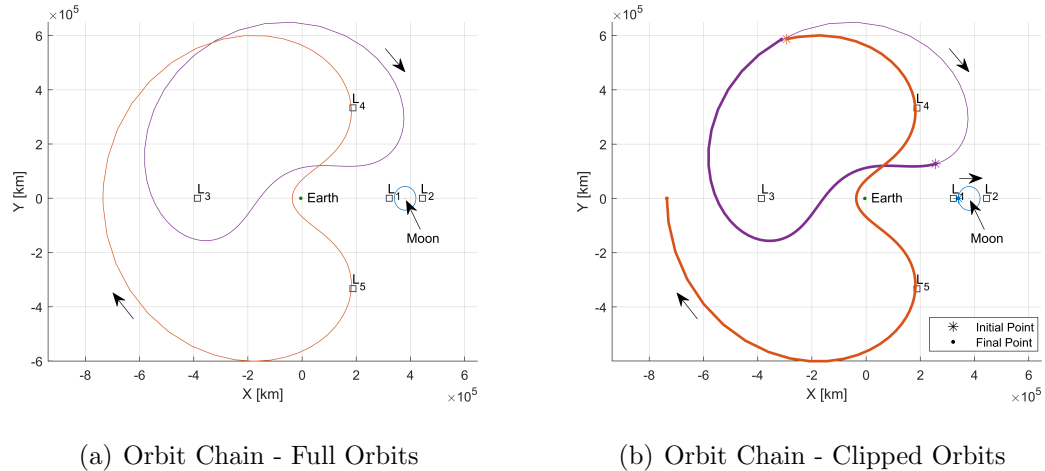


Fig. 4.5. Individual orbits from each orbit family are selected for inclusion in the orbit chain. The initial and final orbits in the chain are the departure and arrival orbits of the resulting low-thrust transfer. The orbits included in the chain are clipped to reduce discontinuities between links and reduce the time of flight of the final transfer.

of the  $L_4$  SPO family could be included as intermediate links to further reduce state and energy discontinuities; however, a single type of intermediate link will suffice to produce a continuous transfer in this case.

### 4.3.2 Orbit Chain Construction: Clip, Subdivide, and Stack

Following selection of the components of an orbit chain, these components can be clipped to reduce discontinuities between links. Figure 4.5(b) offers an example of this technique. The asterisks and dots on this plot indicate the starting and ending point of each orbit, respectively. When a full revolution of an orbit is included in a chain these points are identical. The starting and ending point of the  $L_4$  SPO is selected to be close in position space to the starting and ending points of the DRO because this choice reduces the discontinuity between these two adjacent links. While this placement is advantageous for connecting with the DRO, it actually increases the

discontinuity with respect to the subsequent  $L_3$  Lyapunov orbit. Therefore, a second, partial, revolution of the selected  $L_4$  SPO is included in the orbit chain to bridge this gap. The second revolution of the  $L_4$  SPO begins at the same point as the first, but is clipped such that it ends at one of its intersections with the  $L_3$  Lyapunov orbit. The intersection point farther from the Earth is used for the clipping location because the difference in velocity direction at this point is smaller. Moreover, it is typically harder to converge discontinuities close to primary bodies due to the especially nonlinear dynamics in these regions. The  $L_3$  Lyapunov orbit that immediately follows this orbit chain link is also clipped such that it begins at the intersection point with the  $L_4$  SPO and ends where the orbit crosses the  $xz$ -plane in the  $+x$  direction. Only this partial segment of the  $L_3$  Lyapunov orbit is included to avoid adding extra time of flight to the resulting transfer. Clipping, along with adjustment of the initial point on an orbit, is an important step for reducing state discontinuities within an orbit chain, and thus increasing the likelihood of its leading to a converged solution.

After any necessary clipping of orbit chain links, the subdivision step is performed. Subdivision is the partitioning of orbit chain links into segments; a step that is necessary to make the initial guess compatible with the direct collocation algorithm. As described in Chapter 3, collocation represents a trajectory as a series of segments over which polynomials approximate the dynamics of the chosen model. The discretized trajectory is called a mesh, thus the subdivision of the orbit chain is the definition of the initial mesh for the direct collocation algorithm. The initial mesh defined for the DRO to  $L_3$  Lyapunov transfer is displayed in Figure 4.6(a). Multiple strategies for defining the initial mesh are available, and two are primarily used in this study: even spacing in time or in position.

The default approach for defining the initial mesh is evenly spacing the segment boundary points in time. With this strategy, a desired number of segments for each orbit chain link is defined and the total propagation time of the link is divided such that the time duration of each of the resulting segments is equivalent. The DRO and  $L_4$  SPO links shown in Figure 4.6(a) utilize this mesh definition strategy. Some of the

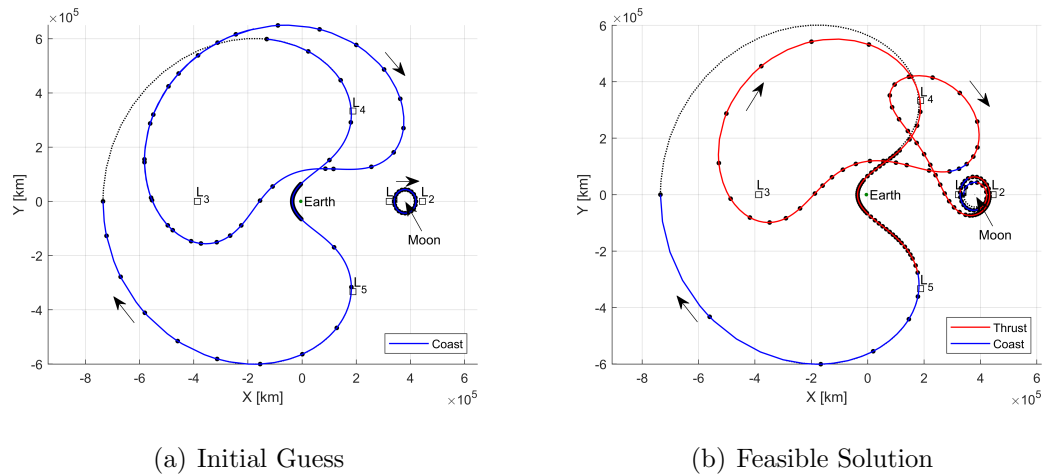


Fig. 4.6. An initial mesh along with the desired number of stacked revolutions is determined for the orbit chain initial guess. The orbit chain leads to a feasible solution with a redistributed mesh, but a geometry similar characteristics to that of the initial guess.

segments along the  $L_4$  SPO appear uneven due to the overlap of the full and partial  $L_4$  SPO revolutions. Evenly spacing segments in time is straightforward and often sufficient for achieving convergence. However, the shortcoming of this approach is apparent when a trajectory passes close to a primary body. During a close approach, motion along a trajectory is rapid, meaning a large distance is covered in a short amount of time. Therefore, when even spacing in time is employed, the spacing of boundary points near a primary body is quite sparse unless a large number of segments are employed. Because position and velocity states change quickly near a primary body, more segments are required to accurately approximate motion, or the collocation algorithm may fail to converge. One solution to this dilemma is to maintain even time spacing between boundary points and utilize a shorter time interval to obtain many segments near the primary. Indeed, this approach is used for the DRO in Figure 4.6(a), which is divided into 30 segments for a single revolution. While this approach works well for the DRO, other orbits may include sections that are both near and far from a primary body. In these cases, employing even time

spacing for all segments will add many extraneous segments and create a larger than necessary collocation problem. Alternate mesh spacing strategies are developed to address this problem.

To achieve a sufficiently fine segment distribution near primary bodies while avoiding a needlessly dense mesh in other regions, one mesh definition strategy is to space segments evenly in position. With this technique, a set Euclidean distance between each boundary point is designated rather than a desired number of segments. An orbit chain link is propagated from end to end, with the Euclidean distance from one boundary point to the next being no more than the set spacing distance. When a low segment spacing distance is used, a fine mesh is generated even near a primary body. However, this strategy can still produce superfluous segments for orbit chain links where only a part of the trajectory passes near a primary body. Therefore, a variant of the even position spacing approach is more commonly employed that utilizes a variable position spacing. In this method, two different segment spacing values are employed; the smaller one is used when a trajectory is within a set radius of a primary body and the other larger one is used everywhere outside this radius. The variable position spacing technique enables a fine spacing to be achieved near gravitational bodies without adding a large number of segments in regions where they are not needed. This strategy is employed for the  $L_3$  Lyapunov orbit link in Figure 4.6(a), because while the majority of this orbit is far from either primary, it does include a close approach of the Earth. The mesh for this link is defined such that a spacing of 4000 km is used when the trajectory is within 10 Earth radii of the center of the Earth, and a spacing of 160,000 km is used everywhere else. These settings produce the dense segment spacing near the Earth evident in Figure 4.6(a), without requiring the same fineness everywhere else along the orbit. This sample transfer problem demonstrates that a suitable mesh definition strategy may be chosen independently for each link of an orbit chain to generate the best overall initial mesh for the problem at hand.

The mesh definition strategy alone does not determine the total number of segments that are employed in a collocation problem. The stacking step of the orbit chain construction process allows additional trajectory, and therefore segments, to be added to an initial guess to improve the likelihood of achieving convergence. An orbit chain that appears to adequately connect two regions of position space may be constructed, but the ease with which this chain is corrected to a continuous transfer is partly a function of the low-thrust acceleration level,  $a_{max}$  employed in the transfer problem. The lower the value of  $a_{max}$ , the more time will be required to execute the desired transfer. Because a fixed-time direct collocation algorithm is employed in this study, the time of flight of a transfer can only be increased by including additional trajectory segments in the initial guess. An example of the benefit of stacking is offered in the example transfer scenario, where three revolutions of the initial DRO are stacked. This choice provides extra trajectory, and therefore additional time of flight that the direct collocation algorithm may employ to correct the discontinuity between the first and second links in the orbit chain. Indeed, this is shown to be the case in Figure 4.6(b), where some of the additional DRO revolutions are “unspooled” to correct the discontinuity between the DRO and  $L_4$  SPO. Alternately, additional links could be included in an orbit chain to provide supplementary time of flight for achieving a transfer; however, the stacking approach is simpler because it avoids the extra steps of identifying extra links. Finally, note that the stacking procedure is only applied to orbit chain links that are periodic orbits; otherwise, stacking introduces additional state discontinuities because the end point of the link is not equivalent to its initial point.

### 4.3.3 Orbit Chain Construction: Define Control History

The final step of the orbit chain assembly process is the definition of a control history for the initial guess. Utilizing dynamical structures to assemble an orbit chain provides an initial guess for the position and velocity history along a transfer;

however, these structures do not typically include any control history information, with the exception of structures generated in the CR3BP+LT. For the vast majority of dynamical structures that do not include control history information, a crude initial guess is developed and employed in the orbit chain. This initial guess requires definition of the thrust vector direction and magnitude for each segment in the orbit chain. Recall that these control values are held constant for the duration of each segment and that the thrust vector direction is fixed in the inertial frame. The initial thrust vector direction is typically set parallel to the direction of the rotating frame velocity vector at the beginning of each segment. In the CR3BP, setting the thrust vector parallel or anti-parallel to the rotating frame velocity vector produces the most rapid increase or decrease in energy, respectively. Most transfers generated with the orbit chain method require some change in energy, thus it is reasonable to define a control history initial guess that most efficiently achieves this change. The direction of the desired change in energy typically determines the + or - direction of the initial thrust vector, i.e., if the destination orbit is at a higher energy (lower Jacobi constant value) than the departure orbit, then the initial thrust vector should be oriented in the + direction of the velocity vector, and vice-versa. Other strategies can be employed to define the initial thrust vector direction; however, these strategies should ensure that the initial guess is a unit vector so that the constraint corresponding to this condition is initially satisfied.

The chosen collocation scheme defines the magnitude of the thrust vector implicitly according to the change in mass over the segment. Thus, specifying this aspect of the control history actually requires an initial guess for the mass history of the transfer. Generally, the initial thrust magnitude is set to a value near zero across the entire transfer to bias the direct collocation algorithm towards a result that uses less thrust. Though the optimization step removes thrust segments to achieve a more mass optimal transfer, using an initial guess with a nonzero thrust magnitude may still bias the algorithm towards a local optimal that requires more mass than would otherwise be the case. However, the initial thrust magnitude is not set exactly to zero

because this can cause numerical difficulties that hinder convergence. Thus a small nonzero value, typically  $1 \times 10^{-8}$  N, is employed. An exception to the null thrust initialization is made if using a larger initial thrust magnitude makes the difference between obtaining a solution or not. There are scenarios where this is the case, because beginning with a nonzero thrust magnitude influences the direct collocation algorithm towards a solution basin where convergence can be obtained. While it is generally preferable to use a null thrust initial guess and adjust other parameters when attempting to obtain a solution, changing the initial thrust magnitude is an acceptable and sometimes necessary step.

The orbit chain constructed for the DRO to  $L_3$  Lyapunov orbit transfer scenario uses a near zero magnitude initial thrust vector as shown in Figure 4.7(a). Additionally, the initial thrust vector direction is set parallel to rotating frame velocity vector because an increase in energy (decrease in Jacobi constant value) is required to transfer from the departure to the destination orbit. The strength of the direct collocation algorithm is highlighted by this step, because this algorithm is able to modify a highly simplistic initial control history to produce a continuous optimal transfer. This robustness is one of the key strengths of the orbit chain and direct collocation methodology.

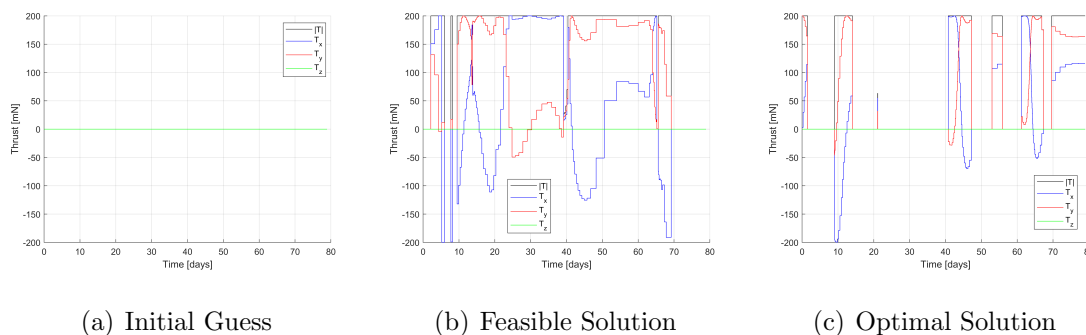


Fig. 4.7. Thrust profiles for the initial guess, feasible solution, and optimal result of the DRO to  $L_3$  Lyapunov transfer. As expected, the thrust profile of the optimized solution consists almost exclusively of thrust arcs at the maximum thrust magnitude.

#### 4.3.4 Orbit Chain to Optimal Solution

Once an orbit chain initial guess is successfully constructed, it is passed to the direct collocation algorithm for convergence. The process of obtaining an optimal solution occurs in two steps. First, the orbit chain initial guess is used to compute a feasible solution, then this solution is optimized with the objective of maximizing the final mass at the end of the transfer. The influence of the orbit chain initial guess on the final result is most apparent in the feasible solution. For example, Figure 4.6(b) illustrates how the feasible solution computed for the DRO to  $L_3$  Lyapunov transfer retains much of the geometry of the orbit chain initial guess. Notably, Figure 4.6(b) also demonstrates how the collocation mesh is redistributed by the hybrid mesh refinement procedure so that a greater density of boundary points occurs when the trajectory is near the Earth or the Moon. Similarity between the initial guess and feasible result is an indicator that the initial orbit chain is well constructed for the desired transfer scenario. A poorly chosen initial orbit chain will lead to a result that looks quite different from the initial guess, if convergence can even be achieved. This behavior suggests that the orbit chain was of little use for guiding the direct collocation algorithm towards a solution. If similarity to the initial orbit chain is particularly desired, an attenuation factor that reduces the size of the update step taken in each iteration can be employed.

The thrust profiles of the initial guess and feasible solution possess fewer similarities. These profiles are offered in Figure 4.6, where the difference in thrust profile between the initial guess and feasible solution is significant. These differences are displayed in Figure 4.7 which shows that the majority of the feasible trajectory includes segments at maximum thrust magnitude. The maximum thrust magnitude employed for this sample scenario and the remainder of the examples in this section is  $T_{max} = 200$  mN, while the corresponding specific impulse is  $I_{sp} = 2000$  seconds. The initial mass of the spacecraft is assumed to be 1000 kg. From departure from the DRO to insertion on the  $L_3$  Lyapunov orbit, a total time of flight of 79 days and a

propellant consumption of 55 kg is required. Because a fixed time direct collocation algorithm is utilized, the time of flight of the initial guess dictates the time of flight of the final optimal solution. Therefore, careful consideration of the desired transfer duration should be undertaken when the orbit chain is constructed. If difficulty obtaining a converged solution is encountered, additional revolutions can be stacked in the orbit chain to provide additional time in which to achieve the desired transfer.

The feasible transfer computed from the initial orbit chain is optimized to produce the final result of the orbit chain and direct collocation procedure. The optimal transfer is displayed in Figure 4.8(b) and its corresponding thrust profile is shown in Figure 4.7(c). Both the configuration space plot and thrust profile demonstrate

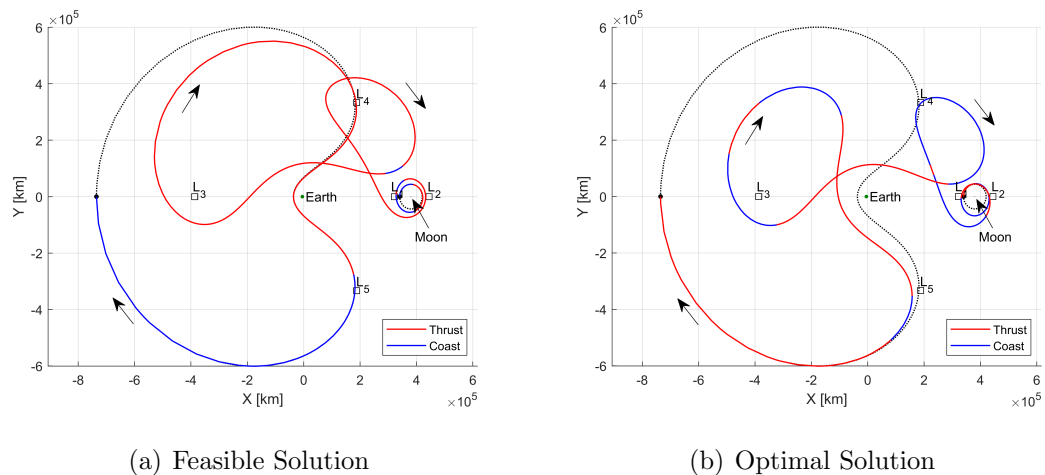


Fig. 4.8. The feasible solution obtained from the orbit chain initial guess is optimized to maximize the mass delivered to the final orbit.

that many of the thrust segments are converged to coast segments to maximize the final mass. To accommodate this change, the geometry of the transfer is altered, and this shift is highlighted in Figure 4.8. While the final optimal low-thrust transfer shares fewer obvious similarities with the initial orbit chain, the choice of initial guess significantly influences the final result. The following section will demonstrate how alternate orbit chains affect the optimal solution for this transfer. Ultimately, the

computed optimal trajectory requires 28 kg of propellant to deliver the spacecraft to the final orbit, a reduction in mass consumption of nearly half compared to the feasible solution.

The orbit chain constructed for the sample transfer scenario examined in this section intentionally employed an intermediate link with a Jacobi constant value between that of the initial and final orbit. As stated previously, this choice is made to bias the resulting transfer towards an energy profile that is monotonic and remains between the Jacobi constant value of the departure and arrival orbits. Plotting the Jacobi constant value of the low-thrust spacecraft as a function of time of flight at each step of the trajectory construction process, as shown in Figure 4.9, highlights whether the desired profile is successfully achieved. The Jacobi constant profile of the

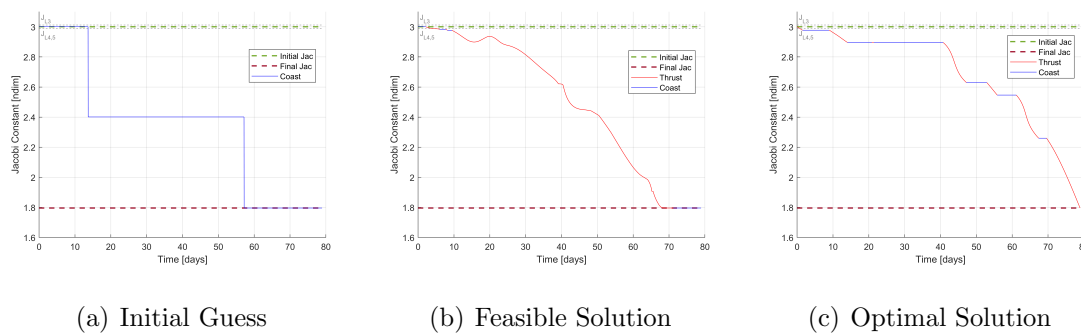


Fig. 4.9. Jacobi constant profiles for the initial guess, feasible solution, and optimal result of the DRO to  $L_3$  Lyapunov transfer.

initial guess displays the energy values of the orbit chain links in similar fashion to Figure 4.4(b), which was employed to select these links. The Jacobi constant profiles of the feasible and optimal solutions reveal that the chosen orbit chain imparted the desired influence on the final solution. The feasible solution does not exhibit an entirely monotonic energy profile, but the energy of the spacecraft does remain between that of the initial and final orbits. The optimal solution maintains the same upper and lower bounds as the feasible result and also exhibits a monotonic trend

in energy. Interestingly, the energy level of the intermediate link in the orbit chain initial guess does not appear to influence the energy at which the extended coast arcs of the optimal solution occur. This shift indicates that while the orbit chain clearly influences the optimal result, it does not provide the exact dynamical structures employed in the final solution. While clear correlations between initial guess and final result cannot always be established, analysis of the energy profiles at these two steps frequently offers insight on how the orbit chain influences the optimal solution.

The orbit chain constructed for this example scenario leads to a successful optimal transfer; however, it is far from the only chain that will produce this result. Alternate choices could be made at any of the orbit chain construction steps and an initial guess that generates a satisfactory solution will likely be the result. Moreover, the orbit chain alone is not what leads to a successful result. The settings of the direct collocation algorithm can make the difference between convergence and failure even for a well constructed orbit chain. The key parameters that affect convergence are listed and discussed in subsequent sections. The flexibility of the orbit chain and direct collocation technique is a strength, especially when it is utilized in a new dynamical regime; however, this same characteristic can also make it difficult to prescribe a specific formula for applying the technique to any given trajectory design scenario. The following section offers examples of the technique's successful application to a variety of trajectory design scenarios. These demonstrations offers guidance on how to utilize the orbit chain and direct collocation technique that can apply to a variety of mission design problems.

#### **4.4 Orbit Chain Examples**

The orbit chain methodology can be applied to many different trajectory design scenarios in a variety of dynamical models. This section demonstrates its application to several additional sample problems posed within the CR3BP, that highlight particular strengths of the orbit chain and direct collocation approach. The first of

these examples shows that the robust nature of the direct collocation and orbit chain technique enables it to compute solutions even if no intermediate arcs are included in an orbit chain. This most simple type of orbit chain is especially viable when the departure and destination orbits are relatively close to one another in configuration space, as is the case for the  $L_1$  and  $L_2$  Lyapunov orbits displayed in Figure 4.10(a). A transfer from the  $L_1$  to the  $L_2$  Lyapunov orbit is computed using an orbit chain

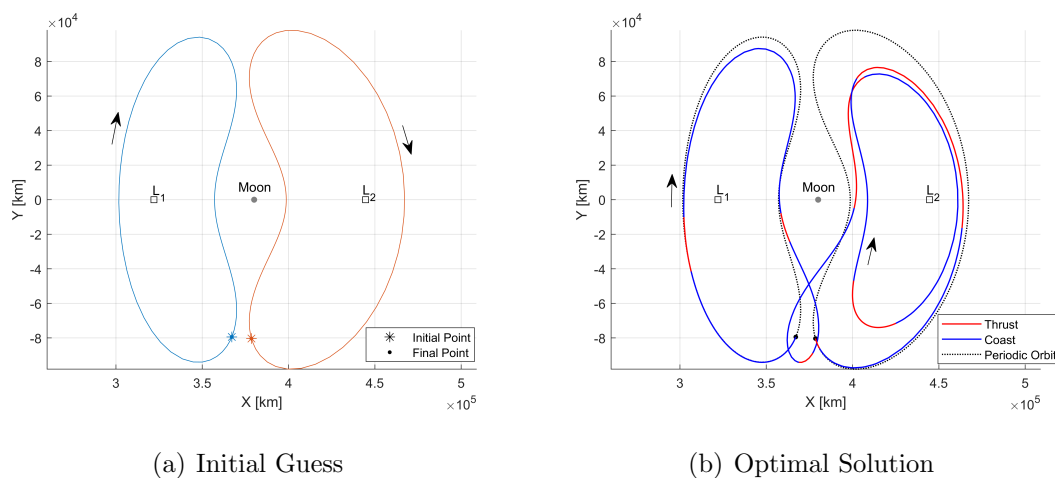


Fig. 4.10. The orbit chain initial guess and final optimal solution for a transfer from an  $L_1$  Lyapunov orbit to an  $L_2$  Lyapunov orbit.

initial guess consisting of one revolution on the departure orbit and two revolutions stacked on the arrival orbit. Despite the absence of invariant manifolds or any other kind of guiding dynamical structures in the orbit chain, this initial guess is sufficient to guide the direct collocation algorithm to the optimal low-thrust transfer displayed in Figure 4.10(b). Tables summarizing the characteristics of each orbit employed for orbit chains in this section and the performance of the resulting low-thrust transfers are provided in Appendix A.

Orbit chains lacking any intermediate links are not only successful for planar transfer problems, but can also be employed for spatial problems such as a transfer between two halo orbits. A transfer from an  $L_1$  halo orbit to an  $L_2$  halo orbit is

generated using an orbit chain consisting of one revolution on the departure orbit and two revolutions on the destination one. The selected halo orbits are displayed in Figure 4.11(a). Note that because these orbits are located farther from the Moon

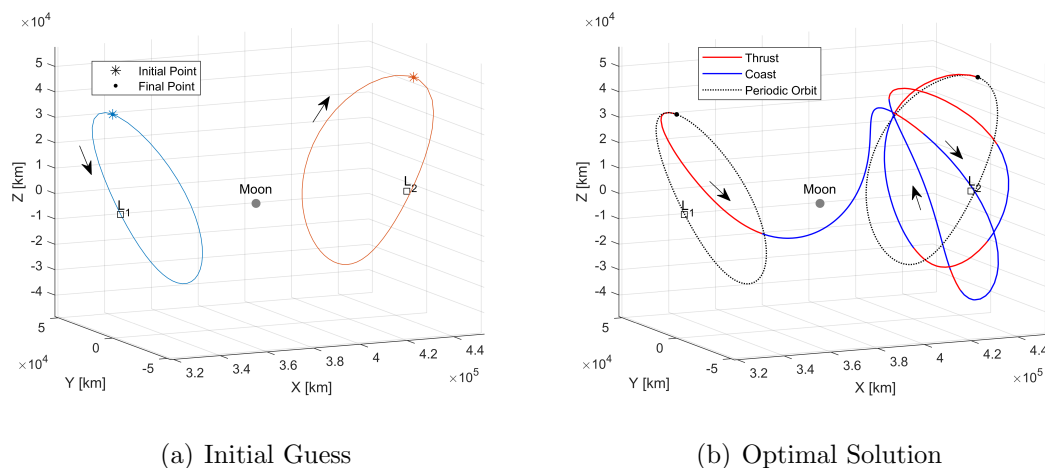


Fig. 4.11. The orbit chain initial guess and final optimal solution for a transfer from an  $L_1$  halo orbit to an  $L_2$  halo orbit.

than the Lyapunov orbits examined in the planar transfer scenario, the resulting two link orbit chain is actually easier to converge. Distance from the Moon reduces the sensitivity of the corrections problem and makes it unnecessary to pay particular attention to the boundary point spacing or attenuation factor size employed. The assembled orbit chain leads to the optimal solution shown in Figure 4.11(b). As with the Lyapunov transfer, the direct collocation algorithm is able to “unspool” the stacked revolutions on either orbit to overcome the large discontinuity between them and compute a continuous solution.

The Lyapunov and halo orbits utilized in the previous two transfers all possess invariant manifolds that can be leveraged to develop transfers between these orbit pairs that require very little, if any, propellant. An initial guess including these manifolds could be passed to the direct collocation algorithm to obtain such a result; however, this approach is not demonstrated here because one of the primary goals

of the orbit chain and direct collocation method is to enable rapid exploration of an unfamiliar dynamical system or problem. The ease with which a simple two link orbit chain yields a solution offers a quick method for assessing the range of geometries and approximate costs for transfers between the orbits of interest. After obtaining a general understanding of the solution space, subsequent analyses can focus on obtaining the lowest possible cost transfer using the powerful but time consuming approach of generating Poincare maps and identifying manifold intersections.

Two link orbit chains are sufficient for generating solutions in some cases, but most trajectory design scenarios require a more precise orbit chain to guide the optimizer to a solution. Three link orbit chain scenarios offer excellent examples of how the composition of an orbit chain influences the resulting solution. Merely by changing the intermediate link in a three link chain, solutions with different characteristics are obtained. A useful demonstration of this effect is encountered by reexamining the DRO to  $L_3$  Lyapunov orbit transfer developed in Section 4.3. The three link orbit chain created for this transfer utilizes an  $L_4$  SPO as an intermediate link, but other orbit families also offer prime candidates for filling this role. Members of the 2:3 resonant orbit family are especially well suited for this transfer scenario because they pass near both the Moon and the  $L_3$  libration point as shown in Figure 4.12(a). Moreover, Figure 4.12(b) illustrates that the 2:3 resonant orbit family spans the gap in energy space between the selected initial and final orbits. Thus, an intermediate link that biases the transfer towards the desired monotonic energy profile can be obtained. With respect to geometry and energy, the 2:3 resonant orbit family offers ideal candidates for inclusion in an orbit chain that facilitates the desired DRO to  $L_3$  Lyapunov orbit transfer.

A balance of geometry and energy is struck when choosing a single member of the 2:3 resonant orbit family for use in the desired orbit chain. Selecting a 2:3 resonant orbit with a Jacobi constant value roughly equivalent to that of the final  $L_3$  Lyapunov orbit ensures that the orbit chain biases the resulting transfer towards a result with a monotonic energy profile. The energy of the selected orbits is provided in Figure

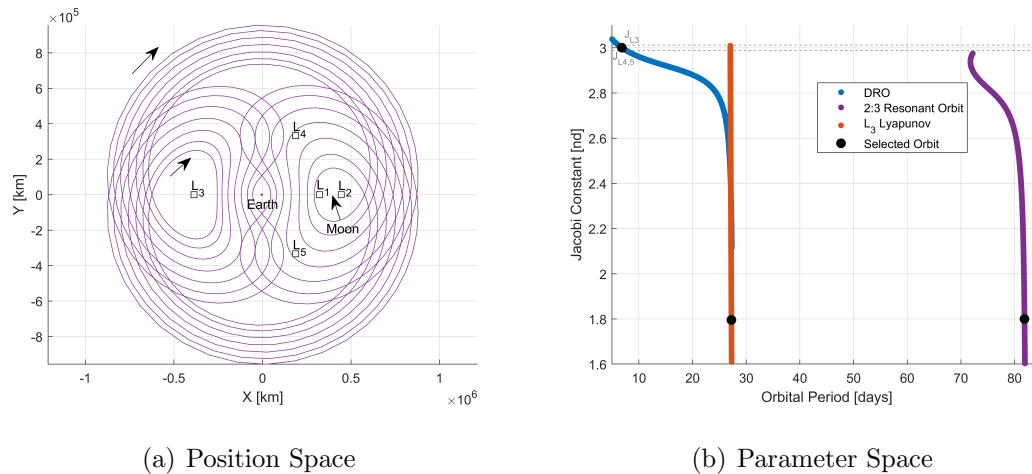


Fig. 4.12. The 2:3 resonant orbit family is selected to provide an intermediate link for a transfer from a DRO to an  $L_3$  Lyapunov orbit because this family bridges discontinuities in position and energy space between the initial and final orbits.

4.12(b), which highlights that the selected DRO and  $L_3$  Lyapunov orbit are the exact same as the those employed in Section 4.3. A compromise is made when considering the geometry of the intermediate orbit, because orbits that are small enough to pass close to the initial DRO only intersect the final  $L_3$  Lyapunov orbit at locations where the velocity vectors are not well aligned. Alternately, 2:3 resonant orbits that are large enough to offer favorable intersections with the final orbit do not pass close to the DRO. Ultimately, an orbit that falls within this latter category is selected because it tends to offer better convergence. However, it is possible to construct orbit chains with smaller members of the 2:3 resonant orbit that also lead to satisfactory results. Figure 4.13(a) shows that the selected resonant orbit is clipped at an  $x$ -axis crossing that is near the initial point on the  $L_3$  Lyapunov orbit. This location is favorable not only because the two links are close in position space, but also because at this point the velocity vectors on both orbits are nearly parallel.

The orbit chain constructed with a 2:3 resonant orbit as the intermediate link is utilized to compute an optimal transfer from the DRO to the  $L_3$  Lyapunov. This

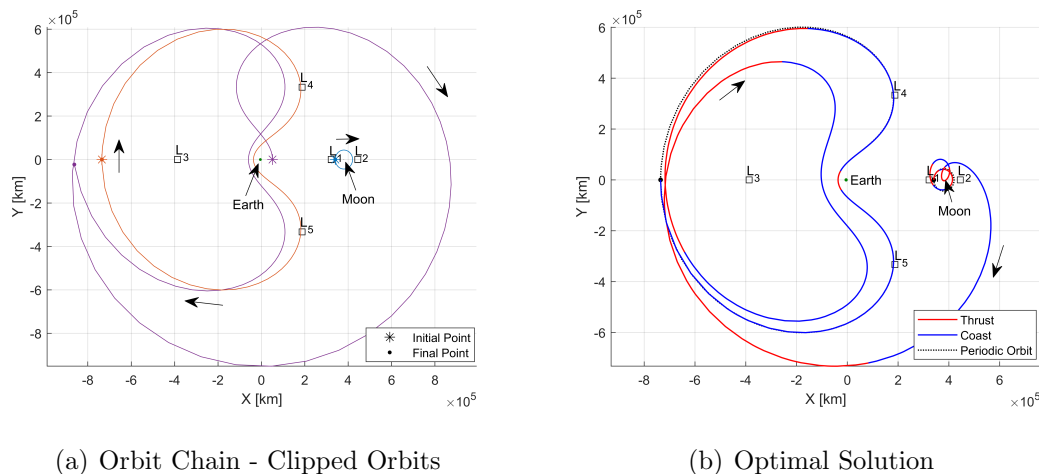


Fig. 4.13. An orbit chain that includes a clipped 2:3 resonant orbit is assembled and used to compute an optimal transfer from a DRO to an  $L_3$  Lyapunov orbit. Contrast this result with that obtained from the alternate orbit chain displayed in Figure 4.5(b) which includes an  $L_4$  SPO.

transfer, displayed in Figure 4.13(b), exhibits a geometry similar to that of the 2:3 resonant orbit and reaches the  $L_3$  Lyapunov orbit by traversing the space on the  $-y$  of the Earth in the rotating frame. This path contrasts with the transfer exhibited in Figure 4.8(b), which arrives at the destination orbit via a route on the exact opposite side of the Earth. Thus, the two orbit chains constructed to achieve the DRO to  $L_3$  Lyapunov orbit transfer demonstrate how the “mix-and-match” approach offered by this methodology is easily exploited to obtain a variety of solution types for the same transfer scenario. It is not possible to assess on the basis of these two transfers alone if one of these two geometries tends to provide lower-cost transfers than the other. However, a more exhaustive analysis that examines the results of these and other potential orbit chains could shed light on this question.

Theoretically, there is no limit on the number of links that can be included in an orbit chain. Links are added when their inclusion is likely to aid convergence towards a solution by reducing discontinuities or increasing time of flight. However, assuming the same number of segments is used for each link, the addition of links expands the

size of the direct collocation problem as it requires that a greater number of design variables be included. This problem can be alleviated by reducing the number of segments that some or all of the orbit chain links are subdivided into, but eventually the addition of links is bound to increase problem size. The trade-off between number of links and problem size should be held in mind as an orbit chain is assembled. Of course, despite the increased computation time, a larger collocation problem that leads to a solution is always preferable to a smaller problem that never converges.

An orbit chain that uses a large number of intermediate links to achieve a low-cost transfer is exemplified in the  $L_2$  Lyapunov to  $L_2$  vertical orbit transfer scenario. While the motion of both these orbit families is symmetric about the  $L_2$  libration point, a large plane change is required to transition from one type of motion to the other. Another type of orbit family, the  $L_2$  axials, includes trajectories that can assist the transition between these two types of motion. An orbit chain that includes multiple members of the  $L_2$  axial orbit family is constructed to facilitate a transfer from an  $L_2$  Lyapunov orbit to an  $L_2$  vertical orbit. This chain is displayed in Figure 4.14(a), which shows that six different axial orbits are included in the assembled chain. While

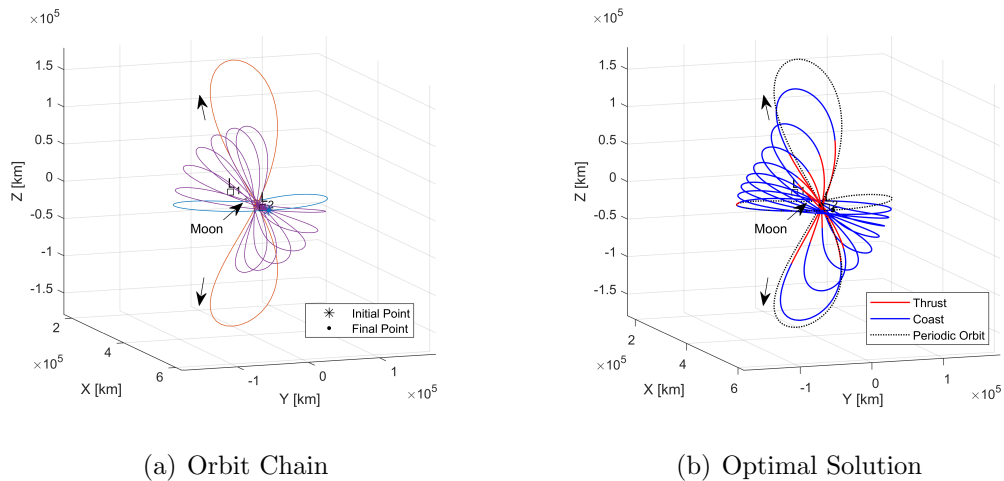


Fig. 4.14. An orbit chain that includes multiple members of the  $L_2$  axial family as intermediate links is used to compute an optimal transfer from an  $L_2$  Lyapunov to an  $L_2$  vertical orbit.

the  $L_2$  axial family does not span the entirety of the energy space between the initial and final orbits, the Jacobi constant values of the selected axials do fall between those of the initial and final orbit.

The axial orbits included in this multi-link orbit chain provide a gradual transition in energy and geometry from the initial to the final orbit. The suitability of the initial guess is evidenced by the fact that the computed optimal solution, displayed in Figure 4.14(b), maintains nearly the same geometry as the initial guess. The connection points between all orbits in the chain lie on the  $x$ - $y$  plane at nearly the same location, thus the discontinuities between links are easily corrected via the addition of brief thrust arcs. This result is evidenced by the fact that all the thrust arcs depicted in Figure 4.14(b) occur near the  $x$ - $y$  plane crossing. This transfer is one of many possible examples that illustrate how any number of links can be included in an orbit chain. A greater or lesser number of intermediate arcs could be included for this transfer and a successful result would likely still be obtained. Rarely if ever is there a single correct orbit chain. As a mission designer develops an intuition for the orbit chain and direct collocation approach, the quantity and type of links to include in a given orbit chain will become more apparent.

The orbit chain methodology can be employed with dynamical structures from any type of dynamical model. Dynamical structures generated in the CR3BP+LT, a CR3BP model augmented with a low-thrust acceleration described in Chapter 2, offer a wealth of new possibilities for creating and converging orbit chains. Recall that the CR3BP+LT model affords equilibrium points, periodic orbits, and invariant manifolds just as in the CR3BP, except that these structures are influenced by the direction and magnitude of the included low-thrust acceleration. Thus, the inclusion of low-thrust dynamical structures in an orbit chain offers geometries that are not available in the natural CR3BP, as well as a defined control history for each low-thrust arc. For example, the orbit chain shown in Figure 4.15(a) includes a low-thrust SPO and an unstable manifold trajectory of this orbit. These two low-thrust arcs are generated using a specific thrust magnitude and direction, and these data points

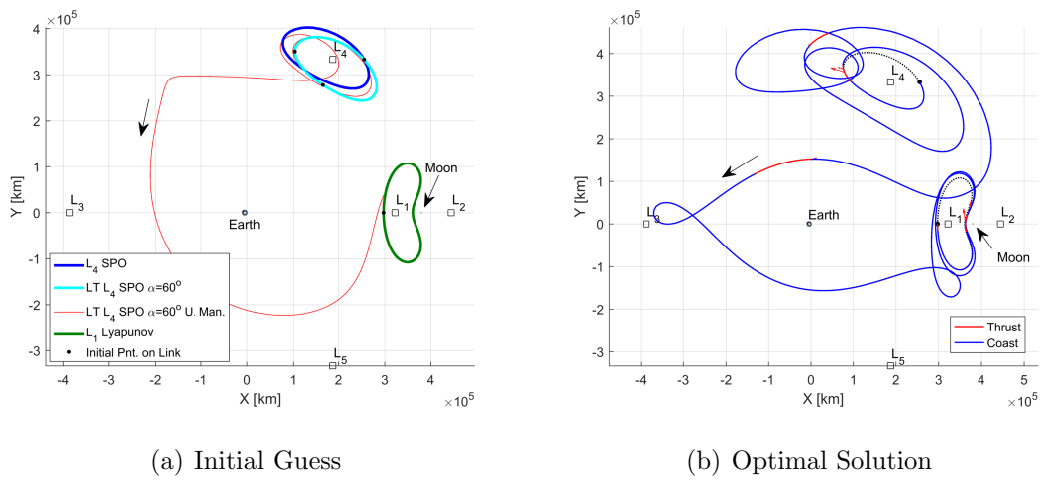


Fig. 4.15. Low-thrust transfer from an  $L_4$  SPO to an  $L_1$  Lyapunov orbit in the Earth-Moon CR3BP. An orbit chain approach leveraging dynamical structures from the CR3BP+LT is utilized. Unlike its natural CR3BP counterpart, the  $L_4$  SPO generated in the CR3BP+LT offers manifolds that are leveraged for trajectory design.

are used in the initial guess for the control profile of the desired transfer from an  $L_4$  SPO to an  $L_1$  Lyapunov orbit. Moreover, SPOs in the natural CR3BP do not permit the generation of invariant manifolds, thus this orbit chain geometry is only possible because structures from the CR3BP+LT are employed. The optimal low-thrust transfer that results from this orbit chain, shown in Figure 4.15(b), is influenced by the geometry of the initial guess, but the control history has been significantly altered. Further exploration has indicated that low-thrust dynamical structures are useful for constructing an initial guess and influencing the geometry of an optimal result, but that the control profiles of these structures are often significantly altered by the optimizer [24]. This is because the low-thrust arcs included in the initial guess assume continuous thrust, and some of this thrusting time is removed by the optimizer to reduce propellant consumption. The CR3BP+LT is one of many different dynamical models in which an orbit chain methodology can be applied to simplify the process of initial guess construction. In Chapter 6, the orbit chain approach is successfully employed in the BCR4BP.

The examples in this section elaborate on the orbit chain and direct collocation technique introduced in previous sections. A comparison of optimal transfers connecting the same two orbits but generated with two different three link orbit chains highlights the intuitive “mix and match” approach offered by the orbit chain method, as well as the adaptability that allows it to accommodate a variety of orbit chain compositions. This same flexibility is again highlighted when structures from a different dynamical model, the CR3BP+LT, are leveraged to compute a transfer from an  $L_4$  SPO to an  $L_1$  Lyapunov orbit. The ability of the direct collocation algorithm to eliminate the large state discontinuities present in the orbit chains assembled for many of these examples exhibits the robustness of this scheme. This robustness combined with the other strengths of the orbit chain approach yields a particularly effective approach to low-thrust trajectory design. The sample problems presented in this chapter are constructed to highlight the strengths of the proposed method. However, to fully demonstrate the merit of the orbit chain and direct collocation technique, it

must be applied to several real world mission design scenarios. Two such scenarios are presented in subsequent chapters and the manner in which the orbit chain and direct collocation approach is applied to these problems is described.

#### 4.5 Direct Collocation and Direct Multiple Shooting

Direct collocation methods are well suited for generating optimal low-thrust solutions from the discontinuous orbit chains assembled in this and subsequent chapters. However, given the diversity of approaches available for solving the low-thrust optimal control problem, it is worth considering whether other strategies perform similarly to direct collocation. Indirect and global optimization methods are not examined because of the characteristics outlined in Chapter 3 that make them ill-suited for the type of optimization problems encountered in this investigation. However, the method of direct multiple shooting is another approach to low-thrust trajectory optimization that merits further consideration due to the many strengths it shares with direct collocation. A rigorous comparison of direct collocation and multiple shooting methods is outside the scope of this study; however, qualitative comparisons available in the literature are reviewed and the result of a direct multiple shooting algorithm applied to an orbit chain from the previous section is examined. The brief analysis undertaken here suggests avenues for further investigation on the effectiveness of the direct multiple shooting method when paired with an orbit chain technique.

While many authors offer qualitative contrasts of collocation and multiple shooting methods, few offer quantitative comparisons. Nonetheless, beneficial insights can be gained from the experiences of previous authors. Lust offers an overview of the various methods available for computing periodic solutions of ordinary differential equations, and these include shooting and collocation techniques [85]. No optimization, either indirect or direct, is considered in Lust's analysis. Lust states that the explicit time integration of the nonlinear ODEs required by shooting procedures may cause these technique to fail where collocation methods succeed. However, he also

asserts that, if the boundary points are well chosen, a multiple shooting technique could be nearly as robust as a collocation technique. Keller also examines shooting and collocation methods as means for solving a TPBVP [86]. He states that the difficulty of determining a suitable initial guess is reduced for finite difference methods, in which he includes collocation. Like Betts, Keller also indicates that the difference between collocation and multiple shooting approaches is often simply a function of the integration step size. Russell focuses more specifically on collocation and declares that the high rate of convergence of this technique should make it competitive with other efficient procedures for solving TPBVP, including multiple shooting [87]. Together, these authors make the case that collocation can be at least as robust as multiple shooting schemes for solving TPBVP, if not more so.

Pairing a collocation or multiple shooting technique with an NLP solver does not appear to introduce significant distinctions in the effectiveness of the two approaches. In his survey of numerical methods for trajectory optimization, Betts notes the various drawbacks of direct collocation and direct multiple shooting techniques, but does not indicate the superiority of one approach over another [37]. This remains the case in a later text by Betts where he also applies both techniques to solve the same example problem. In another survey of optimization techniques, Rao calls direct collocation the “workhorse” for solving optimal control problems. [39] Furthermore, Rao states that while direct shooting methods are quite effective if a simple control parameterization can be employed, direct collocation methods are arguably more powerful as the problems increase in complexity. Grebow and Ozimek both demonstrate the robust nature of direct collocation when they apply it to design lunar pole-sitter orbits. [55, 88] However, they refrain from claims that this approach is superior to a similar direct multiple shooting implementation. The experience of previous authors indicates the suitability of direct collocation for the problems encountered in this investigation, but does not preclude the utility of a direct multiple shooting approach.

The apparent dearth of quantitative comparisons between direct collocation and direct multiple shooting methods applied to the low-thrust optimal control problem

suggests a gap in the literature. Filling this gap would inform mission designers and enable them to intelligently select the optimization technique best suited for their problem. For some problems it can be easier to implement a multiple shooting technique because these approaches leverage “black-box” explicit integration tools, e.g., Matlab’s ode suite of integrators. Thus, understanding when it is acceptable, or even advantageous, to utilize a direct multiple shooting formulation rather than a direct collocation technique would be valuable.

The primary challenge in comparing the effectiveness of the two techniques is that their performance is highly dependent on the specific implementation of each method as well as the nature of the problems they are applied to. Due to these complexities, a rigorous comparison of these two methods is not undertaken here; however, a direct multiple shooting scheme developed for low-thrust trajectory optimization is applied to the orbit chain assembled in Section 4.3. This result demonstrates the potential of utilizing a direct multiple shooting scheme with the orbit chain technique.

Relative to the NLP optimizer, in this case IPOPT, the change from collocation to multiple shooting merely represents a change in the function generator, i.e., the means by which the NLP problem variables are used to calculate the problem constraints. Like the direct collocation framework, the direct multiple shooting approach employed here assumes the thrust vector is constant across each segment. Furthermore, in addition to the CR3BP+LT EOMs presented in Chapter 2, the multiple shooting formulation also propagates the variational equations derived from these EOMs. Propagating these additional ODEs provides many of the partial derivatives required in the Jacobian matrix of the NLP problem, and does so with a high degree of accuracy. Other partial derivatives that appear in the Jacobian are computed analytically, further improving the accuracy and speed of the direct multiple shooting framework. Finally, this formulation also leverages the sparsity of the Jacobian to reduce computation time. Direct shooting schemes similar to the one leveraged in this investigation for low-thrust trajectory optimization are offered by Parrish [89] and Das-Stuart. [30]

The orbit chain assembled in section 4.3 is employed as an initial guess for the direct multiple shooting tool and the resulting transfer is compared with the results of the direct collocation algorithm. The orbit chain initial guess constructed for the DRO to  $L_3$  Lyapunov transfer in section 4.3 is kept as similar as possible where it is used with the direct multiple shooting algorithm. This means that the number of links, number of stacked revolutions, and even the number of segments is kept the same. Likewise, the initial control profile is identical to the direct collocation initial guess. For every segment along the initial guess, the thrust vector has zero magnitude and is oriented parallel to the velocity vector as expressed in the rotating frame. The primary difference between the initial guesses employed for the two different optimization methods is how each segment is discretized. The multiple shooting formulation includes only the boundary points of these segments. The collocation scheme introduces variable nodes which define a polynomial that approximates each segment. The low-thrust transfer computed from this initial guess via direct multiple shooting is plotted in Figure 4.16(a). The direct multiple shooting algorithm converges upon the

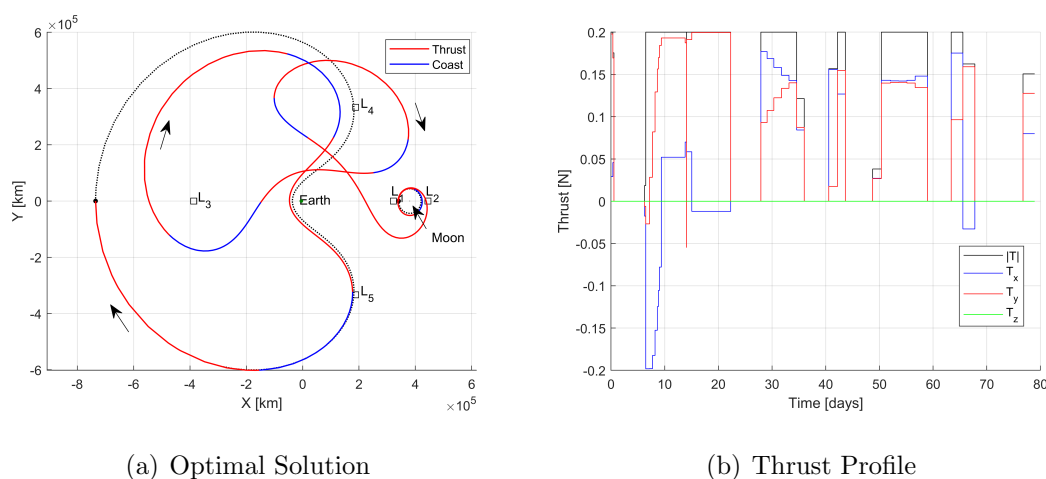


Fig. 4.16. Low-thrust transfer from a DRO to an  $L_4$  Lyapunov orbit in the Earth-Moon CR3BP. This transfer is computed with a direct multiple shooting algorithm using the orbit chain initial guess depicted in 4.6(a).

displayed solution with relative ease and rapidity.

The direct multiple shooting algorithm computes a different local optimal solution than the direct collocation approach. The time of flight of the optimal transfer shown in Figure 4.16(a) is approximately 79 days, the same as the direct collocation result. Although a variable time multiple shooting scheme is employed, the length of the transfer is fixed to simplify comparison with the direct collocation solution. The direct multiple shooting result consumes 36 kg of propellant, roughly 8 kg more than the direct collocation solution. The differences in performance between the direct collocation and direct multiple shooting solutions reflect the alternate route and thrust profile adopted to reach the  $L_3$  Lyapunov orbit. Figure 4.16(a) illustrates that the optimal solution computed with direct multiple shooting maintains more of the initial guess geometry, compared to the direct collocation result displayed in Figure 4.8(b). The thrust profile of the direct multiple shooting result, plotted in Figure 4.16(b), likewise highlights the difference from the direct collocation solution whose thrust profile is provided in Figure 4.7(c). The thrust profile of the latter result clearly requires a similar number of thrust segments, but they are generally shorter in duration. Thus, the direct collocation solution consumes less propellant. Adjusting optimization parameters such as step size and problem bounds may enable the direct multiple shooting algorithm to compute a local optimal solution more similar to the direct collocation result. However, attaining this different result may also require increasing the number of segments in the multiple shooting initial guess.

The thrust profile of the direct multiple shooting result highlights a drawback of the framework chosen to implement this algorithm. The multiple shooting scheme requires fewer segments to compute an accurate solution than the collocation approach, because each segment is explicitly propagated with a highly accurate third-party integrator (in this case, a Runge-Kutta Prince-Dormand (8,9) integrator from the GNU Scientific Library). Moreover, because no mesh refinement scheme is utilized, the number of segments in the initial guess and final solution are equal. Since both the multiple shooting and collocation based optimization approaches use a fixed thrust

vector along each segment, the multiple shooting scheme has fewer opportunities to change the magnitude or direction of the thrust vector. This difference increases the likelihood that the two optimization methods generate distinct results, as is the case here. When the same initial guess discretization is employed for both methods, the result computed by the direct multiple shooting approach exhibits signs that a finer mesh should be employed. The thrust profile displayed in Figure 4.16(b) shows that some segments of the optimal trajectory utilize thrust magnitude values that fall between zero and  $T_{max}$ , a behavior observed when the discretization employed to solve an optimal control problem is too coarse. Subdividing the initial guess into more segments will reduce the “choppiness” of the optimal thrust profile plotted in Figure 4.16(b), leading to the type of bang-bang solution that is expected. Furthermore, this change would likely also improve the optimality of the final result. If a using direct multiple shooting approach like the one implemented here the links between segment number, accuracy and optimality must be considered.

The results of this section suggest that further examination into an orbit chain and direct multiple shooting technique is merited. There may be situations where this pairing is preferred over one that includes direct collocation, either due to ease of implementation or improved convergence behavior. Generalizations concerning whether a direct multiple shooting approach is better or worse than the direct collocation method at pairing with the orbit chain technique are not possible on the basis of one example problem alone. A rigorous comparison with the direct collocation technique would require a range of sample problems with varying levels of complexity. The results would inform the work of mission designers as they seek to identify the tools best suited for solving various low-thrust trajectory design problems.

#### 4.6 Orbit Chain and Direct Collocation Parameter Analysis

The combination of an orbit chain and direct collocation approach to low-thrust trajectory design produces a method with many variables that can be adjusted to

obtain a solution. Some of these variables are changed with each new problem, while others typically remain constant. The number of variables available can make it initially challenging for the unacquainted practitioner of the orbit chain and direct collocation approach to compute solutions, and this problem is compounded by the sensitivity of the procedure to some of these variables. This section details the major parameters that can be adjusted by the user to obtain feasible and optimal solutions, with the goal of diminishing the need for a new user to undergo a tedious process of trial and error.

Understanding the effect of the parameters identified in this section is complicated by the fact that their impact varies based on the mission design problem under consideration. If the problem takes place in an especially sensitive dynamical regime, then the parameter values of the orbit chain and direct collocation approach have an amplified effect. Therefore, a comprehensive analysis of all parameters is not undertaken in this investigation. Instead, a discussion of the key parameters that impact direct collocation convergence is provided and suggestions for how to enhance understanding of the effect of these parameters is provided. Finally, in this investigation, a feasible solution is often computed first, and then used to initialize the optimization step. Thus, changes to the parameters discussed here are typically most effective when seeking an initial feasible solution. However, several parameters unique to the optimization step are discussed as well.

The parameters that impact the composition of the orbit chain initial guess should always be modified first when attempting to obtain convergence with a given orbit chain, because these settings typically have the most impact on whether a solution to the collocation problem is obtained. The primary parameters that dictate the makeup of the orbit chain are covered in the previous sections, including: type and number of intermediate links, the number of revolutions stacked on a link, and the initial distribution of the mesh. The type and number of orbit chain links are the most obvious characteristics of an orbit chain, because these are evident in a configuration space plot of the initial guess. However, the importance of the unseen parameters

should not be underestimated. Failure of the collocation algorithm to converge a given orbit chain can be remedied simply by stacking more revolutions on a given link, thus providing additional trajectory and time of flight with which to achieve the desired transfer. Similarly, adding additional boundary points along an orbit chain link that passes close to a primary body can enable convergence when the collocation algorithm would have otherwise failed. Additional insight on the construction of effective orbit chains is offered by Prado et al. [90,91]

Besides the orbit chain parameters, several criterion of the collocation algorithm itself can be adjusted in an attempt to achieve convergence. The most important of these parameters include the attenuation factor and initial control profile. The first of these, the attenuation factor, is a scalar value utilized to adjust the size of the update step applied at each successive iteration of the collocation algorithm, and is discussed in greater detail in Chapter 3. The wide convergence basin of collocation means that this technique can sometimes produce solutions with very different characteristics than the initial guess. Moreover, when in search of a feasible solution, a collocation algorithm will occasionally “blow-up.” That is, in an attempt to locate a feasible solution, the algorithm drastically alters the initial guess and gets “stuck” attempting to converge transfers that satisfy nearly all of the problem constraints. Examples of this behavior include a transfer that is continuous, but includes a flyby that passes through the Moon or thrust arcs that far exceed the value of  $T_{max}$ . These scenarios can sometimes be avoided by utilizing an attenuation factor that encourages the collocation algorithm to converge upon solutions similar to the initial guess. Of course, if there are no feasible solutions similar to the initial guess, then the attenuation factor will merely hinder progress towards a solution or delay an inevitable failure to converge. However, at times the attenuation factor can make the difference in whether or not a solution is obtained.

The control profile defined for an initial guess is another critical factor that effects whether a feasible or optimal solution is successfully computed. Section 4.3.3 describes how the initial control profile is typically defined by three criterion: thrust vector

direction, throttle value, and maximum thrust magnitude. Altering any of these parameters can make the difference between attaining convergence or not. Perhaps the most obvious parameter that can be changed to facilitate convergence is the maximum thrust magnitude. Raising the maximum available thrust increases the control authority of a spacecraft, typically making it easier to obtain a solution. For this reason, one approach to obtaining a desired low-thrust transfer is to first converge the transfer with a higher value of  $T_{max}$ , and then employ natural parameter continuation to reduce  $T_{max}$  to the desired value. Alternatively, rather than raising  $T_{max}$ , simply changing the initial throttle value can assist convergence. Defining an initial guess such that most or all segments employ a maximum throttle value can bias the collocation algorithm towards results that would otherwise not be obtained. Finally, the direction of the thrust vectors in the initial guess can sometimes affect the outcome of the convergence process. Typically, these vectors are oriented parallel or anti-parallel to the direction of the velocity vector as expressed in the rotating frame. The choice between these two options is made based on whether the energy of the destination orbit is greater or less than that of the initial orbit. However, switching between these two potential thrust vector orientation schemes or even utilizing alternate orientations for the initial thrust vector can help the direct collocation algorithm to converge.

The collocation algorithm implemented in this investigation includes several other parameters that typically remain constant, but which can be adjusted if the aforementioned steps have not lead to convergence. These parameters are the degree of the collocation polynomial, the type of mesh refinement employed, and the value of the minimum radius constraint. The degree of the collocation polynomial can be raised instead of or in combination with increasing the number of segments in the initial guess. Higher degree polynomials approximate the dynamics along a segment more accurately, thus using a higher degree polynomial can enable a collocation scheme to use fewer segments to converge upon a solution. Increasing the degree of the collocation polynomials is especially helpful if a significant portion of a transfer takes place

near a primary body where the dynamics are highly nonlinear. Of course, there are diminishing returns to increasing the value of the polynomial, and doing so must be balanced with the resulting increase in size of the collocation problem. Only 7<sup>th</sup> and 9<sup>th</sup> order Legendre-Gauss polynomials are employed in this investigation.

The type of mesh refinement paired with the collocation algorithm can also influence the characteristics of the solution, and even whether a solution is obtained. Typically, the hybrid mesh refinement technique is employed because this approach produces a highly accurate solution along which error is evenly distributed. At times, utilizing the coarse-hybrid mesh refinement routine can facilitate convergence because this technique redistributes the mesh in an advantageous manner as the collocation algorithm converges upon a more accurate solution.

The minimum radius constraint is introduced in collocation problems to prevent the algorithm from getting “stuck” near gravitational bodies or producing solutions that pass through the surface of one of these bodies. If a transfer is likely to pass near a gravitational body, then a minimum radius constraint with respect to this body should be included. Often the minimum radius value should be at least several times the radius of the body so that the constraint influences the behavior of the collocation algorithm well before it has a chance to get “stuck.” However, performing flybys of gravitational bodies is one way that the optimality of a transfer can be improved as a spacecraft can leverage the gravity of these bodies with a well-timed maneuver to effect large changes in energy. Therefore, if the minimum radius constraint is set too large, the direct collocation algorithm may not converge because it is unable to effectively leverage flybys. Achieving the appropriate balance between these competing factors sometimes requires experimentation with the value of the minimum radius constraint to aid convergence of the direct collocation algorithm.

After a feasible collocation solution is computed it is typically optimized by utilizing it as an initial guess for a direct collocation scheme. The type of NLP solver employed to conduct the optimization dictates the types of parameters available to effect the convergence behavior of the optimization routine. These parameters and

their default values are typically described in the users manual for the given optimizer. However, two types of parameters related to direct optimization that are separate from these optimizer specific settings are the design variable bounds and the scaling method. Utilizing the capability of most optimizers to impose bounds on the design variables is a highly effective means of promoting convergence. The manner in which these bounds are set is described in Chapter 3. This approach can be employed to set tight bounds on an optimization problem, which effectively reduces the solution space explored by the optimization algorithm and makes it easier to compute a solution. If the solution computed using these tight bounds contains design variable values that equal any of the bounds, this is an indicator that the bounds should be expanded. The optimization process is then restarted with wider bounds and using the previously computed solution as an initial guess. Thus, a process of imposing tight bounds that are gradually increased can be an effective means of obtaining an optimal solution.

The other optimization specific set of parameters that can be altered to obtain a solution are the variable and constraint scaling. The scaling approach implemented in this investigation is described in Chapter 3. While these scaling techniques can be helpful, they are not always applied to solve every optimization problem. Because all variables in the direct collocation problem are nondimensionalized using the characteristic quantities described in Chapter 2, the need for further scaling is somewhat reduced. Nonetheless, scaling can be helpful. Applying variable scaling, constraint scaling, or both, can aid convergence towards an optimal solution. As described previously, utilizing constraint scaling requires the definition of acceptable convergence thresholds in dimensional units, and these values can be experimented with individually in efforts to promote convergence.

More thorough investigation of how the orbit chain and direct collocation parameters included in this section impact convergence behavior would provide valuable insight that can enhance the overall effectiveness of the technique. The most common parameters adjusted to facilitate convergence have been discussed, but there

are others not considered that may also play a role. Further analysis is required to improve understanding of how best to employ the orbit chain and direct collocation technique. Experience from solving the real world low-thrust mission design problems presented in the next two chapters offers additional insight on best practices for implementing this trajectory design framework.

## 5. GATEWAY MISSION DESIGN

NASA and many of its partners have expressed a renewed interest in returning humans to the Moon, which has led to increased focus on trajectory design in cislunar space. A major component of NASA's strategy for returning to the Moon and continuing on to Mars is the Gateway. The Gateway will be an intermittently crewed space station that serves as a platform for missions to the lunar surface and beyond the Earth-Moon system [92]. The nominal orbit of the Gateway will be a 9:2 synodic resonant near rectilinear halo orbit (NRHO). This orbit is selected due to its high stability, favorable eclipse avoidance properties, and continual line of sight with the Earth. The Gateway space station will utilize powerful low-thrust engines to transfer to this orbit and to navigate to other orbits in the lunar vicinity. Compared to a chemical propulsion system of the same mass, these efficient engines will expand the range and lifetime of the Gateway. The total thrust magnitude provided by its engines is much higher than other current low-thrust spacecraft; however, given the massive size of the Gateway space station, its maximum low-thrust acceleration is actually quite small. The Gateway mission's use of the 9:2 NRHO along with its low-thrust capability make it a compelling mission from a trajectory design perspective. This mission necessitates the development of low-thrust transfers between a variety of multi-body orbits in the Earth-Moon system for a spacecraft with very limited control authority. Application of the orbit chain and direct collocation trajectory design framework to this challenging trajectory design scenario is the focus of this chapter.

Multiple aspects of the Gateway mission make it a beneficial application for demonstrating the orbit chain and direct collocation trajectory design framework. First, the methodology proposed in this investigation is specifically tailored to low-thrust trajectory design, and low-thrust propulsion will be the primary means by which the Gateway navigates within the cislunar environment. Secondly, the nominal

staging orbit for the Gateway, the 9:2 NRHO, does not possess invariant manifolds (the dynamical structures often used for the construction of transfers to and from other multi-body orbits). However, the orbit chain technique does not require invariant manifold paths, as other orbits near the 9:2 NRHO can be included in an orbit chain that is converged via direct collocation to produce transfers to and from the NRHO. Fortunately, a wide variety of orbits exist in the immediate vicinity of the 9:2 NRHO that can be leveraged to guide the direct collocation algorithm to optimal low-thrust solutions. Finally, the relatively low maximum acceleration level available to Gateway makes this a helpful trajectory design scenario for testing the limits of the orbit chain technique. When very low acceleration magnitudes are employed the geometry and energy profiles of low-thrust transfers are often nonintuitive, and the orbit chain technique is an effective tool for rapidly exploring this unfamiliar solution space.

In this chapter the orbit chain and direct collocation approach is applied to construct transfers for the Gateway spacecraft that depart from the 9:2 NRHO and arrive at other multi-body orbits in the vicinity of the Moon. Destinations of interest include a distant retrograde orbit, a low-amplitude halo orbit, and a northern NRHO. Orbit chain initial guesses for transfers to these orbits are assembled using a variety of intermediate orbits. These intermediate orbits are selected to generate two types of geometry for each transfer, exterior and interior. In the first type of geometry, the spacecraft may depart the vicinity of the Moon and embark on one or more transits about the Earth. During these long transits, while the spacecraft is far from either primary, the required changes in plane and energy may be executed. Alternatively, some trajectories remain relatively close to the Moon during the entirety of a transfer, and this geometry is denoted interior. All solutions are initially computed in the CR3BP, and are subsequently transitioned to an ephemeris model for validation. Finally, one solution is selected for conducting missed thrust analysis, which reveals the times when a trajectory is most sensitive to a missed thrust event. This chap-

ter demonstrates that the orbit chain and direct collocation technique is an effective approach to trajectory design for the Gateway mission.

## 5.1 Background

As the Gateway program is ongoing, the specific details of the mission and spacecraft will likely change as the program matures. The information presented in this chapter is accurate as of the time of writing. Barring significant alterations to the Gateway architecture, this methodology can be adapted to any changes to Gateway that occur during its development. An overview of the Gateway mission as it is currently envisioned is presented here. Additionally, literature on trajectory design strategies and solutions previously developed for Gateway is reviewed. Lastly, the approach to missed thrust analysis employed in this investigation is discussed with a survey of relevant literature.

### 5.1.1 Mission Overview

The Gateway spacecraft will facilitate human and robotic exploration of the Moon and serve as a proving ground for the development of capabilities essential for missions to Mars. NASA intends the Gateway to consist of several modules that, at minimum, provide, power, propulsion, habitation, and an airlock, as seen in Figure 5.1. The first of these modules, the power and propulsion element (PPE), is being developed by Maxar Technologies and is scheduled for launch in 2022 [94]. Following delivery of the PPE to the 9:2 NRHO, the remainder of the Gateway will be assembled incrementally over several years. As with the International Space Station, the Gateway's construction and operation will include international collaboration. The initial spacecraft mass in this investigation is 39 metric tons, in line with the estimated total mass of the Gateway after its complete assembly [34].

Multiple low-thrust engines will enable the Gateway to complete its required transfer and station keeping tasks. The current baseline PPE configuration includes six

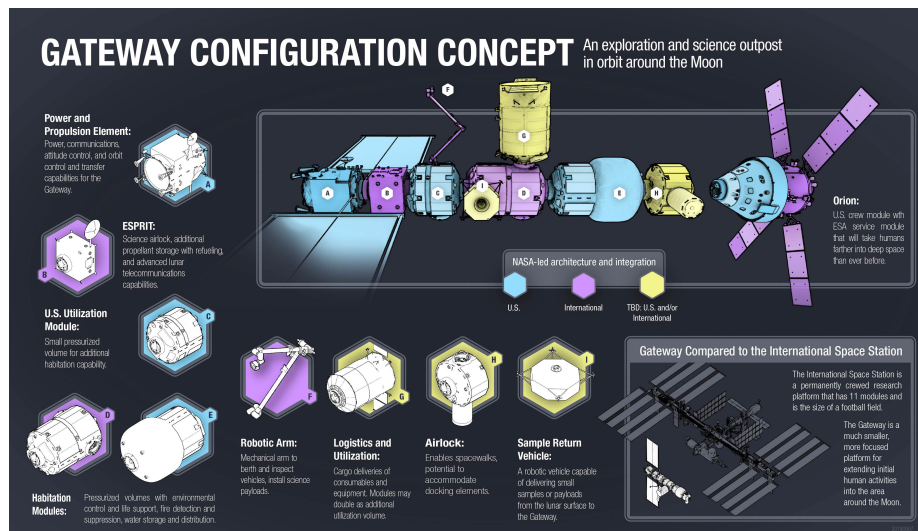


Fig. 5.1. Concept for the Gateway spacecraft [93].

low-thrust engines [95]. Two of these engines will be 13 kW Advanced Electric Propulsions Systems (AEPS) developed by Aerojet Rocketdyne [96, 97] in collaboration with NASA, and the other four are 6 kW Hall effect thrusters built by Busek and Maxar. Together, these engines provide approximately 50 kW of beginning of life propulsive power, though it is unlikely that they will be used simultaneously at any point in the Gateway’s mission lifetime. Therefore, the maximum thrust value used to design transfer trajectories in this investigation is lower than the total thrust capability the engines could technically provide. This analysis uses a maximum thrust of  $T_{max} = 1.1326$  N, which is consistent with the work performed by McCarty, Burke, and McGuire [34]. Additionally, this work assumes a 90% duty cycle is employed, making the maximum thrust available to the Gateway for a typical transfer  $T = 0.9 * T_{max}$ . Despite being equipped with multiple engines that utilize cutting edge low-thrust propulsion technology, the control authority of the fully assembled Gateway spacecraft is extremely limited. Control authority is best expressed in terms of the maximum acceleration a spacecraft can impart at any given instant in time. Considering its mass and maximum thrust capability, the maximum acceleration Gateway

is capable of is,  $a_{max} = 2.904 \times 10^{-5} \text{ m/s}^2$ , which is an order of magnitude lower than other recent low-thrust missions, e.g., Deep Space 1 and Dawn. The low maximum acceleration magnitude available to Gateway is the primary challenge associated with trajectory design for this spacecraft.

The Gateway is intended to spend the vast majority of its mission lifetime in its nominal staging orbit, a 9:2 synodic resonant NRHO. This orbit was selected after extensive analysis of a variety of candidate orbits [98–100]. The near rectilinear halo orbits are a subset of the halo family of orbits in the CR3BP. The NRHOs are all stable or nearly stable orbits, which reduces the propellant required for stationkeeping. The 9:2 NRHO is a single member of the group of NRHOs that exist within the southern  $L_2$  halo family. It possesses a unique 9:2 resonance with the synodic period of the Earth-Moon system, which means that nine revolutions of the 9:2 NRHO are equal to two synodic periods in the Earth-Moon system, where one synodic period equals approximately 29.5 days. This resonance offers the 9:2 NRHO favorable eclipse avoidance properties, for the orbit may be designed such that prolonged eclipses of the Sun by the Earth are avoided. Another advantageous property of the 9:2 NRHO is its geometry; it not only provides a continual line-of-sight with the Earth, but also ensures that the majority of each orbit is spent within view of the lunar south pole, where the majority of the upcoming human exploration activities are expected to occur. While the 9:2 NRHO offers an excellent location for the Gateway to carry out most of its mission objectives, some tasks may require it to temporarily relocate to other orbits in the lunar vicinity. For example, a transfer to an NRHO in a northern halo family may be required to gain easier access for landers to the Moon's northern latitudes. The design of low-thrust transfers from the 9:2 NRHO to other orbits such as this one is the focus of this chapter.

### 5.1.2 Previous Contributions

Transfers to and from NRHOs to other orbits in the Earth-Moon system were of interest prior to the inception of the Gateway project and since this project began, several studies focusing on transfers for this specific spacecraft have been conducted. Alternate orbits of interest to the Gateway project include distant retrograde orbits (DRO), other NRHOs, and low-amplitude halo orbits, all of which are depicted in Figure 5.4. Capdevila presents families of impulsive transfer options between  $L_2$  NRHOs and lunar DROs [101] and Zimovan continues this work by incorporating arcs from other multi-body orbits into transfers between these orbits [102]. Low-thrust transfers between DROs and members of the southern  $L_2$  halo family, including NRHOs, are also examined by Parrish [89]. Lantoine offers an innovative method for designing highly efficient transfers from an NRHO to a DRO that leverages Moon-to-Moon transfer arcs generated in the Sun-Earth CR3BP [103]. Most recently, McCarty et al. examine transfers from an NRHO to a DRO, as well as several other destination orbits for a spacecraft with the mass and engine characteristics planned for the Gateway [34, 104]. This investigation extends the work of these authors by applying an orbit chain and direct collocation approach to compute similar transfers from an NRHO to other multi-body orbits of interest.

### 5.1.3 Missed Thrust Background

Missed thrust analysis is a critical step in the mission design process for low-thrust spacecraft. Trajectories designed for spacecraft with conventional chemical engines include maneuvers that require engine burns lasting minutes. In contrast, low-thrust trajectories frequently require thrust arcs lasting days, weeks, or even months at a time. Because a low-thrust spacecraft's engines are expected to operate for a significantly larger proportion of its time of flight, any event that inhibits engine operation is more likely to have an impact on the trajectory. The most likely event that would prevent engine operation is a spacecraft entering into safe mode. This mode is a

default configuration that a spacecraft can assume upon encountering any number of internal or external anomalies, from a software error to cosmic rays striking electronic components. In safe mode a spacecraft continues only its most essential functions while its operators determine how to address the cause of the safing event. Entering safe mode is not a rare occurrence for spacecraft, and past low-thrust missions have encountered safe modes that significantly disrupted their planned trajectories [105]. The Deep Space 1 and Dawn missions offer the most prominent examples of this scenario [106, 107]. Given the higher probability of a safing event occurring during a maneuver, low-thrust trajectories must be designed with sensitivity to this possibility in mind. This aspect of the design process is denoted missed thrust analysis, and ascertains the portions of a spacecraft trajectory where the occurrence of a missed thrust event causes the most additional propellant consumption. In the worst possible case, recovery from a missed thrust event may demand more propellant than the spacecraft can supply, thus causing mission failure. Identifying the sections of a trajectory that are most susceptible to such a catastrophe allows mission designers to redesign the trajectory with increased robustness.

As a consequence of the importance of accounting for missed thrust events in low-thrust mission design, a growing body of research has developed to address this topic. Much work has focused on missed thrust analysis, that is, analysing the sensitivity of a low-thrust trajectory to missed thrust events. More recently, attention has been paid to missed thrust design, where robustness to missed thrust events is incorporated into the trajectory design process from the very beginning. An analysis of the margins that should be utilized for a low-thrust mission to account for the occurrence of missed thrust events is conducted by Oh et al. [108]. Explorations of the types of safing events that can cause thrust outages for low-thrust spacecraft are offered by Imken et al. [105] and this work is employed by Pujari, Imken, and Lightsey [109] to model such safing events. Various strategies for conducting missed thrust analysis are available, this investigation follows an approach similar to the scheme presented by McCarty and Grebow [110]. Other frameworks for missed thrust analysis are

offered by Laipert and Longuski [111], Rubinsztein, Sood, and Laipert [112], and Sarli et al. [113]. Furthermore, techniques for missed thrust design are presented by Olympio [114, 115], Ozaki et al. [116–118], and Tsuda [119]. This investigation focuses on missed thrust analysis and utilizes some of the strategies for this process developed by previous authors.

## 5.2 Gateway Methodology

The computation of Gateway transfers is conducted with the same strategy employed for the simpler orbit chains presented in the previous chapter. However, because the low-thrust acceleration level is quite low for the Gateway spacecraft, additional steps are necessary. Namely, a continuation process is employed to achieve transfers that utilize the correct low-thrust acceleration level. The complete sequence of steps employed to go from a discontinuous orbit chain in the CR3BP to an optimal low-thrust transfer in the ephemeris model is outlined in this section. Additionally, the process of conducting missed thrust analysis on a computed low-thrust transfer is detailed.

### 5.2.1 Sample Transfer Computation

A multi-step procedure is employed to transition an orbit chain initial guess to an optimal transfer in an ephemeris model. The process begins with the construction of an orbit chain using dynamical structures available in the CR3BP. This chain is then employed as an initial guess for the direct collocation algorithm. Experience indicates that, for spacecraft with low maximum acceleration values, it is often challenging to transition directly from a discontinuous orbit chain to a continuous transfer at the desired acceleration level. Instead, it is often easier to obtain a transfer using a slightly higher low-thrust acceleration level and then to incrementally decrease this value to the desired value. Although this process requires more steps, it is frequently the most reliable way of obtaining the desired low-thrust solution. The schematic in

Figure 5.2 outlines the procedure employed to transform orbit chain initial guesses to optimal low-thrust solutions in the CR3BP.

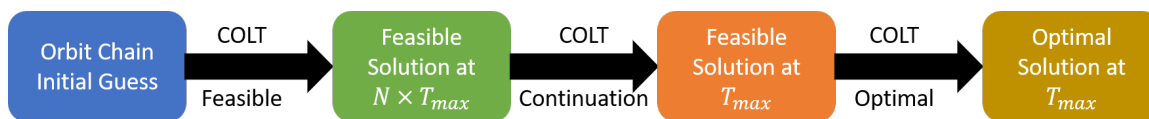


Fig. 5.2. Schematic of trajectory design framework for computing optimal Gateway transfers beginning with an orbit chain initial guess.

Following assembly of an orbit chain initial guess, a feasible low-thrust transfer with a maximum thrust value  $N$  times that of the desired maximum thrust value,  $T_{max}$ , is converged. There is no set rule as to what value of  $N$  should be employed to obtain the first transfer in the continuation process. If the selected value of  $N$  is too high then it is unlikely that the thrust level can be continued all the way down to  $N = 1$ ; however, if the value of  $N$  is not high enough, then it may not be possible to converge the orbit chain in the first place. Experience indicates that a thrust level approximately 1.5 to 2 times that of the desired thrust level is sufficient to achieve convergence while still enabling the resulting transfer to be continued down to  $N = 1$ . In this investigation a value of  $N = 2$  is employed to converge feasible transfers from the orbit chain initial guess, i.e., two times the maximum thrust capability of the Gateway spacecraft. Once a feasible solution is computed using the orbit chain initial guess, natural parameter continuation is applied to lower the maximum thrust value and thereby the maximum acceleration value of the spacecraft in the transfer.

Each successive step of the continuation process can compute either a feasible or an optimal solution. Less computational time is required to obtain a feasible solution; however, at times computing optimal solutions allows the continuation process to successfully reach the desired maximum thrust value when it would otherwise fail. A compromise between these two approaches is to optimize only the first solution in the continuation process and compute feasible solutions for the remainder of the continuation steps. Regardless of which approach is employed, a successful imple-

mentation of the continuation process will lead to a transfer that utilizes the desired maximum acceleration level.

After a low-thrust transfer at the desired thrust level is obtained, the solution is optimized. Even when the result produced at the conclusion of the continuation process is already optimized it is sometimes possible to meaningfully improve its optimality by repeating the optimization process with minor changes. These changes include increasing the density of the solution mesh. This step provides more opportunities along the transfer for the thrust magnitude and direction to be changed, thus yielding a more optimal solution. Additionally, the bounds of an optimization problem can be increased, allowing the optimizer greater freedom to potentially improve local optimal solutions. Once a satisfactory optimal solution is obtained, the process of transitioning the solution to a higher fidelity model can begin.

Optimal Gateway transfers computed in the CR3BP are transitioned to an ephemeris model to demonstrate that the solutions persist in a higher fidelity model. The process utilized to transition the Gateway transfers is identical to the general process outlined in Chapter 4. The initial and final orbits of each transfer are converged separately from the transfer itself, which is converged with constraints that require it to depart and insert from selected points on these separately converged ephemeris orbits. The proximity of the Gateway transfer scenarios to the Moon increases the difficulty of achieving convergence in the ephemeris model because slight fluctuations in the position of the Moon have significant effects on the trajectory. As no specific dates are presently required for any of the transfer scenarios examined, there is freedom to select the initial epoch of each transfer according to what eases the conversion process to the ephemeris model. This flexibility, in addition to careful placement of the departure and insertion points on the separately converged initial and final orbits, enables the successful transition of all trajectories to a full ephemeris model. If alternate dates for the ephemeris transfers are desired, these may be obtained by applying a continuation process to the converged ephemeris transfer to gradually change its initial epoch.

The selection of a initial epoch for each transfer that eases transition to the ephemeris model is made by scanning through a range of possible dates within a set time period. In this case, the month of June 2024 is the month that all computed transfers will begin. Each CR3BP solution is converted to the ephemeris based inertial frame and propagated in the ephemeris model. This step generates a discontinuous initial guess whose general outline, when plotted in configuration space, should resemble that of the original CR3BP solution. The discontinuities between successive segments in the initial guess will vary in magnitude based on the selected initial epoch. A range of departure epochs within the chosen month are scanned and the average discontinuities between all segments are recorded for each epoch tested. Then the epoch that leads to the lowest average velocity discontinuity is selected, as this metric is often the dominant factor in determining the likelihood of an initial guess converging. If desired, a larger range of dates could be scanned to determine the most favorable initial epoch; however, this change would require greater computational time.

### 5.2.2 Missed Thrust Analysis

The missed thrust analysis scheme employed in this investigation analyzes the sensitivity of a trajectory to missed thrust events by introducing these events at successive intervals on a baseline solution. The analysis procedure begins with an already computed low-thrust solution. In this case, CR3BP solutions presented in Section 5.3.1 are subjected to analysis. The pre-computed low-thrust trajectory is termed the baseline solution and offers a point of comparison for the results of the missed thrust analysis.

After a baseline solution is selected, a time interval between successive missed thrust events is defined. The procedure presented here examines the effect of a single missed thrust event of a fixed duration, introduced at different times on the baseline trajectory in an iterative process. This procedure ultimately provides a complete pic-

ture of the baseline trajectory's sensitivity to the missed thrust event. The total time of flight of the baseline trajectory and the interval between successive missed thrust events determines the number of iterations this process will take. The smaller the time spacing is, the more comprehensive the missed thrust analysis will be, because the effect of a missed thrust event will be assessed at more times on the baseline trajectory. However, a finer time spacing will also require more computational time, thus a balance between time and accuracy must be struck. An interval of 4 hours between successive missed thrust events is employed.

Once a time interval for the introduction of successive missed thrust events is chosen, the duration of the missed thrust event must also be defined. A realistic thrust outage time is dependent on a variety of spacecraft and mission factors. However, conservative outage times are usually several days or longer. Thus, thrust outage times of 3, 5, 7 and 14 days are examined.

The final parameter defined prior to the commencement of the missed thrust analysis is the duration of the margin time appended to the end of the baseline solution. Extra time of flight is often required for a spacecraft to recover from a missed thrust event. Therefore, additional trajectory is added to the end of the baseline solution to provide ample time for the spacecraft to reach its destination following a missed thrust event. This extra trajectory is added by ballistically propagating the final periodic orbit for the desired length of margin time, beginning at the final point of the baseline transfer. This additional trajectory is subdivided into segments and affixed to the end of the baseline solution. The newly extended baseline is then converged while the added segments are forced to remain coast segments. This constraint preserves the original baseline, while providing additional trajectory that can be utilized following a missed thrust event. Generally, the duration of the added margin time should scale with the length of the thrust outage; however, a constant margin of 20 days is employed for missed thrust analyses so that the results of analyses conducted with several different outage times are easily compared. This duration is sufficient for the longest missed thrust event examined in the present analysis. A

schematic of a baseline low-thrust solution with added margin time and a defined missed thrust time interval is offered in Figure 5.3(a). The definition of the three time parameters: missed thrust time interval, the outage durations, and margin durations, completes the setup of the missed thrust analysis procedure.

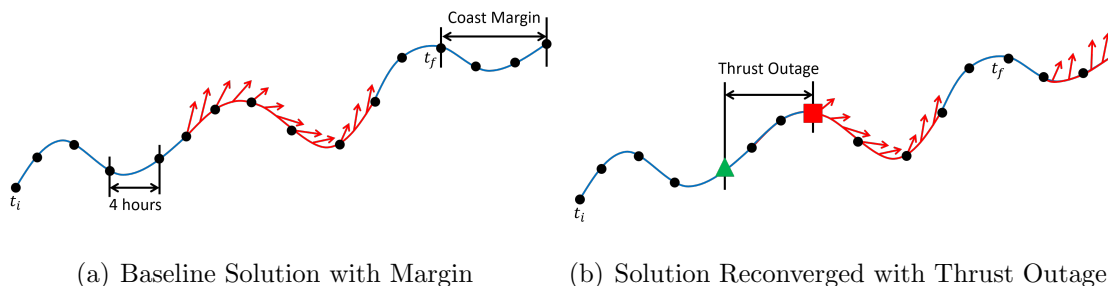


Fig. 5.3. Missed thrust analysis schematic. (a) An evenly spaced missed thrust time interval is applied to an existing low-thrust solution and time margin is appended to the end of the trajectory. (b) A thrust outage period is enforced on the newly modified trajectory, and the added margin is utilized to achieve the desired end state.

After the missed thrust problem is defined, an iterative process of optimizing the baseline solution with forced thrust outages at different times begins. This procedure essentially “walks” the thrust outage period along the entire trajectory, beginning at the first time in the predefined interval. Boundary points are added to the baseline trajectory at the exact start and stop times of the missed thrust event. This addition allows all segments that fall between these new points to be fixed as coast segments, while the remainder of the trajectory is free to change to satisfy the problem constraints. This freedom includes the margin at the end of the trajectory where thrust segments can now be introduced. Figure 5.3(b) offers a schematic of a solution converged following the introduction of a missed thrust event. Note that the section of trajectory originally designated margin in Figure 5.3(a) now includes thrust segments in Figure 5.3(b). With each successive step of the missed thrust procedure the times of the thrust outage period are updated, so that it begins at a new time in the predefined interval.

The shifting times of the thrust outage period allow the size of the optimization problem to change with each step. Because it is assumed that all trajectory before the initial thrust outage time is flown without incident, all boundary points that occur prior to this time are excluded from the optimization problem. As a result, the optimization problem solved with each successive step of the missed thrust procedure reduces in size with each iteration. The thrust outage period is transitioned along the entirety of the baseline trajectory until the initial time of the missed thrust event coincides with the final time of the baseline solution (excluding the added margin time). Because each step of the missed thrust analysis is independent, the procedure lends itself to parallelization, which substantially reduces the wall-clock time required to complete the analysis.

The results of the missed thrust analysis offer insight into the locations on the original low-thrust trajectory that are most sensitive to the occurrence of a missed thrust event. In some cases the introduction of a missed thrust event may prevent the trajectory from being reconverged. In this situation, it may be possible to achieve convergence by adjusting the optimizer settings or including additional coast margin at the end of the trajectory. However, if these steps fail, a more drastic redesign may be required. One strategy employed to improve the results of a missed thrust analysis is to design the baseline low-thrust trajectory with a lower thrust level than the  $T_{max}$  of the spacecraft, i.e., to use an engine duty-cycle below 1. This technique generates a trajectory that is more robust to missed thrust events because if one occurs, the spacecraft can then utilize its maximum thrust capability to reach the same destination that was originally attained with a lower thrust level. In this investigation, a duty cycle of 0.9 is employed to compute all transfers in Section 5.3 while a duty cycle of 1 is permitted during the missed thrust analysis. The results of this phase reveal the insights available from missed thrust analysis.

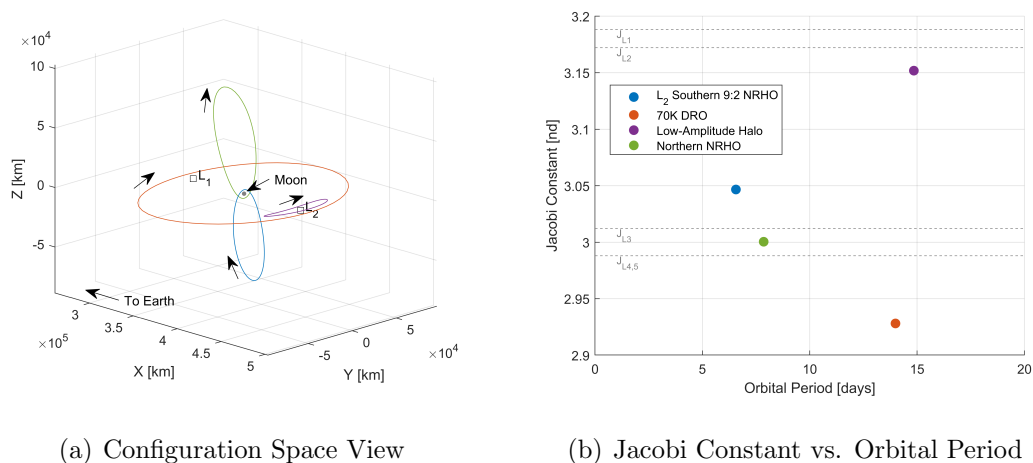
In summary, the steps of the missed thrust analysis procedure implemented in this investigation are:

1. Select baseline optimal low-thrust transfer.

2. Define time interval between successive missed thrust events.
3. Designate duration of a missed thrust event.
4. Define time span of margin appended to the end of the baseline trajectory.
5. Cycle through successive missed thrust events. At each step solve a low-thrust optimization problem that includes the missed thrust event and all subsequent trajectory (including margin).
6. Record the delivered spacecraft mass and whether the direct collocation algorithm converges at the conclusion of each step.

### 5.3 Sample Transfers

The orbit chain and direct collocation technique is employed to develop low-thrust transfers from the 9:2 NRHO to a variety of multi-body orbits that may be destinations of interest for the Gateway spacecraft. The destination orbits examined in this investigation are a distant retrograde orbit, a low-amplitude halo orbit, and a northern  $L_1$  NRHO. Because the maximum excursion in the  $\hat{z}$  direction for the selected halo orbit is quite small, it is termed low-amplitude. These orbits, along with the 9:2 NRHO, are displayed in Figure 5.4(a). It is clear from this plot that transfers from the 9:2 NRHO to the DRO or low-amplitude halo orbit require significant plane changes. A trajectory to either of these orbits necessitates a nearly  $90^\circ$  plane change. Alternately, although the northern NRHO lies in nearly the same orbital plane as the 9:2 NRHO, its opposing direction of motion requires a  $180^\circ$  rotation within the plane that is analogous to a change in argument of perigee. The alternative to this maneuver is a sudden change in the direction of velocity near the Moon, and this not only requires a large  $\Delta v$  but is likely infeasible with a low-thrust engine. Differences in orbit geometry is one of several factors to consider when designing a transfer. The discrepancy in energy between the departure and arrival orbits must also be weighed. The Jacobi constant values of the four primary orbits examined in this study are plot-



(a) Configuration Space View

(b) Jacobi Constant vs. Orbital Period

Fig. 5.4. Orbits of interest for the Gateway spacecraft.

ted as a function of their period in Figure 5.4(b). This plot shows that the destination orbit with the largest difference in energy from the 9:2 NRHO is the DRO, closely followed by the low-amplitude halo orbit. Extended thrust maneuvers are required to overcome these disparities in energy along with the differences geometry.

Two types of transfer geometries, interior and exterior, are computed for each pair of departure and arrival orbits. While imprecise, these two categories help classify the various types of transfer geometries that arise when constructing transfers from the 9:2 NRHO to other orbits. Both of these transfer geometries can be desirable and results indicate that one type is not clearly superior to the other. The results demonstrate that an orbit chain and direct collocation approach is capable of computing both types of transfers. Following the development of optimal low-thrust transfers in the CR3BP, all transfers are validated in an ephemeris model and a subset of trajectories are subjected to missed thrust analysis. Overall, despite the varied energies and geometries of the target orbits, an orbit chain and direct collocation approach is capable of generating optimal low-thrust transfers for the Gateway spacecraft that withstand subsequent ephemeris validation.

Table 5.1.

Jacobi constant, period, and initial state values for departure and destination orbits used to compute Gateway transfers. All quantities are presented in nondimensional units.

	9:2 NRHO	DRO	Low-Amplitude Halo Orbit	Northern NRHO
Jacobi Constant	3.0466	2.9281	3.1518	3.0004
Period	1.5091	3.2181	3.4150	1.8064
$x$	1.0219	0.8051	1.1808	0.9253
$y$	-7.0043E-04	3.5921E-05	-2.2127E-05	-5.2460E-07
$z$	-0.1820	0	8.2714E-03	0.2191
$\dot{x}$	-8.9630E-04	5.0407E-05	-2.1395E-05	-8.3998E-07
$\dot{y}$	-0.1029	0.5202	-0.1563	0.1210
$\dot{z}$	3.4282E-03	0	-2.6562E-06	2.0272E-06

### 5.3.1 9:2 NRHO to DRO Transfers

Low-thrust transfers from an NRHO to a DRO have been a focus of study since the inception of the Gateway project. The highly stable DRO family offers a range of attractive staging orbit candidates for the Gateway spacecraft or other assets destined for lunar orbit. The DRO in this investigation has a radius from the Moon of approximately 70,000 km at its  $x$ -axis crossings, hence it is denoted the 70K DRO. This particular DRO was a potential destination orbit for the Asteroid Redirect Mission (ARM), and is examined here so that insights gained from the ARM analysis can benefit the Gateway mission.

Due to the low perilune altitude of the 9:2 NRHO, it is especially advantageous to include other orbits as intermediate links when constructing an orbit chain for an NRHO to DRO transfer. Without these intermediate links, the direct collocation

algorithm might converge upon solutions that pass through the surface of the Moon. The selection of orbit families that offer useful intermediate links is guided by an examination of geometry and energy, as discussed in Chapter 4. The family of 3:4 resonant orbits offers useful candidates for the assembly of orbit chains that yield exterior type transfers from the NRHO to the DRO. This planar family includes orbits that perform close flybys of the Moon and cross the path of the 70K DRO in the same direction of motion. A subset of orbits from the planar 3:4 resonant orbit family are displayed in Figure 5.5(a). Moreover, Figure 5.6(a) shows that members of

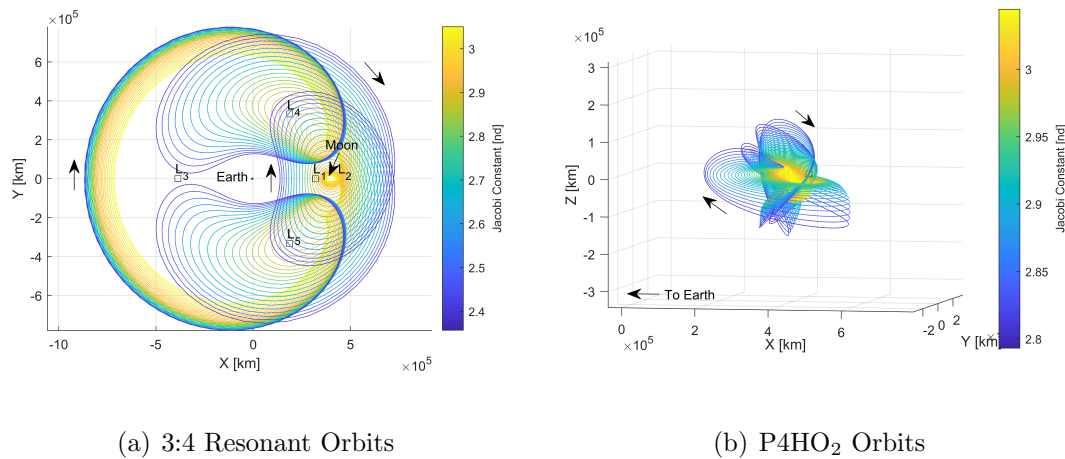


Fig. 5.5. Subsets of the orbit families from which intermediate links are selected for the construction of orbit chains that link the chosen NRHO and DRO.

the 3:4 resonant orbit family span the entire range of Jacobi constant values between the 9:2 NRHO and DRO. Another orbit family whose members cover nearly the same range of Jacobi constant values are the P4HO<sub>2</sub> orbits [120, 121]. The Jacobi constant values of a subset of this family are plotted as a function of orbital period in 5.6(b). The P4HO<sub>2</sub> orbit family, which bifurcates from the NRHOs, includes orbits near the 9:2 NRHO that possess similar out-of-plane geometry. As this family evolves, subsequent members exhibit increasingly planar motion as shown in Figure 5.5(b). An orbit chain that includes several members of this family can generate a low-thrust

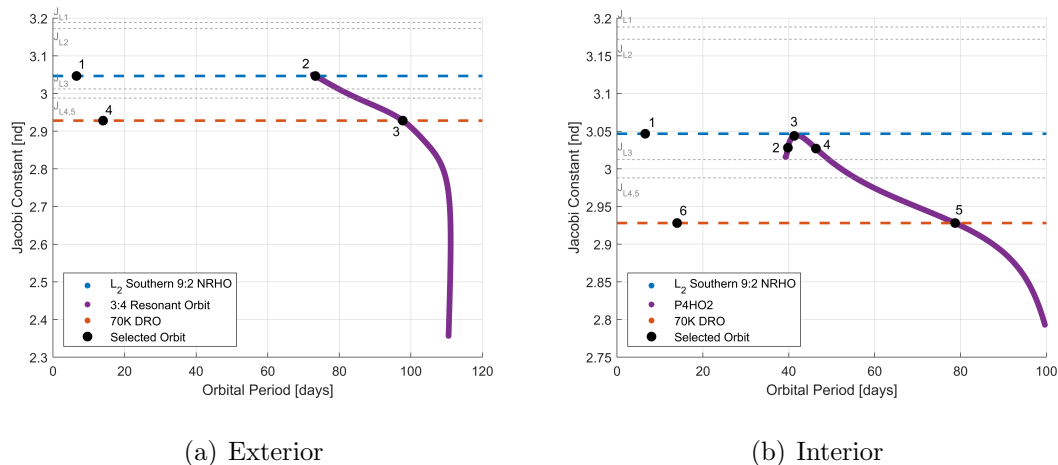


Fig. 5.6. Jacobi constant values as a function of orbital period for the orbits selected for the construction of orbit chains that link the chosen NRHO and DRO.

transfer that progresses through the P4HO<sub>2</sub> orbits, thus approaching the energy and planar geometry of the DRO. The two orbit families selected for the construction of NRHO to DRO transfers produce favorable results, but the flexibility of the orbit chain process means that these are only two of several potentially useful choices.

Following the identification of orbit families that offer useful intermediate links, specific members of these families are selected for use in orbit chains. The black markers in Figure 5.6 indicate the chosen orbits. For the exterior type NRHO to DRO transfer, 3:4 resonant orbits near the Jacobi constant value of the departure and arrival orbits are selected. The chosen orbits are plotted in position space in Figure 5.7 which shows that the resonant orbits are clipped so that only a section of each orbit is used. Clipping is performed to reduce the total time of flight of the initial guess and to produce more favorable connections between orbit chain links. The first resonant orbit is clipped such that it begins at approximately the same  $x$  value as the apoapse of the 9:2 NRHO. Although other points along the resonant orbit pass closer to the 9:2 NRHO, these points occur very close to the Moon, a region with high sensitivity, which make correcting the resulting discontinuity difficult. Experience

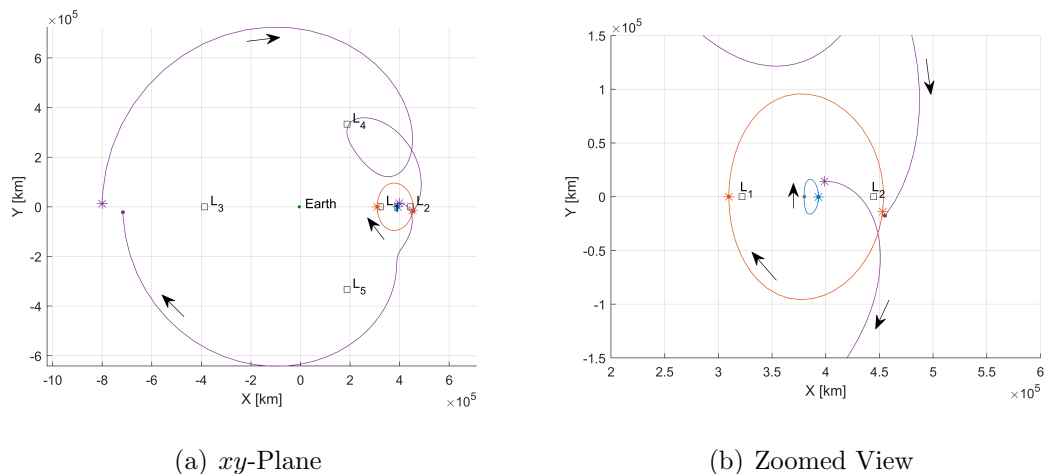


Fig. 5.7. Orbit chain initial guess for an NRHO to DRO exterior type transfer plotted in position space.

indicates that the likelihood of convergence is improved by clipping the resonant orbit at the location indicated in Figure 5.7(b). The first resonant orbit is included up until its  $x$ -axis crossing on the opposite side of the Earth. At this point, it is clipped and the second 3:4 resonant orbit employed in the orbit chain begins. Locating the discontinuity between resonant orbits at this position is beneficial because it is far from either primary and offers the direct collocation algorithm ample space for the insertion of thrust arcs to eliminate the discontinuity. The segment of the second 3:4 resonant orbit included in the orbit chain continues until it intersects the path of the 70K DRO. The subsequent link in the orbit chain is a section of the DRO that begins where the resonant orbit is clipped and continues to the initial point of the DRO on the opposite side of the Moon. The final link in the orbit chain is then a full revolution of the DRO that begins and ends at this same point. In total, the orbit chain assembled as an initial guess for the exterior NRHO to DRO transfer consists of five links. States associated with the beginning of each link along with parameter settings utilized to converge this and all following orbit chains are provided in Appendix B.

It is evident from the plots in Figure 5.6 that the selected orbit families consist of many additional members that could be included in the constructed orbit chains. While these additional orbits may reduce state and energy discontinuities between orbit chain links, they would also increase time of flight. Orbit chains with a greater number of intermediate links can also lead to successful NRHO to DRO transfers; however, these additional orbits are avoided here in an effort to keep the total time of flight from growing too large. The maximum additional time of flight added by each potential link is quickly assessed by examining the period of each orbit plotted in Figure 5.6. Of course, additional time of flight is incurred if multiple revolutions are stacked on a chosen link. Time of flight can also be reduced if the selected orbit is clipped so that only a section of it is employed in the orbit chain.

After an orbit chain is assembled, it is passed to the direct collocation algorithm for convergence. The process of transitioning from the discontinuous orbit chain to an optimal low-thrust transfer that employs the desired engine parameters is detailed in Figure 5.2. While the steps remain the same for every transfer presented here, this procedure can be straightforward or arduous depending on the characteristics of the desired transfer. In general, it is easier to compute the exterior type transfers because they involve less motion in the sensitive region near the Moon. This benefit is seen in the exterior NRHO to DRO transfer, whose final locally optimal result is displayed in Figure 5.8. While not evident in Figure 5.7, the initial and final links of this orbit chain include multiple revolutions of each orbit, three of the NRHO and four of the DRO. These additional revolutions are critical for achieving convergence because the extra time of flight they contribute provides the time necessary for the Gateway spacecraft to depart the NRHO and arrive at the DRO. Figure 5.8(b) illustrates how the stacked revolutions on the NRHO and DRO are “unspooled” by the direct collocation algorithm to create a continuous low-thrust transfer. The transfer displayed in Figure 5.8 requires 399 kg ( $\Delta v = 234$  m/s) of propellant and a total time of flight of 164 days. The key parameters for this, and all subsequent Gateway transfers computed in the CR3BP, are summarized in Table 5.2.

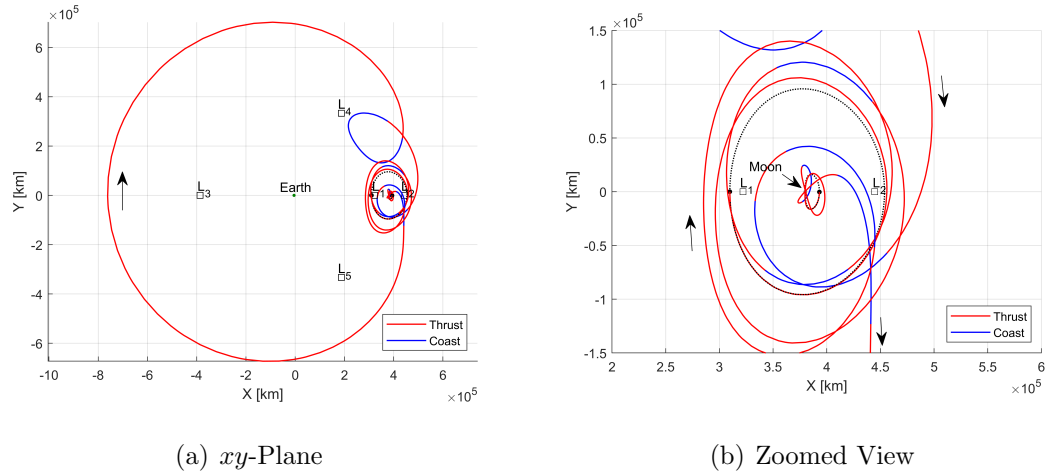


Fig. 5.8. Optimal exterior type transfer from an NRHO to a DRO, computed in the CR3BP and plotted in position space.

An orbit chain composed of members of the  $P4HO_2$  family is employed to compute an interior type NRHO to DRO transfer. Multiple members of the  $P4HO_2$  family must be included in the orbit chain to ease the required plane change and to allow adequate time for the transfer to be completed. A half revolution of the first  $P4HO_2$  orbit included in the orbit chain is employed to connect the 9:2 NRHO to the other  $P4HO_2$  orbits. This half revolution begins near the 9:2 NRHO and ends at the purple dot marker shown in Figure 5.9(b). The next  $P4HO_2$  orbit included in the chain begins and ends at a point near the end of the previous link, and is indicated by a purple asterisk in Figure 5.9(b). The connection points of the remaining  $P4HO_2$  orbits in the chain are placed at the same location on each orbit, and are also marked by purple asterisks. Positioning the discontinuities between links at this location on each  $P4HO_2$  orbit is advantageous because it is one of the farthest excursions from the Moon for this orbit geometry. Thus, the sensitivity associated with correcting the discontinuities between links is reduced. The connection point on the DRO, the final link in the orbit chain, is placed at the location on the orbit that is closest to the end of the previous link, that is, at the  $x$ -axis crossing on the right side of

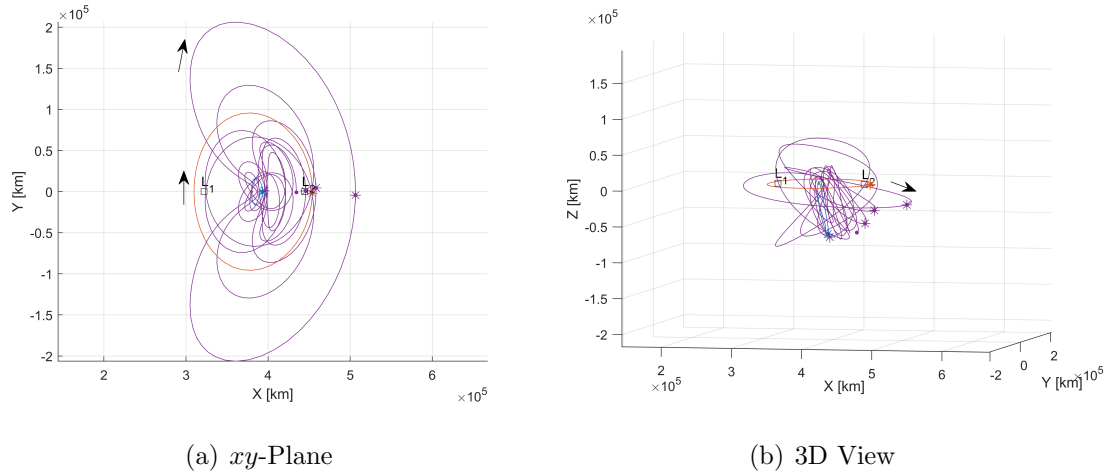


Fig. 5.9. Orbit chain initial guess for an NRHO to DRO interior type transfer plotted in position space.

the Moon in Figure 5.9. The intermediate P4HO<sub>2</sub> selected for inclusion in the orbit chain possesses Jacobi constant values between those of the initial and final orbits, as shown in Figure 5.6(b). However, the intermediate orbits here are not selected to have a strictly monotonic energy trend because doing so would result in larger state space discontinuities. Altogether, the orbit chain assembled as an initial guess for the interior NRHO to DRO transfer consists of six links.

The six link orbit chain constructed to compute an interior type NRHO to DRO transfer is delivered to the direct collocation algorithm, which ultimately generates a continuous optimal low-thrust transfer. Figure 5.10 displays the optimal solution produced by the process described in Section 5.2.1. While the resulting transfer is chaotic in appearance, it clearly retains elements of the geometry present in the original orbit chain. These geometric similarities are most evident in the farthest excursions from the Moon, for example, the two lobes of the largest P4HO<sub>2</sub> in Figure 5.9(a) are present, though modified, in Figure 5.10(a). This same commonality is also apparent in the three-dimensional views of the orbit chain and final transfer, which show similarities in the out-of-plane geometry. Once again, additional revolutions are

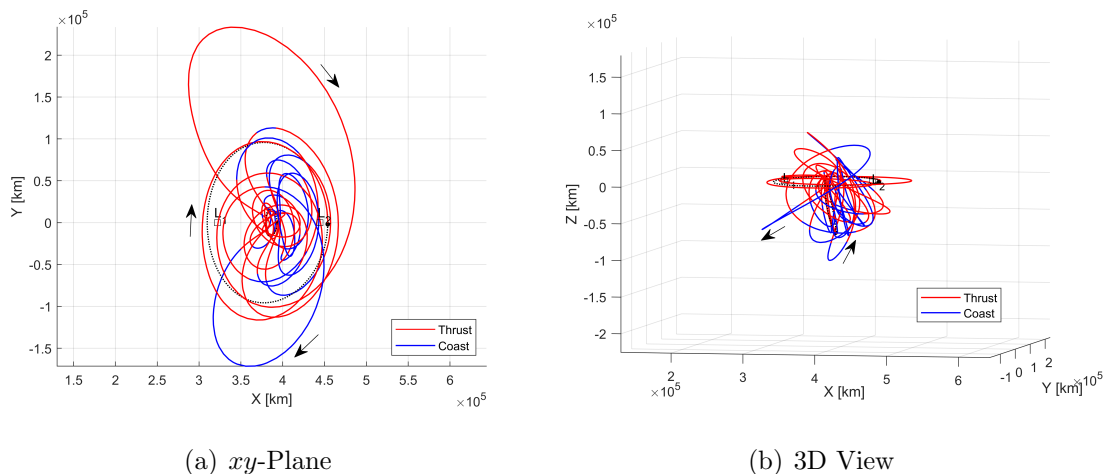


Fig. 5.10. Optimal interior type transfer from an NRHO to a DRO, computed in the CR3BP and plotted in position space.

stacked on the initial and final links of the orbit chain to aid convergence; however, in this case, only two revolutions are included for each link. The interior type NRHO to DRO transfer requires 402 kg ( $\Delta v = 236$  m/s) of propellant and a total time of flight of 227 days. While the time of flight of the interior NRHO to DRO transfer is over two months longer than the exterior version, the total propellant consumption is nearly the same. Due to the extended coast arcs in the interior NRHO to DRO transfer, it is possible that the time of flight of this result could be decreased. These two results demonstrate that practical transfers from the 9:2 NRHO to a DRO can be achieved for both exterior and interior type geometries. Further study is required to assess whether one of these geometry types has favorable properties not considered here, such as eclipse avoidance or an unimpeded line-of-sight for communications.

The geometry, and, to an extent, the propellant consumption of both types of NRHO to DRO transfer remain consistent when they are transitioned to an  $N$ -body ephemeris model that includes the Earth, Moon, and Sun. No specific departure or arrival dates are currently required for these transfers. Thus, in an effort to ease the transition to the ephemeris model, the initial epoch of each transfer is selected

by identifying the date that yields the lowest average velocity discontinuity between segments when the CR3BP result is first imported to the ephemeris model. The month of June 2024 is chosen, and dates within this month are scanned to identify the initial epoch that meets the desired selection criteria. The initial epochs employed for each ephemeris transfer are presented in Table 5.3 which also summarizes the Gateway ephemeris transfer results. Plots in the  $xy$ -plane of the exterior and interior NRHO to DRO transfers transitioned to the ephemeris model are presented in Figure 5.11. Comparison of these configuration space plots with the CR3BP results displayed in

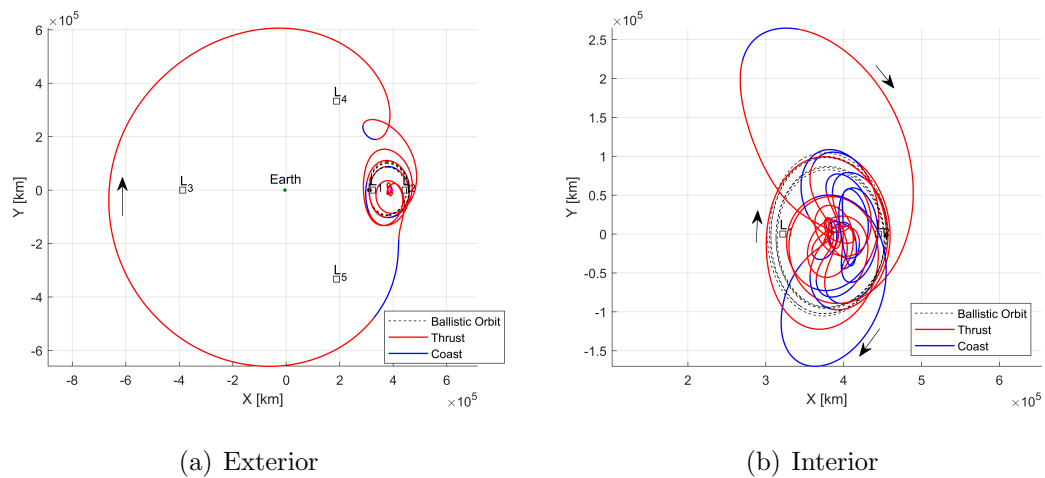


Fig. 5.11. Optimal exterior and interior type transfers from an NRHO to a DRO, computed in an ephemeris model and plotted in the  $xy$ -plane.

Figures 5.8(a) and 5.10(a) reveals the consistency between the results of the two models.

Disparities between the CR3BP and ephemeris results are more apparent when the transfers' propellant consumptions computed in the two models are compared. While the interior type transfer requires nearly the same propellant mass, the exterior transfer consumes approximately 100 kg more propellant. The reason for such a large difference between the CR3BP and ephemeris results is unclear, but may be largely due to the selected initial epoch. The initial epoch selected for a transfer in the

ephemeris model can significantly influence the geometry and propellant consumption of the computed result. The relative positions of the included point masses may work in favor of the desired transfer for some epochs, thus reducing the propellant cost, while other epochs may hinder the transfer. Thus, a more complete picture of the performance of these transfers in an ephemeris model can only be obtained by computing them for a range of initial epochs. A single ephemeris solution for each transfer type is presented here because the goal is merely to demonstrate that the computed solutions, despite their complexity, are indeed viable in an ephemeris model that includes all of the most relevant gravitational bodies. The results offered in Figure 5.11 validate the computed exterior and interior type transfers in the ephemeris model, thus indicating that the orbit chain and direct collocation approach utilized to compute these transfers for the Gateway spacecraft is a practical framework.

### 5.3.2 9:2 NRHO to Low-Amplitude Halo Orbit Transfers

A low-amplitude  $L_2$  halo orbit is of interest to the Gateway project not as a final destination, but as a waypoint that offers access to other locations in the Earth-Moon system and beyond. The stable and unstable invariant manifolds of a low-amplitude halo orbit provide paths that transit to orbits about  $L_1$ , include close approaches of Earth, or depart the Earth-Moon system. If not employed by Gateway itself, these low-energy pathways could be utilized by other spacecraft departing from or arriving at Gateway. Therefore, transfers of the Gateway to a low-amplitude halo orbit where these departures or rendezvous may take place are explored in this investigation. Low-amplitude halo orbits are not formally defined in literature, but this category generally includes halo orbits whose maximum excursion in the  $z$  direction is small compared to other members of the halo family. The particular halo orbit selected for this investigation belongs to the northern  $L_2$  halo family, and possesses a maximum  $+z$  amplitude of 3182 km. Many other similar orbits in the northern and southern

$L_2$  halo families could have been selected and would likely yield results quite similar to those shown here.

In contrast to the DRO employed in the previous section, the selected low-amplitude halo orbits possess a Jacobi constant value higher than that of the 9:2 NRHO. Therefore, other orbit families with different ranges of Jacobi constant are examined for useful intermediate orbit candidates. The most obvious of these families is the  $L_2$  halo orbits because this family includes both the initial and final orbits for the present transfer. A subset of the members of the  $L_2$  halo family are displayed in Figure 5.12. These orbits are members of the southern part of this family, i.e., those members whose maximum excursion from the  $xy$ -plane is in the  $-z$  direction. The destination halo orbit is in the northern part of the  $L_2$  halo family, but, due to its low-amplitude, it is very near the southern  $L_2$  halo orbits. The  $L_2$  halo orbits also bridge the gap in

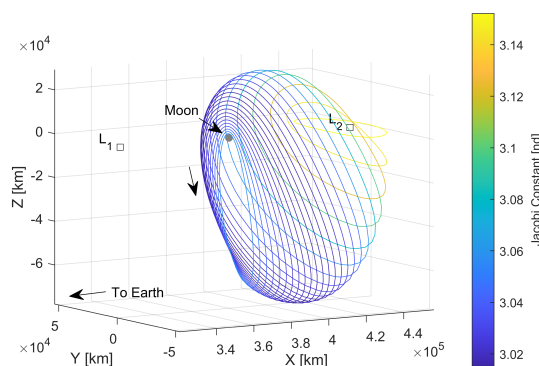


Fig. 5.12. A subset of the southern members of the  $L_2$  Halo orbit family colored according to Jacobi constant value.

energy between the initial and final orbit as illustrated in Figure 5.13(a). Members of this family of orbits are selected to construct an orbit chain that leads to an interior type transfer from the 9:2 NRHO to the low-amplitude halo orbit.

It is more challenging to identify intermediate orbits that offer useful orbit chain links for an exterior type transfer from the 9:2 NRHO to a low-amplitude halo orbit.

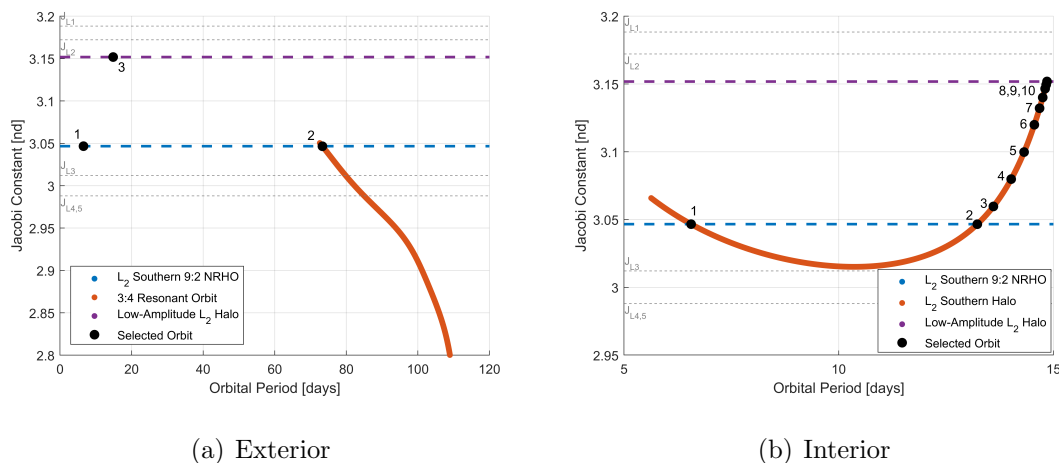


Fig. 5.13. Jacobi constant values as a function of orbital period for the orbits employed to construct orbit chains for the exterior and interior NRHO to low-amplitude  $L_2$  halo transfers.

Resonant orbits are employed to construct exterior transfers for the other destination orbits in this investigation; unfortunately, the resonant orbits with geometry useful for the construction of this type of transfer do not possess Jacobi constant values at the same level as the low-amplitude halo orbit. Therefore, an orbit chain that includes resonant orbits which span the gap in energy between the departure and arrival orbits cannot be constructed. However, the previous transfer scenario demonstrated the existence of a 3:4 resonant orbit whose Jacobi constant value is equal to that of the 9:2 NRHO and which offers geometries that facilitate an exterior type transfer. Therefore, the family of 3:4 resonant orbits is employed once again to provide intermediate links in an orbit chain connecting the 9:2 NRHO and a low-amplitude halo orbit.

A single member of the family of 3:4 resonant orbits is utilized to construct an orbit chain that yields an exterior transfer from the 9:2 NRHO to the low-amplitude halo orbit. A 3:4 resonant orbit at nearly the same energy level as the 9:2 NRHO is selected, and the Jacobi constant value of this orbit in relation to the initial and final orbits is displayed in Figure 5.13(b). The selected 3:4 resonant orbit is included

as two distinct links in the assembled orbit chain, clipped at different locations. The first use of the 3:4 resonant orbit is clipped near the Moon around the same  $x$  value as the apoapse of the 9:2 NRHO. This point is indicated with a red asterisk in Figure 5.14(b). This initial resonant orbit link continues until it terminates at its closest

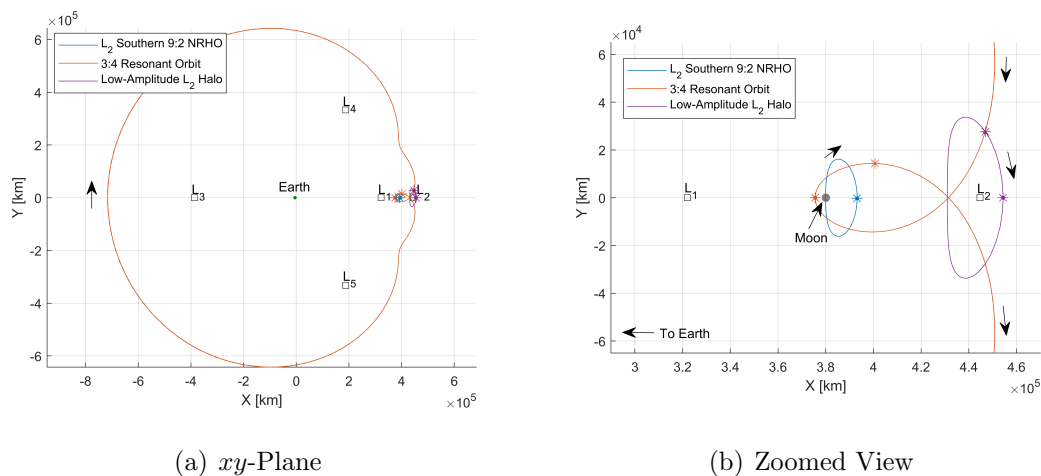


Fig. 5.14. Orbit chain initial guess for an NRHO to low-amplitude  $L_2$  halo exterior transfer plotted in position space.

approach to the Moon where  $y = 0$ . This terminus is also the beginning of the second resonant orbit link in the orbit chain and is marked with another red asterisk in Figure 5.14(b). The second resonant orbit includes an additional transit around the Earth before it is clipped where it appears to cross the path of the low-amplitude halo orbit as viewed in the  $xy$ -plane. This crossing is marked by a purple asterisk in Figure 5.14(b). A partial revolution of the low-amplitude halo orbit is included as the next link in the orbit chain followed by a full revolution of the halo orbit which constitutes the final link in the assembled chain. In its entirety, the constructed orbit chain includes two transits around the Earth-Moon system that follow the exact same 3:4 resonant orbit, as displayed in Figure 5.14(a). Alternate orbit chain assemblies for this exterior transfer could include members of the  $L_2$  Lyapunov family or the stable invariant manifolds of the destination  $L_2$  halo orbit. These additional orbit

chain links could reduce the discontinuities in geometry and energy present in the orbit chain offered in Figure 5.14.

With the selected 3:4 resonant orbit as the sole intermediate link, the orbit chain assembled to generate an exterior transfer from the 9:2 NRHO to the low-amplitude halo is passed to the direct collocation algorithm. Three revolutions of the initial NRHO and four revolutions of the final halo orbit are stacked to aid convergence via the provision of additional time of flight. This orbit chain is successfully converged, producing a low-thrust transfer that executes the required plane change gradually over the course of the two transits about the Earth-Moon system, as shown in Figure 5.15(a). The stacked revolutions of the initial and final orbits are distributed

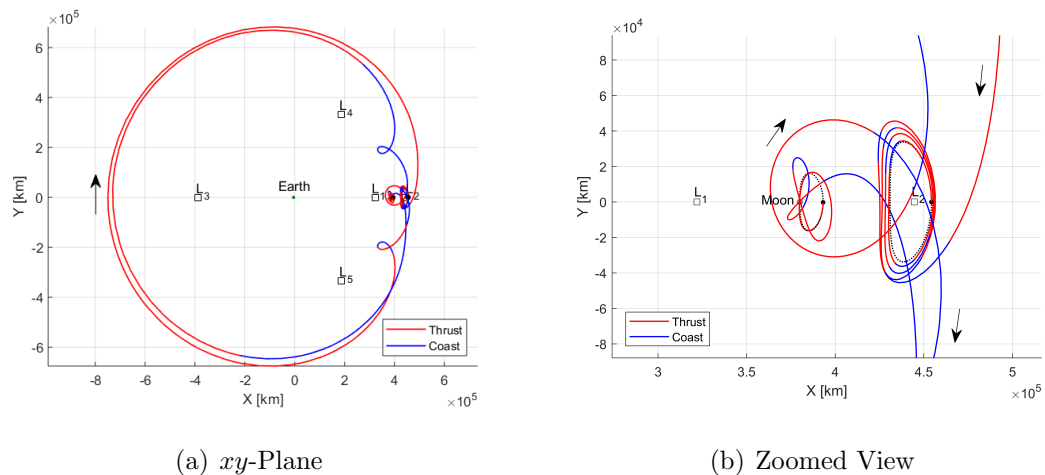


Fig. 5.15. Optimal exterior type transfer from an NRHO to a low-amplitude  $L_2$  halo, computed in the CR3BP and plotted in position space.

to facilitate departure and arrival, respectively, and Figure 5.15(b) highlights this behavior. The transfer displayed in Figure 5.15 requires 492 kg ( $\Delta v = 289$  m/s) of propellant and a total time of flight of 225 days, and these parameters are summarized in Table 5.2. As an alternative to the exterior geometry, an interior transfer from the 9:2 NRHO to the low-amplitude halo orbit is computed using an orbit chain that includes multiple members of the southern part of the  $L_2$  halo family. Figure

5.13(b) illustrates that when plotted as a function of orbital period, the Jacobi constant values of this family do not follow a monotonic trend. The Jacobi constant value of the destination halo orbit is higher than that of the 9:2 NRHO; thus, to encourage a monotonic energy profile in the optimal result, the assembled orbit chain should only include intermediate links with Jacobi constants at or above that of the NRHO. However, the southern  $L_2$  halo orbits closest to the NRHO in position space possess Jacobi constant values less than that of the NRHO. To avoid this decrease in energy, the first intermediate halo orbit included in the orbit chain is selected to possess approximately the same energy, but a significantly larger period as the initial NRHO. This difference in period is displayed in Figure 5.13(b) and the resulting gap in position space between the first and second members of the orbit chain is apparent in Figure 5.16(a). After this initial jump, the remaining orbits in the chain are more similar in energy and geometry. The configuration space plot in Figure 5.16 shows

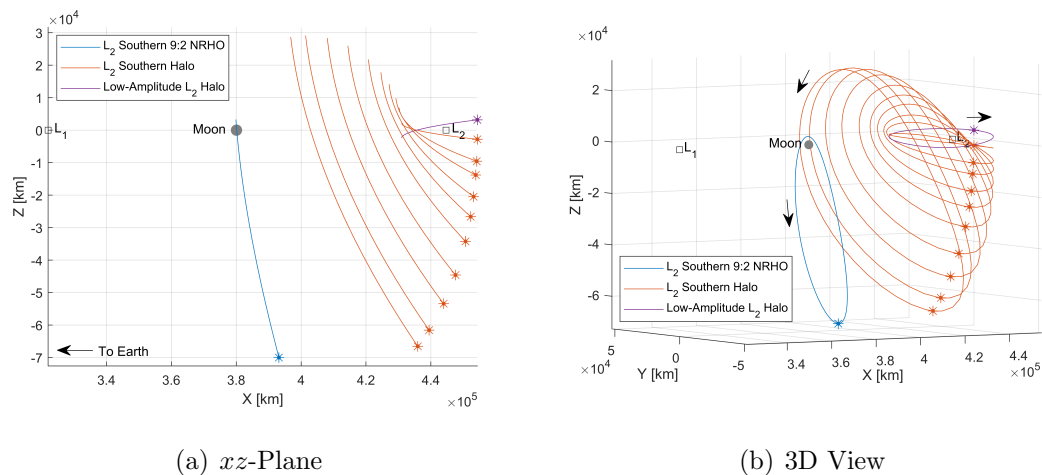


Fig. 5.16. Orbit chain initial guess for an NRHO to low-amplitude  $L_2$  halo interior type transfer plotted in position space.

that, as they approach the  $L_2$  libration point, the southern halo orbits became increasingly planar. Therefore, a transfer from the very out of plane 9:2 NRHO to the

low-amplitude halo orbit is accomplished simply by transferring between successive members of the  $L_2$  halo family.

The orbit chain constructed from members of the southern  $L_2$  halo family is employed to compute an interior transfer from the 9:2 NRHO to the low-amplitude halo orbit. The resulting transfer, displayed in Figure 5.17, exhibits how the original orbit chain is modified to obtain an optimal low-thrust transfer. The assembled orbit

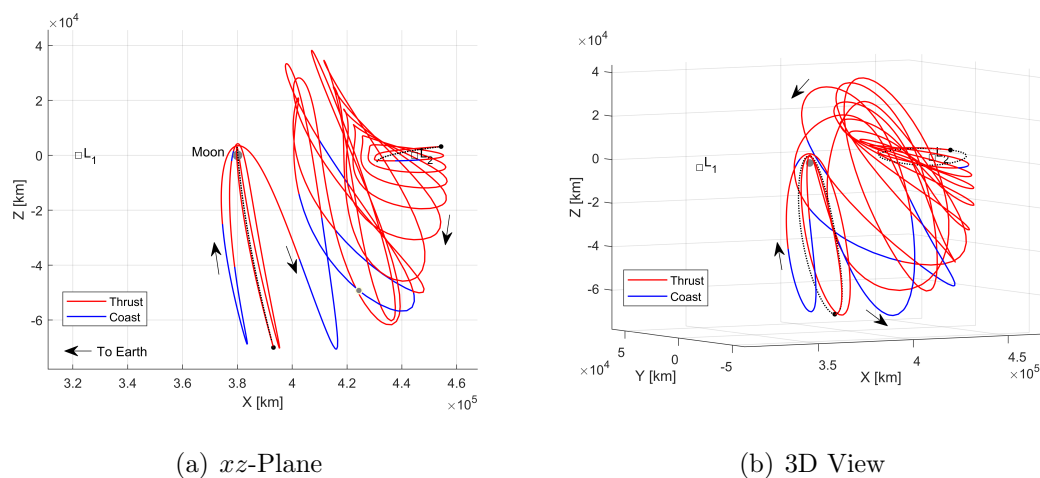


Fig. 5.17. Optimal interior type transfer from an NRHO to a low-amplitude  $L_2$  halo, computed in the CR3BP and plotted in position space.

chain includes three revolutions of the 9:2 NRHO and a single revolution for all other links. These stacked revolutions are distributed by the direct collocation algorithm to create a continuous transfer that spans the gap between the first and second halo orbits. The distributed revolutions produce a trajectory that briefly passes to the  $L_1$  side of the Moon before a close lunar flyby that enables the spacecraft to transit the gap in position space between the first and second orbits in the chain. The initial departure from the 9:2 NRHO exhibits geometry that is similar to orbits within the butterfly family [55, 121]. Experience indicates that similar patterns occur for other transfers which begin in the 9:2 NRHO. Indeed, another instance of this behavior is shown in Section 6.3.3. The remaining halo orbits included in the chain are modified

such that they form a quasi-periodic like structure. This structure, which consists primarily of thrust arcs, enables a gradual plane change from the NRHO to the final halo orbit. In total, the transfer displayed in Figure 5.17 requires 515 kg ( $\Delta v = 303$  m/s) of propellant and a total time of flight of 178 days.

With only one solution for each transfer type, it is not possible to state whether either the exterior or interior transfer from the NRHO to the low-amplitude halo orbit is superior, especially because this assessment is highly situation dependent. The duration of the interior transfer is roughly 1.5 months less than that of the exterior transfer; however, it necessitates about 20 kg more propellant. The higher propellant cost may be worth the shorter time of flight and a geometry that remains near the Moon, but this judgement must be made using mission requirements that are not presently available. Overall, these results indicate that both transfer types are viable options for transiting between the desired orbits. Moreover, it is likely that very similar geometry and performance would be obtained for most other low-amplitude  $L_2$  halo orbits.

Both types of transfer, exterior and interior, are successfully validated in an ephemeris model that includes the Earth, Moon, and Sun. The geometry and propellant consumption of the ephemeris transfers are similar to those of the CR3BP results, as evidenced by the configuration space plots displayed in Figure 5.18 and the performance characteristics summarized in Table 5.3. Once again the initial epochs for these ephemeris transfers are selected to reduce velocity discontinuities in the initial guess. For the chosen initial epochs, the exterior type transfer requires nearly 15 kg more propellant, while the interior transfer demands slightly less than the corresponding CR3BP results. These discrepancies are within the expected range of variation when transitioning low-thrust trajectories to an ephemeris model. Thus, the ephemeris results displayed in Figure 5.18 further validate the efficacy of the orbit chain and direct collocation approach to computing low-thrust transfers for the Gateway mission.

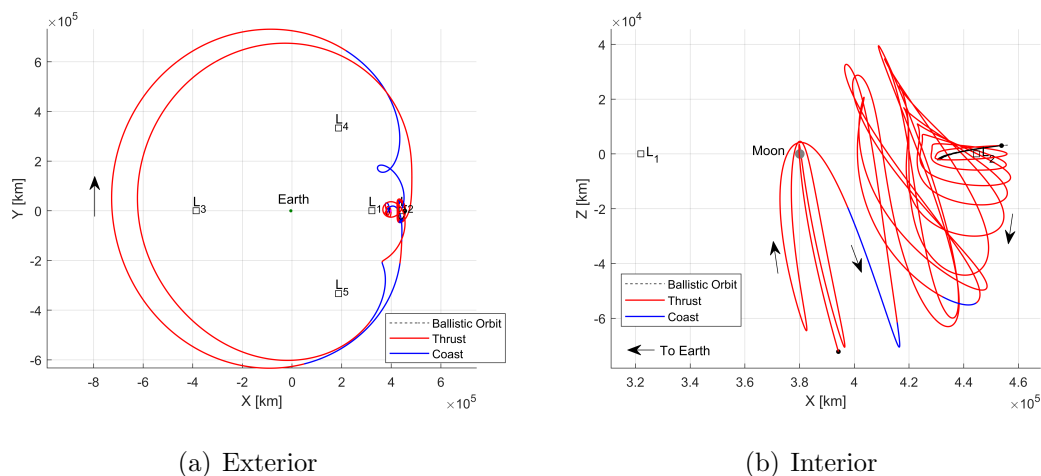


Fig. 5.18. Optimal exterior and interior type transfers from an NRHO to a low-amplitude halo orbit, computed in an ephemeris model.

### 5.3.3 9:2 NRHO to Northern $L_1$ NRHO Transfers

An NRHO within the northern members of the  $L_1$  halo family is another destination of interest for the Gateway mission. This orbit offers similar benefits to the 9:2 southern NRHO, but is oriented such that its apoapse is located over the northern pole of the Moon, as displayed in Figure 5.19(a). This configuration is useful if line-of-sight of the Moon's northern hemisphere from the Gateway is required for an extended period of time by human or robotic operations in this region. Thus, transfers from the nominal 9:2 NRHO to a northern NRHO are examined here.

The Jacobi constant value of the selected northern NRHO is less than that of the 9:2 NRHO, but out of the three destination orbits examined, it is the most similar in value to this orbit. This nearness in energy is countered by a large difference in configuration space. As noted in Section 5.3, a large plane change is required to efficiently transition from the southern to the northern NRHO. Two means of executing this plane change are examined, and these are facilitated with the use of several types of intermediate orbits. Like the transfer from the 9:2 NRHO to the low-amplitude halo orbit, the interior type transfer to the northern NRHO will utilize

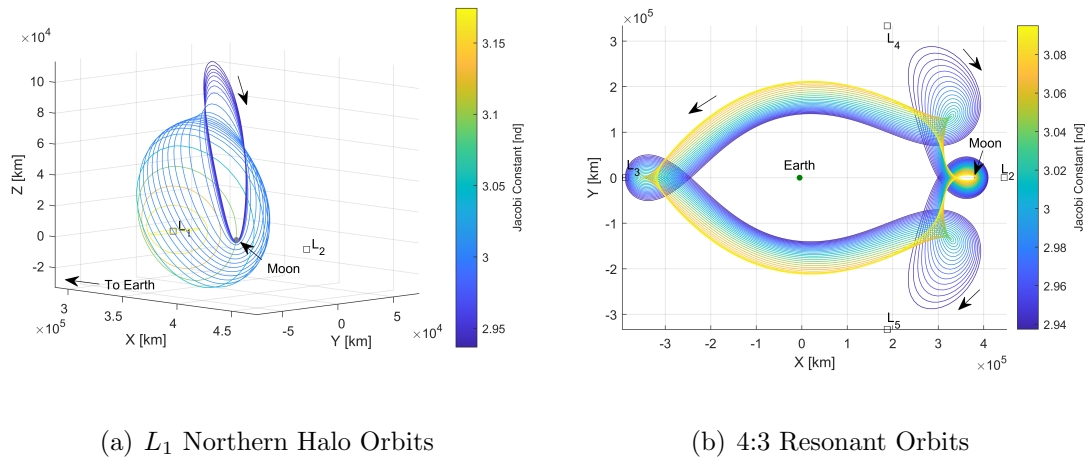


Fig. 5.19. Orbit families from which intermediate links are selected for the construction of orbit chains used to compute exterior and interior NRHO to an  $L_1$  northern NRHO transfers.

multiple members of the  $L_1$  and  $L_2$  families of halo orbits to transition along these families towards the destination orbit. The exterior type transfer will instead utilize another type of resonant orbit family in addition to the already examined 3:4 resonant orbits to aid in transitioning motion from the vicinity of the  $L_2$  libration point to the  $L_1$  libration point. The new family of orbits examined in this section are the 4:3 resonant orbits, displayed in Figure 5.19(b). This family of orbits exhibits motion near the  $L_1$  libration point in the same direction of motion as the lower amplitude members of the  $L_1$  halo family. By combining a member of the 4:3 resonant orbit family with members of the 3:4 resonant orbit family in an orbit chain, a useful initial guess for the transfer from a southern to a northern NRHO can be obtained.

The orbit chain employed to compute the exterior transfer from the 9:2 NRHO to the selected northern NRHO incorporates clipped sections of two types of resonant orbit. This initial guess is inspired by the results of McCarty, Burke, and McGuire [34]. The same transfer scenario is examined by these authors and their result is similar in geometry to the orbit chain initial guess assembled here, and thus similar to the

resulting transfer as well. Figure 5.20(a) illustrates that the two selected resonant orbit families span the entire range of Jacobi constant values between the initial and final orbits of this transfer. The two orbit chain links that immediately follow the

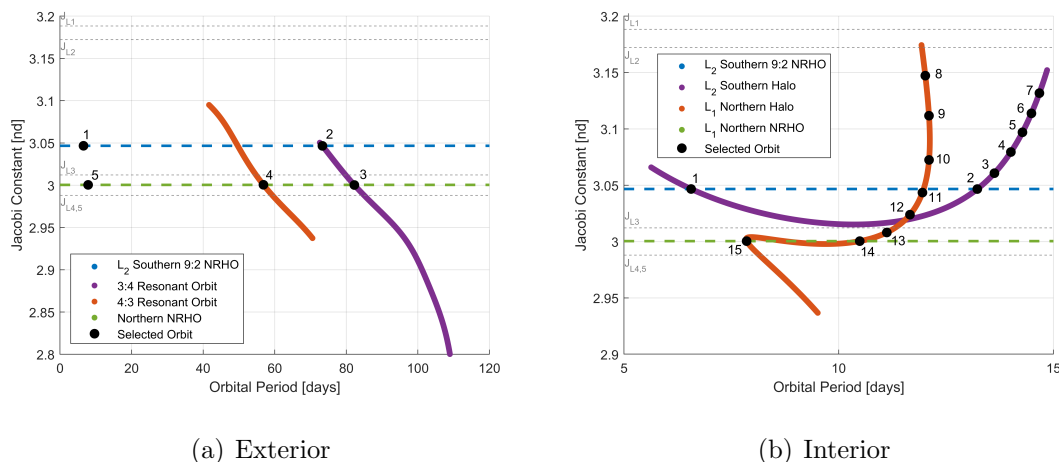


Fig. 5.20. Jacobi constant values as a function of orbital period for the orbits employed to construct orbit chains for the exterior and interior NRHO to low-amplitude  $L_2$  halo transfers.

initial orbit are members of the 3:4 resonant orbit family; the two members selected from this family possess Jacobi constant values similar to those of the departure and destination orbits, respectively. Next, a member of the 4:3 resonant orbit family is chosen that has nearly the same Jacobi constant value as the final northern NRHO. The complete orbit chain assembled for the exterior transfer from the southern to the northern NRHO is displayed in Figure 5.21. The two 3:4 resonant orbits in the orbit chain are clipped so that they connect near  $y = 0$  on the  $-x$  side of the Earth; recall, this same approach was taken for the exterior NRHO to DRO transfer. Furthermore, as in the previous two transfers, the 3:4 resonant orbits are clipped so that they do not begin or end at their closest approach to the Moon, but rather at some desired distance from the Moon. The second 3:4 resonant orbit employed in the orbit chain is actually clipped such that it ends at one of its intersection points with the selected

4:3 resonant orbit, as seen in Figure 5.21(b). The entirety of the selected 4:3 resonant

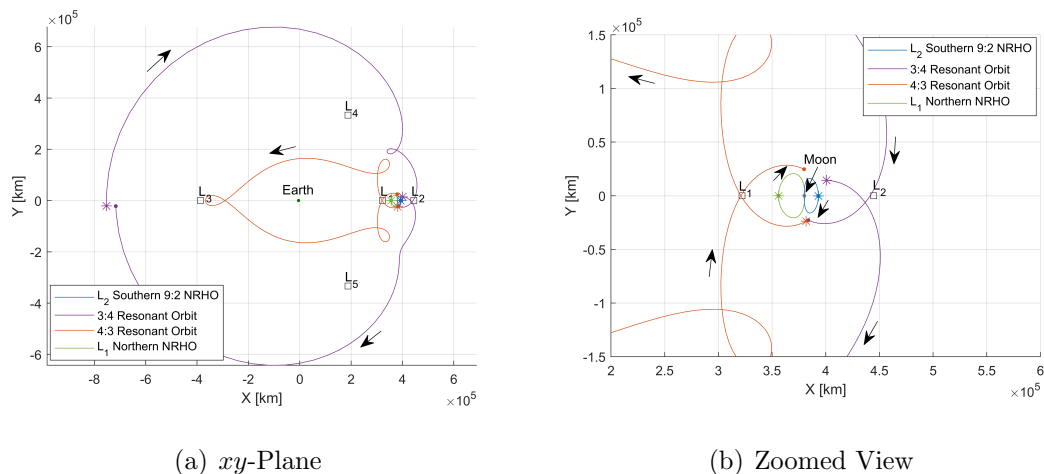


Fig. 5.21. Orbit chain initial guess for an NRHO to an  $L_1$  northern NRHO exterior type transfer plotted in position space.

orbit is then employed up until its next close approach of the Moon, at which point the orbit is clipped such that it ends near  $x_{Moon}$ , that is the location of the Moon on the  $x$ -axis. The complete orbit chain, displayed in Figure 5.22, offers a geometry that aids the transition from the southern to the northern NRHO and provides ample time in which to achieve this transfer.

The orbit chain constructed for the exterior transfer from the southern to the northern NRHO successfully guides the direct collocation algorithm to an optimal low-thrust solution. Figure 5.22 displays the low-thrust transfer obtained at the conclusion of the computation process outlined in Figure 5.2. The resulting transfer retains much of the same geometry as the orbit chain, indicating that this initial guess was useful for obtaining the final result. Three revolutions of the initial and final NRHOs are stacked in the initial guess, and single revolutions of all other orbit chain links are employed. The lengthy resonant orbit segments included in the orbit chain provide ample time for the desired transfer to be conducted and allow the required plane change to occur gradually during the transits around the Earth. The

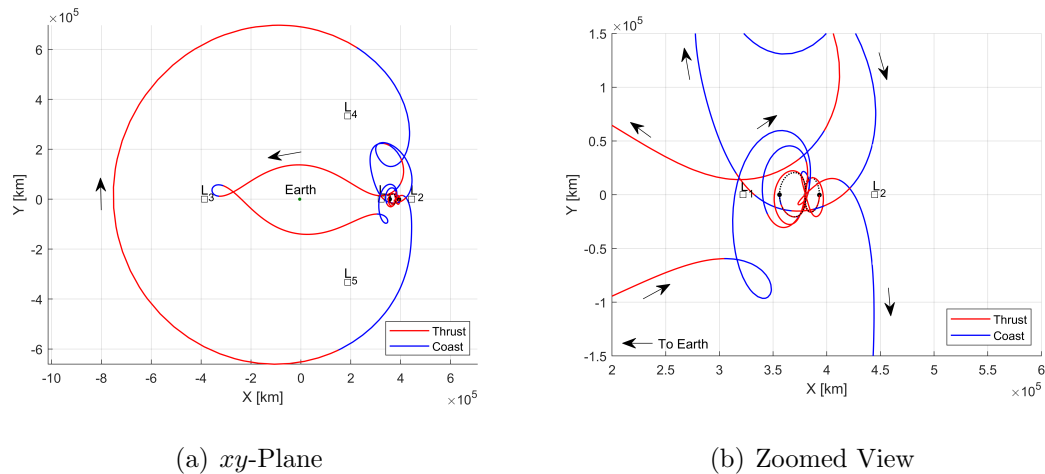


Fig. 5.22. Optimal exterior type transfer from an NRHO to an  $L_1$  northern NRHO, computed in the CR3BP and plotted in position space.

transfer displayed in Figure 5.22 requires 236 kg ( $\Delta v = 138$  m/s) of propellant and a total time of flight of 176 days.

A variety of orbit families are suitable for the construction of interior type transfers from the southern to northern NRHO; in this analysis a straightforward approach is employed that leverages numerous orbits from the  $L_1$  and  $L_2$  halo families. The concept of moving up or down a family of halo orbits to transfer from one member to another is exploited in Section 5.3.2 to obtain an interior transfer from the 9:2 NRHO to the low-amplitude halo. Here this idea is expanded to first move “up” the southern  $L_2$  halo family and then “up” the northern  $L_1$  halo family. The challenge with this approach is the large gap in state space between the final member of the southern  $L_2$  halo family and the initial member of the northern  $L_1$  halo family employed in the orbit chain. The work of Haapala and Howell [15] serves to fill this gap by highlighting the role invariant manifolds can play in offering low-cost transits between these types of orbits. Haapala and Howell present a transfer from a southern  $L_2$  halo orbit to a northern  $L_1$  halo orbit that utilizes the unstable and stable invariant manifolds of each orbit, respectively. These same two halo orbits are included in the orbit chain

constructed in this investigation, with the intent of biasing the resulting transfer to utilize the same invariant manifold structures observed by Haapala and Howell. Of course, the invariant manifold structures themselves could be included in the orbit chain; however, this step is avoided to determine whether a similar result can be obtained without the additional process of generating and selecting suitable invariant manifold paths.

With the first and last members of each halo orbit family to be included in the orbit chain selected, the task of choosing additional intermediate links to reduce the discontinuities between these orbits remains. Figure 5.20(b) shows that a relatively even spacing in Jacobi constant between successive intermediate links is used when selecting additional intermediate orbits from the  $L_1$  and  $L_2$  halo families. The exception to this rule occurs between the initial and final NRHOs and their adjacent links. In both cases a jump along the orbit family is made to avoid including intermediate links whose Jacobi constant values are below those of the initial or final orbits. These gaps between successive links are evident both in the parameter space plot displayed in Figure 5.20(b) and the plot of the orbit chain in configuration space in Figure 5.23. Figure 5.23(a) reveals that, unlike the other orbits included from the northern  $L_1$  halo family, the initial point on the first orbit used from this family is located at the lowest  $z$  excursion of the orbit. The connection point is shifted for this first orbit to reduce the state discontinuity between it and the final member of the southern  $L_2$  halo orbit family included in the chain. The discrepancy between the initial and subsequent members of the northern  $L_1$  halo family is mitigated by including an additional half revolution of the initial halo orbit that ends at the maximum  $z$  excursion of the orbit. This point is indicated with a red dot marker in Figure 5.23(a), and it is clearly the point on this orbit that is closest to the initial point of the next link in the chain. Overall, many members of the  $L_1$  and  $L_2$  halo orbit families are included in the orbit chain for the interior southern to northern NRHO transfer. The large number of orbits included helps reduce the state and energy discontinuities between

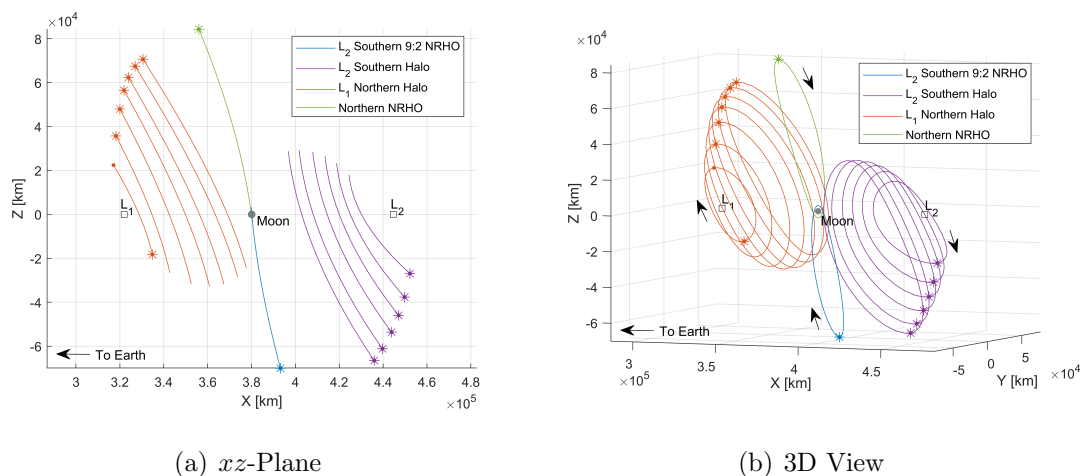


Fig. 5.23. Orbit chain initial guess for an NRHO to an  $L_1$  northern NRHO interior type transfer plotted in position space.

the initial and final orbits, though it also significantly increases the time of flight of the resulting transfer.

The orbit chain consisting solely of members of the  $L_1$  and  $L_2$  halo families leads to a successful interior type transfer from the 9:2 NRHO to a northern NRHO. The many halo orbits included in the initial guess are transformed by the direct collocation algorithm into complicated quasi-periodic like structures concentrated about the  $L_1$  and  $L_2$  libration points. These structures are apparent in Figure 5.24, which displays the computed low-thrust transfer. Transit from the  $L_1$  to the  $L_2$  region is accomplished in a single crossing of the  $xz$ -plane centered at the Moon. Though the resulting transfer does not utilize the same invariant manifold paths observed by Haapala and Howell, it is unclear whether any other such structures are leveraged instead. The  $xz$  plane view highlighted in Figure 5.24(a) reveals that the low-thrust transfer includes brief crossings from one “side” of the Moon to the other during departure or insertion from the initial and final NRHOs respectively. The same behavior is observed in the interior NRHO to low-amplitude halo orbit displayed in Figure 5.17. In total, the interior low-thrust transfer from the 9:2 NRHO to a northern NRHO requires 425 kg

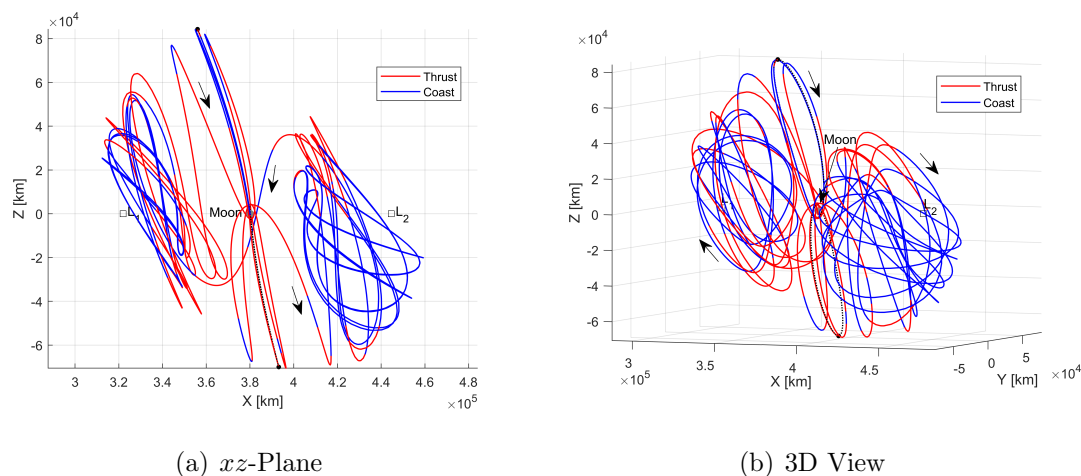


Fig. 5.24. Optimal interior type transfer from an NRHO to an  $L_1$  northern NRHO, computed in the CR3BP and plotted in position space.

of propellant ( $\Delta v = 250$  m/s) and a total time of flight of 355 days. The significant amount of coasting time indicates that it may be possible to remove some of the halo orbits included in the initial guess and still compute an optimal result, thereby reducing the protracted time of flight and possibly the propellant consumption.

The exterior and interior type transfers computed from the 9:2 NRHO to a northern NRHO are successfully validated in an ephemeris model that includes the Earth, Moon, and Sun. The geometry and propellant consumption of these transfers remains reasonably close to the CR3BP results. Figure 5.25 offers views of both ephemeris results. The most noticeable change in geometry is in the exterior type trajectory displayed in Figure 5.25(a). Aside from the slight difference in the orientation of the second transit around the Earth, there are few perceptible differences. The initial epochs for both transfers are selected to reduce velocity discontinuities in the initial guess, and are provided in Table 5.4. For the selected epochs, the propellant consumption of both transfers is less than their CR3BP counterparts, but still within the expected range of variance. Altogether, the ephemeris results displayed in Figure 5.25 and summarized in Table 5.3 validate the ability of the orbit chain and direct

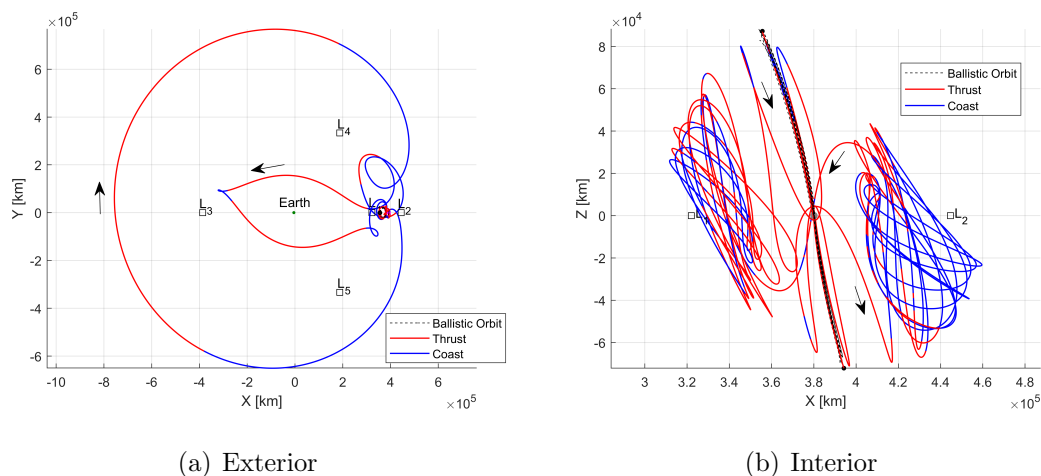


Fig. 5.25. Optimal exterior and interior type transfers from the 9:2 NRHO to a northern  $L_1$  NRHO, computed in an ephemeris model.

collocation approach to generate practical trajectories from the 9:2 NRHO to other orbits of interest.

### 5.3.4 Summary of Transfers from the 9:2 NRHO

The results of this section demonstrate that transfers are available from the 9:2 NRHO to a variety of other orbits of interest in the lunar region. The performance of all six transfers computed in the CR3BP and ephemeris models are summarized here in Tables 5.2 and 5.3, respectively. Moreover, the initial epochs employed to compute the ephemeris transfers are provided in Table 5.4. The limited number of results computed for each trajectory type prevent broad generalizations about the superiority of any one transfer option. However, several observations and comparisons can be made.

First, utilizing an interior rather than an exterior type transfer from the 9:2 NRHO does not guarantee a shorter time of flight or reduced propellant consumption. For the transfers to the DRO and northern NRHO, the interior option requires a longer

Table 5.2.  
Summary of Gateway transfers computed in the CR3BP.

Transfer Type	Time of Flight [days]	$\Delta m$ [kg]	$\Delta v$ [m/s]
NRHO to DRO - Exterior	163.91	399.04	234.27
NRHO to DRO - Interior	227.46	401.56	235.76
NRHO to Low-Amp. Halo - Exterior	225.24	492.07	289.24
NRHO to Low-Amp. Halo - Interior	178.17	515.04	302.83
NRHO to North NRHO - Exterior	175.92	235.84	138.17
NRHO to North NRHO - Interior	355.33	425.07	249.64

time of flight. Moreover, the propellant consumption of the interior and exterior transfers are comparable for the transfers to the DRO and low-amplitude halo, and significantly more propellant consumption is demanded by the interior transfer to the northern NRHO. Both time of flight and propellant consumption are highly dependent on the initial guess, and it is possible that different results could be obtained if further experimentation with suitable orbit chains were conducted for each transfer scenario.

The construction of every orbit chain involves a trade-off between state discontinuities and time of flight. Intermediate orbits are included in an orbit chain to reduce state discontinuities between subsequent links; however, the addition of these links also increases the time of flight. Too few links in an orbit chain may hinder or even prevent convergence, while too many could lead to a large optimization problem and an overly long low-thrust transfer. Striking a proper balance between these two factors can be challenging, and it is likely that the time of flight of the transfers presented in this section could be reduced with further experimentation. Most notably, while the interior transfer to the northern NRHO includes many intermediate links, it may be possible to converge a similar transfer with fewer intermediate orbits and shorten the transfer duration.

Table 5.3.  
Summary of Gateway transfers computed in an ephemeris model including the Earth, Moon, and Sun.

Transfer Type	Time of Flight [days]	$\Delta m$ [kg]	$\Delta v$ [m/s]
NRHO to DRO - Exterior	163.91	501.39	294.75
NRHO to DRO - Interior	227.46	404.25	237.35
NRHO to Low-Amp. Halo - Exterior	225.24	505.69	297.30
NRHO to Low-Amp. Halo - Interior	178.17	513.84	302.12
NRHO to North NRHO - Exterior	175.92	210.35	123.19
NRHO to North NRHO - Interior	355.33	412.27	242.08

Additional trial and error with the orbit chains assembled in this section could also lead to orbit chains with reduced state discontinuities that are more easily converged to optimal solutions. For example, paths on the invariant manifolds of the low-amplitude orbit could be leveraged as intermediate links in an orbit chain constructed to facilitate a transfer to this orbit. The invariant manifolds of intermediate orbits utilized in orbit chains assembled for other destination orbits could also prove useful. An orbit chain with reduced state discontinuities will typically converge with fewer iterations and less computational time, and may permit the reduction or even elimination of the continuation process employed to obtain Gateway transfers with the correct low-thrust acceleration level. The continuation process is time consuming, and occasionally a solution computed with a higher low-thrust acceleration level cannot be continued down to the desired thrust level. Thus ideally, an improved initial guess would dispose of the need for the continuation process step.

The exterior transfers examined here are similar in geometry and destination to those obtained by McCarty et al. [34], thus the work of these authors offers a convenient point of comparison. McCarty et al. employ a global optimization algorithm

Table 5.4.

Julian dates of initial epochs used to compute each Gateway transfer in an ephemeris model.

Transfer Type	Julian Date [days]
NRHO to DRO - Exterior	2460472.16
NRHO to DRO - Interior	2460487.92
NRHO to Low-Amp. Halo - Exterior	2460480.81
NRHO to Low-Amp. Halo - Interior	2460463.01
NRHO to North NRHO - Exterior	2460482.84
NRHO to North NRHO - Interior	2460462.50

to compute their transfers [122]; all three of the exterior type transfers computed in their work require less propellant than those generated in this investigation. However, the geometries, performance, and time of flight of the transfers computed here are near enough to those computed by McCarty et al. to indicate that reasonable results are obtained. Moreover, it is probable that employing the results of this section in a global optimization scheme similar to the one in McCarty et al. would lead to results with similar levels of propellant consumption. Indeed, it is possible that the orbit chain initial guesses themselves could be directly linked with such a strategy. This pairing would provide the global optimization process with an good initial guess while skipping the intervening step of computing a single optimal point solution for the desired transfer.

#### 5.4 Missed Thrust Analysis

Missed thrust analysis is conducted for the exterior transfer computed from the 9:2 NRHO to the DRO. The intent is to demonstrate an approach to missed thrust

analysis and highlight how direct collocation can be employed in this aspect of the trajectory design process. It is not necessary to conduct a missed thrust analysis for all computed Gateway trajectories to achieve this purpose. However, if any of the solutions presented in Section 5.3 were utilized in an actual mission, missed thrust analysis would be an essential step. Missed thrust analysis is conducted in the CR3BP to reduce computation time; however, similar results are likely to be found if the analysis is repeated in an ephemeris model.

A range of thrust outage periods are examined to provide an understanding of the baseline trajectory's robustness to missed thrust events of varying severity. In the event of a thrust outage, ample time must be afforded for engineers on the ground to identify and respond to the root cause of the event. The amount of time this process requires depends upon the complexity of the initial error; thus, the sensitivity of the baseline trajectory to a range of outage times must be understood. Outage times of 5, 7, and 14 days are explored. Together these results offer insight on how increasing outage times impact the missed thrust analysis.

A missed thrust analysis that employs a five day outage time is examined first. The results of the analysis are summarized in Figure 5.26 which plots the total propellant consumption of each computed transfer as a function of the initial time of the thrust outage period. Thus, each marker in Figure 5.26 represents a unique low-thrust solution, each of which includes a thrust outage period that begins at a different time. The color of each marker designates whether a new transfer was successfully computed when a thrust outage, beginning at the indicated time, was introduced. Blue markers denote a successfully recovered solution while red markers indicate failure. Note, the  $y$ -axis values of the red markers do not reflect the actual propellant consumption of these transfers at the end of the optimization routine. Rather, these red markers are plotted with the same  $y$  value as the baseline solution to improve the clarity of the plot. The actual propellant consumption of some of these failed cases lies far outside the range of the successfully recovered cases, thus trends in the

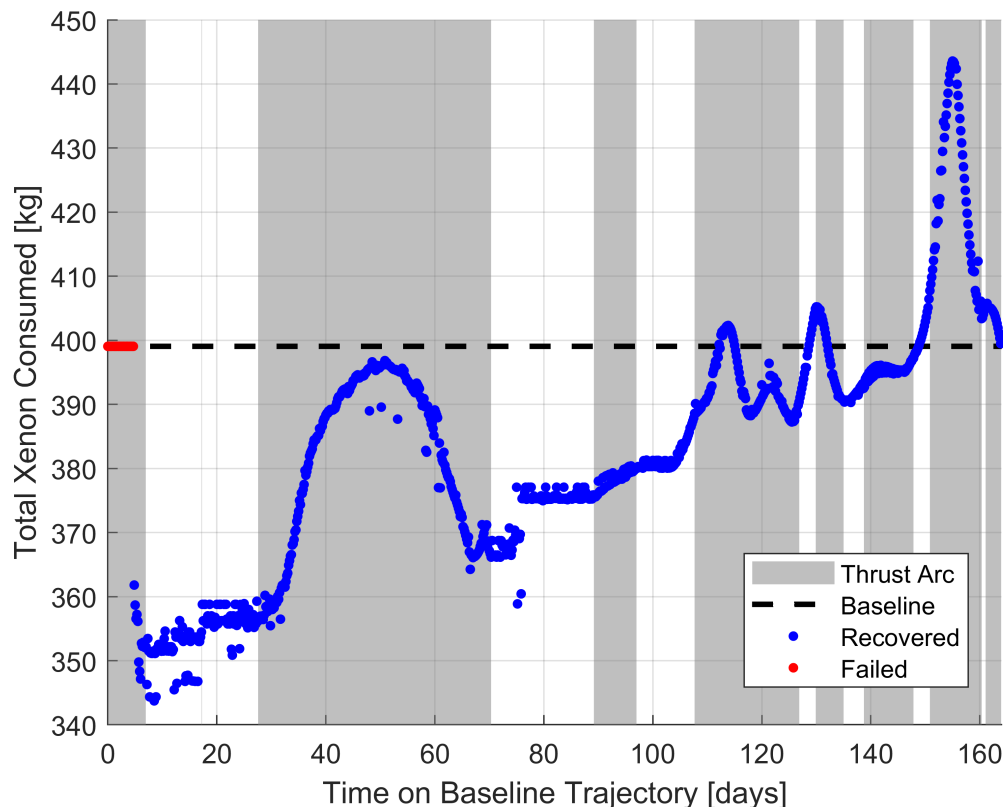


Fig. 5.26. Missed thrust analysis results for 5 day thrust outage time.

successful cases would be obscured if the true propellant consumption of the failed cases was used to locate the red markers.

Trends in the missed thrust analysis are correlated with the thrust profile of the baseline solution, therefore it is useful to plot the thrust profile along with these results. The thrust profile of the baseline solution is outlined with white and grey shading in Figure 5.26, where these colors indicate thrust and coast arcs, respectively. For comparison, the thrust profile of the NRHO to DRO Gateway transfer is also provided in Figure 5.27(a). Inspection of this plot reveals that the grey shaded regions in Figure 5.26 correspond to thrust arcs that utilize, the maximum available thrust value.

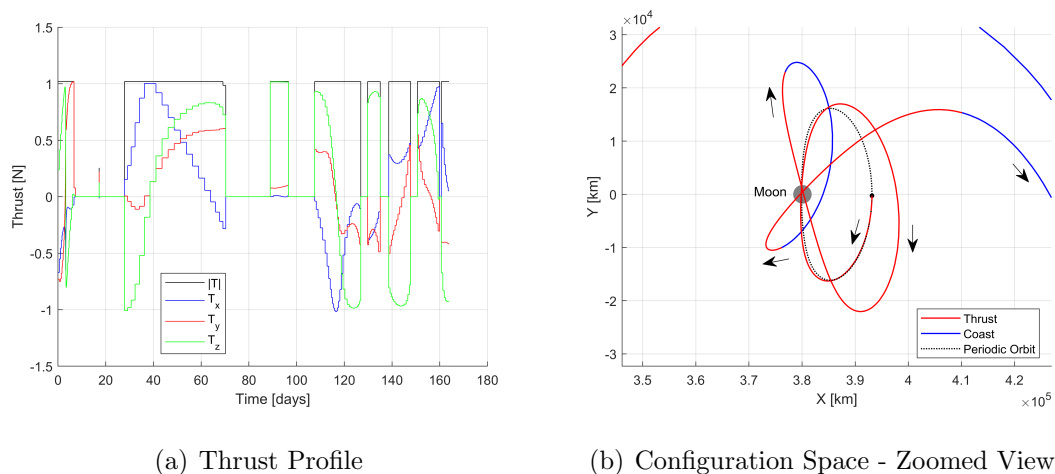


Fig. 5.27. Thrust profile and zoomed configuration space plot corresponding to the Gateway transfer from a 9:2 NRHO to a DRO.

The missed thrust analysis generates many different optimal low-thrust transfers. Given the 4 hour time interval between thrust outage events employed for this analysis the total number of transfers represented in Figure 5.26 is 984. Some of these solutions are essentially identical to the baseline because the thrust outage period falls entirely within a preexisting set of coast arcs. However, if the thrust outage occurs within any part of a thrust arc, a new transfer to the DRO is computed. The extent to which this new solution differs from the baseline depends on where in the thrust arc the outage occurs.

Two distinct trends are apparent in the results of the missed thrust analysis. First, Figure 5.26 exhibits a linear trend in propellant consumption, where total propellant consumption is higher when a thrust outage occurs later in a trajectory. The second pattern evident in the missed thrust results is that propellant consumption spikes when a thrust outage occurs during a thrust arc. The peaks of these spikes are not necessarily centered at the middle of a thrust arc, and in some cases a thrust arc can include more than one peak. The causes of these two trends are distinct, and thus explained separately.

The linear trend observed in Figure 5.26 results from the ability to leverage the full duty cycle of the engines after a missed thrust event, rather than leveraging the 90% duty cycle that is employed to converge the transfers presented in Section 5.3. This ability means that the earlier a missed thrust event occurs on the baseline trajectory, the more time is available for the higher duty cycle to be employed. Counter-intuitively, the higher thrust level actually enables a lower total propellant consumption because the duration of thrust arcs can be shortened due to the increased effectiveness of the engines. Allowing Gateway to utilize a 100% duty cycle for the entirety of a transfer following a missed thrust event does not necessarily reflect how the spacecraft would operate in reality. It may be that a higher duty cycle is employed temporarily until a sufficient recovery from the missed thrust event is achieved. However, it is easier to implement a general policy of permitting a 100% duty cycle for the purposes of the missed thrust analysis. Following this analysis, individual cases can be reexamined with different thrust policies if desired.

The second trend observed in the the missed thrust results is spikes in propellant consumption when a thrust outage overlaps with all or part of a planned low-thrust maneuver. The baseline solution is optimized such that the timing of low-thrust maneuvers maximizes the mass delivered to the final orbit, thus it is expected that an interruption of these maneuvers will result in a transfer that requires more propellant to reach the same destination. However, this expectation does not account for the fact that a higher duty cycle is permitted following a missed thrust event. Therefore, some missed thrust results actually require less total propellant than the baseline, even with the missed thrust event, because a 100% duty cycle is enabled. The peaks of each spike in propellant consumption are generally located nearer the leading edge of each thrust arc because a thrust outage at the beginning of a thrust arc has a greater impact on the resulting trajectory than if one were to occur over halfway through a planned maneuver. However, the geometry of the thrust arc does affect this trend. For example, the thrust arc lasting from approximately 108 to 127 days includes two spikes in propellant consumption with different amplitudes. This thrust

arc corresponds to the spiral down to the DRO observed in Figure 5.8(b), and lasts for one complete revolution around the Moon. Two regions on roughly opposite sides of this loop are particularly sensitive to missed thrust events; however, a thrust outage in the first of these regions has greater impact than one during the second.

Despite spikes in propellant consumption none of the cases that successfully recover from a missed thrust event utilize more propellant than is available onboard Gateway. The transfer that requires the most propellant only uses about 45 more kilograms than the baseline solution, which is well within Gateway's propellant mass budget. These results are of course bolstered by the 100% duty cycle afforded to Gateway following recovery. The only region of concern on the baseline transfer occurs at the beginning of the trajectory.

Unsurprisingly, the missed thrust analysis indicates that the most sensitive section of the baseline trajectory is a thrust arc near the Moon. The occurrence of a 5 day thrust outage early on in the NRHO to DRO Gateway transfer causes the optimizer to fail to converge to a new solution even with the added 20 day margin. These failed cases occur within the first 5 days of the transfer and all fall within the initial thrust arc. A total of 29 cases, about 3%, of the missed thrust analysis fail to converge. The section of trajectory corresponding to this thrust arc is plotted in configuration space in Figure 5.27(b). This initial thrust arc allows the Gateway to escape the 9:2 NRHO and depart the lunar vicinity to begin its transit around the Earth. The highly nonlinear dynamics near the Moon mean that even small changes to the trajectory in this region can have significant effects on its downstream behaviour. Thus, a thrust outage during this critical maneuver has an understandably large impact. The failure of the optimizer to reconverge when a thrust outage occurs at the beginning of the trajectory is not necessarily an indicator that it is impossible to reach the final orbit in this scenario. It may be possible to compute a new transfer if a different transfer geometry is introduced, or if steps are taken to improve the robustness of the optimization routine.

Some amount of “noise” is apparent in this first and subsequent missed thrust solutions. That is, individual results that do not neatly fit the two broad trends just described. The most obvious example of such noise is apparent in the first coast arc that lasts from approximately 7 to 27 days on the baseline trajectory. Because the thrust outages that fall within this period occur within a preexisting thrust arc the results of each optimal transfer should be relatively similar and follow a neat positive linear trend. Instead, the computed solutions are scattered around the mean of this linear trend, and this scattering represents the direct collocation algorithm converging upon solutions in similar but different optimal basins. This jumping between basins is again the case when a sizable leap in propellant consumption is observed at around 75 days in Figure 5.26. A smoother set of missed thrust analysis results could likely be obtained with adjustments to the direct collocation algorithm that discourage this jumping behavior.

Extending the duration of the thrust outage has the expected result of increasing the number of cases that fail to converge as well as the propellant consumption of cases that do. Figure 5.28 features summaries of the missed thrust analysis results obtained when 7 and 14 day thrust outage periods are employed. In both cases the

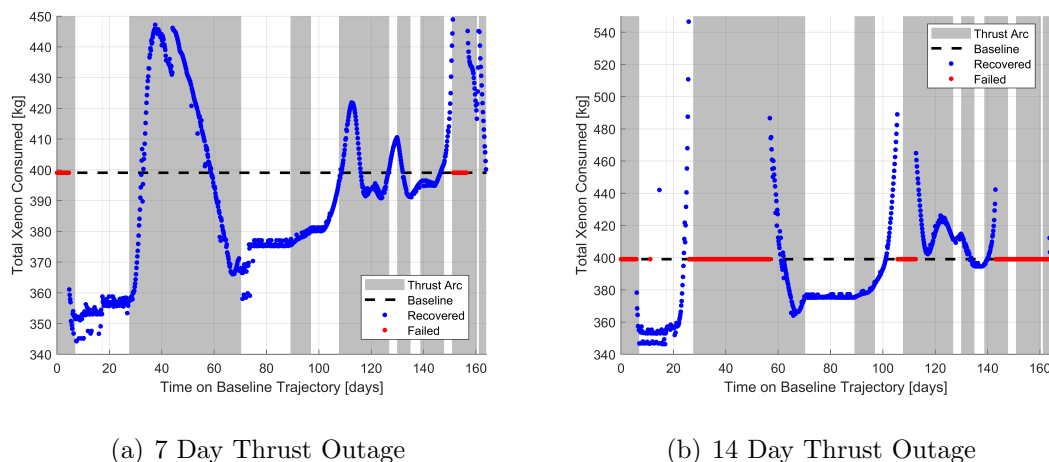


Fig. 5.28. Summaries of missed thrust analysis results when 7 and 14 day thrust outage times are employed.

sensitive region at the beginning of the baseline transfer persists, and even grows. However, the extended outage times also cause failed cases in new regions of the baseline. For example, the results of generated with the 7 day thrust outage, shown in Figure 5.28(a), reveal an area near the end of the baseline solution where the optimizer fails to converge. This region corresponds to the final approach of the DRO. The difficulty caused by a thrust outage occurring here is multiplied when the outage time is doubled to 14 days. For this duration all missed thrust cases fail to reconverge when an outage occurs later than 143 days on the baseline trajectory. It is likely that more cases at the end of the baseline trajectory could be reconverged if greater freedom were permitted for where the transfer inserts onto the DRO. This freedom could be introduced by increasing the margin time added to the end of the baseline, or by modifying the direct collocation algorithm so that the transfer is free to connect with a range of points on the final DRO. In total, the percentage of failed missed thrust analysis cases are 6% and 39% for the 7 and 14 day thrust outage scenarios, respectively.

The results of the missed thrust analysis suggest several approaches for designing a more robust NRHO to DRO transfer. Moreover, these strategies are likely applicable to the other five Gateway transfers computed in this investigation. First, the initial escape from the 9:2 NRHO should likely be redesigned to reduce the sensitivity of this phase of the transfer to missed thrust events. One approach would be to create a more immediate escape from the NRHO that does not include any additional loops around the Moon. Thus, if a thrust outage does occur, the Gateway is already on a path away from the sensitive region around the Moon, therefore a successful transfer to the final orbit is more likely to be recovered following the thrust outage. Another region of the baseline trajectory that could benefit from modification is the final approach to the DRO. Several thrust arcs during this phase enable the Gateway to successfully insert upon the final orbit. As suggested previously, greater freedom in the insertion location on the DRO could reduce the failure rate due to missed thrust events in this region. Additionally, it may be beneficial to include additional revolutions near the

DRO for this phase that provide slack to utilize in the event of a thrust outage. A simple way to implement this change is to stack additional revolutions of the final DRO in the orbit chain employed to converge the initial guess.

The results of the 14 day missed thrust scenario highlight that the baseline solution likely needs to be modified if thrust outages of this duration are expected. When thrust outages are 2 weeks long, even missed thrust events that occur during the long transit around the Earth-Moon system, far from either body, pose significant challenges. Adding more time margin to the end of the baseline trajectory may increase the number of recovered trajectories in Figure 5.28(b), but it is unlikely to fix every case. Increasing the robustness of the NRHO to DRO transfer to 14 day missed thrust events may require utilizing missed thrust design strategies such as those proposed by the authors noted in Section 5.1.3.

Missed thrust analysis is not conducted for interior type transfers; however, the results of the current analysis suggest that interior transfers could be particularly difficult to make robust to missed thrust events. For the same reason that the introduction of a thrust outage during the initial thrust arc of the NRHO to DRO transfer poses difficulty, it will be challenging to accommodate similar outages on interior trajectories where the majority of the transfer takes place near the Moon. This proximity to the Moon is especially the case for the interior NRHO to DRO transfer, which includes multiple close flybys of the Moon. Further analysis is required, but if this type of transfer geometry does prove difficult it would be a reason to favor exterior type trajectories for achieving the transfers of interest to the Gateway mission.

## 6. LUNAR ICECUBE MISSION DESIGN

The number of CubeSats launched per year has increased considerably in the last decade and there are no signs of slowing. This trend is motivated by the low cost and low risk of CubeSat missions compared to their larger counterparts supporting more complex missions. The evolution of CubeSat applications is enabled by advancements in spacecraft technology miniaturization and a greater availability of launch opportunities. The vast majority of CubeSat missions, thus far, have remained in low-Earth orbit (LEO); however, an increasing number of missions are pursuing applications in regions well beyond LEO. The two MarCO spacecraft became the first interplanetary CubeSats when they were deployed from the cruise stage of the *Insight* lander and flew by Mars in 2018 [123]. In the near future, thirteen CubeSats will launch as secondary payloads aboard the Artemis-1 mission, which delivers an uncrewed *Orion* spacecraft on a test flight around the Moon. All of these CubeSats are bound for destinations beyond LEO. Some, such as the Near Earth Asteroid Scout (NEA Scout) and the CubeSat for Solar Particles (CuSP), will reach heliocentric space. Others, such as Lunar IceCube, Lunar Flashlight, and LunaH-Map, expect to enter orbits about the Moon. The CubeSats aboard Artemis-1 further demonstrate the utility of the CubeSat platform in more far-flung regions of space and motivate the development of similar mission scenarios. Already, a new set of CubeSat missions are being developed as secondary payloads for Artemis-2.

While the CubeSat revolution brings extraordinary new opportunities for conducting science and demonstrating new technologies, it also introduces new challenges. Despite technological improvements, ambitious CubeSat mission planning often involves learning to do “more with less.” As a result of the challenges, some mission design scenarios are enabled only via innovative trajectory design approaches that fully exploit natural dynamics. The Lunar IceCube (LIC) concept offers an excellent

example of the challenges. The current concept for operations involves the delivery of a 6U CubeSat to a low lunar orbit (LLO), where LIC will collect data on water transport throughout the lunar surface. Inherent in the task is a challenging trajectory design scenario, as the huge change in energy required to transfer from the initial deployment state to LLO is compounded by the limited control authority of the LIC low-thrust engine. Furthermore, as a secondary payload, LIC is subject to shifts in the launch date and in other conditions required by the primary mission. These challenges necessitate a trajectory design strategy that is flexible and incorporates natural forces to assist with achieving the required energy change.

This investigation extends the framework introduced by Pritchett, Howell and Folta [124, 125] for designing the LIC baseline trajectory. The proposed framework addresses some of the challenges of the Lunar IceCube trajectory design problem by utilizing dynamical structures available in the Bicircular Restricted Four-Body Problem (BCR4BP) and a robust direct collocation algorithm. Designing in the BCR4BP enables the gravitational force of the Sun to be smoothly leveraged to achieve part of the required energy change while avoiding the additional perturbations of a full ephemeris model. A key feature of the proposed design approach is the use of a staging orbit near the Moon to split the trajectory into two phases: the first from spacecraft deployment to the staging orbit and the second from the staging orbit to the science orbit. This strategy allows the two halves of the LIC trajectory to be designed mostly independently, thus simplifying the redesign process if deployment conditions are modified. Moreover, a periodic orbit in the BCR4BP is employed as the staging orbit to leverage its invariant manifolds for the design of efficient paths to and from the staging orbit. Another crucial component in the proposed framework is a direct collocation algorithm to collect the initial guesses produced in the BCR4BP and deliver optimal low-thrust trajectories. The robust convergence properties of direct collocation facilitate a wider variety of initial guesses despite large discontinuities in states and/or time. Together, these key design choices produce a design process that directly addresses some of the key challenges of the Lunar IceCube mission. After an

overview of the necessary background, the proposed trajectory design framework is described. Using the proposed strategies, sample Lunar IceCube trajectories are constructed in the BCR4BP for four different deployment dates. Additionally, transfers to a different final orbit are explored in response to the recent interest in alternate mission profiles for LIC. Finally, a portion of these trajectories are validated in an ephemeris model. While the trajectory design procedure is applied to the Lunar IceCube mission, it is sufficiently general for a wide variety of low-thrust missions, especially those with limited control authority.

## 6.1 Background

The initial phases of development for the Lunar IceCube (LIC) mission began in the early 2010s. While the specific objectives and composition of LIC have changed, its ultimate destination, an orbit in the lunar vicinity, remains the same. The challenge of designing a low-thrust trajectory from the Earth to the Moon for LIC has motivated many researchers to investigate this problem, and this work builds on their efforts. A brief overview of the LIC spacecraft and mission follows, including the pertinent literature.

### 6.1.1 Mission Overview

Selected in 2015 for launch aboard Artemis-1, the LIC mission is a collaborative effort led by Morehead State University and supported by Goddard Space Flight Center (GSFC), the Jet Propulsion Laboratory (JPL), and Busek [126]. The primary objective of this mission is an investigation of the presence and transport of lunar volatiles across a broad swath of the Moon's surface, with a particular focus on water. To enable collection of this data, the 6U CubeSat, depicted in Figure 6.1, conducts science operations in a highly inclined low lunar orbit (LLO) with a perilune altitude of 100 km. This orbit enables LIC's primary science instrument, BIRCHES, to collect IR spectral measurements across a range of longitudes on the sunlit side of the Moon.



Fig. 6.1. Artist rendition of Lunar IceCube in lunar orbit. Credit: Morehead State University

The full set of Keplerian orbital elements that define the current science orbit are summarized in Table 6.1; the orbit selection is driven by the science requirements and the desire to maximize spacecraft lifetime while minimizing the station-keeping costs [127]. Ultimately, science measurements collected by LIC will complement data from similar past and contemporary missions, e.g., LCROSS and Lunar Flashlight, to provide a more complete understanding of environmental processes on the Moon.

The transfer trajectory to the science orbit and any station-keeping control strategy are accomplished via a BIT-3 Busek ion thruster, which is capable of a maximum thrust level equal to 1.24 mN, a specific impulse ( $I_{sp}$ ) of 2640 seconds, and stores up to 1.5 kg of propellant [32]. Given the total 14 kg mass of LIC, these engine characteristics deliver a maximum acceleration of  $8.857 \times 10^{-5} \text{ m/s}^2$ . This value is comparable to the maximum acceleration values for other recent low-thrust spacecraft like Dawn [6]. The primary mission design challenge for LIC is a massive change in energy required to transfer from the high-energy deployment state near the Earth to the low-energy

Table 6.1.

Lunar IceCube science orbit Keplerian orbital elements defined in a Moon-centered inertial frame. Inclination is measured relative to the Moon’s equator and the right ascension of the ascending node (RAAN) is defined with respect to the vernal equinox vector.

Orbital Element	Value
Semi-Major Axis, $a$	4271.4 km
Eccentricity, $e$	0.5697
Inclination, $i$	89.35°
RAAN, $\Omega$	65°
Argument of Periapsis, $\omega$	355°

LLO, much of it delivered by this low-thrust engine. While the initial velocity of LIC relative to the Earth is less than escape velocity, the subsequent ballistic path includes a flyby of the Moon that enables LIC to escape the Earth-Moon system. Low-thrust maneuvers are initiated shortly after deployment to prevent escape. In contrast to this high-energy deployment, the LIC science orbit possesses an energy sufficiently low to ensure that the spacecraft is securely captured at the Moon. While accomplishing this transfer with a low-thrust engine presents challenges, it also offers a unique opportunity to demonstrate the utility of this type of propulsion system for future CubeSat missions beyond LEO.

### 6.1.2 Previous Contributions

Despite the trajectory design challenges of the LIC mission, engineers at GSFC have developed baseline trajectories for a range of potential deployment dates; however, additional work is required to streamline the design process. A baseline trajectory, developed at GSFC, which utilizes a launch date of November 6<sup>th</sup> 2020, is plotted in Figure 6.2. The expected launch date for Artemis-1 is presently in flux;

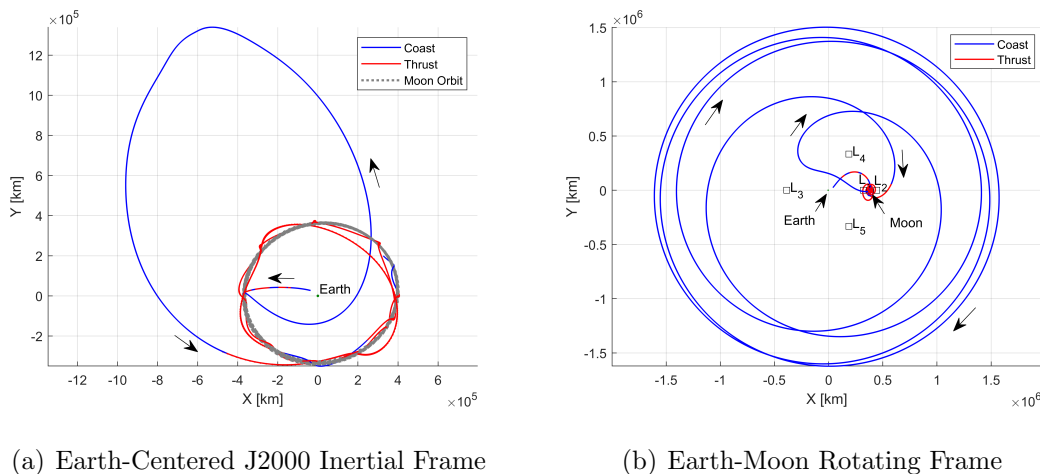


Fig. 6.2. Baseline Lunar IceCube trajectory developed for a November 6<sup>th</sup>, 2020 launch date and computed in an ephemeris model.

however, a range of dates from early November 2020 through the following year are under consideration. Each time a new deployment state and epoch is selected, the baseline trajectory must be redesigned. Moreover, experience has demonstrated that varying the launch date can significantly impact the geometry of any trajectories that deliver LIC to the specified science orbit. Given the challenges of trajectory design and the variability of the launch date, a systematic approach for generating a transfer for LIC from deployment to a selected science orbit is desirable. Such a framework must offer strategies for designing the LIC transfer that are applicable regardless of launch date, and that reduce the time required to develop a baseline for a given launch date. The necessity for such a framework has motivated a number of researchers to formulate innovative trajectory design approaches for LIC. The present investigation builds upon this excellent body of work. Moreover, these researchers draw upon a wealth of literature on trajectory design with dynamical systems theory.

Given a challenging trajectory design scenario and uncertain launch conditions, engineers at GSFC have employed the results from several investigations on LIC trajectory design. A strategy that utilizes the high-fidelity General Mission Analysis

Tool (GMAT) to design an LIC trajectory with a capture orbit at the Moon is offered by Mathur [128]. An innovative design approach for LIC is also presented by Bosanac, Folta, Cox, and Howell; the Lunar IceCube trajectory is subdivided into three phases: deployment, phasing and energy adjustment, and lunar capture. A strategy for linking these phases that incorporates periapse maps and phasing arcs generated in the Sun-Earth Circular Restricted Three-Body Problem (CR3BP) or the BCR4BP is developed by Bosanac et al. [129–131]. Particular focus on the dynamics of the lunar capture phase is delivered separately by Folta et al. [132]. The strategy by Bosanac et al. is effective, and the recent investigation by Pritchett, Howell, and Folta expands upon this work by approaching the design problem with a framework that utilizes BCR4BP dynamical structures and direct collocation [124,125]. The current analysis offers greater detail on this recent strategy and demonstrates an extension via its application to transfer design to an alternate final science orbit.

In addition to the previous work on LIC, this current investigation is influenced by a greater body of literature on leveraging the influence of the Sun to design transfers from the Earth to the Moon. Belbruno and Miller demonstrate new types of Earth-to-Moon trajectories by simultaneously incorporating the gravitational influence of the Sun in addition to the Earth and Moon. Strategies for utilizing this acceleration to develop low-energy trajectories from the Earth to the Moon are developed by many authors, including Koon et al. [133], Gómez et al. [134], as well as Parker and Martin [135]. The work of these authors is applied to the Genesis [136] and GRAIL [137] missions among several others. Low-energy trajectory design techniques are also applied to design low-thrust trajectories to the Moon by Mingotti et al. [138] and Zanutta et al. [139]. The current investigation employs direct collocation to compute low-thrust transfers, building on the work of additional authors such as Enright and Conway [140] as well as Grebow, Ozimek, and Howell [18] who also employ this algorithm to generate low-thrust Earth-to-Moon transfers. Perez-Palau and Epenoy explore similar transfers using an indirect optimal control approach in a four-body dynamical model [141]. Some authors investigating low-energy trajectory

design also demonstrate transfers from Earth-Moon halo orbits to LLO, a strategy employed in this investigation. Parker and Anderson [142] offer an impulsive transfer, while Mingotti et al. demonstrate a low-thrust result [143]. Recently, Cheng et al. [144] and Cao et al. [145] have more closely examined impulsive transfers from halo orbits to LLO in the CR3BP.

## 6.2 Trajectory Design Framework

The proposed trajectory design framework is distinguished by three key features: modeling directly in the BCR4BP, employing a staging orbit, and computing low-thrust transfers with a direct collocation technique. Together, these design choices deliver a flexible and robust procedure for constructing the LIC trajectory. A staging orbit near the Moon divides the mission design challenge into two phases, as illustrated in Figure 6.3. Phase 1 occurs from deployment to the staging orbit and Phase

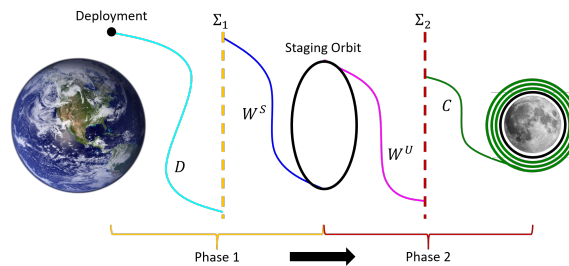


Fig. 6.3. Schematic of a trajectory design framework for the nominal Lunar IceCube mission profile.

2 passes from the staging orbit to the destination orbit, nominally the low lunar altitude science orbit. Use of the staging orbit facilitates the division of the end-to-end Lunar IceCube trajectory into these two distinct phases, thus, mitigating some of the design challenge. Initial guesses for each phase are generated nearly independently. Discrepancies in epoch between the two phases that result from this independence are overcome by maintaining the staging orbit until reaching the desired departure epoch.

Initial guesses for both phases in the trajectory design framework are assembled with the aid of two different maps. These maps display intersections with the hyperplanes  $\Sigma_1$  and  $\Sigma_2$ , defined by the Sun angles  $\theta_{S_1}$  and  $\theta_{S_2}$ , respectively. The first map captures intersections of  $\Sigma_1$  by forward propagated deployment trajectory arcs,  $D$ , and backward propagated paths on the stable manifold for the staging orbit,  $W^S$ . Similarly, the second map captures intersections of  $\Sigma_2$  by forward propagated trajectories along the unstable manifold of the staging orbit,  $W^U$ , and backward propagated capture trajectory arcs,  $C$ . Close alignments between hyperplane intersections of forward and backward propagated trajectories are identified and their corresponding trajectory segments are assembled into an initial guess for the direct collocation tool COLT. When the pre-specified destination orbit in Phase 2 is shifted from an LLO to a near rectilinear halo orbit, an alternate orbit chain approach is employed to construct an initial guess.

### 6.2.1 Nearest Neighbor Search Algorithm

The proposed trajectory design framework employs maps to aid the construction of initial guesses that are passed to the direct collocation algorithm. Maps capture the returns of trajectory segments to a particular hyperplane,  $\Sigma$ . Frequently, maps facilitate the identification of close connections between two sections of a spacecraft trajectory, e.g., one propagated forward in time and the other backward. Points along these trajectories that intersect the selected hyperplane are displayed on the map. Sample hyperplanes include a physical plane in configuration space, e.g., the  $xy$ -plane, or a representation of the state vectors at the occurrence of a specific epoch. In this investigation the Sun angle,  $\theta_S$ , defines hyperplanes for two different maps. Parameters such as position, velocity, or energy at the hyperplane intersections may be displayed on the map. The maps in this analysis include points, i.e., hyperplane crossings, from many trajectories, and each trajectory potentially possesses multiple returns to the hyperplane. Due to the large number of points and multiple dimensions

representing each point plotted on the map, it is challenging to visually identify the best links between trajectory segments. Therefore, a nearest neighbor search algorithm aids the identification of points on maps that share similar characteristics.

Nearest Neighbor (NN) algorithms are employed in many computer science fields under a variety of names [146]. Fundamentally, the nearest neighbor problem involves locating the point  $\mathfrak{p}$  from within a larger set of points  $\mathbb{P}$  with the shortest distance to a given point  $\mathfrak{q}$ , assuming all points occupy a space of dimension  $\mathbb{D}$  [147]. In the present application, hyperplane intersections of the forward propagated group of trajectories provide one set of points, while intersections of the backward propagated trajectories comprise the other set. Thus, an NN search is ideally suited for identifying close connections between these two sets. The tool *Poincare*, developed at JPL, employs NN algorithms for this purpose [148]. In this investigation, Matlab's `knnsearch` algorithm is employed for the NN search. Furthermore, a standardized Euclidean distance metric is employed to compute the distances between points. Eight parameters associated with each hyperplane intersection are utilized as the NN search criteria in this investigation: the six position and velocity states, the value of the Hamiltonian,  $H$ , and the angle of the  $xy$ -plane projection of the velocity vector with respect to  $\hat{x}$ . While the Hamiltonian and the in-plane velocity vector angle do not include any information not available in the state vectors, their inclusion is observed to improve the quality of the “matches” identified by the NN search algorithm. Because these eight parameters can possess different magnitudes, the standardized Euclidean distance metric applies scaling to prevent one set of parameters from biasing the search. The standard deviations for each of the NN search parameters are used as scaling factors. If desired, these scaling factors may be further weighted to emphasize close matches in specific parameters. These capabilities enable the NN search algorithm as a useful tool for complementing, or even replacing, visual inspection of the maps.

### 6.2.2 Staging Orbit Selection

A staging orbit aids in dividing the LIC transfer into two distinct phases to be designed with relative independence. The staging orbit simplifies the design problem, alleviates epoch mismatches, and offers useful dynamical structures. It is advantageous to decompose the LIC trajectory design problem into multiple phases, because this reduction produces several smaller problems that are easier to design and optimize. Other researchers employ a similar approach for developing LIC transfer solutions [131]. As long as solutions for Phase 1 and 2 arrive at or depart the staging orbit, respectively, the total transfer solution is continuous in position and velocity. However, a complete solution must also be continuous in time, and designing the LIC trajectory as a series of smaller problems potentially introduces timing discontinuities between phases. Fortunately, the staging orbit also offers a remedy for this challenge. Timing discrepancies between the end of Phase 1 and the beginning of Phase 2 are eliminated by remaining in the staging orbit until reaching the desired departure epoch. Finally, many staging orbit candidates in the BCR4BP possess invariant manifold structures that offer energy-efficient paths for inserting on or departing from the staging orbit. These structures guide the trajectory design process for Phases 1 and 2.

A variety of periodic and quasi-periodic structures available in the BCR4BP are available to be leveraged as staging orbits for the LIC trajectory design problem. However, only one staging orbit candidate is examined in this investigation, a 2:1 synodic resonant halo orbit about the Earth-Moon  $L_2$  libration point, depicted in Figure 6.4. This orbit is selected because of its location at the Earth-Moon  $L_2$  gateway, its out-of-plane nature, and its simplicity relative to quasi-periodic orbits. Following an initial lunar flyby, the high-energy deployment of LIC sends the spacecraft well beyond the orbital radius of the Moon. When LIC finally returns and again approaches the Earth-Moon vicinity, it most frequently arrives via the Earth-Moon  $L_2$  gateway. Given this behavior, a staging orbit positioned in the Earth-Moon  $L_2$

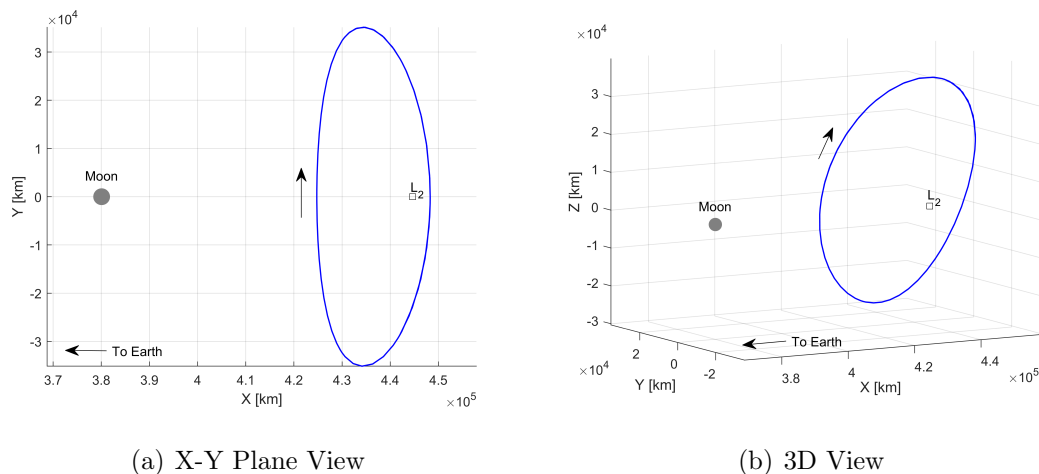


Fig. 6.4. Two views of a 2:1 synodic resonant halo orbit computed in the Sun-Earth-Moon BCR4BP and displayed in the Earth-Moon rotating frame. This orbit is generated about the Earth-Moon  $L_2$  libration point, and is used as a staging orbit in the proposed design framework.

gateway with invariant manifold structures that guarantee transit through the gateway is selected. Additionally, as the current LIC science orbit is highly inclined with respect to the Moon's equatorial plane, an out-of-plane staging orbit is selected to reduce the plane change that is required to access the science orbit and potentially leverage natural flows to further effect a plane change. A variety of quasi-periodic orbits in the BCR4BP are located at the Earth-Moon  $L_2$  gateway and also exhibit out-of-plane motion; however, these orbits are more complex to generate and do not offer the exact periodicity that is most convenient for eliminating epoch discontinuities. Thus, a periodic orbit is employed in this investigation and an exploration of the utility of QPOs for this application is reserved for future work.

The 2:1 synodic resonant halo orbit in the BCR4BP possesses important differences in geometry compared to its CR3BP and ephemeris counterparts. A member of the northern  $L_2$  halo family in the CR3BP that possess a 2:1 synodic resonance is used as an initial guess to generate the same halo orbit in the BCR4BP. Two revolutions of the CR3BP orbit are stacked and then converged to yield a BCR4BP orbit

as displayed in Figure 6.4. While the CR3BP and BCR4BP versions of this orbit possess the same time per revolution, they exhibit notably different geometries as is apparent in Figure 6.5. The difference in geometry is most prominent along the  $\hat{z}$ -axis

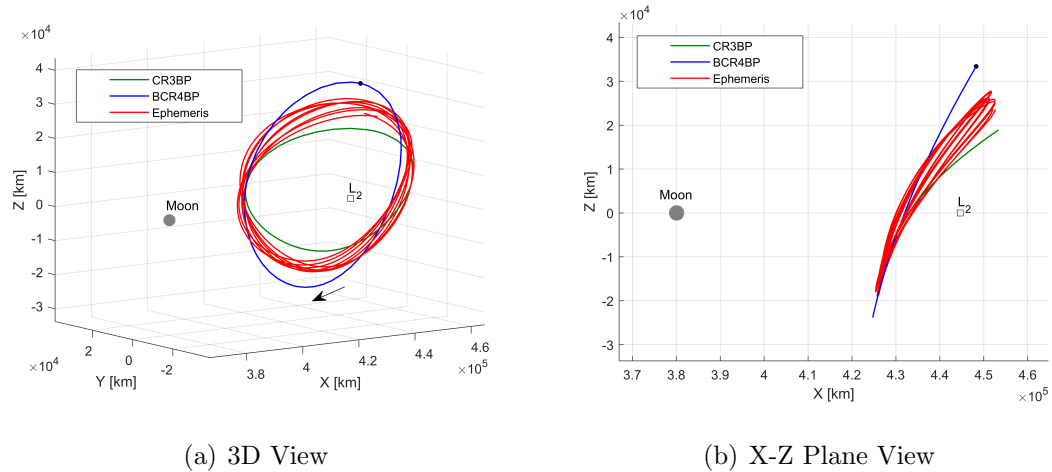


Fig. 6.5. Comparison of the selected staging orbit in three different models. Significant differences in geometry are apparent between the three orbits, particularly when viewed in the X-Z plane. The CR3BP northern  $L_2$  halo orbit possessing a 2:1 synodic resonance is used as an initial guess for the same orbit in the BCR4BP. The BCR4BP result is then employed as an initial guess for an ephemeris orbit with similar motion.

direction; the BCR4BP halo orbit possess greater excursions in the positive and negative out-of-plane directions associated with this component than the corresponding CR3BP orbit. The dynamical justifications for this shift in geometry are not clearly articulated; however, these orbits are consistent with similar variations between the CR3BP and BCR4BP versions for other periodic orbits, for example, the 9:2 synodic resonant NRHO [27, 149]. This variation in geometry is particularly important when transfers computed in the BCR4BP are transitioned to an ephemeris model because some of the geometries available in the BCR4BP are not easily replicated in this latter model.

The ephemeris version of the 2:1 synodic resonant halo orbit that is selected for use as a staging orbit is computed using the BCR4BP orbit as an initial guess. Multiple revolutions of the BCR4BP orbit are stacked and these are transitioned to the ephemeris model where they are corrected to be a continuous trajectory. When transitioning the staging orbit to an ephemeris model from the BCR4BP, it is essential to select an initial epoch that corresponds well with the initial Sun angle of the orbit. This initial guess and transition process generate the orbit displayed in Figure 6.5. The plotted ephemeris orbit exhibits similar geometry to its CR3BP and BCR4BP counterparts, but with distinct differences. These differences may be a result of the process employed to transition the desired orbit between the three models considered in Figure 6.5. A similar procedure for achieving this transition is discussed by Boudad et al. [27]. Further investigation is required to develop strategies for transitioning solutions between models in a manner that preserves desirable characteristics.

Though the difference in geometry between the BCR4BP and ephemeris versions of the staging orbit can make transitioning LIC transfers to the ephemeris model more challenging, it is still possible. Moreover, the inclusion of the Sun in the BCR4BP means that the dynamics along other sections of the LIC transfers computed in this model are more similar to those of an ephemeris model, and therefore easier to transition. Overall, the differences between periodic orbits in the CR3BP, BCR4BP, and ephemeris model add challenges to the process of transitioning results to an ephemeris model, but do not eliminate the utility of employing the BCR4BP in this trajectory design framework.

### 6.2.3 Phase 1 Trajectory Design: Deployment to Staging Orbit

Design of Phase 1 for the LIC trajectory is facilitated by the creation of maps that display intersections of  $\Sigma_1$  along trajectories propagated forward from deployment and backward along the stable trajectories on the invariant manifold of the staging orbit. To expand the options available from these maps, a range of  $D$  and  $W^S$  trajectory

arcs are generated. Different  $W^S$  arcs are produced by changing the state and epoch corresponding to the departure point from the periodic orbit. In contrast, because the deployment state and epoch are fixed, a span of  $D$  trajectory segments is generated by varying the thrust force direction prior to the first lunar flyby. The deployment dates and corresponding initial Sun angle used in this investigation are displayed in Table 6.2.

Table 6.2.

Deployment dates and corresponding Sun angles considered for Lunar IceCube. At the time of writing Lunar IceCube is scheduled to launch in November 2020.

Deployment Date	Initial Sun Angle [rad]
Oct. 9 <sup>th</sup> , 2018	6.1557
Jun. 27 <sup>th</sup> , 2020	4.8193
Nov. 6 <sup>th</sup> , 2020	2.0185
Mar. 1 <sup>st</sup> , 2021	2.6943

Trajectories propagated forward in time from the deployment condition,  $D$ , are split into three parts, an initial coast interval, a thrust segment, and a second coast interval. An example of this subdivision is displayed in Figure 6.6(a). In this case, the duration of the first coast segment is set to 0.8 days. This time is variable, and can be modified either during the formulation of the initial guess or by the direct collocation algorithm; however, a minimum of 8 hours must be reserved for performing spacecraft systems checkouts and collecting tracking data following deployment.

Following the initial coasting interval, a multi-day thrust segment is introduced. A thrust segment of three days is introduced in this investigation; however, this value is variable and is modified to adjust the post-flyby behavior of the deployment trajectory. The direction of the thrust vector along this segment is varied to generate a range of deployment trajectories. The angle,  $\alpha$ , determines the thrust vector direc-

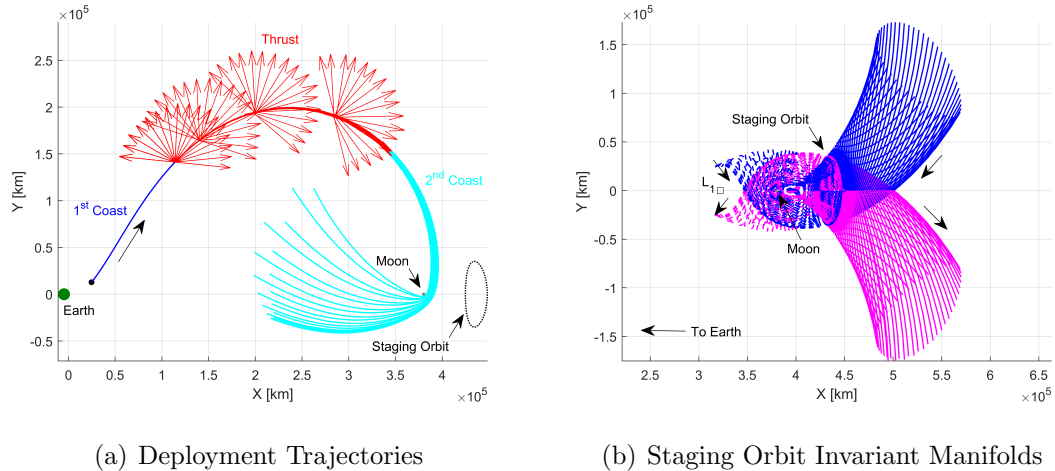


Fig. 6.6. (a) Sample range for deployment trajectories in the creation of a Phase 1 map, plotted in the Earth-Moon rotating frame. The first coast period is 0.8 days, the thrust segment is 3 days, and the second coast section is 4 days. Thrust vectors span a range of  $\alpha$  angle values from 0 to  $360^\circ$  in the velocity-normal-binormal frame. Trajectories that impact the Moon are omitted. (b) Stable (blue) and unstable (magenta) manifold trajectories plotted in the Earth-Moon rotating frame and originating from the 2:1 resonant  $L_2$  halo orbit displayed in Figure 6.4.

tion, measured, relative to the  $\hat{v}$  unit vector in the velocity-normal-binormal (VNB) frame. This frame is defined such that the  $\hat{v}$  unit vector is in the direction of the spacecraft velocity vector expressed in the rotating frame, as depicted in Figure 6.7. Additionally, the  $\hat{n}$  unit vector is in the direction of the spacecraft's angular momentum vector relative to the barycenter, and the  $\hat{b}$  unit vector is defined to complete the orthonormal set,  $\hat{b} = \hat{v} \times \hat{n}$ . The angle  $\alpha$  determines the direction of the thrust vector in the  $vb$ -plane, and no out-of-plane, i.e.,  $\hat{n}$  component of the thrust vector, is introduced. By varying  $\alpha$  from  $0^\circ$  to  $360^\circ$ , many different post-flyby trajectories are generated, as seen in Figure 6.6(a). An out-of-plane angle in the VNB frame is omitted to reduce the number of variables that are varied to generate post-flyby trajectories; however the potential benefits of introducing such a variable could be explored in future work. Following the thrust segment, a second coast segment is propagated until

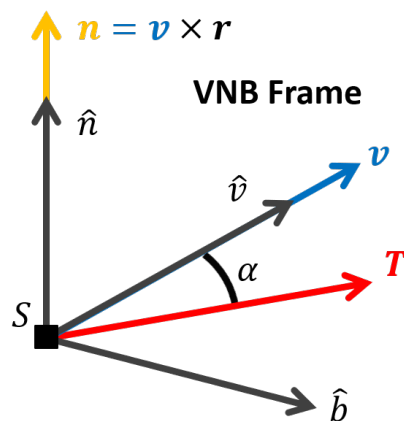


Fig. 6.7. Illustration of the orientation of the thrust vector,  $\mathbf{T}$ , in the velocity-normal-binormal (VNB) frame. The origin of this frame is centered on the spacecraft  $S$ . The vector  $\mathbf{r}$  is the position vector from the barycenter of the rotating frame to the spacecraft, and  $\mathbf{v}$  is the spacecraft velocity expressed in the rotating frame. The cross product of these two vectors,  $\mathbf{n} = \mathbf{v} \times \mathbf{r}$ , yields the angular momentum vector of the spacecraft with respect to the barycenter. The vector  $\hat{n}$  is defined such that  $\hat{v}$ ,  $\hat{n}$ , and  $\hat{b}$  are an orthonormal set.

a limit on either the number of days or the distance from the barycenter is reached. Intersections of these  $D$  trajectory arcs with the hyperplane  $\Sigma_1$  are recorded and used to generate the map. Any  $D$  trajectory arcs that impact the Moon are excluded from the map.

The forward propagated  $D$  trajectory arcs are linked to trajectories propagated backwards in time along the stable manifold,  $W^S$ , of the staging orbit. The stable invariant manifolds associated with periodic orbits offer efficient paths onto the orbits. Thus, using these trajectories to guide LIC to the staging orbit should lead to a solution that requires less propellant than other potential insertion paths. Figure 6.6(b) displays trajectories along the stable manifold. These manifold paths flow either in the positive or negative  $x$  direction. In the former case, trajectories on the manifold tend to escape the Earth-Moon system, and these paths offer more useful connection points with the  $D$  trajectory arcs. Stepping off the periodic orbit and

onto the stable manifold at different states and epochs around the orbit generates a variety of manifold paths.

A map is created to facilitate the process of joining the two halves of the Phase 1 LIC trajectory by recording the intersections of the  $D$  and  $W^S$  trajectory arcs on the hyperplane  $\Sigma_1$ . Trajectories are propagated until reaching either a maximum time limit or a maximum distance from the Earth. In this case, a maximum time of 100 days and a maximum Earth distance of  $3 \times 10^6$  km are employed for both the  $D$  and  $W^S$  propagation. A set of sample maps is displayed in Figure 6.8, where the Sun angle at which events are recorded is  $\theta_{S_1} = 318^\circ$ . The events that occur

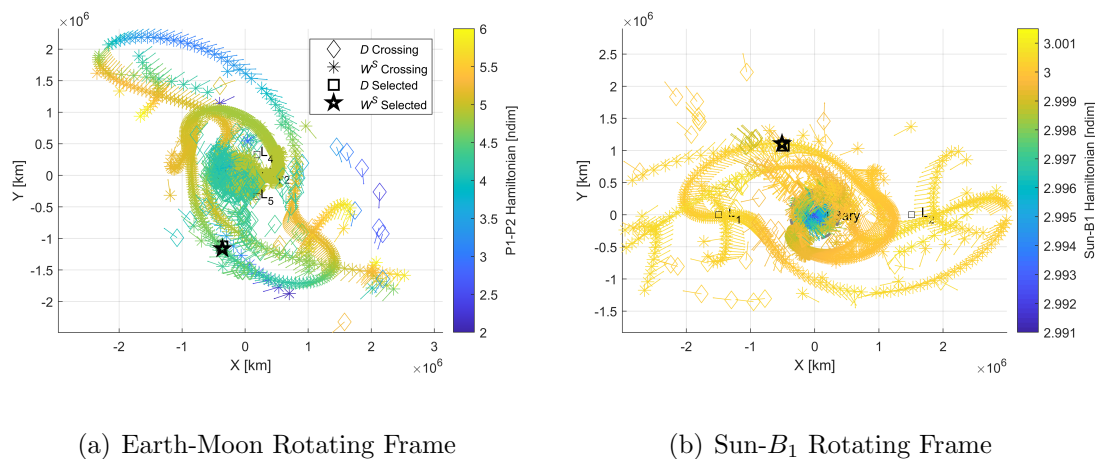


Fig. 6.8. Map of  $\Sigma_1$  intersections of the forward propagated  $D$  and backward propagated  $W^S$  trajectory arcs in the BCR4BP plotted in the Earth-Moon and Sun- $B_1$  rotating frames. Intersections are projected in the  $xy$ -plane for both frames. This map is generated for the November 2020 deployment and using a  $\Sigma_1$  Sun angle of  $\theta_{S_1} = 318^\circ$ .

along the  $D$  trajectories are plotted as diamonds, while the events on the  $W^S$  arcs are marked as asterisks. The same events are plotted in the Earth-Moon and Sun- $B_1$  rotating frames; however, the Earth-Moon rotating frame map is referenced most frequently in this investigation. Each map marker is colored according to the value of the Hamiltonian,  $H$ , for the spacecraft at the time of the event. Additionally,

the spacecraft's  $xy$ -plane velocity direction is plotted as an arrow centered at the marker. Adding this extra information (essentially, a glyph [15]) to each plot aids the visual identification of close matches between  $D$  and  $W^S$  trajectories. However, despite these additional map features, the large number of points on each map make it challenging to visually identify promising intersections.

To alleviate the difficulty of visually identifying intersections that align trajectories from  $D$  and  $W^S$  propagations, an NN algorithm is employed. Using the inputs and weighting from Section 6.2.1, the NN algorithm rapidly identifies the best matches on a given map. As a consequence of the speed of the NN algorithm, it is possible to rapidly search maps across a range of  $\theta_{S_1}$  values. To identify the most promising Phase 1 initial guesses, maps are generated for  $\theta_S$  values from  $0^\circ$  to  $360^\circ$  incorporating an interval of  $1^\circ$ . The top three NN algorithm results from each of these maps are compiled and examined manually to determine the candidates to test as an initial guess. The collection of NN algorithm results are sorted according to the lowest values for discontinuities in either position magnitude, velocity magnitude, Hamiltonian, or in-plane velocity pointing error. Matches that balance discontinuities in each of these categories or possesses extremely low values for the discontinuities in any one quantity are selected for use as an initial guess. The rapid search capability offered by the NN algorithm allows the best matches from hundreds of thousands of possibilities to be quickly identified. This technique improves the quality of the matches that are selected and, therefore, the utility of the initial guesses generated for Phase 1. A close match, identified by the NN algorithm, is highlighted in Figure 6.8. The  $D$  and  $W^S$  trajectories are propagated to the selected intersection times and used as an initial guess for the direct collocation algorithm.

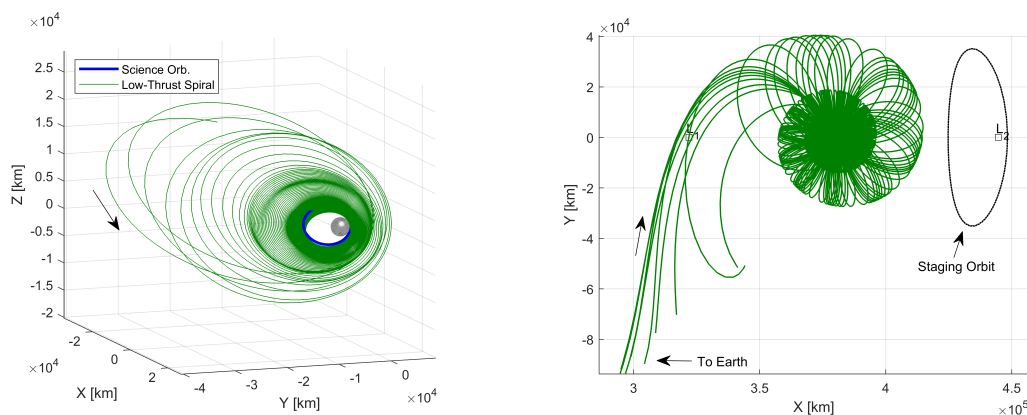
#### 6.2.4 Phase 2 Trajectory Design: Staging Orbit to Science Orbit

Phase 2 along the nominal LIC trajectory consists of the transfer from the staging orbit to the science orbit. An initial guess for this phase is assembled in a manner

similar to Phase 1; intersections with  $\Sigma_2$ , along a range of forward and backward propagated trajectories, are plotted on a map to select the initial guess. In this case, paths along the unstable manifold,  $W^U$ , of the staging orbit comprise the forward propagated trajectory segments, as depicted in Figure 6.3. The backward propagated segments,  $C$ , consist of trajectories propagated with low-thrust, in reverse time, from different true anomaly values along the specified science orbit. The map used to link the forward and backward propagated trajectories consists of intersections with  $\Sigma_2$ , defined by the Sun angle  $\theta_{S_2}$ , along these trajectory segments.

Trajectories along the unstable manifold,  $W^U$ , from the staging orbit offer energy efficient paths for departing the orbit and initiate a spiral down path to the science orbit. Apart from their inverse direction, these trajectories behave similarly to those along the stable manifold and are displayed in Figure 6.6(b). Paths on  $W^U$  offer a variety of locations and epochs at which to depart the staging orbit, and intersections with  $\Sigma_2$  along these trajectories populate the Phase 2 map.

To generate a range of  $C$  trajectories that insert onto the final orbit, backward propagation is initiated from true anomaly values on the orbit that span the full  $360^\circ$  range. The backward propagation assumes an anti-velocity control law; that is, the thrust vector is always oriented along the  $-\hat{v}$  direction in the VNB frame as displayed in Figure 6.7. Recall that the VNB frame is defined relative to the velocity vector as defined in the rotating frame. Moreover, the magnitude of the thrust vector is set equal to the maximum thrust of the LIC engine. Application of this control law produces a trajectory that, in forward time, gradually spirals down to the final science orbit, as plotted in Figure 6.9(a). While the magnitude and direction of the thrust vector are constant for all backward propagated trajectories, using a range of true anomaly values to initialize propagation ensures that each trajectory evolves differently, as apparent in Figure 6.9(b). Trajectories are again propagated until reaching either a maximum time limit or a maximum distance from the Earth. In this case,  $W^U$  arcs are propagated for a maximum time of 100 days while  $C$  trajectory segments are propagated up to 200 days. Both types of trajectories are propagated



(a) Single backward propagated trajectory in the Moon-centered J2000 inertial frame. (b) Multiple backward propagated trajectories in the Earth-Moon rotating frame generated by initiating propagation at different true anomaly values on the science orbit.

Fig. 6.9. Backward propagation from the science orbit with a constant maximum thrust anti-velocity thrust vector.

to a maximum distance from the Earth of  $6 \times 10^5$  km. Intersections with  $\Sigma_2$  along each propagated trajectory are recorded and added to the Phase 2 map.

To generate the  $C$  trajectory arcs, an epoch for insertion onto the science orbit as well as a spacecraft mass at insertion must be assumed. Reasonable inferences for these values introduced during the initial guess formulation are later adjusted by the direct collocation algorithm to ensure a continuous final result. Experience with previous analyses suggests that the total duration of the LIC transfer is approximately one year. This duration is added to the deployment date to produce an estimated epoch at science orbit insertion (SOI). The SOI epoch is then employed to compute a corresponding Sun angle,  $\theta_{SOI}$ , and the angle between the inertial and rotating frames,  $\zeta_{SOI}$ , both required to propagate the  $C$  trajectory arcs in the BCR4BP. Earlier investigations also indicate that LIC consumes approximately half of the available propellant mass to execute the transfer from deployment to science orbit, therefore a final mass at SOI,  $m_{SOI}$ , of 13.25 kg is assumed. While this variable can be adjusted

in the direct collocation algorithm, the initial guess estimate does bias the  $m_{SOI}$  value for the converged Phase 2 solution. However, this bias is overcome by increasing  $m_{SOI}$  via a natural parameter continuation process after an initial solution is converged. Finally, even without suitable insight or intuition for guidance in selecting the epoch and mass at SOI, the robustness of the direct collocation algorithm increases the likelihood that poor estimates for these values still produce useful initial guesses.

Intersections with  $\Sigma_2$  along the  $W^U$  and  $C$  trajectory segments generated for Phase 2 are projected onto the  $xy$ -plane and colored according to their  $H$  value. These three parameters, along with the in-plane direction of the velocity vector, assist with visual identification of close matches between trajectory segments. A sample map is displayed in Figure 6.10(a), where the Sun angle that defines  $\Sigma_2$  is  $\theta_{S_2} = 75^\circ$ . The

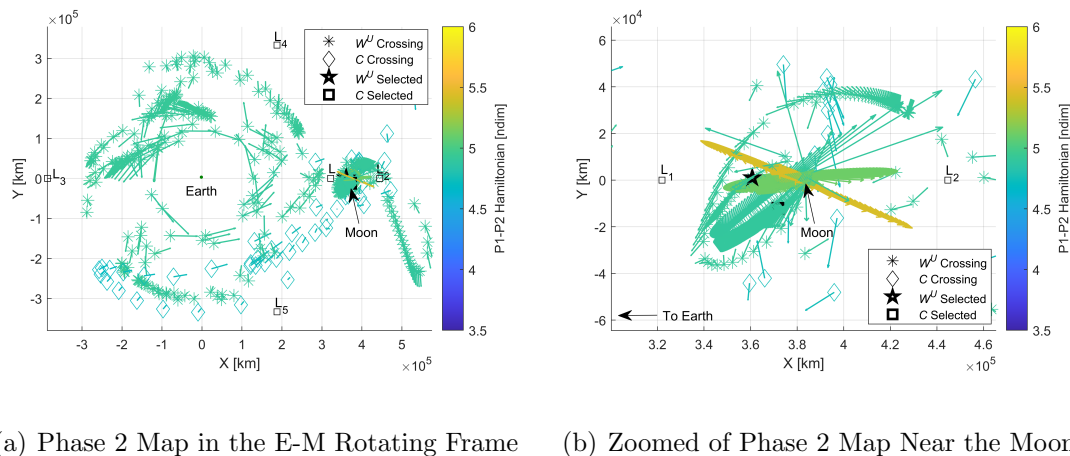


Fig. 6.10. Map of  $\Sigma_2$  intersections of the forward propagated  $W^U$  and backward propagated  $C$  trajectory arcs in the BCR4BP. Intersections are projected in the  $xy$ -plane of the Earth-Moon rotating frame, and the Sun angle selected for  $\Sigma_2$  is  $\theta_{S_2} = 66^\circ$ . The zoomed view displays an intersection selected by the NN search algorithm. This map corresponds to the October 2018 deployment date and assumes an SOI epoch of midnight on September 24<sup>th</sup>, 2019.

intersections that occur along the  $C$  arcs are plotted as diamonds, while those on the  $W^U$  paths are displayed as asterisks. The process employed in Phase 1 for compiling

the best NN algorithm results from maps across a range of  $\theta_S$  values is again employed in Phase 2. The rapid search capability offered by the NN algorithm is especially advantageous in Phase 2 because it is generally more challenging to identify useful matches from the map. This difficulty arises as the nonlinear dynamics near the Moon evolve, increasing the sensitivity of the corrections process. The heightened sensitivity heightens the importance of the construction of initial guesses with small state discontinuities. A close match identified with this process, is highlighted in Figure 6.10(b). The deployment and manifold trajectories propagated to the selected intersection times are then used as an initial guess for the direct collocation algorithm.

Modifications to COLT's nominal collocation scheme enable design of a continuous low-thrust transfer from the staging orbit to the final science orbit for LIC. The low-thrust spiral required to transfer between these two orbits is typically long and includes many revolutions. This type of trajectory is challenging to optimize using the collocation framework implemented in COLT, which employs Cartesian coordinates to represent position and velocity states. Other collocation schemes that utilize modified equinoctial elements (MEE) have successfully optimized low-thrust spiral trajectories [150,151]. However, rather than implement a complex multi-phase collocation scheme that mixes Cartesian and MEE coordinates, a simplified approach is introduced. This strategy divides Phase 2 into two halves: one is solved with direct collocation and the other is explicitly propagated backward in time from science orbit insertion (SOI).

The backward propagated section of the LIC trajectory is updated in the direct optimization process by the addition of three design variables and a constraint. The three design variables govern: the backward propagation time from SOI,  $\tau_{spiral}$ , the true anomaly value on the science orbit at insertion,  $\nu_{SOI}$ , and the spacecraft mass at insertion,  $m_{SOI}$ . These three variables are appended to the design variable vector that is typically employed for direct collocation,  $\mathbf{X}$ , to form the set of design variables used for Phase 2 of the LIC transfer,  $\mathbf{X}_{spiral}$ , i.e.,

$$\mathbf{X}_{spiral} = [\mathbf{X}, \tau_{spiral}, \nu_{SOI}, m_{SOI}]. \quad (6.1)$$

By including these variables in the corrections process, the evolution of the spiraling LIC trajectory is allowed to change and is joined with the section of the transfer that departs from the staging orbit at a match point. A constraint is added to ensure state and mass continuity between these two halves of the LIC trajectory. Experience suggests that convergence is improved when the match point for this constraint is located at least several lunar radii beyond the Moon. This convergence difficulty is due to the increased sensitivity of the constraint partials when the match point is too near the Moon. Therefore, the initial guesses provided by the Phase 2 map are filtered so that the potential match point is located at least 3 lunar radii from the Moon.

With the addition of the three design variables and continuity constraint, a single direct collocation problem is solved to generate a continuous low-thrust transfer from the staging to the science orbit. Because a sub-optimal control law is used for the spiraling portion of the trajectory, the result of the direct collocation algorithm is not a fully optimized low-thrust transfer. However, optimization aids in minimizing the propellant consumed before the explicitly propagated spiraling phase begins. Additionally, because the selected control law ensures the maximum rate of change of the spacecraft's energy, reducing the time required to achieve lunar capture, propellant consumption is also reduced. Finally, after an initial solution for Phase 2 is computed, a continuation process increase the mass delivered to the science orbit. In this approach, a feasible solution with a fixed mass at science orbit insertion,  $m_{SOI}$ , is computed and the value of  $m_{SOI}$  is raised at each continuation step. Despite the sub-optimality of the low-thrust spiral, this approach for designing Phase 2 of the LIC trajectory generates successful trajectories in the BCR4BP that deliver LIC to the desired science orbit while remaining well within the allocated propellant mass. Moreover, this technique achieves this goal without the complexity of a multi-phase collocation scheme.

### 6.2.5 Phase 2 Trajectory Design: Staging Orbit to NRHO

An alternate destination under consideration for LIC is a 9:2 synodic resonant near rectilinear halo orbit (NRHO), henceforth denoted the 9:2 NRHO. This same NRHO currently serves as the nominal orbit for the upcoming Gateway mission. The orbit is a member of the southern halo orbit family evolving from the Earth-Moon  $L_2$  libration point. Transferring to the 9:2 NRHO would afford LIC the opportunity to demonstrate operations in this type of multi-body orbit prior to its use by the Gateway mission. The trajectory design challenge of transitioning from the selected staging orbit to a 9:2 NRHO offers an excellent application of the orbit chain approach demonstrated in previous chapters.

As a result of the flexibility and robustness afforded by the use of the staging orbit and the direct collocation algorithm, it is straightforward to adapt the LIC trajectory design framework to a new Phase 2 destination. Because the 9:2 NRHO is at a higher energy level than the low-altitude science orbit, the change in energy required to reach the NRHO does not necessitate a long low-thrust spiral. Consequently, constructing an initial guess for this alternate Phase 2 transfer scenario employs a simpler orbit chain approach. Initial guess assembly follows the same procedure outlined in Chapter 4, except the periodic orbits employed in this case exist in the BCR4BP rather than the CR3BP. One or more revolutions for each periodic orbit are stacked along the departure and arrival orbits, and the resulting initial guess appears in Figure 6.11. A thrust magnitude of nearly zero and an anti-velocity thrust vector orientation is initially assumed for all segments. This relatively uninformed initial guess is sufficient for the direct collocation algorithm to compute an optimal low-thrust transfer. However, a continuation process is often required to lower the maximum thrust magnitude from a slightly higher value to the 1.24 mN available to LIC.

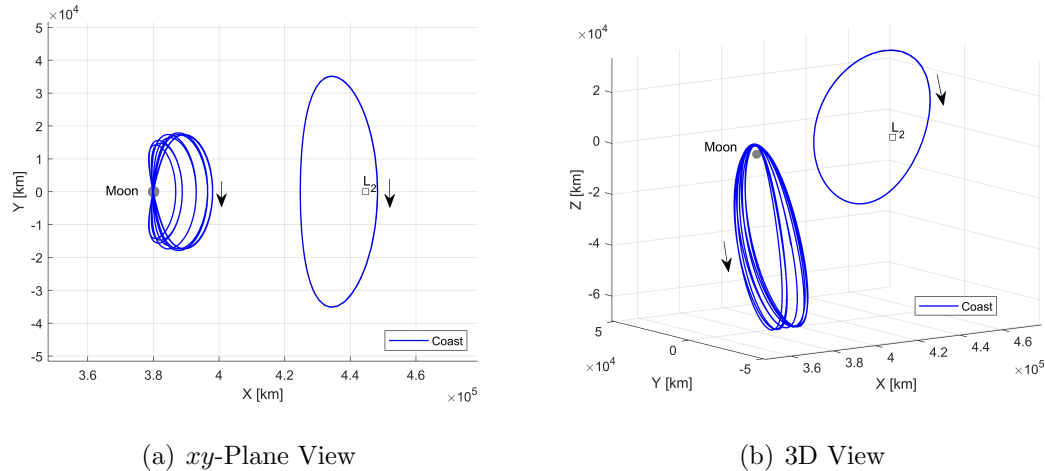


Fig. 6.11. Initial guess for a transfer from the 2:1 synodic resonant E-M  $L_2$  northern halo orbit to the 9:2 synodic resonant E-M  $L_2$  southern near rectilinear halo orbit in the BCR4BP.

### 6.2.6 Design Framework Summary

The proposed trajectory design framework offers a systematic approach for constructing a Lunar IceCube transfer from deployment to the final orbit beginning only with an initial state and epoch. The required steps, described in detail in the preceding sections, are summarized here:

1. Define Lunar IceCube deployment state and epoch.
2. Select staging orbit that splits the LIC transfer into Phase 1 and 2.
3. Create a Phase 1 map by propagating deployment arcs with varying thrust profiles forward in time and trajectories on the stable manifold of the staging orbit backward in time. On the map, record intersections of the hyperplane  $\Sigma_1$  that is defined by the Sun angle  $\theta_1$ .
4. Identify close intersections of forward and backward propagated arcs on the Phase 1 map by employing a nearest neighbor algorithm, and use the corresponding arcs to construct an initial guess for Phase 1.

5. Utilize direct collocation to converge an optimal low-thrust solution for Phase 1 of the LIC transfer.
6. If the destination orbit is a low lunar orbit, then create a Phase 2 map by propagating trajectories forward in time on the unstable manifold of the staging orbit and low-thrust spirals backward in time from different true anomaly values on the final orbit. On the map, record intersections of the hyperplane  $\Sigma_2$  that is defined by the Sun angle  $\theta_2$ .
7. Select close intersections of forward and backward propagated arcs from the Phase 2 map by employing a nearest neighbor algorithm, and use the corresponding arcs to construct an initial guess for Phase 2.
8. If the destination orbit is the 9:2 NRHO, construct an initial guess with an orbit chain technique.
9. Use the result of Steps 6 and 7 or Step 8 to converge a low-thrust solution for Phase 2 of the LIC transfer using direct collocation. Use the delivered mass to the staging orbit from Phase 1 as the initial mass for Phase 2.
10. Combine the results of Phases 1 and 2 and the intervening time on the staging orbit to obtain the complete transfer characteristics.

The standardized procedure outlined by these steps is adaptable to a range of potential launch dates or final orbits. Thus, the baseline LIC trajectory may be quickly adapted to changes in the mission profile that occur prior to launch.

### 6.3 Lunar IceCube Results

The previous framework is effective for designing LIC trajectories from deployment to the destination orbit over a range of potential launch dates. Phase 1 results offering examples of the available transfer geometries are included. Phase 2 results from the staging orbit to both the low lunar orbit and the 9:2 NRHO are constructed. The

Phase 2 results demonstrate the challenges and opportunities in the highly nonlinear lunar environment. A subset of results generated in the BCR4BP are selected for validation in an ephemeris model that includes the Earth, Moon, and Sun.

### 6.3.1 Phase 1 Results: Deployment to a Staging Orbit

An initial guess for Phase 1 of the Lunar IceCube trajectory is assembled by employing the NN search algorithm to identify close matches between intersections of the  $D$  and  $W^S$  trajectories with the  $\Sigma_1$ . The top NN search algorithm results from maps over a range of  $\theta_{S_1}$  values are examined to identify the most promising candidates and the available transfer geometries. One such match is highlighted by black markers in Figure 6.8, where the black square indicates the deployment event and the black five-pointed star denotes the manifold event. The trajectories that correspond to the selected match are plotted in the Sun- $B_1$  and Earth-Moon rotating frames in Figures 6.12(a) and 6.12(b), respectively. These trajectories, and all others that correspond to the map intersections in Figure 6.8, are generated with the November 2020 deployment date. While a discontinuity between the forward and

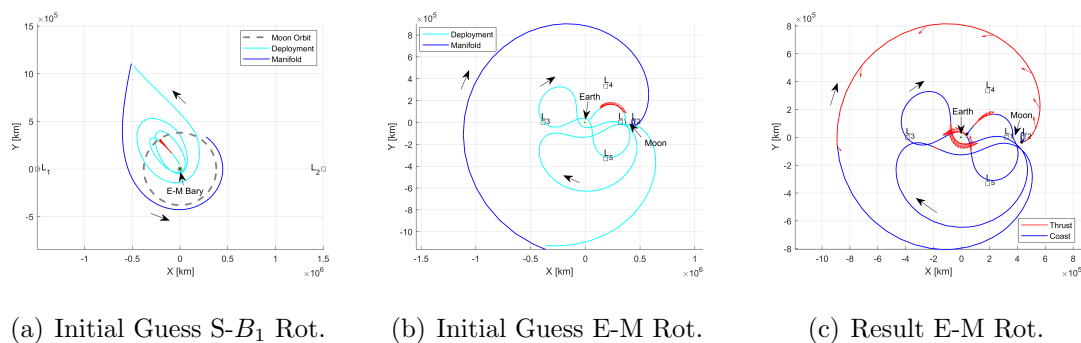


Fig. 6.12. Initial guess and BCR4BP result for Phase 1 of the Lunar IceCube trajectory given a November 2020 deployment date. The resulting transfer requires 117 days and 0.10 kg of propellant. The initial guess is displayed in the Sun- $B_1$  (S- $B_1$ ) and Earth-Moon (E-M) rotating (rot.) frames.

backward propagated trajectories is evident, the NN search criteria used to identify matches between  $\Sigma_1$  crossings yield a promising initial guess. This initial guess is passed to COLT, which eliminates the discontinuity by inserting additional thrust segments. The optimized trajectory in the BCR4BP that results from this initial guess is displayed in Figure 6.12(c), and consumes 0.1 kg of propellant to reach the staging orbit in 117 days. The time of flight (TOF) and mass consumption,  $\Delta m$ , for all Phase 1 transfers examined for this investigation are offered in Table 6.3 located in Section 6.3.4. An initial 8-hour coasting interval following deployment is preserved in the converged solution to allow time for systems checkout prior to the initiation of the first thrust arc. This solution emerges from the collocation algorithm computes this solution with relatively few iterations; moreover, the geometry of the initial guess is generally preserved in the direct collocation result. These two factors indicate that the initial guess identified from the Phase 1 map is useful in guiding the algorithm towards a solution.

The strong influence of the initial guess on the final result is more evident when alternate solutions are examined. For a single deployment date, a variety of transfer geometries offered by the Phase 1 maps are viable. These transfers range from 90 to over 200 days in duration and are primarily distinguished by the number of Earth close approaches and lunar flybys. Generally, the longer duration transfers require less propellant due to the inclusion of additional flybys or the opportunity to include thrust arcs at more optimal times, such as Earth close approach. While launch conditions determine the most favorable transfer geometries, every launch date yields a plethora of options. A Phase 1 transfer generated for the June 2020 launch date, plotted in Figure 6.13, offers an example of an alternate geometry. This transfer possesses no Earth close approaches and instead incorporates several transits around the Earth-Moon system before delivering the spacecraft into the staging orbit. In total, this transfer requires more time and propellant to execute, but avoids the complications associated with implementing an Earth close approach. The June 2020 Phase 1 solution is validated in an ephemeris model and the geometry and propellant

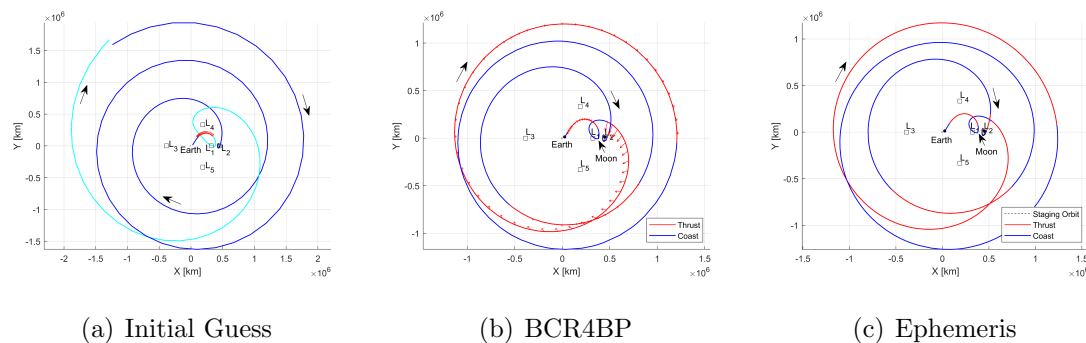


Fig. 6.13. Initial guess (a) and BCR4BP (b) solutions for Phase 1 of the Lunar IceCube trajectory given a June 2020 deployment date. The resulting BCR4BP transfer requires 140 days and 0.21 kg of propellant. The BCR4BP transfer is validated in an ephemeris model (c) where it maintains similar characteristics.

consumption for the resulting trajectory, displayed in Figure 6.13(c), remain nearly identical to the BCR4BP solution. This similarity indicates that, given the current transition process, the BCR4BP result reasonably approximates the transfer in the ephemeris model for Phase 1 of the Lunar IceCube transfer.

The Phase 1 transfer designed for the March 2021 launch date offers an example of a trajectory to the staging orbit with a long time of flight, but which requires very little propellant. The initial guess for this transfer is displayed in Figure 6.14(a) where it is observed that the selected deployment and stable manifold arcs include three close approaches of the Earth. Analysis of these trajectories in the Sun- $B_1$  rotating frame reveals that these close approaches lead to three apoapses with respect to  $B_1$  that occur well beyond the orbital radius of the Moon. The optimized trajectory generated from this initial guess, offered in Figure 6.14(b), preserves much of the geometry from the initial guess. Several thrust arcs are added near the Earth close approaches along the trajectory where these maneuvers incur the largest impact on the subsequent path of the spacecraft. These close approaches of the Earth, rather than the long time of flight, are the primary drivers for this trajectory requiring the least amount of propellant of all the Phase 1 trajectories, only 0.08 kg. Trajectories that include

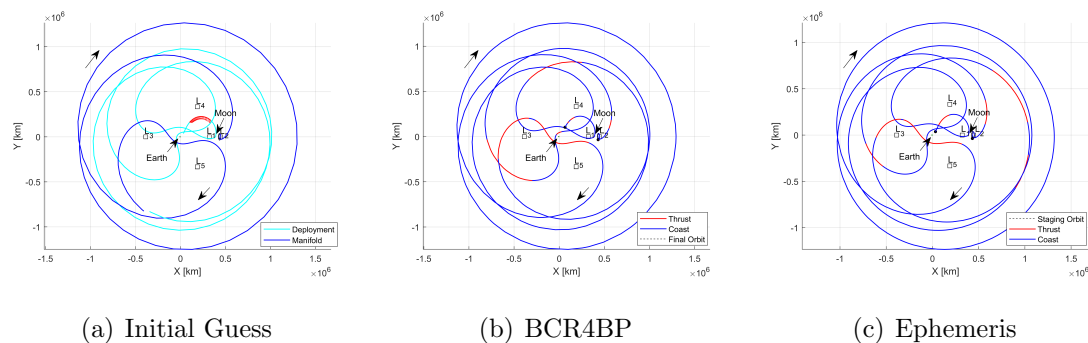


Fig. 6.14. Initial guess (a) and BCR4BP (b) solution for Phase 1 of the Lunar IceCube trajectory given a March 2021 deployment date. The resulting transfer requires 194 days and 0.08 kg of propellant. The BCR4BP transfer is validated in an ephemeris model (c) where it maintains similar characteristics.

multiple Earth close approaches or additional lunar flybys tend to possess longer times of flight, often with a longer duration, thus, seemingly requiring will require less propellant than shorter alternatives. However, the Phase 1 trajectory generated for the June 2020 deployment date demonstrates that a longer time of flight without any additional lunar flybys or Earth close approaches does not inherently reduce propellant consumption. The small change in mass for the Phase 1 trajectory in the BCR4BP is preserved when the trajectory is transitioned to an ephemeris model. Indeed, Figure 6.14(c) demonstrates that the ephemeris result is very similar to the BCR4BP solution. The March 2021 Phase 1 result highlights the benefit of multiple Earth close approaches for reducing propellant costs.

Additional lunar flybys, not just Earth close approaches, also offer propellant savings, without significantly lengthening the time of flight. A trajectory that demonstrates the utility of lunar flybys is computed for the final deployment condition tested in this investigation, a date in October 2018. In the Earth-Moon rotating frame, the initial path for the deployment trajectory appears similar for all four deployment dates. However, examination in the inertial or Sun- $B_1$  rotating frames reveals that the initial Sun angle for each deployment state is quite different. The values of the initial

Sun angle employed for each deployment condition are offered in Table 6.2, included in Section 6.2.3. These differences in epoch, along with changes to the deployment state, cause the paths to the staging orbit to be quite different for each deployment date. The October 2018 Phase 1 trajectory displayed in Figure 6.15 includes two Earth close approaches that appear similar to the November 2020 transfer. However,

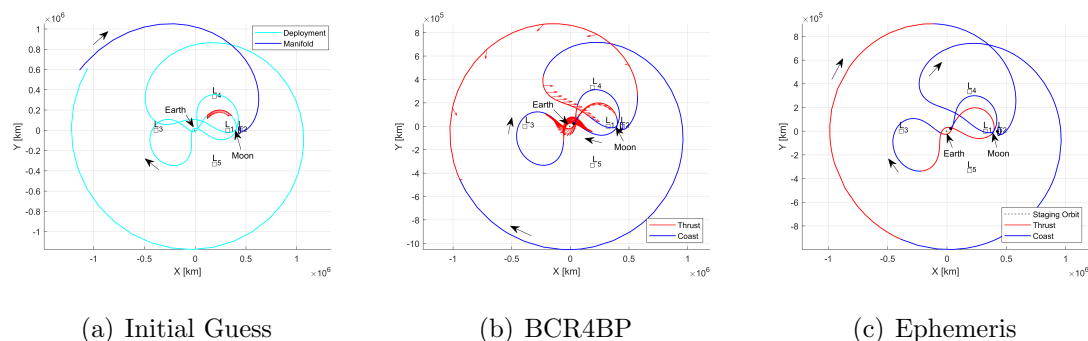


Fig. 6.15. Initial guess (a) and BCR4BP (b) solution for Phase 1 of the Lunar IceCube trajectory given an October 2018 deployment date. The resulting transfer requires 110 days and 0.1 kg of propellant. The BCR4BP transfer is validated in an ephemeris model (c) where it maintains similar characteristics.

this trajectory also incorporates a second lunar flyby, rendering this trajectory the shortest in duration of all the Phase 1 transfers while only requiring slightly more propellant than the similar November 2020 result. The geometry and performance of this transfer also remains consistent when transitioned to an ephemeris model as observed in Figure 6.15(c).

Despite the different deployment dates, all four Phase 1 transfers leverage the tidal forces of the Sun to reach the staging orbit near the Moon. The use of tidal forces is evidenced by the fact that the apoapse furthest from the Earth-Moon barycenter,  $B_1$ , in all four transfers occurs either in the second or fourth quadrants as viewed in the Sun- $B_1$  rotating frame, in Figure 6.16. In these quadrants, the acceleration from the Sun is acting in the same direction as the prograde motion of LIC about the Earth-Moon barycenter,  $B_1$ . Therefore, the Sun's acceleration tends to circularize

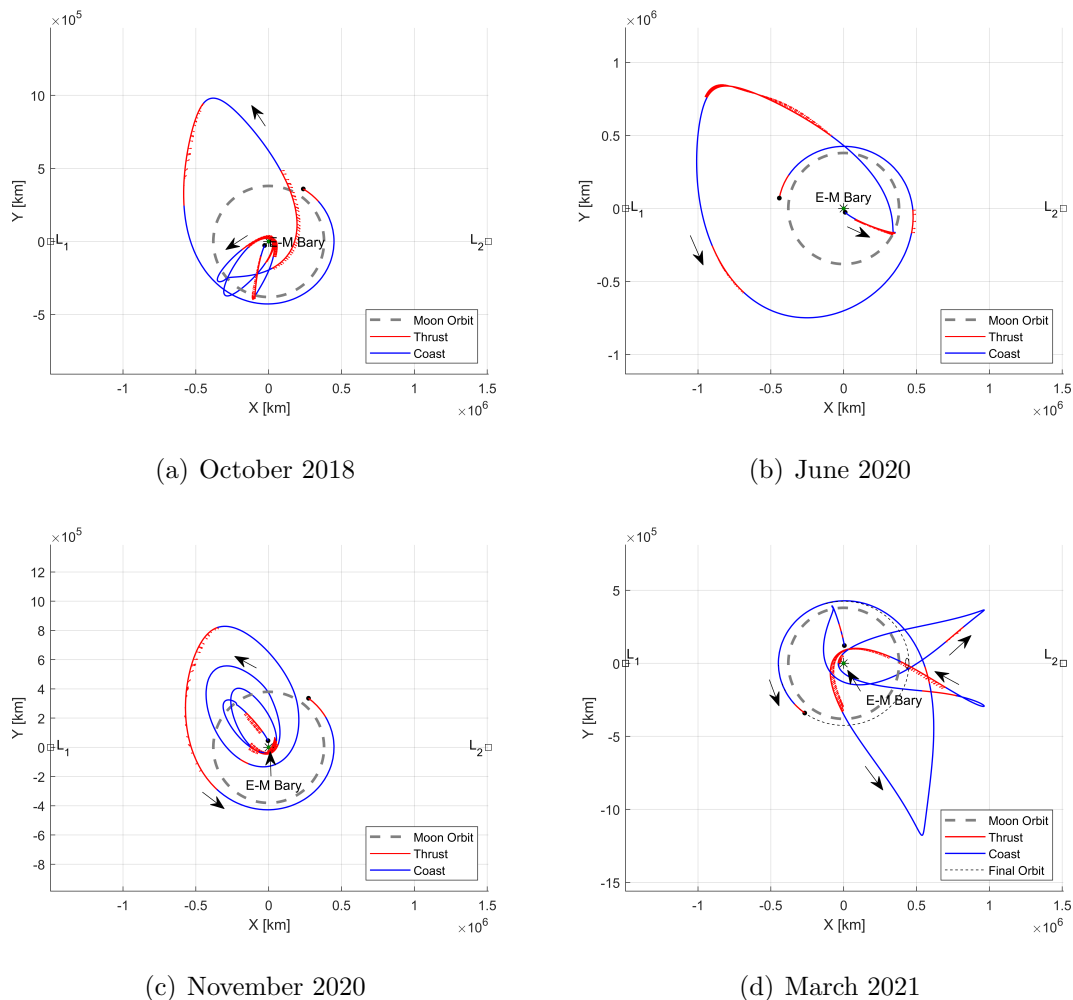


Fig. 6.16. Phase 1 transfers computed in the BCR4BP and displayed in the Sun- $B_1$  rotating frame. For all four transfers the apoapse furthest from the Earth-Moon (E-M) barycenter occurs in the second or fourth quadrants of the Sun- $B_1$  rotating frame. This geometry leverages the tidal forces of the Sun to raise the periapse of LIC about the E-M barycenter to the orbital radius of the Moon.

the LIC orbit about  $B_1$ , helping raise its periapse to the radius of the Moon's orbit. This framework for understanding the influence of a primary body, e.g., the Sun, on trajectories centered around a secondary body, e.g., the Earth, is well documented and has been leveraged for trajectory design by a number of authors [26, 152, 153].

Many different transfer geometries and durations are offered by the NN search results from Phase 1 maps. The examples in Figures 6.12 through 6.15 are a small subset of the variety of options available. By experimenting with the top search results from maps generated with a range of  $\theta_{S_1}$  values, a variety of initial guess geometries lead to an array of optimized solutions. The flexibility of this approach and the diversity of solutions yields highly adaptable designs for different mission constraints and deployment conditions.

### 6.3.2 Phase 2 Results: Staging Orbit to Science Orbit

A solution for Phase 2 of the LIC trajectory is computed in a manner similar to the approach for Phase 1, although some information from the Phase 1 result must be carried over to Phase 2. A close match between the  $\Sigma_2$  hyperplane crossings on a Phase 2 map is identified and the corresponding trajectory segments are employed as an initial guess for a direct collocation algorithm. The direct collocation algorithm then delivers a continuous solution by adding thrust arcs where required. While little information from Phase 1 is required to generate the initial guess for Phase 2, the time of flight and final mass for a specific Phase 1 transfer is necessary to actually converge to a Phase 2 transfer. This information initializes the spacecraft mass and  $\angle_{SOI}$  angle for Phase 2, thus ensuring that Phase 2 is continuous with the previous phase.

Nearby intersections of  $W^U$  and  $C$  arcs on a Phase 2 map are located using the NN search algorithm. An example of a close match between the  $\Sigma_2$  crossings on a Phase 2 map is identified in Figure 6.10(b). Because the staging orbit and the science orbit are significantly out-of-plane, the  $xy$ -plane view of the Phase 2 map in Figure 6.10(b) is deceptive. Hyperplane crossings that appear to overlap in this map may differ significantly when the  $\hat{z}$  position and velocity components are considered. Conversely, potentially useful matches may be obscured if intersections with larger  $+z$  components are plotted on top of them. Thus, use of the NN search algorithm

is even more essential for Phase 2 maps, as it ensures that close matches are not overlooked.

After a promising match is identified, the corresponding trajectory segments are employed to construct an initial guess. The trajectories corresponding to the intersections selected in Figure 6.10(b) are displayed in Figure 6.17. The endpoints along the

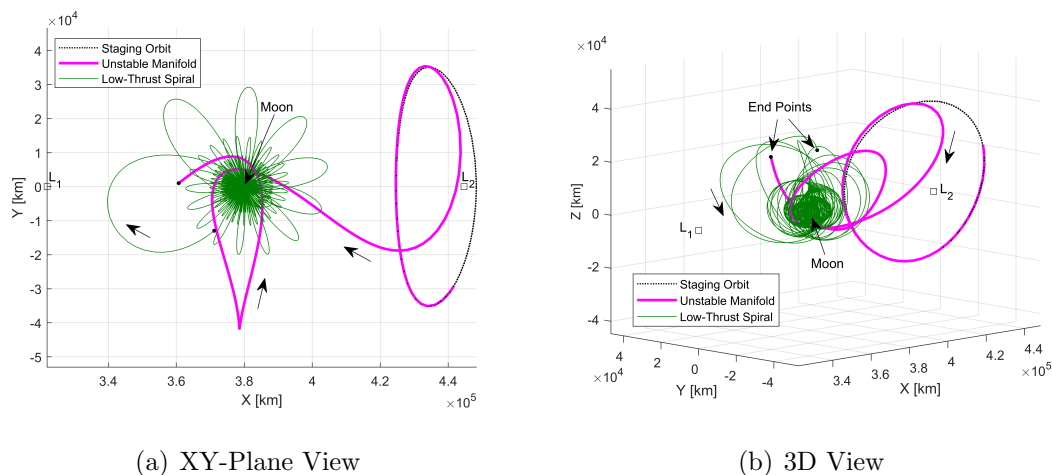


Fig. 6.17. Initial guess for Phase 2 of the Lunar IceCube trajectory. The endpoints of the unstable manifold and the low-thrust spiral trajectory are indicated with a black circle. This initial guess corresponds to the NN match highlighted in Figure 6.10 which is generated for the October 2018 deployment date.

unstable manifold and low-thrust spiral trajectories are indicated with black circles. Continuity between the departure arc from the staging orbit, solved via collocation, and the explicitly propagated low-thrust spiral is enforced by matching these endpoints. While the position and velocity discontinuities between these endpoints are generally smaller in magnitude in Phase 2 as compared to Phase 1, it is frequently more difficult to achieve convergence because these discontinuities occur so near the Moon. However, a number of strategies for improving the likelihood of convergence are available.

Several techniques are employed to assist the direct collocation algorithm in converging to a Phase 2 result. As previously noted, the primary cause of the challenges in convergence is the proximity of the state discontinuities to the Moon. The nonlinear dynamics near the Moon increases the sensitivity of the direct collocation algorithm, thus it is more difficult to achieve convergence. The first strategy employed to improve convergence is simply moving the endpoints of the unstable manifold trajectory and the low-thrust spiral farther from the Moon. To accomplish this shift, the initial guess is generated such that these endpoints are located at least three lunar radii from the center of the Moon. All Phase 2 map crossings closer than this distance are excluded from consideration. Distancing the endpoints and, thus, the eventual match point further from the Moon decreases the sensitivity of the direct collocation algorithm and, therefore, convergence is more likely. In addition to this approach, several features of the direct collocation algorithm are potentially leveraged to achieve convergence. These include: bounding the design variables, scaling variables and constraints, as well as including a minimum radius constraint with respect to the Moon.

The final strategy introduced to increase the likelihood of convergence is providing COLT “more” trajectory on the initial periodic orbit, and therefore more time, with which to achieve the desired transfer. “Stacking” additional revolutions of the staging orbit prior to departure along the unstable manifold path [23]. Four additional revolutions along the staging orbit are added to the initial guess displayed in Figure 6.17. Thus, the initial guess ultimately passed to COLT consists of these four revolutions, the unstable manifold trajectory, and the backward propagation parameters, i.e., the three additional design variables, that produce the low-thrust spiral displayed in Figure 6.17. Stacking additional staging orbit revolutions also accounts for discrepancies between the SOI epoch estimated for initial guess design and the actual SOI epoch determined by the Phase 1 transfer selected to initialize the mass and  $\varpi_{SOI}$  angle in Phase 2. Several iterations of the Phase 2 initial guess design process may be required if the estimated SOI epoch requires too many or too few stacked staging orbit revolutions.

The initial guess displayed in Figure 6.17 is passed to the direct collocation algorithm, COLT, for convergence. From this initial guess, the COLT algorithm delivers the low-thrust transfer in Figure 6.18, which requires approximately 229 days and 0.5 kg of propellant. The solution displayed in Figure 6.18 shows that the stacked

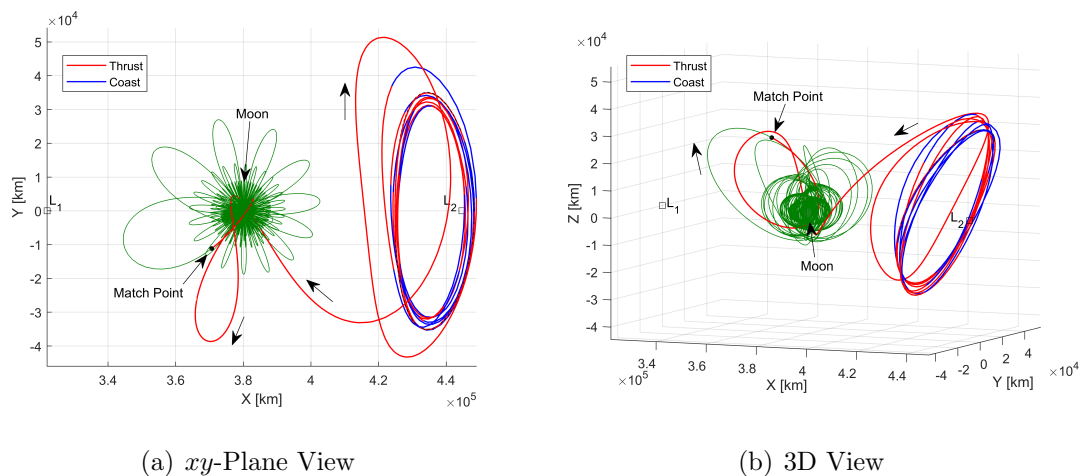


Fig. 6.18. Converged result for Phase 2 of the Lunar IceCube trajectory given the initial guess presented in Figure 6.17. The Phase 1 result for the October 2018 deployment is used to initialize this transfer. The resulting transfer requires 229 days and 0.5 kg of propellant.

staging orbit revolutions included in the initial guess are distributed somewhat by the direct collocation algorithm, thereby demonstrating the utility of adding more trajectory to the initial guess by stacking staging orbit revolutions. These revolutions along with the subsequent lunar flyby achieve the changes in energy necessary to deliver the spacecraft to the beginning of the low-thrust spiral. The distribution of these revolutions is more evident in the three-dimensional view of the transfer offered in Figure 6.18(b). A significant number of lengthy coast arcs are included along the revolutions near the staging orbit which indicates the possibility to reduce the number of staging orbit revolutions stacked in the initial guess for this transfer, thus, reducing the transfer time. After several revolutions, the spacecraft departs the vicinity of the staging orbit and continues through a powered lunar flyby to insert on

the explicitly propagated low-thrust spiral trajectory. This geometry is influenced by the close lunar flyby included in the initial guess.

The Phase 2 transfer converged for the June 2020 deployment date also exhibits geometry that remains near the Moon. In this case, rather than leveraging a lunar flyby, the plane change required to match the beginning of the low-thrust spiral is achieved via repeated revolutions in the vicinity of the staging orbit, as displayed in Figure 6.19. The three-dimensional view of this motion, offered in Figure 6.19(b),

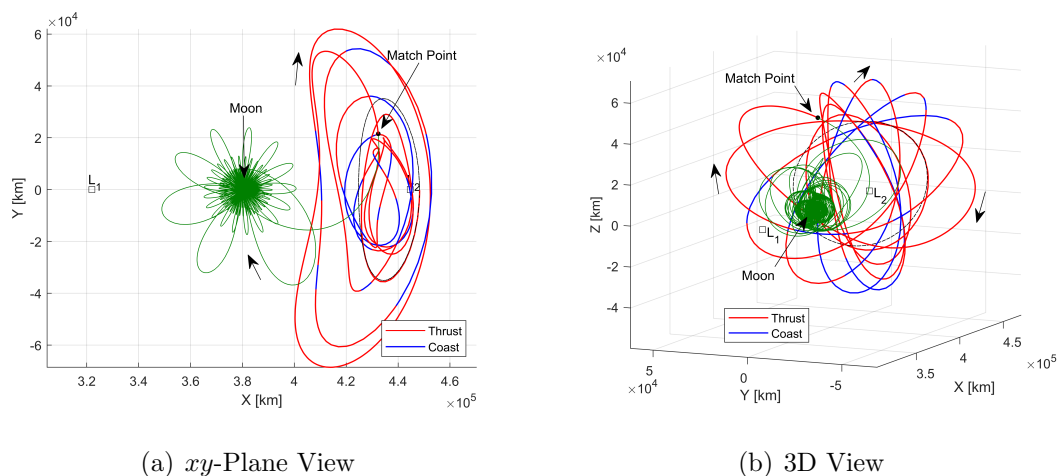


Fig. 6.19. Converged result for Phase 2 of the Lunar IceCube trajectory. This transfer is initialized using the Phase 1 result for the June 2020 deployment.

clearly illustrates the quasi-periodic character of the revolutions near the staging orbit prior to insertion on the low-thrust spiral. Compared to the Phase 2 transfer for the October 2018 deployment date, this June transfer possesses nearly the same time of flight, 230 days, but requires more propellant mass, 0.64 kg. However, this geometry may be preferred because it avoids the complications of a low-altitude lunar flyby.

A Phase 2 transfer similar to the previous two results, but which utilizes fewer revolutions near the staging orbit is computed for the March 2021 deployment date. Two views of the optimized Phase 2 transfer are displayed in Figure 6.20. These plots

illustrate, as compared to the previous two Phase 2 transfers, this transfer requires relatively fewer revolutions in the vicinity of the staging orbit before connecting with the beginning of the spiral down to the science orbit. This characteristic is the result

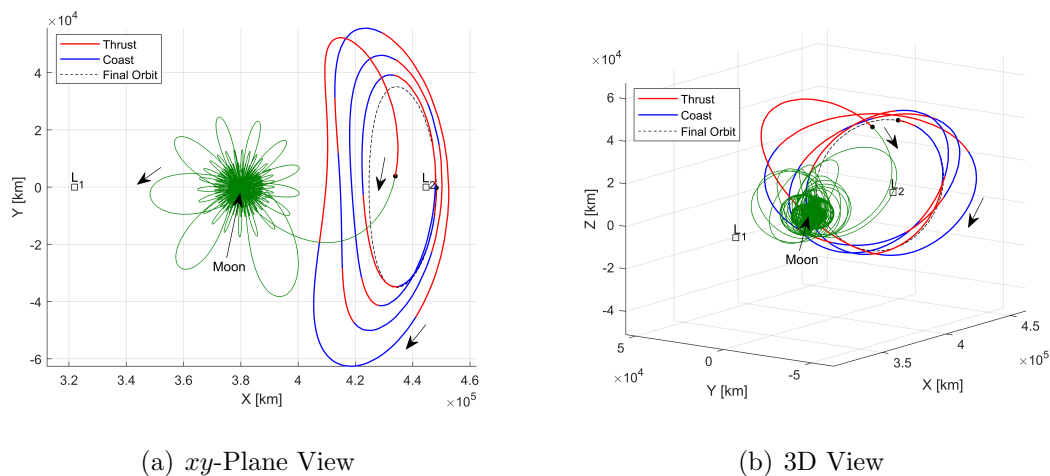


Fig. 6.20. Converged result for Phase 2 of the Lunar IceCube trajectory. This transfer is initialized using the Phase 1 result for the March 2021 deployment.

of employing only one stacked revolution along the staging orbit in the initial guess used to compute this transfer. In this case only one revolution is required to set up an initial guess that leads to convergence. The reduced number of initial revolutions leads to a significantly lower time of flight, i.e., 153 days. This transfer time is nearly 3 months less than the next shortest Phase 2 transfer which requires 229 days. However, a comparable difference is not observed with propellant consumption where 0.51 kg is required for the March 2021 Phase 2 transfer, approximately the same as the requirement for the other dates. The fact that Phase 2 transfer is achieved with comparatively fewer revolutions indicates that it is likely possible to remove extraneous revolutions from the previous two Phase 2 transfers to shorten their transfer time.

Phase 2 transfers generally fall into one of two categories: transfers that remain near the Moon, as seen already, and those that include one or more transits around

the Earth. These categories are succinctly termed interior and exterior type transfers, respectively. The latter of these two options is observed in a Phase 2 initial guess generated for the November 2020 deployment date. A close connection is identified on a Phase 2 map generated with  $\Sigma_2$  defined by a Sun angle of  $\theta_{S_2} = 75^\circ$ , and the resulting initial guess is displayed in Figure 6.21. While the path along the unstable manifold

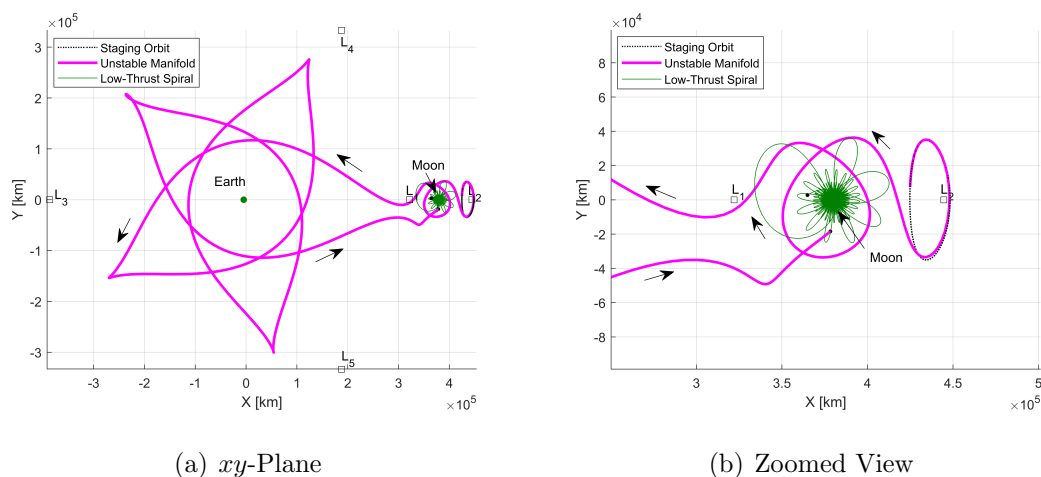


Fig. 6.21. Initial guess for Phase 2 of the Lunar IceCube trajectory generated for the November 2020 deployment date.

that is selected for this initial guess travels far away from the Moon, the actual endpoint is still relatively close to the beginning of the low-thrust spiral. Despite the discontinuity, COLT uses this initial guess to compute the low-thrust transfer plotted in Figure 6.22. The converged result preserves the geometry of the departure from the staging orbit and the initial flyby of the Moon. The subsequent transits around the Earth, as well as the reentry through the  $L_1$  gateway, are modified by the direct collocation algorithm to achieve a mass optimal transfer. In contrast to the previous Phase 2 results, this transfer achieves the required plane change during the transits around the Earth rather than through repeated revolutions near the staging orbit. Because a large section of this trajectory is located far away from either primary, such transfers are often easier to converge. Ultimately, the spacecraft is transferred

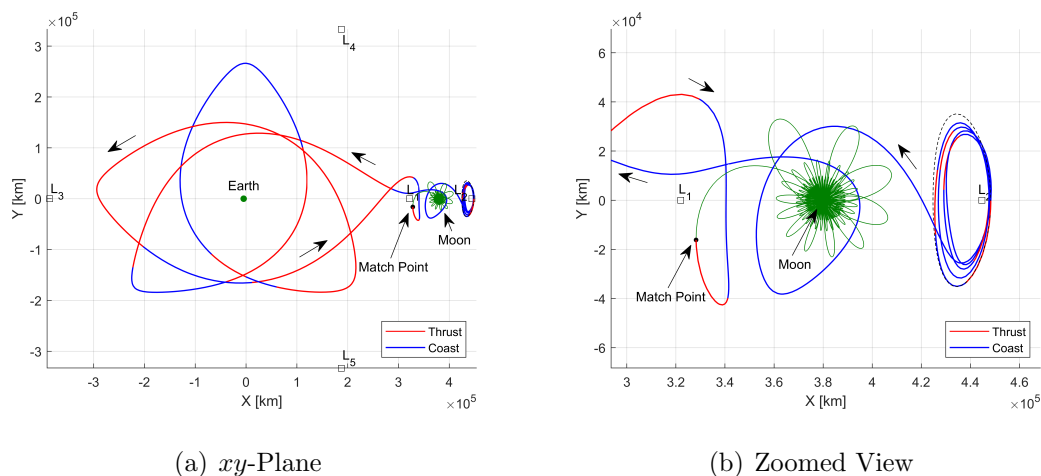


Fig. 6.22. Converged result for Phase 2 of the Lunar IceCube trajectory. This transfer is initialized using the Phase 1 result for the November 2020 deployment.

from the staging orbit to the science orbit in 233 days, requiring 0.65 kg of propellant mass.

The two basic types of Phase 2 transfer options, interior and exterior geometries, are available regardless of the deployment date. This constancy is because the majority of these transfers occur well within the Earth-Moon system where the gravitational influences of these two bodies dominate. In this region the influence of the Sun is sufficiently small that it has less effect on the available geometries regardless of the value of  $\theta_S$ . Thus, it is possible to design Phase 2 of the transfer in the CR3BP, this investigation utilizes the BCR4BP in Phase 2 to maintain consistency with Phase 1. Despite the additional complexity, the proposed framework enables successful design of Phase 2 transfers in the BCR4BP for all four deployment dates examined. A summary of the Phase 2 transfers constructed in the BCR4BP for all of the deployment dates is available in Table 6.3.

The modifications to the COLT algorithm that enable convergence of Phase 2 transfers from the staging orbit to the low-altitude science orbit also add challenges

in producing results in an ephemeris model using the same formulation. There are several reasons that contribute to this difficulty, the first being the increased computation time. Explicit propagation in an ephemeris model is inherently slower than in the BCR4BP because repeated calls to collect the ephemeris data are required. Therefore, each iteration of the direct collocation algorithm requires multiple seconds when converging Phase 2 in an ephemeris model. An additional complication is the difference in the evolution of the explicitly propagated low-thrust spiral between the BCR4BP and ephemeris models. This difference is exhibited in Figure 6.23, where the spirals are quite similar at the beginning of the propagation, but begin to drastically diverge as the spiral is propagated for more time. Some of the divergence between

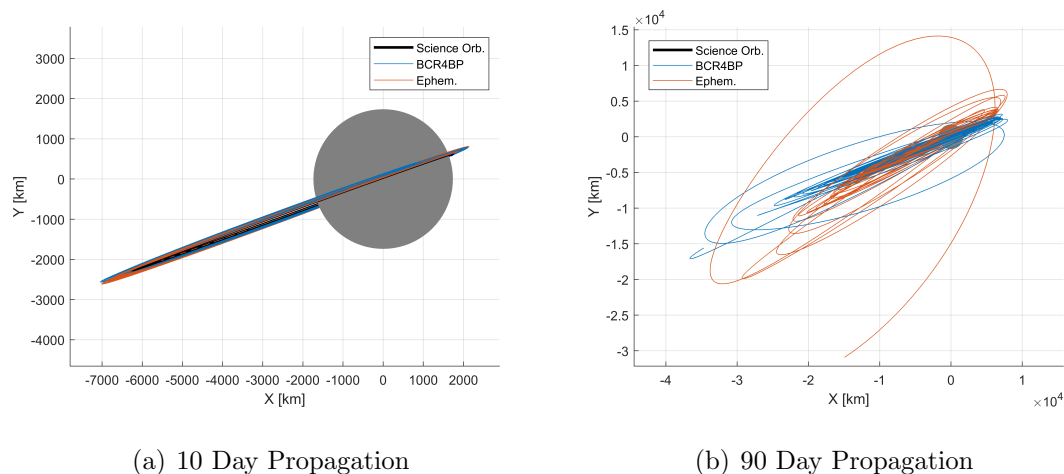


Fig. 6.23. Comparison of low-thrust spiral trajectories propagated in the BCR4BP and ephemeris models and displayed in a Moon-centered inertial frame. The ephemeris model includes the Earth, Moon, and Sun.

the two propagations is due to the accumulation of numerical error; some reflects the differences between the BCR4BP and the ephemeris models. As a result of these differences, a Phase 2 result converged in the BCR4BP will likely incur a large initial error at the match point when transitioned to an ephemeris model. This error alone is not sufficient to eliminate the utility of the corrections strategy employed for Phase 2.

However, the problem is compounded by the requirement for the Phase 2 match point to be located at least 3 lunar radii from the Moon. This guideline, as discussed in Section 6.2.4, requires that the low-thrust spiral be propagated over a longer duration so that the matchpoint is located farther from the Moon; unfortunately this longer duration also increases the error between the BCR4BP and ephemeris spirals. Consequently, distancing the matchpoint from the Moon, which aids convergence in the BCR4BP, hinders convergence in the ephemeris model. The final challenge for converging results in the ephemeris model is the difference between the 2:1 resonant  $L_2$  halo orbit in the BCR4BP and its ephemeris model analog obtained with the current transition process. This difference, as noted in Section 6.2.2, introduces a substantial error between the initial point on the staging orbit in the BCR4BP and ephemeris model. One solution to these challenges is to change the method used to converge Phase 2 transfers in an ephemeris model. An alternate formulation is proposed in Section 6.4 that would likely enable the Phase 2 results converged in the BCR4BP to be successfully transitioned to a full ephemeris model. Another approach for addressing the challenges that arise from the difference between the 2:1 resonant  $L_2$  halo orbit in the BCR4BP and its ephemeris analog is to experiment with the process employed to transition the orbit between models. It is possible that alternate strategies could generate ephemeris trajectories that more closely resemble the BCR4BP orbit.

### 6.3.3 Phase 2 Results: Staging Orbit to NRHO

The orbit chain technique offers a straightforward approach for constructing an optimal low-thrust transfer from the selected staging orbit to a 9:2 NRHO. No intermediate orbit chain links are employed; stacking revolutions on the initial and final orbits is sufficient to converge to a continuous result. However, sometimes it is necessary to utilize a continuation process in  $T_{max}$  to produce a transfer with the correct maximum thrust value. Typically a transfer using  $T_{max} = 1.74$  mN or  $T_{max} = 2.24$  mN is computed initially and then continued to the required value of  $T_{max} = 1.24$  mN.

mN. This continuation process could perhaps be mitigated, or even eliminated, if intermediate orbits, for example members of the  $L_2$  southern halo family in the CR3BP, are included in the orbit chain. Whether or not intermediate orbits are employed, the orbit chain technique is an effective approach for computing transfers from the staging orbit to the 9:2 NRHO.

The direct collocation results, computed from an orbit chain initial guess, deliver the LIC to the 9:2 NRHO in less time and with less propellant than a transfer to the low-altitude science orbit. A sample transfer, displayed in Figures 6.24 and 6.25, requires approximately 6 months and 0.2 kg of propellant mass. This result is com-

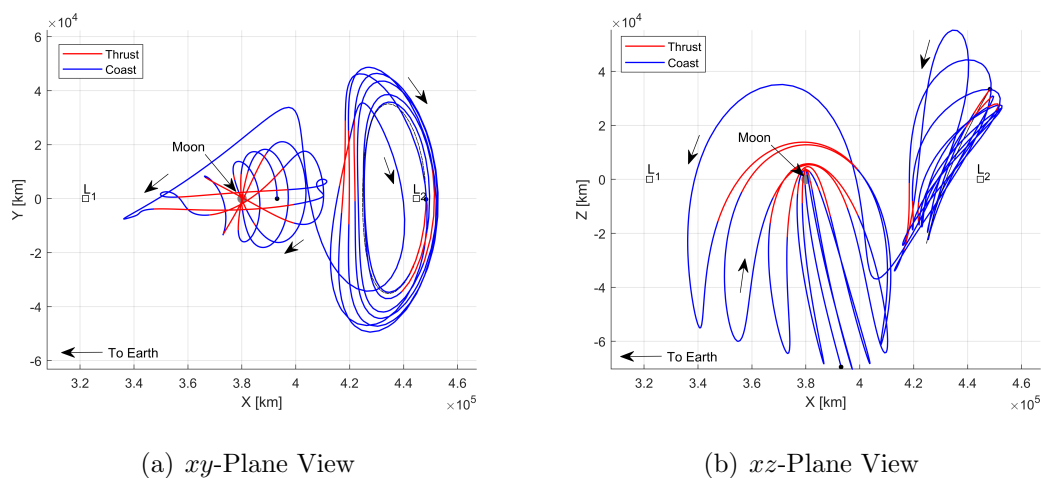


Fig. 6.24. Projections of the optimal low-thrust transfer for LIC from the staging orbit to the 9:2 NRHO in the  $xy$ -plane and  $xz$ -planes. This transfer is initialized using the Phase 1 result for the March 2021 deployment.

puted assuming an initial launch date in March 2021; however, similar solutions that employ the other three launch dates are also computed. The same orbit chain initial guess delivers transfers for all four dates. Only the initial spacecraft mass and value of  $\mathcal{J}_{SOI}$  are altered for each launch date to match the results from the Phase 1 transfer to the staging orbit. The orbit chain initial guess is composed of three stacked copies of the 2:1 halo orbit and one 9:2 NRHO. As a single orbit period includes multiple

revolutions for both orbit types, the number of revolutions observed in the initial guess and the converged result is greater than the number of stacked orbits. Because the initial guess for all four deployment dates remains largely the same, the geometry of all four resulting transfers is very similar. Therefore, only plots of the transfer computed for a March 2021 deployment are displayed. The differences between the four transfers are more clearly highlighted when their thrust profiles and total propellant consumption are compared.

The orbit chain initial guess that is utilized for all four deployment dates is manipulated by the direct collocation algorithm to achieve a continuous and optimal final result. The direct collocation algorithm distributes the stacked revolutions of the 2:1 halo orbit into a quasi-periodic like structure that helps achieve the plane change necessary to transfer to the 9:2 NRHO. This behavior is similar to some of the transfers to the low-altitude lunar orbit observed in the previous section. The transfer from the staging orbit to the vicinity of the 9:2 NRHO requires only 4 months out of the full 6 month total time of flight. The final two months are spent approximately following the structure of the 9:2 NRHO with brief periods of thrusting near periapse. Because the majority of this section of the trajectory consists of coast arcs, it is likely that some of these revolutions near the Moon could be removed to shorten the time of flight of the transfer. The thrust profile for the transfer, in Figure 6.25(b), demonstrates the short duration of the thrust arcs that occur in the final two months of the transfer.

The characteristics of the staging orbit to 9:2 NRHO transfers computed for all four deployment dates are largely preserved when they are transitioned to an ephemeris model. The ephemeris version of the transfer, computed for a June 2020 deployment date, is offered in Figure 6.26. The primary difference in geometry between the transfers computed in the BCR4BP and ephemeris models is that the ephemeris repeated revolutions near the Moon possess apoapses that are less distributed in the  $\hat{x}$  direction. This trend is also observed when transitioning the ballistic BCR4BP 9:2 NRHO to an ephemeris model. Generally, the apoapse locations collapse towards

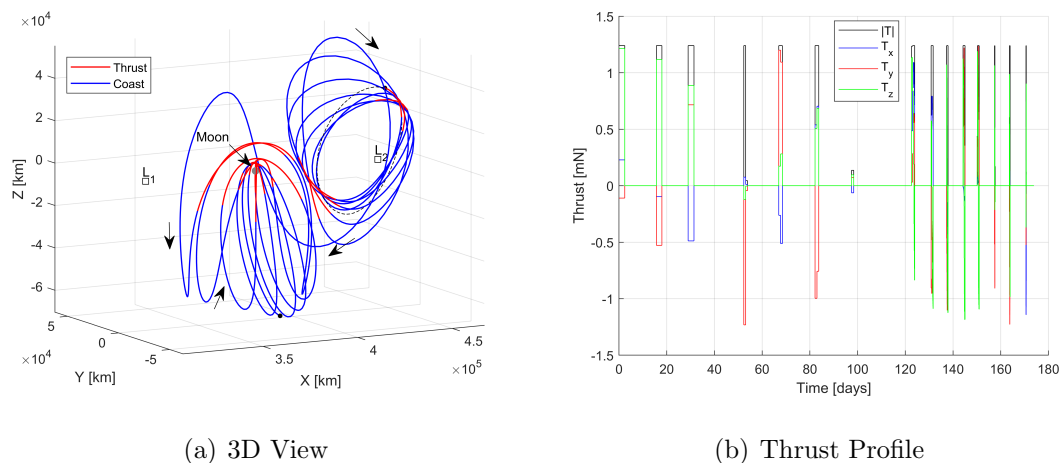


Fig. 6.25. Three-dimensional configuration space view and the thrust profile of the optimal low-thrust transfer for LIC from the staging orbit to the 9:2 NRHO. This transfer is initialized using the Phase 1 result for the March 2021 deployment.

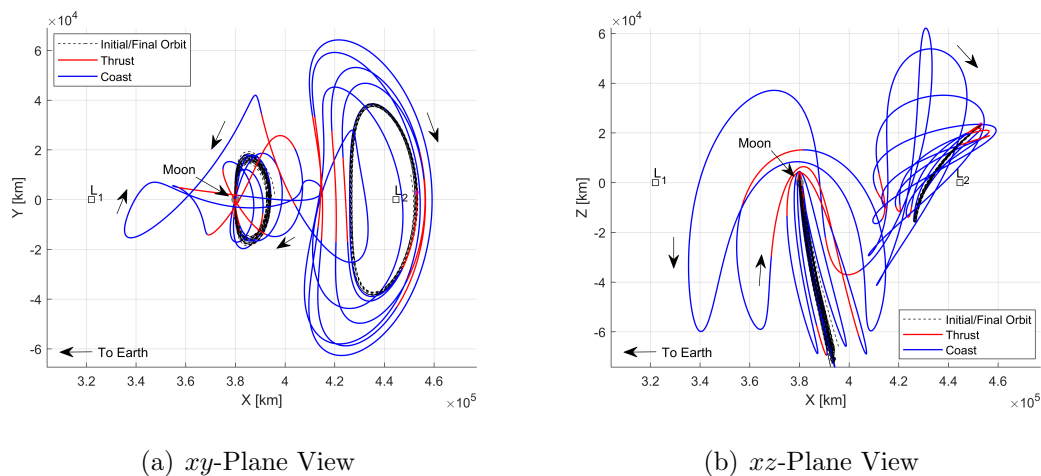


Fig. 6.26. Projections of the optimal low-thrust transfer for LIC from the staging orbit to the 9:2 NRHO in the  $xy$ -plane and  $xz$ -planes. This transfer is initialized using the Phase 1 result for the March 2021 deployment.

the  $x$  position of apoapse on the CR3BP 9:2 NRHO. Therefore, it is not surprising that this same behavior is observed in the transfer to the 9:2 NRHO. This change in

geometry renders the location of the final insertion point along the BCR4BP transfer onto the 9:2 NRHO a critical factor for ensuring a smooth transition to an ephemeris model. If the final insertion point on the BCR4BP 9:2 NRHO is one of the outer revolutions of this orbit, i.e., a revolution with a maximum deviation along the  $\hat{x}$ -axis with respect to the apoapse location of the CR3BP NRHO, then a large discrepancy exists between the final point on the BCR4BP transfer and the insertion point on the ephemeris 9:2 NRHO. This discrepancy is a result of the fact that the apoapse location of the ephemeris 9:2 NRHO is more similar in geometry to the CR3BP 9:2 NRHO than its BCR4BP counterpart. If the insertion point on the 9:2 NRHO is selected appropriately for the BCR4BP transfer, then the overall geometry of the transfer is retained in the transition to the ephemeris model. However, the thrust profile is likely altered so that the ephemeris model transfer requires slightly more or less propellant than the BCR4BP result, depending on the deployment date as apparent in Table 6.6.

#### 6.3.4 Combined Transfer Trajectory Summaries

Combining the results computed for Phases 1 and 2 of the LIC trajectory yields a complete deployment to destination orbit trajectories. Discrepancies between the value of the Sun angle at the end of Phase 1 and the beginning of Phase 2 are accommodated by “waiting” in the staging orbit until the desired Sun angle occurs. For this reason, up to one synodic period of additional transfer time is generally added to the total transfer time of flight to accommodate this phasing time. The results demonstrate the flexibility and robustness of the method; however, each transfer is not necessarily the most optimal trajectory for each deployment date in terms of propellant consumption or time of flight. While it is possible to improve performance with respect to these parameters, all trajectories here reach the final orbit with a time of flight of about one year or less and with well over one third of the available

propellant mass remaining. This level of performance is similar to that observed for previous transfers developed with alternate techniques.

### Transfers to the Low-Altitude Science Orbit

The LIC trajectories computed in the BCR4BP, from deployment to the low-altitude lunar orbit, are summarized in Table 6.3. For these trajectories, the maximum phasing time required is just over 10 days and the minimum is less than one day. Over two thirds of the total time of flight (TOF) is spent in Phase 2, where the long transfer to the beginning of the low-thrust spiral is followed by the lengthy spiral itself. Substantial time savings could be achieved by developing a strategy to reduce the TOF of this phase. In total, all four transfers reach the science orbit about one year after deployment.

Table 6.3.

Summary of sample transfers to the low-altitude lunar orbit for all four deployment dates, computed in the BCR4BP. Given characteristics are time of flight (TOF), change in mass ( $\Delta m$ ), and final mass.

Deployment Date	Phase 1		Phasing	Phase 2		Total		Final
	$\Delta m$	TOF	Time	$\Delta m$	TOF	$\Delta m$	TOF	Mass
	[kg]	[days]	[days]	[kg]	[days]	[kg]	[days]	[kg]
Oct. 9 <sup>th</sup> , 2018	0.11	109.82	7.72	0.49	228.87	0.60	346.31	13.40
Jun. 27 <sup>th</sup> , 2020	0.21	139.90	0.89	0.64	229.85	0.85	370.64	13.15
Nov. 6 <sup>th</sup> , 2020	0.10	117.39	10.24	0.55	233.39	0.65	361.02	13.35
Mar. 1 <sup>st</sup> , 2021	0.08	194.46	24.93	0.51	153.14	0.59	372.54	13.41

The transfer times and propellant consumption values in Table 6.3 are comparable to past baseline trajectories. While some of the transfers computed within this framework require more time and propellant than previous baseline solutions, several

steps are available that may reduce these parameters. First, some of the staging orbit revolutions added in Phase 2 can be removed. While the additional staging orbit revolutions in the the initial guess are useful to achieve convergence, it may be possible to remove them after a transfer is converged. For example, some of the revolutions near the staging orbit that include long coast arcs, as seen in Figure 6.19, could likely be removed. Removing excess trajectory arcs will reduce transfer time. Second, using a multi-stage collocation algorithm to solve Phase 2 increases the mass delivered to the final orbit, particularly because the majority of propellant consumption occurs in this phase. A multi-stage approach would permit the low-thrust spiral to the science orbit to be fully optimized, thereby increasing  $m_{SOI}$ . These two steps lead to reductions in both time of flight and propellant consumption for the LIC transfer; the latter step is discussed in Section 6.4 along with other profitable areas on which to focus future work.

Three of the four transfers computed for Phase 1 of the LIC trajectory are verified in an ephemeris model that includes the Earth, Moon, and Sun. In contrast to Phase 2 transfers to low lunar orbit, results from Phase 1 analysis in the BCR4BP are often relatively straightforward to transition to an ephemeris model. An exception is the case of the November 2020 deployment date and this instance suggests potential improvements to the proposed framework. A summary of the LIC Phase 1 transfers that are successfully transitioned to an ephemeris model is offered in Table 6.4. In terms of both geometry and propellant consumption, the BCR4BP and ephemeris results for the Phase 1 transfers match quite closely, indicating that the BCR4BP is a fitting model for designing this phase of the LIC trajectory.

The failure of the November 2020 Phase 1 transfer to transition to an ephemeris model is likely due to an unfortunate combination of the geometry of the initial lunar flyby and the position of the Earth and Moon at the initial epoch. When viewed in the Earth-Moon rotating frame, the November 2020 transfer is the only one of the Phase 1 transfers whose initial lunar flyby passes between the Earth and the Moon rather than transiting around the far side of the Moon. At the same time

the actual distance between the Earth and the Moon shortly after the November 2020 deployment is roughly 20000 km less than the constant distance of 384748 km assumed in the BCR4BP. The confluence of the flyby geometry and the nearness of the Moon implies that the Moon is actually too close to achieve the desired flyby in an ephemeris model. This discrepancy likely leads the direct collocation algorithm to fail as it attempts to adjust this very sensitive section along the Phase 1 trajectory. Unfortunately, with the current framework, a flyby geometry that passes on the far side of the Moon cannot be achieved due to the simplistic way the initial thrust profile is defined. An alternate initial thrust profile could be achieved if a  $B$ -plane targeting procedure was employed to obtain a specific configuration for the initial lunar flyby. Potential alterations of the Phase 1 initial guess generation procedure that allow greater flexibility for achieving a desired flyby geometry are discussed in the final section of this chapter.

Table 6.4.

Summary of sample Phase 1 transfers from deployment to the staging orbit, computed in an ephemeris model. Given characteristics are time of flight (TOF), change in mass ( $\Delta m$ ), and final mass.

Deployment Date	Phase 1		Final
	$\Delta m$ [kg]	TOF [days]	Mass [kg]
Oct. 9 <sup>th</sup> , 2018	109.82	0.10	13.90
Jun. 27 <sup>th</sup> , 2020	139.90	0.21	13.79
Nov. 6 <sup>th</sup> , 2020	–	–	–
Mar. 1 <sup>st</sup> , 2021	194.46	0.08	13.92

## Transfers to the 9:2 NRHO

The LIC trajectories that arrive at the 9:2 NRHO require lower times of flight and less propellant than those that reach the LLO. This trend is expected, because the 9:2 NRHO possesses a substantially higher energy than the LLO, so less time and propellant is required to decrease the energy from that of the staging orbit. A summary of the transfers computed in the BCR4BP from deployment to the 9:2 NRHO for four different deployment dates is offered in Table 6.5. Note that the Phase 1 results in Table 6.5 are the exact same as those in Table 6.3 because changes to the Phase 2 destination do not effect the results of Phase 1. This consistency emphasizes the flexibility of the staging orbit approach, one of its key strengths. The BCR4BP transfers summarized in Table 6.5 all deliver LIC to the NRHO within about a year or less and with more than two thirds of its propellant mass remaining.

Table 6.5.

Summary of sample transfers to the 9:2 NRHO for all four deployment dates, computed in the BCR4BP. Given characteristics are time of flight (TOF), change in mass ( $\Delta m$ ), and final mass.

Deployment Date	Phase 1		Phasing	Phase 2		Total		Final
	$\Delta m$	TOF	Time	$\Delta m$	TOF	$\Delta m$	TOF	Mass
	[kg]	[days]	[days]	[kg]	[days]	[kg]	[days]	[kg]
Oct. 9 <sup>th</sup> , 2018	0.11	109.82	7.72	0.22	173.92	0.33	291.46	13.67
Jun. 27 <sup>th</sup> , 2020	0.21	139.90	0.89	0.19	173.92	0.4	314.71	13.60
Nov. 6 <sup>th</sup> , 2020	0.10	117.39	10.24	0.26	173.92	0.36	301.54	13.64
Mar. 1 <sup>st</sup> , 2021	0.08	194.46	24.93	0.07	173.92	0.14	393.31	13.86

The Phase 2 transfer to the 9:2 NRHO does not require a long low-thrust spiral, therefore, many of the complications discussed in Section 6.3.2 that add convergence difficulties in transferring to the science orbit in an ephemeris model no longer arise.

Thus, it is possible to transition this type of Phase 2 trajectory from the BCR4BP to an ephemeris model and to deliver end-to-end ephemeris transfers. Key parameters for these ephemeris transfers from deployment to the 9:2 NRHO are summarized in Table 6.6. While the propellant consumption for these transfers varies somewhat between BCR4BP and ephemeris models, the results are sufficiently similar that the BCR4BP result still offers a reasonable approximation of the ephemeris solutions.

Table 6.6.

Summary of sample transfers to the 9:2 NRHO for all four deployment dates, computed in an ephemeris model. Given characteristics are time of flight (TOF), change in mass ( $\Delta m$ ), and final mass.

Deployment Date	Phase 1		Phasing	Phase 2		Total		Final
	$\Delta m$	TOF	Time	$\Delta m$	TOF	$\Delta m$	TOF	Mass
	[kg]	[days]	[days]	[kg]	[days]	[kg]	[days]	[kg]
Oct. 9 <sup>th</sup> , 2018	0.11	109.82	7.72	0.25	173.92	0.36	291.46	13.64
Jun. 27 <sup>th</sup> , 2020	0.21	139.90	0.89	0.17	173.92	0.38	314.71	13.62
Nov. 6 <sup>th</sup> , 2020	–	–	10.24	0.17	173.92	0.17	184.16	13.83
Mar. 1 <sup>st</sup> , 2021	0.08	194.46	24.93	0.10	173.92	0.18	393.31	13.82

## 6.4 Concluding Remarks

This investigation presents a framework for constructing an LIC trajectory from deployment to the final orbit. The approach utilizes dynamical structures available in the BCR4BP along with the robust properties of direct collocation to create a trajectory design framework capable of addressing the LIC spacecraft’s limited control authority and need for adaptability. Employing a staging orbit to divide the trajectory design problem into two distinct phases eases the design challenge by permitting solutions to each phase to be developed largely independently of one another. The

use of a staging orbit and two phase strategy also enables the final destination of LIC to be easily changed from a low altitude lunar orbit to a 9:2 NRHO without the need to redesign the post-deployment lunar approach.

Results indicate that the proposed framework generates continuous trajectories in the BCR4BP that deliver LIC to its final orbit with a reasonable time of flight and well within the allocated propellant mass. The use of maps and a nearest neighbor algorithm to design each phase of the LIC trajectory offers many options for geometry and other key transfer characteristics. This is particularly true for Phase 1, where transfers with either no or many additional lunar flybys can be designed by selecting different map intersections. This flexibility enables the proposed strategy to adapt to changes in launch date, a trait that is demonstrated by providing complete trajectory designs for four different launch dates. Phase 2 of the LIC transfer exhibits less variation in geometry, but even here there are differences to be found as illustrated by the exterior and interior transfer types in Section 6.3.2. Generally Phase 2 trajectories are more challenging to converge and greater care must be taken when setting up the initial guess and direct collocation algorithm.

Many of the results generated in the BCR4BP with the proposed framework can be transitioned to an ephemeris model with minimal modifications. Section 6.3.4 provides tables that summarize results computed in the BCR4BP and ephemeris models using the proposed methodology. These tables demonstrate that the differences in propellant consumption between solutions generated in both models is small compared to the total available propellant mass. Moreover, plots of the ephemeris trajectories in configuration space presented in the preceding sections show that the actual geometry is likewise quite similar. Unfortunately, the methods employed to converge the Phase 2 LIC trajectories from the staging orbit to LLO do not translate well to an ephemeris model making it difficult, if not impossible, to transition these results using the current approach. However, this does not mean that these results cannot be replicated in a higher fidelity model. Rather, a different approach for achieving this transition is required and is an area for future work.

Creating and optimizing low-thrust spiral trajectories like the one found in this study is a well-established sub-field within the discipline of astrodynamics. A variety of approaches with various strengths and weaknesses have been developed to generate optimal low-thrust spirals. The strategy employed in this study is one of the simplest possible techniques: explicit propagation with continuous anti-velocity thrusting. As the approach is modified to be compatible with the existing direct collocation tools, the final result of the process is a sub-optimal result. Because of the simplicity and alterations, the suggested procedure, which is already challenging to use in the BCR4BP, is infeasible in an ephemeris model, as discussed at the close of Section 6.3.2. The inability to transition the spiraling Phase 2 transfers to an ephemeris model is more due to the inadequacy of the tools than the discrepancy between models. Therefore, a change in the tools employed will likely enable the generation of ephemeris versions of Phase 2 transfers to the LLO. Many alternate techniques are available; however, one of the most promising may be a collocation scheme that parameterizes the low-thrust spiral using modified equinoctial elements (MEE) as presented by Falck or Olikara [150, 151]. A primary reason that the strategies employed by these authors are better suited for long spiraling trajectories is that when formulated using the MEEs, the values of the equations of motion change more slowly compared to when Cartesian coordinates are used. This behavior allows the spiraling trajectories to be discretized into fewer segments, thus making the direct collocation problem tractable by reducing its size. A *multi-phase* direct collocation algorithm could combine the current parameterization employed in COLT and a new MEE parameterization to pose a single direct optimization problem that can be solved to generate a fully optimal transfer from the staging orbit to LLO. Implementing these changes is nontrivial. However, the final result will be a tool that not only generates more optimal transfers in the BCR4BP, but is also able to transition these transfers to an ephemeris model.

An area for future work that could lead to more optimal Phase 1 solutions is to construct the initial deployment trajectory by targeting a B-plane coordinate rather

than varying a constant angle,  $\alpha$ , in the VNB frame. Propagating deployment trajectories with a range of fixed thrust vector directions in the VNB frame is a fast but simplistic way of generating an array of options for the initial post-deployment path. This approach can omit some deployment trajectories that are not attainable with such a simple thrust profile. Targeting a B-plane coordinate instead will produce a more comprehensive set of potential flyby trajectories, and the complete set of flyby options may include a path that produces a more optimal Phase 1 result than could have been found with the current approach. Additionally, targeting a B-plane is the technique that is actually used during spacecraft operations to achieve a desired flyby, therefore utilizing this method in the design process could ease the transition to implementing the final trajectory design. The primary disadvantage of targeting a B-plane rather than selecting a fixed thrust direction is that the former option requires more computational time, because the targeting process will require multiple iterations to achieve convergence for each target. However, this increase in time may be offset by the broader array of flyby options that result. Further study will be required to understand whether this trade-off is worthwhile.

Examining alternate staging orbits and conducting missed thrust analysis are two additional areas where future work should focus. The motivation for the selection of the staging orbit employed in this investigation is detailed in Section 6.2.2, but other staging orbit candidates may meet some or all of the criteria used in this process. In particular, quasi-periodic orbits (QPO) about the  $L_2$  libration point offer a greater range of staging orbit options and invariant manifold geometries. The incorporation of BCR4BP QPOs into the proposed LIC trajectory design framework would expand the array of manifold paths available for designing Phases 1 and 2; this inclusion could lead to initial guesses with reduced state discontinuities and perhaps more optimal transfers. Finally, missed thrust analysis is an essential step in the low-thrust mission design process, as it reveals the sensitivity of a given low-thrust trajectory to unexpected thrust outages. The LIC trajectories designed in this investigation include many long duration thrust segments, and, particularly in Phase 2, these

segments occur in the sensitive regions near one of the primary bodies. Missed thrust analysis is critical for determining if these and other thrust segments are so sensitive that a thrust outage could lead to a catastrophic course deviation. Furthermore, LIC's limited power necessitates that thrust segments occasionally be interrupted to perform other essential tasks, e.g., communication back to Earth. A missed thrust analysis will indicate at what times it is most convenient to perform these activities.

Many avenues for future work are apparent, and pursuing these topics would enhance the accuracy and adaptability of the proposed framework. Even without these potential additions, the methodology presented in this chapter offers a systematic approach for constructing an LIC trajectory from deployment to final orbit. This procedure is adaptable to changes in launch date and generates transfers that fall within the time of flight and propellant mass allotted to this phase of the LIC mission. Lastly, the proposed framework is applicable to other small satellite missions that will be deployed as secondary payloads on launches similar to Artemis-1. Its utility reaches well beyond the present application.

## 7. CONCLUSION

The promise of low-thrust propulsion technology continues to increase as research in this area produces more powerful engines. Further development of methods for low-thrust trajectory design will enable mission designers to fully harness the potential of this evolving technology, and the framework presented in this investigation offers one such advancement. Combining the strengths of existing orbit chain and direct collocation strategies yields an overall framework for low-thrust trajectory design that is intuitive, flexible, and robust. This strategy is not only demonstrated with straightforward example problems, but with application to the challenging trajectory design scenarios encountered by the Gateway and Lunar IceCube spacecraft. The results of these sample applications are summarized here and recommendations for future work are offered.

### 7.1 Investigation Summary

The dynamical models and optimal control theory utilized in this investigation are presented before the proposed framework is outlined and tested. The CR3BP and BCR4BP dynamical models are employed in the Gateway and Lunar IceCube sample problems, respectively. These simplified dynamical models include the essential forces relevant to each sample application, but apply simplifications that make the trajectory design problem more tractable. After preliminary mission design is conducted in these simplified dynamical models, low-thrust trajectories are transitioned to a higher fidelity model based on ephemeris data and the N-body equations of motion. Low-thrust trajectory design presents a continuous optimal control problem, and here the problem is addressed by applying a direct collocation scheme to discretize the continuous problem and transform it into an NLP problem. Direct collocation is the

method of choice because its adaptability and robustness complement the objectives of this investigation and make the method well suited for pairing with an orbit chain technique. The direct collocation algorithm implemented here is termed COLT and is tailored to solve the types of low-thrust trajectory design problem encountered here. This algorithm, in concert with an orbit chain strategy, offers a trajectory design framework capable of solving the challenging Gateway and Lunar IceCube trajectory design problems.

### 7.1.1 Orbit Chain and Direct Collocation Technique

Combining an orbit chain strategy with direct collocation yields a systematic approach to low-thrust trajectory design. Orbit chaining entails the linking together of various dynamical structures, e.g., periodic orbits and their invariant manifolds, to form an initial guess for a low-thrust transfer. The links that form an orbit chain are selected by analyzing the differences in energy and geometry between the initial and final orbits. After the components of an orbit chain are selected, they may be clipped and stacked to further tailor an initial guess to a given transfer scenario. The definition of the initial control profile is the final step before the direct collocation algorithm converges the orbit chain initial guess. Low-thrust transfers between periodic orbits in the CR3BP are used to demonstrate the steps of orbit chain assembly and illustrate the flexibility of this approach. The intermediate links in an orbit chain are easily interchanged to generate different transfers between the same initial and final orbits. Moreover, the number and types of orbits included in a chain are highly flexible. In this investigation, the constructed chains utilize dynamical structures from the CR3BP, CR3BP+LT, and BCR4BP models. Overall, orbit chaining offers a flexible and relatively simple approach to initial guess construction for low-thrust trajectory design.

### 7.1.2 Gateway Mission Design

Low-thrust transfers from the 9:2 NRHO to other potentially advantageous libration point orbits in the lunar vicinity are possible using the engine parameters and propellant mass budget currently planned for the Gateway spacecraft. Transfers from the 9:2 NRHO to a DRO, low-amplitude halo orbit, and a northern  $L_1$  NRHO are computed; moreover, exterior and interior type transfer geometries are obtained for all three scenarios. These results indicate that utilizing an interior rather than an exterior transfer geometry does not guarantee a shorter time of flight or reduced propellant consumption. However, both time of flight and propellant consumption are highly dependent on the initial guess, and it is possible that different results could be obtained if further experimentation with suitable orbit chains were conducted for each transfer scenario. Overall, the success of these example scenarios demonstrates the utility of the orbit chain and direct collocation methodology even for spacecraft with extremely limited control authority.

The missed thrust analysis applied to the exterior NRHO to DRO transfer result exhibits that the COLT algorithm may also be utilized for this step of the trajectory design process. The results highlight the sensitive regions of the NRHO to DRO transfer, and illustrate that even for a five day thrust outage it is challenging to reconverge the baseline transfer if the outage occurs along a particularly sensitive part of the trajectory. The most sensitive region is the beginning of the trajectory when the spacecraft is departing the NRHO and passes very close to the Moon. As expected, the number of failed cases in the missed thrust analysis increases as the duration of the thrust outage is lengthened. These results offer a demonstration of one approach for employing direct collocation for missed thrust analysis, and more work is necessary to complete this phase of the design process for the computed transfers.

### 7.1.3 Lunar IceCube Mission Design

The orbit chain and direct collocation technique framework generates a complete Lunar IceCube trajectory in the BCR4BP. The proposed scheme utilizes a staging orbit to divide the trajectory design process into two distinct phases, which eases the design challenge by enabling trajectories for each phase to be designed largely independently. The multi-phase approach also supplies increased flexibility by permitting the same Phase 1 trajectory result to be utilized for a range of potential Phase 2 transfers. Two destination orbits are examined: one low lunar orbit that requires a long sub-optimal low-thrust spiral to reach, and a 9:2 NRHO which necessitates significantly less time of flight and propellant to reach. The flexibility of the proposed framework also enables quick adaptation to changes in launch date; Lunar IceCube trajectories are generated for four different deployment dates from 2018 to 2021. This resilience is advantageous for the Lunar IceCube mission in particular because, as a secondary payload, it is subject to the needs of the primary mission and must be adaptable to any changes in deployment conditions that this mission requires.

The Lunar IceCube trajectories generated for each launch date satisfy mission requirements in the BCR4BP and, in many cases, an ephemeris model as well. All computed end-to-end trajectories deliver the spacecraft to the final orbit with a substantial mass margin remaining. When the Phase 1 trajectories are analyzed in a Sun-B1 rotating frame, it is evident that each one leverages the perturbing acceleration of the Sun to achieve the change in energy required for insertion upon the science orbit. Moreover, many of the trajectories obtained in the BCR4BP are successfully transitioned to an ephemeris model. Three of the four Phase 1 trajectories are re-converged in an ephemeris model that includes the Earth, Moon and Sun, and the resulting transfers perform similarly to their BCR4BP counterparts. Likewise, Phase 2 trajectories from the staging orbit to a 9:2 NRHO in the BCR4BP are transitioned to an ephemeris model and these too exhibit similar mass consumption when re-converged in the higher-fidelity model. Unfortunately, the method employed to

compute Phase 2 trajectories to the selected LLO is not well suited for implementation in an ephemeris model. Potential modifications to this method that may enable convergence in an ephemeris model are discussed both in Chapter 6 and in the future work section of this chapter.

## 7.2 Recommendations for Future Work

Many avenues for future work are apparent, both with regard to the orbit chain and direct collocation technique itself and with the two sample applications. Improvements to the fundamental technique and the algorithms that enable it will broaden the range of trajectory design scenarios it is applicable to. Furthermore, continued investigation of the Gateway and Lunar IceCube trajectory design scenarios may produce superior solutions that require less time of flight or propellant. Opportunities for future work are described below by topic.

### 7.2.1 Orbit Chain and Direct Collocation

- *Minimum Radius Constraint* - One of the greatest challenges encountered with COLT is the tendency of the algorithm to get “stuck” when a trajectory passes very close to a primary body. This challenge is not unique to COLT, but it is frequently encountered here because the constructed orbit chains often provide a coarse initial guess. The significant discontinuities and simplistic control history included in the initial guess require the optimization process to make drastic alterations as it seeks a solution. These significant changes can lead to one or more trajectory segments being shifted such that they pass beneath the surface of the Moon. This scenario hinders the convergence process, as the highly nonlinear dynamics near the Moon increase the difficulty of computing beneficial updates to the design variables. Moreover, because the minimum radius constraint is enforced only at the variable nodes of each segment, the aforementioned scenario can occur even without a constraint violation. Meeting

this challenge requires a more comprehensive approach to enforcing a minimum radius constraint. Investigation of how to adequately enforce a minimum radius constraint would enhance the robustness of the orbit chain and direct collocation technique.

- *Orbit Chain Construction* - The initial guess construction process offered by the orbit chain and direct collocation technique involves many design choices, from what structures to include in a chain to the direction of the initial thrust vector. The relative importance of each of these choices for facilitating convergence is discussed qualitatively in Section 4.6; however, additional analysis could offer more concrete steps for the construction of effective orbit chain initial guesses. Prado offers guidance on the selection of links for an orbit chain [90, 91], and continued investigation in this vein could yield similarly beneficial results. A more systematic approach to orbit chain design will expedite the design process by indicating the appropriate type and number of intermediate links to include in an orbit chain, thus avoiding the challenges in the convergence process that can result from too few or too many intermediate links. Furthermore, analysis of other aspects of orbit chain construction, e.g., number of segments or the initial control profile, could yield similar benefits. Greater understanding of how each of these parameters impacts the convergence process would allow their values to be more purposefully selected.
- *Orbit Chain and Trajectory Sensitivity* - It may be advantageous to more closely examine the sensitivity to perturbations of each dynamical structure employed in an orbit chain and how this sensitivity impacts the robustness of the resulting low-thrust transfer. Establishing quantitative or even qualitative correlations between the sensitivity of an orbit chain's components and the sensitivity of the corresponding low-thrust transfer would enable engineers to more intelligently construct an orbit chain initial guess to produce a transfer with a desired set of characteristics.

- *Global Optimization Outer Loop* - The orbit chain construction process as presented in this investigation requires the involvement of an intelligent mission designer. However, it is possible that much if not all of this process can be automated. Utilizing a global optimization algorithm of the type discussed in Section 3.2.3 to explore many different orbit chain formulations could yield superior low-thrust solutions while requiring reduced involvement from a mission designer. Restrepo and Russell [16, 17], Beeson et al. [46], and Das-Stuart [30], all offer approaches that utilize a precomputed catalog, a global optimization technique, or both to assemble an “orbit chain like” initial guess that is converged into a continuous transfer. The work of these authors, among others, could be drawn upon along with the orbit chain guidelines developed in this investigation to inform the creation of a hybrid approach to orbit chain trajectory design. This approach would employ an outer loop guided by a global optimization technique for the construction of an orbit chain initial guess. Following this step, the initial guess would be transformed into an optimal low-thrust solution via the direct collocation method described in this investigation.
- *Direct Multiple Shooting* - Further investigation is needed to determine the efficacy of utilizing a direct multiple shooting algorithm in comparison to an orbit chain approach. Preliminary investigation indicates that an efficiently implemented direct multiple shooting algorithm could be nearly as robust as a direct collocation method. Moreover, direct multiple shooting typically generates a smaller optimization problem, thereby potentially decreasing the computation time required to obtain a solution. However, this benefit may be offset by the fact that direct multiple shooting requires explicit propagation. Additional examination will indicate when a direct multiple shooting could be leveraged with an orbit chain technique. This knowledge would aid the designer in determining the most appropriate method for diverse mission design scenarios.

- *Analytic First and Second Derivatives* - The partial derivatives of the defect and continuity constraints utilized within COLT are computed via complex-step differentiation. If implemented efficiently, it would likely require less computational time to compute these derivatives analytically instead. Moreover, the second-derivatives necessary to determine an optimal solution are currently approximated by a limited-memory quasi-Newton method within the IPOPT software package. However, more accurate approaches for computing these second-derivatives are available. Increased accuracy of the second derivatives would likely improve the accuracy of the optimal solutions computed with COLT and reduce the number of iterations required to reach these solutions. A variety of approaches including analytic expressions, automatic differentiation, or second-order complex-step differentiation may be leveraged to compute the second-order derivatives. Though initially time consuming, deriving the expressions required to evaluate these derivatives analytically would offer long-term benefits of accuracy and efficiency.

### 7.2.2 Gateway Mission Design

- *Alternate Orbit Chain Construction* - Testing alternate orbit chain initial guesses may reduce the time required to compute an optimal solution and could offer more optimal final results. The continuation process employed to obtain low-thrust transfers requires extended computation time and is sometimes unable to produce the desired result. Improved initial guesses for Gateway transfers may enable the elimination of the continuation process, or, at the very least, a reduction in the number of continuation steps required. Improving an initial guess may entail reducing discontinuities between links by increasing the quantity or type of orbits included as intermediate links. Some of the converged Gateway transfers appear to exploit natural dynamical structures that were not included in the original guess. Examples include motion that appears to correspond to

quasi-periodic orbits as well as some of the higher period orbits described by Zimovan et al. [121]. These characteristics indicate that explicitly incorporating these dynamical structures into an orbit chain initial guess may facilitate convergence. Similarly, as some of the Gateway transfers, particularly the interior type ones, include significant amounts of coasting, it seems that there could be alternate orbit chain formulations that generate transfers with shorter times of flight.

- *Global Optimization Algorithm* - The exterior type transfers computed by McCarty et al. [34] indicate that lower cost, lower time of flight versions of the trajectories computed in this investigation are available. A global optimization algorithm similar to the one employed by McCarty et al. may be a helpful tool for identifying these superior optimal solutions. Utilizing an orbit chain result to initialize a global optimization algorithm may reduce the time spent searching for a superior optimal solution. Combining the rapidity with which the orbit chain and direct collocation technique is able to supply an optimal result with the broad solution space search provided by the global optimization procedure could yield an efficient process for obtaining superior optimal low-thrust transfers for Gateway.
- *Robust Missed Thrust Analysis and Design* - Taking steps to improve the robustness of the missed thrust analysis process will offer more informative results and possibly reduce the required computation time for the analysis. Ideally there should be no failed cases in the missed thrust analysis. The cases that fail in the current analysis should instead be converged to solutions with extremely high propellant consumption. Achieving this result requires changes to the direct collocation algorithm that enhance its robustness, thus enabling convergence even in these challenging scenarios. The path to improvement is not immediately apparent, although improving the minimum radius constraint, as discussed previously, would like offer a significant benefit. Improving the robustness of the

missed thrust analysis tools will enable the interior type transfers computed in this investigation to be thoroughly tested to determine if they are too sensitive to missed thrust events to be practical. Finally, potential uses of direct collocation for missed thrust design should be explored for the Gateway mission, among other sample applications. Improved methods for missed thrust design have the potential to not only enhance the robustness of low-thrust trajectories, but also significantly reduce the time a mission designer must spend conducting missed thrust analysis. It is possible that the robustness and relative computational efficiency of direct collocation make this algorithm well-suited for conducting missed thrust design.

### 7.2.3 Lunar IceCube Mission Design

- *B-Plane Targeting for Initial Lunar Flyby* - More optimal Phase 1 solutions could result from constructing the initial deployment trajectory by targeting a B-plane coordinate rather than varying a constant angle in the VNB frame. While the current approach is fast, it can omit deployment trajectories that are not attainable with a simplistic initial thrust profile. Targeting a B-plane coordinate instead will produce a more comprehensive set of potential flyby trajectories, and the complete set of flyby options may include a path that produces a more optimal Phase 1 result than could have been found with the current strategy. The B-plane targeting process will require more computational time to produce the same number of deployment trajectories, and further study is required to determine whether this trade-off is worthwhile.
- *Alternate Staging Orbits* - Other periodic or quasi-periodic orbits (QPO) in the BCR4BP may be beneficial staging orbit candidates. In particular, alternate orbits, either due to geometry or energy, may offer improved access to the selected final LLO. A potentially useful category of orbits are the QPOs about the  $L_2$  libration point. These orbits offer a greater range of staging orbit options and

invariant manifold geometries. The incorporation of BCR4BP QPOs into the proposed LIC trajectory design framework would expand the array of manifold paths available for designing Phases 1 and 2. This inclusion could lead to initial guesses with reduced state discontinuities and perhaps more optimal transfers.

- *Multi-Phase Approach to Low-Thrust Spiral* - A multi-phase direct collocation algorithm would enable the optimization of Phase 2 transfers in the BCR4BP and offer the flexibility required to successfully transition transfers to an ephemeris model. The ability to setup a multi-phase problem would allow the current parameterization employed in COLT and a new modified equinoctial element (MEE) parameterization to be used to pose a single direct optimization problem that can be solved to generate a fully optimal transfer. Previous literature on computing low-thrust spirals via direct collocation demonstrates that an MEE parameterization is well suited for this application. The final result of implementing a multi-phase capability and an MEE parameterization will be a tool that not only generates more optimal transfers in the BCR4BP, but is also able to transition these transfers to an ephemeris model.
- *Missed Thrust Analysis* - An extensive missed thrust analysis of the type presented for the Gateway spacecraft is essential to ensure the practicality of the proposed LIC trajectory designs. The same missed thrust analysis strategy employed for Gateway can be applied to LIC to reveal the regions of the presented Phase 1 and 2 trajectories that are most sensitive to missed thrust events. The results of this analysis may suggest alterations to the trajectory design framework presented in Section 6.2 that will enhance the robustness of the LIC trajectory to missed thrust events.

## REFERENCES

## REFERENCES

- [1] J. Kepler, *Kepler's Conversations with Galileo's Sidereal Messenger*. New York: Johnson Reprint Corporation, 1965, translated by E. Rosen.
- [2] J. Verne, *From the Earth to the moon, and Around the moon*. New York: Heritage Press, 1970.
- [3] E. Y. Choueiri, "A Critical History of Electric Propulsion: The First 50 Years (1906-1956)," *Journal of Propulsion and Power*, vol. 20, no. 2, pp. 193–203, 2008.
- [4] J. Sovey, V. Rawlin, and M. Patterson, "A synopsis of ion propulsion development projects in the United States - SERT I to Deep Space 1," in *35th Joint Propulsion Conference and Exhibit*, Los Angeles, CA, 1999.
- [5] M. D. Rayman, "The Successful Conclusion of the Deep Space 1 Mission: Important Results Without a Flashy Title," in *53rd International Astronautical Congress*, Houston, TX, 2002, pp. 1–13.
- [6] C. Russell and C. Raymond, Eds., *The Dawn Mission to Minor Planets 4 Vesta and 1 Ceres*, 1st ed. New York: Springer-Verlag, 2012.
- [7] J. Kawaguchi, A. Fujiwara, and T. Uesugi, "Hayabusa-Its technology and science accomplishment summary and Hayabusa-2," *Acta Astronautica*, vol. 62, no. 10, pp. 639–647, 2008.
- [8] K. C. Howell, B. T. Barden, and M. W. Lo, "Application of Dynamical Systems Theory to Trajectory Design for a Libration Point Mission," *The Journal of the Astronautical Sciences*, vol. 45, no. 2, pp. 161–178, 1997.
- [9] W. S. Koon, M. W. Lo, J. E. Marsden, and S. D. Ross, "Heteroclinic connections between periodic orbits and resonance transitions in celestial mechanics," *Chaos: An Interdisciplinary Journal of Nonlinear Science*, vol. 10, no. 2, pp. 427–469, 2000.
- [10] G. Gómez, W. S. Koon, M. W. Lo, J. E. Marsden, J. J. Masdemont, and S. D. Ross, "Connecting orbits and invariant manifolds in the spatial restricted three-body problem," *Nonlinearity*, vol. 17, no. 5, pp. 1571–1606, 2004.
- [11] S. Ross and M. Lo, "The lunar L1 gateway-portal to the stars and beyond," in *AIAA Space 2001 Conference and Exposition*, Albuquerque, New Mexico, 2001, pp. 47–68.
- [12] M. W. Lo and J. S. Parker, "Chaining Simple Periodic Three Body Orbits," in *AAS/AIAA Astrodynamics Specialist Conference*, Lake Tahoe, California, 2005.

- [13] J. S. Parker, K. E. Davis, and G. H. Born, “Chaining periodic three-body orbits in the EarthMoon system,” *Acta Astronautica*, vol. 67, no. 5-6, pp. 623–638, 2010.
- [14] M. Vaquero and K. C. Howell, “Leveraging Resonant-Orbit Manifolds to Design Transfers Between Libration-Point Orbits,” *Journal of Guidance, Control, and Dynamics*, vol. 37, no. 4, pp. 1143–1157, 2014.
- [15] A. F. Haapala and K. C. Howell, “A Framework for Constructing Transfers Linking Periodic Libration Point Orbits in the Spatial Circular Restricted Three-Body Problem,” *International Journal of Bifurcation and Chaos*, vol. 26, no. 05, 2016.
- [16] R. L. Restrepo and R. P. Russell, “A Database of Planar Axi-Symmetric Periodic Orbits for the Solar System,” in *AAS/AIAA Astrodynamics Specialist Conference*, Stevenson, Washington, 2017.
- [17] ———, “Patched Periodic Orbits: A Systematic Strategy for Low Energy Transfer Design,” in *AAS/AIAA Astrodynamics Specialist Conference*, Stevenson, Washington, 2017.
- [18] D. J. Grebow, M. T. Ozimek, and K. C. Howell, “Design of Optimal Low-Thrust Lunar Pole-Sitter Missions,” *The Journal of Astronautical Sciences*, vol. 58, no. 1, pp. 55–79, 2011.
- [19] M. T. Ozimek, D. J. Grebow, and K. C. Howell, “A Collocation Approach for Computing Solar Sail Lunar Pole-Sitter Orbits,” *Open Aerospace Engineering Journal*, vol. 3, pp. 65–75, 2010.
- [20] J. F. C. Herman, “Improved Collocation Methods to Optimize Low-Thrust Low-Energy Transfers in the Earth-Moon System by,” Ph.D. dissertation, University of Colorado, Boulder, Colorado, 2015.
- [21] N. L. Parrish, J. S. Parker, S. P. Hughes, and J. Heiligers, “Low-Thrust Transfers From Distant Retrograde Orbits To L2 Halo Orbits in the Earth-Moon System,” in *International Conference on Astrodynamics Tools and Techniques*, Darmstadt, Germany, 2016.
- [22] R. E. Pritchett, K. C. Howell, and D. J. Grebow, “Low-Thrust Transfer Design Based on Collocation Techniques: Applications in the Restricted Three-Body Problem,” in *AAS/AIAA Astrodynamics Specialist Conference*, Stevenson, Washington, 2017.
- [23] R. E. Pritchett, E. Zimovan, and K. C. Howell, “Impulsive and Low-Thrust Transfer Design Between Stable and Nearly-Stable Periodic Orbits in the Restricted Problem,” in *2018 AIAA/AAS Space Flight Mechanics Meeting*, Orlando, Florida, 2018.
- [24] R. Pritchett, A. D. Cox, K. C. Howell, D. C. Folta, and D. Grebow, “Low-Thrust Trajectory Design Via Direct Transcription Leveraging Structures from the Low-Thrust Restricted Problem,” in *69th International Astronautical Congress*, Bremen, Germany, 2018, pp. 1–16.
- [25] I. Newton, *The Principia: Mathematical Principles of Natural Philosophy*. Berkely California: University of California Press, 1999.

- [26] K. K. Boudad, “Disposal Dynamics From The Vicinity Of Near Rectilinear Halo Orbits In The Earth-Moon-Sun System,” Master’s thesis, Purdue University, 2018.
- [27] K. Boudad, K. Howell, and D. Davis, “Dynamics of Synodic Resonant Near Rectilinear Halo Orbits in the Bicircular Four-Body Problem,” *Advances in Space Research*, 2020.
- [28] M. Jorba-Cuscó, A. Farrés, and À. Jorba, “Two Periodic Models for the Earth-Moon System,” *Frontiers in Applied Mathematics and Statistics*, vol. 4, no. July, pp. 1–14, 2018.
- [29] T. A. Pavlak, “Trajectory Design and Orbit Maintenance Strategies in Multi-Body Dynamical Regimes,” Ph.D. dissertation, Purdue University, 2013.
- [30] A. Das-Stuart, “Artificial Intelligence Aided Rapid Trajectory Design in Complex Dynamical Environments,” Ph.D., Purdue University, 2019.
- [31] M. D. Rayman, P. Varghese, D. H. Lehman, and L. L. Livesay, “Results from the Deep Space 1 Technology Validation Mission,” *Acta Astronautica*, vol. 47, no. 2-9, pp. 475–487, 2000.
- [32] *BIT-3 RF Ion Thruster*, Busek Space Propulsion and Systems, 2019.
- [33] K. Nishiyama, S. Hosoda, K. Ueno, R. Tsukizaki, and H. Kuninaka, “Development and testing of the hayabusa2 ion engine system,” *Transactions of the Japan Society for Aeronautical and Space Sciences, Aerospace Technology Japan*, vol. 14, no. ists30, pp. 1–15, 2016.
- [34] S. L. Mccarty, L. M. Burke, and M. L. Mcguire, “Analysis of Cislunar Transfers From a Near Rectilinear Halo Orbit With High Power Solar Electric Propulsion,” in *AAS Astrodynamics Specialists Conference*, Snowbird, UT, 2018, pp. 1–14.
- [35] J. T. Betts, *Practical Methods for Optimal Control and Estimation Using Non-linear Programming*, 2nd ed. Philadelphia, Pennsylvania: Society for Industrial and Applied Mathematics, 2010.
- [36] J. M. Longuski, J. J. Guzmán, and J. E. Prussing, *Optimal Control with Aerospace Applications*. New York: Springer, 2014.
- [37] J. T. Betts and W. P. Huffman, “Mesh Refinement in Direct Transcription Methods for Optimal Control,” *Optim. Control Appl. Meth*, vol. 19, no. April 1997, pp. 1–21, 1998.
- [38] B. A. Conway, “A Survey of Methods Available for the Numerical Optimization of Continuous Dynamic Systems,” *Journal of Optimization Theory and Applications*, vol. 152, no. 2, pp. 271–306, 2012.
- [39] A. Rao, “A survey of numerical methods for optimal control,” *Advances in the Astronautical Sciences*, vol. 135, pp. 497–528, 2009.
- [40] F. Topputo and C. Zhang, “Survey of Direct Transcription for Low-Thrust Space Trajectory Optimization with Applications,” *Abstract and Applied Analysis*, vol. 2014, 2014. [Online]. Available: <http://dx.doi.org/10.1155/2014/851720>

- [41] J. R. Stuart, “A Hybrid Systems Strategy for Automated Spacecraft Tour Design and Optimization,” Ph.D. dissertation, Purdue University, 2014.
- [42] J. Englander, B. Conway, and T. Williams, “Optimal Autonomous Mission Planning Via Evolutionary Algorithms,” *Spaceflight Mechanics*, vol. 140, no. Part 1, pp. 833–852, 2011.
- [43] C. H. Yam, D. Izzo, and D. D. Lorenzo, “Low-thrust trajectory design as a constrained global optimization problem,” *Proceedings of the Institution of Mechanical Engineers, Part G: Journal of Aerospace Engineering*, vol. 225, no. 11, pp. 1243–1251, 2011.
- [44] D. Izzo, C. I. Sprague, and D. V. Taylor, “Machine Learning and Evolutionary Techniques in Interplanetary Trajectory Design,” in *Modeling and Optimization in Space Engineering*. Springer, 2019, pp. 191–210.
- [45] S. N. Williams and V. Coverstone-Carroll, “Mars Missions Using Solar Electric Propulsion,” *Journal of Spacecraft and Rockets*, vol. 37, no. 1, pp. 71–77, 2000.
- [46] R. Beeson, V. Shah, J. Aurich, and D. Ellison, “Automated Solution of Low Energy Trajectories,” in *AAS/AIAA Astrodynamics Specialist Conference*, Stevenson, Washington, 2017, pp. 1–20.
- [47] G. Whiffen, “Static/Dynamic Control for Optimizing a Useful Objective,” pp. 1–50, 2002. [Online]. Available: <http://www.google.com/patents/US6496741>
- [48] G. J. Whiffen and J. Sims, “Application of a Novel Optimal Control Algorithm to Low-Thrust Trajectory Optimization,” in *AAS/AIAA Space Flight Mechanics Meeting*, San Antonio, TX, 2003, pp. 1–36.
- [49] G. Whiffen, “Mystic: Implementation of the static dynamic optimal control algorithm for high-fidelity, low-thrust trajectory design,” no. August, pp. 1–12, 2006. [Online]. Available: <http://trs-new.jpl.nasa.gov/dspace/handle/2014/40782>
- [50] G. Lantoine and R. P. Russell, “A Hybrid Differential Dynamic Programming Algorithm for Constrained Optimal Control Problems. Part 1: Theory,” *Journal of Optimization Theory and Applications*, vol. 154, no. 2, pp. 382–417, 2012.
- [51] ———, “A Hybrid Differential Dynamic Programming Algorithm for Constrained Optimal Control Problems. Part 2: Application,” *Journal of Optimization Theory and Applications*, vol. 154, no. 2, pp. 418–442, 2012.
- [52] E. Pellegrini, “Multiple-Shooting Differential Dynamic Programming with Applications to Spacecraft Trajectory Optimization,” Ph.D. dissertation, The University of Texas at Austin, 2017.
- [53] J. D. Aziz, J. S. Parker, D. J. Scheeres, and J. A. Englander, “Low-thrust many-revolution trajectory optimization via differential dynamic programming and a sundman transformation,” *Advances in the Astronautical Sciences*, vol. 160, pp. 529–548, 2017.
- [54] J. D. Aziz, D. J. Scheeres, and G. Lantoine, “Hybrid Differential Dynamic Programming in the Circular Restricted Three-Body Problem,” *Journal of Guidance, Control, and Dynamics*, vol. 42, no. 5, pp. 963–975, 2019.

- [55] D. J. Grebow, “Trajectory Design in the Earth-Moon System and Lunar South Pole Coverage,” Ph.D. dissertation, Purdue University, 2010.
- [56] P. E. Gill, W. Murray, and M. A. Saunders, “SNOPT: An SQP Algorithm for Large-Scale Constrained Optimization,” *SIAM Journal on Optimization*, vol. 12, no. 4, pp. 979–1006, 2002.
- [57] P. E. Gill, W. Murray, and M. a. Saunders, “User Guide for SNOPT Version 7,” University of California, San Diego, Tech. Rep., 2008.
- [58] A. Wachter and L. T. Biegler, “On the Implementation of a Primal-Dual Interior Point Filter Line Search Algorithm for Large-Scale Nonlinear Programming,” *Mathematical Programming*, vol. 106, no. 1, pp. 25–57, 2006.
- [59] M. Canon, C. Cullum, and E. Polak, *Theory of Optimal Control and Mathematical Programming*. New York: McGraw-Hill, 1970.
- [60] L. Collatz, *The Numerical Treatment of Differential Equations*. Springer Berlin Heidelberg, 1960.
- [61] C. de Boor, “The Method of Projections as Applied to the Numerical Solution of Two Point Boundary Value Problems Using Cubic Splines,” Ph.D. dissertation, University of Michigan, 1966.
- [62] R. D. Russell and L. F. Shampine, “A Collocation Method for Boundary Value Problems,” *Numerische Mathematik*, vol. 28, pp. 1–28, 1972.
- [63] J. Ahlberg, E. Nilson, and J. Walsh, “Chapter ii the cubic spline,” in *The Theory of Splines and Their Applications*, ser. Mathematics in Science and Engineering. Elsevier, 1967, vol. 38, pp. 9 – 74.
- [64] C. R. Hargraves and S. W. Paris, “Direct trajectory optimization using nonlinear programming and collocation,” *Journal of Guidance, Control, and Dynamics*, vol. 10, no. 4, pp. 338–342, 1987.
- [65] A. L. Herman and B. A. Conway, “Direct optimization using collocation based on high-order Gauss-Lobatto quadrature rules,” *{AIAA} Journal of Guidance, Control, and Dynamics*, vol. 19, no. 3, pp. 522–529, 1996.
- [66] P. Williams, “Hermite-Legendre-Gauss-Lobatto Direct Transcription in Trajectory Optimization,” *Journal of Guidance, Control, and Dynamics*, vol. 32, no. 4, pp. 1392–1395, 2009.
- [67] U. Ascher, J. Christiansen, and R. Russell, “COLSYS - A Collocation Code for Boundary-Value Problems,” in *Codes for Boundary-Value Problems in Ordinary Differential Equations*, ser. Lecture Notes in Computer Science, B. Childs, M. Scott, J. W. Daniel, E. Denman, and P. Nelson, Eds. Berlin, Heidelberg: Springer Berlin Heidelberg, 1979, no. 76, pp. 164–185.
- [68] E. J. Doedel, R. C. Paffenroth, A. R. Champneys, T. F. Fairgrieve, A. Kuznetsov, B. Sandstede, and X. Wang, “AUTO2000: Continuation and Bifurcation Software for Ordinary Differential Equations,” California Institute of Technology, Pasadena, CA, Tech. Rep., 2001.

- [69] J. Betts and W. Huffman, “Sparse Optimal Control Software SOCS,” The Boeing Company, Seattle, Washington, Tech. Rep., 1997.
- [70] D. J. Grebow and T. A. Pavlak, “MColl: Monte Collocation Trajectory Design Tool,” in *AAS/AIAA Astrodynamics Specialist Conference*, Stevenson, Washington, 2017.
- [71] S. Hughes, J. Knittel, W. Shoan, Y. Kim, C. Conway, and D. Conway, “Benchmarking the Collocation Stand-Alone Library and Toolkit (CSALT),” in *26th International Symposium on Space Flight Dynamics*, Maysuyama, Japan, 2017, pp. 1–7.
- [72] J. T. Betts, “Survey of Numerical Methods for Trajectory Optimization,” *Journal of Guidance, Control, and Dynamics*, vol. 21, no. 2, pp. 193–207, 1997.
- [73] D. J. Grebow and T. A. Pavlak, “AMMOS Report on Mesh Refinement for Collocation Methods,” Jet Propulsion Laboratory, Pasadena, CA, Tech. Rep., 2015.
- [74] R. D. Russell and J. Christiansen, “Adaptive mesh selection strategies for boundary value problems,” *SIAM Journal of Numerical Analysis*, vol. 15, no. 2, pp. 59–80, 1978.
- [75] C.-W. de Boor, “Good approximation by splines with variable knots ii,” in *Conference on the Numerical Solution of Differential Equations*, ser. Lecture Notes in Mathematics, vol. 363. New York: Springer, 1973, pp. 12–20.
- [76] D. J. Grebow and T. A. Pavlak, “AMMOS Report on Collocation Methods,” Jet Propulsion Laboratory, Pasadena, CA, Tech. Rep., 2015.
- [77] P. Gill, W. Murray, M. Saunderson, and M. Wright, *Practical Optimization*. London, England: Academic Press, 1991.
- [78] J. R. R. A. Martins, P. Sturdza, and J. J. Alonso, “The complex-step derivative approximation,” *ACM Transaction on Mathematical Software (TOMS)*, vol. 29, no. 3, pp. 245–262, 2003.
- [79] D. Garza, “Application of automatic differentiation to trajectory optimization via direct multiple shooting,” Ph.D. Dissertation, University of Texas, Austin, Texas, 2003.
- [80] A. Griewank, *Evaluating Derivatives Principles and Techniques of Algorithmic Differentiation*, 2nd ed. Philadelphia, Pennsylvania: SIAM, 2008.
- [81] R. D. Neidinger, “Introduction to automatic differentiation and matlab object-oriented programming,” *SIAM Review*, vol. 52, no. 3, pp. 545–563, 2012.
- [82] A. F. Haapala, “Trajectory Design in the Spatial Circular Restricted Three-Body Problem Exploiting Higher-Dimensional Poincare Maps,” Ph.D. dissertation, Purdue University, 2014.
- [83] B. McCarthy, “Characterization of Quasi-Periodic Orbits for Applications in the Sun-Earth and Earth-Moon Systems,” Master’s thesis, Purdue University, 2018.

- [84] T. M. V. Escibano, “Spacecraft Transfer Trajectory Design Exploiting Resonant Orbits in Multi-Body Environments,” Ph.D. dissertation, Purdue University, 2013. [Online]. Available: <http://docs.lib.purdue.edu/dissertations/AAI3605166/>
- [85] K. Lust, “Numerical Bifurcation Analysis of Periodic Solutions of Partial Differential Equations,” Ph.D. dissertation, Katholieke Universiteit Leuven, 1997.
- [86] H. B. Keller, *Numerical Solution of Two Point Boundary Value Problems*. Philadelphia, Pennsylvania: Society for Industrial and Applied Mathematics, 1976.
- [87] R. D. Russell, “Collocation for Systems of Boundary Value Problems,” *Numerische Mathematik*, vol. 23, no. 2, pp. 119–133, 1974.
- [88] M. T. Ozimek, “Low-Thrust Trajectory Design and Optimization of Lunar South Pole Coverage Missions,” Ph.D. Dissertation, Purdue University, 2010.
- [89] N. L. O. Parrish, “Low Thrust Trajectory Optimization in Cislunar and Translunar Space,” Ph.D., University of Colorado Boulder, 2018.
- [90] B. Prado, K. C. Howell, D. C. Folta, and R. E. Pritchett, “Extended Mission Options for the Lunar IceCube Low-Thrust Spacecraft by Leveraging the Dynamical Environment,” in *71st International Astronautical Congress*, Paris, France, 2020, forthcoming.
- [91] B. Prado, K. Howell, and D. Folta, “An Energy-Informed Adaptive Algorithm for Low-Thrust Spacecraft Cislunar Trajectory Design,” in *AAS/AIAA Astrodynamics Specialist Conference*, South Lake Tahoe, CA, 2020, pp. 1–20, forthcoming.
- [92] C. Warner, “NASA’s Lunar Outpost will Extend Human Presence in Deep Space,” 2018. [Online]. Available: <https://www.nasa.gov/feature/nasa-s-lunar-outpost-will-extend-human-presence-in-deep-space>
- [93] E. Mahoney, “Q&A: NASA’s New Spaceship,” 2018. [Online]. Available: <https://www.nasa.gov/feature/questions-nasas-new-spaceship>
- [94] B. Inclán, G. Anderson, and J. Russell, “NASA Awards Artemis Contract for Lunar Gateway Power, Propulsion,” 2019. [Online]. Available: <https://www.nasa.gov/press-release/nasa-awards-artemis-contract-for-lunar-gateway-power-propulsion>
- [95] R. Ticker, M. Gates, D. Manzella, A. Biaggi-Labiosa, and T. Lee, “The Gateway Power and Propulsion Element: Setting the Foundation for Exploration and Commerce,” in *AIAA Propulsion and Energy Forum and Exposition, 2019*, no. August, Indianapolis, Indiana, 2019.
- [96] P. Y. Peterson, D. A. Herman, H. Kamhawi, J. D. Frieman, W. Huang, T. Verhey, D. Dinca, K. Boomer, L. Pinero, K. Criswell, S. J. Hall, A. Birchenough, J. H. Gilland, R. R. Hofer, J. E. Polk, V. Chaplin, R. B. Lobbia, C. E. Garner, and M. K. Kowalkowski, “Overview of NASA’s Solar Electric Propulsion Project,” in *Proceedings of the 36th IEPC*, 2019, pp. 1–14.

- [97] D. Herman, T. Tofil, W. Santiago, H. Kamhawi, J. Polk, J. S. Snyder, R. Hofer, F. Picha, and G. Schmidt, "Overview of the Development of the Advanced Electric Propulsion System (AEPS)," in *35th International Electric Propulsion Conference*, Atlanta, Georgia, 2017, pp. 1–18.
- [98] R. Whitley and R. Martinez, "Options for Staging Orbits in Cis-Lunar Space," in *IEEE Annual Aerospace Conference*, Big Sky, Montana, 2016, pp. 1–9.
- [99] R. Whitley, R. Martinez, G. Condon, J. Williams, and D. Lee, "Targeting Cis-lunar Near Rectilinear Halo Orbits for Human Space Exploration," *AAS/AIAA Astrodynamics Specialist Conference Space 2017*, pp. 1–20, 2017.
- [100] R. J. Whitley, D. C. Davis, M. McGuire, L. Burke, B. McCarthy, R. Power, and K. Howell, "Earth-Moon Near Rectilinear Halo and Butterfly Orbits for Lunar Surface Exploration," *AAS/AIAA Astrodynamics Specialists Conference, Snowbird, Utah*, pp. 1–20, 2018.
- [101] L. Capdevila, "A Transfer Network Linking Earth, Moon and the Libration Point Regions in the Earth-Moon System," Ph.D., Purdue University, West Lafayette, IN, 2016.
- [102] E. Zimovan, "Characteristics and Design Strategies for Near Rectilinear Halo Orbits within the Earth-Moon System," Ph.D. dissertation, Purdue University, 2017.
- [103] G. Lantoine, "Efficient NRHO to DRO Transfers in Cislunar Space," in *AAS/AIAA Astrodynamics Specialist Conference*, Stevenson, Washington, 2017, pp. 1–18.
- [104] M. L. McGuire, L. M. Burke, S. L. McCarty, K. J. Hack, R. J. Whitley, D. C. Davis, and C. Ocampo, "Low Thrust Cis-Lunar Transfers Using a 40 kW-Class Solar Electric Propulsion Spacecraft," in *AAS/AIAA Astrodynamics Specialist Conference 2017*, Stevenson, Washington, 2017.
- [105] T. Imken, T. Randolph, M. DiNicola, and A. Nicholas, "Modeling Spacecraft Safe Mode Events," *IEEE Aerospace Conference Proceedings*, vol. 2018-March, pp. 1–13, 2018.
- [106] M. D. Rayman and P. Varghese, "The Deep Space 1 Extended Mission," *Acta Astronautica*, vol. 48, no. 5-12, pp. 693–705, 2001.
- [107] D. J. Grebow, G. J. Whiffen, D. Han, and B. M. Kennedy, "Dawn Safing Approach to Ceres Re-Design," in *AAS/AIAA Astrodynamics Specialist Conference*, no. September, Long Beach, California, 2016, pp. 1–11.
- [108] D. Y. Oh, D. Landau, T. Randolph, P. Timmerman, J. Chase, J. Sims, and T. Kowalkowski, "Analysis of system margins on deep space missions utilizing solar electric propulsion," *44th AIAA/ASME/SAE/ASEE Joint Propulsion Conference and Exhibit*, no. July, pp. 1–30, 2008.
- [109] S. Pujari, T. Imken, and G. Lightsey, "Exploration of Safing Event Models for Interplanetary Spacecraft," *IEEE Aerospace Conference Proceedings*, vol. 2019-March, pp. 1–17, 2019.

- [110] S. L. McCarty and D. Grebow, "Missed Thrust Analysis and Design for Low Thrust Cislunar Transfers," in *AAS/AIAA Astrodynamics Specialist Conference*, South Lake Tahoe, CA, 2020, forthcoming.
- [111] F. E. Laipert and J. M. Longuski, "Automated Missed-Thrust Propellant Margin Analysis for Low-Thrust Trajectories," *Journal of Spacecraft and Rockets*, vol. 52, no. 4, pp. 1135–1143, 2015.
- [112] A. Rubinsztein, R. Sood, and F. E. Laipert, "Neural Network Based Optimal Control: Resilience to Missed Thrust Events," in *AAS/AIAA Astrodynamics Specialist Conference*, Portland, ME, 2019, pp. 1–14.
- [113] B. V. Sarli, J. A. Atchison, M. T. Ozimek, J. A. Englander, and B. W. Barbee, "Double asteroid redirection test mission: Heliocentric phase trajectory analysis," *Journal of Spacecraft and Rockets*, vol. 56, no. 2, pp. 546–558, 2019.
- [114] J. T. Olympio and C. H. Yam, "Deterministic method for space trajectory design with mission margin constraints," in *61st International Astronautical Congress 2010*, Prague, CZ, 2010, pp. 1–12.
- [115] J. T. Olympio, "Designing robust low-thrust interplanetary trajectories subject to one temporary engine failure," in *20th AAS/AIAA Space Flight Meeting*, San Diego, CA, 2010, pp. 1–19.
- [116] N. Ozaki and R. Funase, "Robust-Optimal Trajectory Design against Disturbance for Solar Sailing Spacecraft Naoya," *AIAA/AAS Astrodynamics Specialist Conference, AIAA SPACE and Astronautics Forum and Exposition 2016*, no. September, pp. 1–19, 2016.
- [117] N. Ozaki, S. Campagnola, R. Funase, and C. H. Yam, "Stochastic Differential Dynamic Programming with Unscented Transform for Low-Thrust Trajectory Design," *Journal of Guidance, Control, and Dynamics*, vol. 41, no. 2, pp. 1–11, 2017.
- [118] N. Ozaki and R. Funase, "Tube Stochastic Differential Dynamic Programming for Robust Low-Thrust Trajectory Optimization Problems," *2018 AIAA Guidance, Navigation, and Control Conference*, no. January, 2018.
- [119] Y. Tsuda, "Stochastic Event-Robust Deoptimization Technique for Low Thrust Trajectory Design," in *AAS/AIAA Astrodynamics Specialist Conference*, 2017, pp. 1–16.
- [120] E. M. Zimovan-Spreen and K. C. Howell, "Dynamical Structures Nearby NRHOs with Applications in Cislunar Space," in *AAS/AIAA Astrodynamics Specialists Conference*, Portland, ME, 2019, pp. 1–20.
- [121] E. M. Zimovan-Spreen, K. C. Howell, and D. C. Davis, "Near rectilinear halo orbits and nearby higher-period dynamical structures: orbital stability and resonance properties," *Celestial Mechanics and Dynamical Astronomy*, vol. 132, no. 5, 2020.
- [122] S. L. McCarty, L. M. Burke, and M. McGuire, "Parallel Monotonic Basin Hopping for Low Thrust Trajectory Optimization," in *AIAA SciTech Forum and Exposition - Space Flight Mechanics Meeting*, Kissimmee, FL, 2018.

- [123] J. Schoolcraft, A. T. Klesh, and T. Werne, “MarCO: Interplanetary Mission Development On a CubeSat Scale,” in *SpaceOps 2016 Conference*, ser. SpaceOps Conferences. American Institute of Aeronautics and Astronautics, May 2016.
- [124] R. E. Pritchett, K. C. Howell, and D. C. Folta, “Low-Thrust Trajectory Design for a Cislunar CubeSat Leveraging Structures from the Bicircular Restricted Four-Body Problem,” in *70th International Astronautical Congress*, Washington D.C., 2019, pp. 1–18.
- [125] R. Pritchett, K. Howell, and D. Folta, “A Trajectory Design Framework Leveraging Low-Thrust for the Lunar IceCube Mission,” in *5th IAA Conference on University Satellite Missions and CubeSat Workshop*, Rome, Italy, 2020, pp. 1–21.
- [126] P. Clark, B. Malphrus, R. MacDowall, D. C. Folta, A. Mandell, C. Brambora, D. Patel, S. Banks, K. Hohman, V. Hruby, K. Brown, J. Kruth, and R. Cox, “Lunar Ice Cube: Determining Volatile Systematics Via Lunar Orbiting Cube-sat,” *European Planetary Science Congress*, vol. 10, pp. EPSC2015–61, Oct 2015.
- [127] A. J. Mazarr and D. C. Folta, “Low-Thrust Station-Keeping for a Highly Elliptical Polar Orbit at the Moon,” in *AAS/AIAA Astrodynamics Specialist Conference*, Snowbird, Utah, 2018, pp. 1–31.
- [128] R. Mathur, “Low Thrust Trajectory Design and Optimization: Case Study of a Lunar CubeSat Mission,” in *6th International Conference on Astrodynamics Tools and Techniques*. Darmstadt, Germany: Emergent Space Technologies, Inc., 2016, pp. 1–11.
- [129] N. Bosanac, “Leveraging Natural Dynamical Structures to Explore Multi-Body Systems,” Ph.D. dissertation, Purdue University, 2016.
- [130] N. Bosanac, A. D. Cox, K. C. Howell, and D. C. Folta, “Trajectory design for a cislunar cubesat leveraging dynamical systems techniques: The lunar icecube mission,” in *27th AAS/AIAA Space Flight Mechanics Meeting*, San Antonio, Texas, February 2017.
- [131] —, “Trajectory design for a cislunar CubeSat leveraging dynamical systems techniques: The Lunar IceCube mission,” *Acta Astronautica*, vol. 144, pp. 283–296, 2018.
- [132] D. C. Folta, N. Bosanac, A. D. Cox, and K. C. Howell, “The lunar icecube mission design: Construction of feasible transfer trajectories with a constrained departure,” *Advances in the Astronautical Sciences*, vol. 158, pp. 1369–1387, 2016.
- [133] W. S. Koon, M. W. Lo, J. E. Marsden, and S. D. Ross, “Low energy transfer to the moon,” *Celestial Mechanics and Dynamical Astronomy*, vol. 81, no. 1, pp. 63–73, 2001.
- [134] G. Gómez, W. Koon, M. Lo, J. Marsden, J. Masdemont, and S. Ross, “Invariant manifolds, the spatial three-body problem and space mission design,” *Advances in the Astronautical Sciences*, vol. 109, pp. 3–22, 2002.

- [135] J. Parker and M. Lo, “Shoot the moon 3d,” *Advances in the Astronautical Sciences*, vol. 123, pp. 2067–2086, 2006.
- [136] M. Lo, B. Williams, W. Bollman, D. Han, Y. Hahn, J. L. Bell, E. A. Hirst, R. Corwin, P. Hong, K. Howell, B. Barden, and R. Wilson, “Genesis Mission Design,” *The Journal of Astronautical Sciences*, vol. 49, no. 1, pp. 169–184, 2001.
- [137] M. K. J. Chung, S. J. Hatch, J. A. Kangas, S. M. Long, R. B. Roncoli, and T. H. Sweetser, “Trans-Lunar Cruise Trajectory Design of GRAIL (Gravity Recovery and Interior Laboratory) Mission,” in *AIAA/AAS Astrodynamics Specialist Conference*, Toronto, Ontario, Canada, 2010, pp. 1–7.
- [138] G. Mingotti, F. Topputo, and F. Bernelli-Zazzera, “Low-energy, low-thrust transfers to the Moon,” *Celestial Mechanics and Dynamical Astronomy*, vol. 105, no. 1, pp. 61–74, 2009.
- [139] A. Zanzottera, G. Mingotti, R. Castelli, and M. Dellnitz, “Intersecting invariant manifolds in spatial restricted three-body problems: Design and optimization of Earth-to-halo transfers in the Sun-Earth-Moon scenario,” *Communications in Nonlinear Science and Numerical Simulation*, vol. 17, no. 2, pp. 832–843, 2012.
- [140] P. J. Enright and B. A. Conway, “Discrete Approximations to Optimal Trajectories Using Direct Transcription and Nonlinear Programming,” *Journal of Guidance, Control, and Dynamics*, vol. 15, no. 4, pp. 994–1002, 1992.
- [141] D. Pérez-Palau and R. Epenoy, “Fuel optimization for low-thrust Earth-Moon transfer via indirect optimal control,” *Celestial Mechanics and Dynamical Astronomy*, vol. 130, no. 2, pp. 1–29, 2018.
- [142] R. L. Parker Jeffrey S.; Anderson, *Low-Energy Lunar Trajectory Design*. Pasadena, California: Deep Space Communications and Navigation Systems, Jet Propulsion Laboratory, 2013.
- [143] G. Mingotti, F. Topputo, and F. Bernelli-Zazzera, “Efficient invariant-manifold, low-thrust planar trajectories to the Moon,” *Communications in Nonlinear Science and Numerical Simulation*, vol. 17, no. 2, pp. 817–831, 2012.
- [144] Y. Cheng, G. Gómez, J. J. Masdemont, and J. Yuan, “Study of the transfer between libration point orbits and lunar orbits in EarthMoon system,” *Celestial Mechanics and Dynamical Astronomy*, vol. 128, no. 4, pp. 409–433, 2017.
- [145] P. Cao, B. He, and H. Li, “Analysis of direct transfer trajectories from LL2 halo orbits to LLOs,” *Astrophysics and Space Science*, vol. 362, no. 9, 2017.
- [146] G. Shakhnarovich, P. Indyk, and T. Darrell, “Introduction,” in *Nearest-Neighbor Methods in Learning and Vision*, 1st ed. Cambridge, Massachusetts: MIT Press, 2005, ch. 1, pp. 1–12.
- [147] K. L. Clarkson, “Nearest-Neighbor Searching and Metric Space Dimensions,” in *Nearest-Neighbor Methods in Learning and Vision*, 1st ed. Cambridge, Massachusetts: MIT Press, 2005, ch. 2, pp. 15–59.

- [148] M. Vaquero and J. Senent, “Poincare : A Multi-Body, Multi-System Trajectory Design Tool,” in *7th International Conference on Astrodynamics Tools and Techniques*, Oberpfaffenhofen, Germany, 2018, pp. 1–12.
- [149] K. Boudad, K. Howell, and D. Davis, “Near Rectilinear Halo Orbits in Cis-lunar Space Within the Context of the Bicircular Four-Body Problem,” in *2nd IAA/AAS SciTech Forum*, Moscow, Russia, 2019, pp. 1–20.
- [150] R. D. Falck, N. Glenn, and J. W. Dankanich, “Optimization of Low-Thrust Spiral Trajectories by Collocation,” in *AIAA/AAS Astrodynamics Specialist Conference*, Minneapolis, Minnesota, 2012, pp. 1–17.
- [151] Z. P. Olikara, “Framework for Optimizing Many-Revolution Low-Thrust Transfers,” in *AAS Astrodynamics Specialists Conference*, Snowbird, Utah, 2018, pp. 1–19.
- [152] D. C. Davis, “Multi-Body Trajectory Design Strategies Based on Periapsis Poincare Maps,” Ph.D. dissertation, Purdue University, 2011.
- [153] H. Yamakawa, J. Kawaguchi, N. Ishii, and H. Matsuo, “On earth-moon transfer trajectory with gravitational capture,” in *Advances in the Astronautical Sciences*, vol. 85, no. 1. Publ by Univelt Inc, 1993, pp. 397–416.

## APPENDICES

## A. ORBIT CHAIN TECHNIQUE APPENDIX

The transfers displayed in Section 4.4 are summarized here. First, the time of flight and propellant consumption for all of these transfers is displayed in Table A.1. Following this, Tables A.2 through A.7 provide the data necessary to reconstruct the CR3BP orbit chain initial guesses employed to compute each transfer. The orbit chain that includes dynamical structures from the CR3BP+LT is not included due to the increased complexity of this initial guess. The first three rows of the tables that summarize each orbit chain provide: the number of revolutions, the number of segments per revolution, and propagation time for each link in the orbit chain. The names of these quantities are abbreviated in each table as Num. Rev.'s, Num. Seg.'s/Rev., and Prop. Time, respectively. Furthermore, all times, positions, and velocities are presented in nondimensional units. Finally, for compactness, states whose values equal zero are omitted from each table. For example, no  $z$  or  $\dot{z}$  states are included in Table A.2 because this transfer is entirely planar.

Table A.1.  
 Summary of orbit chain example transfers. The initial mass for each transfer is  $m_0 = 1000$  kg.

Transfer Scenario	Time of		Change in	
	Flight [days]	Final Mass [kg]	Mass [kg]	Mass [kg]
$L_1$ to $L_2$ Lyap.	52.786	988.556	11.444	
$L_1$ to $L_2$ Halo Orbit	40.750	984.657	15.343	
DRO to $L_3$ Lyap. with $L_4$ SPO	78.924	972.291	27.709	
DRO to $L_3$ Lyap. with 2:3 Resonant Orbit	93.463	971.560	28.440	
$L_2$ Lyap. to $L_2$ Vertical with $L_2$ Axials	157.760	985.905	14.095	
$L_4$ SPO to $L_1$ Lyap. with CR3BP+LT	200.756	998.482	1.518	

Table A.2.  
Orbit chain setup data for DRO to  $L_3$  Lyapunov orbit with  $L_4$  SPO transfer. All quantities are presented in nondimensional units.

	DRO	$L_4$ SPO	$L_4$ SPO	$L_4$ SPO	$L_3$ Lyap.
Num. Rev.'s	2	1	1	1	1
Num. Seg.'s/Rev.	20	20	10	10	10
Prop. Time	1.570021	6.344853	3.660134	5.005213	
$x$	0.885234	0.665269	0.665269	-0.754147	
$y$	0	0.331093	0.331093	1.527199	
$\dot{x}$	0	-0.872797	-0.872797	1.469879	
$\dot{y}$	0.470671	-0.249403	-0.249403	0.344570	

Partial Rev.

Table A.3.  
Orbit chain setup data for  $L_1$  to  $L_2$  Lyapunov orbit transfer. All quantities are presented in nondimensional units.

	$L_1$ Lyapunov	$L_1$ Lyapunov
Num. Rev.'s	1	2
Num. Seg.'s/Rev.	20	20
Prop. Time	3.870246	4.134450
$x$	0.954202	0.983711
$y$	-0.206436	-0.208751
$\dot{x}$	-0.077760	-0.055593
$\dot{y}$	-0.189855	0.198993

Table A.4.  
Orbit chain setup data for  $L_1$  to  $L_2$  halo orbit transfer. All quantities are presented in nondimensional units.

	L1 Halo	L2 Halo
Num. Rev.'s	1	2
Num. Seg.'s/Rev.	20	20
Prop. Time	2.786604	3.292387
$x$	0.828389	1.163324
$z$	0.103044	0.115930
$y$	0.218573	-0.204261

Table A.5.  
Orbit chain setup data for DRO to  $L_3$  Lyapunov orbit transfer with 2:3 resonant orbit. All quantities are presented in nondimensional units.

	DRO	2:3 Resonant Orbit	$L_3$ Lyapunov
Num. Rev.'s	2	1	1
Num. Seg.'s/Rev.	20	20	10
Prop. Time	1.570021	12.089330	6.264487
$x$	0.885234	0.408948	-1.910927
$y$	0.470671	1.581490	1.704300

Table A.6.  
 Part 1 of the orbit chain setup data for  $L_2$  Lyapunov to  $L_2$  vertical orbit transfer. All quantities are presented in nondimensional units.

	$L_2$ Lyapunov	$L_2$ Axial	$L_2$ Axial	$L_2$ Axial	$L_2$ Axial
Num. Rev.'s	1	1	1	1	1
Num. Seg.'s/Rev.	10	10	10	10	10
Prop. Time	4.329246	4.314477	4.336327	4.368672	
$x$	1.220582	1.217542	1.203800	1.181613	
$y$	-0.429415	-0.423593	-0.400792	-0.360585	
$z$	0	0.059878	0.155396	0.242573	

Table A.7.  
 Part 2 of the orbit chain setup data for  $L_2$  Lyapunov to  $L_2$  vertical orbit transfer. All quantities are presented in nondimensional units.

	$L_2$ Axial	$L_2$ Vertical				
Num. Rev.'s	1	1	1	1	1	1
Num. Seg.'s/Rev.	10	10	10	10	10	10
Prop. Time	4.399218	4.418021	4.422165	4.422165	5.692085	
$x$	1.155626	1.129788	1.111156	1.111156	1.100025	
$y$	-0.306078	-0.239334	-0.178303	-0.178303	-0.324640	
$z$	0.320668	0.389713	0.437828	0.437828	0.601867	

## B. GATEWAY MISSION DESIGN APPENDIX

This appendix offers the data necessary to reconstruct the CR3BP orbit chain initial guesses for each type of Gateway transfer presented in Chapter 5. The first three rows of the tables that summarize each orbit chain provide: the number of revolutions, the number of segments per revolution, and propagation time for each link in the orbit chain. The names of these quantities are abbreviated in each table as Num. Rev.'s, Num. Seg.'s/Rev., and Prop. Time, respectively. Furthermore, all times, positions, and velocities are presented in nondimensional units. When a transfer includes more links than can be fit in a single table the information is split over multiple tables.

Table B.1.  
Orbit chain setup data for 9:2 NRHO to DRO exterior type transfer. All quantities are presented in nondimensional units.

	9:2 NRHO	3:4 Res. Orbit	3:4 Res. Orbit	Partial DRO	DRO
Num. Rev.'s	3	1	1	1	4
Num. Seg.'s/Rev.	10	20	20	5	10
Prop. Time	1.509150	8.290637	10.467734	1.536336	3.218083
$x$	1.021870	1.037061	-2.079035	1.177407	0.805067
$y$	-7.0043E-04	0.037295	0.033381	-0.036086	3.5921E-05
$z$	-0.181982	0	0	0	0
$\dot{x}$	-8.9630E-04	0.552909	0.026623	-0.060835	5.0407E-05
$\dot{y}$	-0.102922	0.006090	1.535686	-0.491767	0.520173
$\dot{z}$	0.003428	0	0	0	0

Table B.2.  
 Part 1 of the orbit chain setup data for 9:2 NRHO to DRO interior type transfer. All quantities are presented in nondimensional units.

	9:2 NRHO	Partial P4HO <sub>2</sub>	P4HO <sub>2</sub>	P4HO <sub>2</sub>
Num. Rev.'s	2	1	1	1
Num. Seg.'s/Rev.	10	10	20	20
Prop. Time	1.509150	4.606535	9.490311	10.651958
$x$	1.021870	1.027785	1.158663	1.191342
$y$	-7.004332E-04	0.002919	0.002043	0.011654
$z$	-0.181982	-0.193140	-0.141818	-0.094972
$\dot{x}$	-8.962965E-04	0.003807	0.002218	0.013919
$\dot{y}$	-0.102922	-0.138660	-0.288708	-0.369781
$\dot{z}$	0.003428	-0.009822	-0.001719	-0.004878

Table B.3.  
 Part 2 of the orbit chain setup data for 9:2 NRHO to DRO interior type transfer. All quantities are presented in nondimensional units.

	P4HO <sub>2</sub>	DRO
Num. Rev.'s	1	2
Num. Seg.'s/Rev.	20	10
Prop. Time	18.105851	3.218083
$x$	1.316275	1.179586
$y$	-0.011292	-0.005047
$z$	-0.071267	0
$\dot{x}$	-0.010309	-0.008536
$\dot{y}$	-0.601531	-0.497790
$\dot{z}$	9.888924E-04	0

Table B.4.  
Orbit chain setup data for 9:2 NRHO to low-amplitude halo orbit exterior type transfer. All quantities are presented in nondimensional units.

	9:2 NRHO		Partial 3:4		Partial 3:4		Partial $L_2$		$L_2$	
	Res. Orbit	Res. Orbit	Res. Orbit	Res. Orbit	Halo	Halo	Halo	Halo		
Num. Rev.'s	3	1	1	1	1	1	4			
Num. Seg.'s/Rev.	10	20	5	5	10	10	10			
Prop. Time	1.509150	16.760489	16.313133	0.538171	3.414972					
$x$	1.021870	1.041370	0.976174	1.161700	1.180832					
$y$	-7.0043E-04	0.037252	0	0.071753	-2.2127E-05					
$z$	-0.181982	0	0	0.005678	0.008271					
$\dot{x}$	-8.9630E-04	0.534650	0	0.061589	-2.1395E-05					
$\dot{y}$	-0.102922	-0.016535	1.409546	-0.089925	-0.156252					
$\dot{z}$	0.003428	0	0	0.009194	-2.6562E-06					

Table B.5.  
 Part 1 of the orbit chain setup data for 9:2 NRHO to low-amplitude halo orbit interior type transfer. All quantities are presented in nondimensional units.

	9:2 NRHO		$L_2$		$L_2$		$L_2$		$L_2$	
			Halo	Halo	Halo	Halo	Halo	Halo	Halo	Halo
Num. Rev.'s	3		1	1	1	1	1	1	1	1
Num. Seg.'s/Rev.	10		10	10	10	10	10	10	10	10
Prop. Time	1.509150		3.041782	3.127969	3.223292	3.292387	3.347210			
$x$	1.021870		1.133081	1.142197	1.153800	1.163324	1.171378			
$y$	-7.0043E-04		0	0	0	0	0			
$z$	-0.181982		-0.172923	-0.160003	-0.138891	-0.115930	-0.088997			
$\dot{x}$	-8.9630E-04		0	0	0	0	0			
$\dot{y}$	-0.102922		-0.225154	-0.222573	-0.215129	-0.204261	-0.189574			
$\dot{z}$	0.003428		0	0	0	0	0			

Table B.6.  
 Part 2 of the orbit chain setup data for 9:2 NRHO to low-amplitude halo orbit interior type transfer. All quantities are presented in nondimensional units.

	$L_2$	$L_2$	$L_2$	$L_2$	$L_2$	$L_2$	$L_2$
	Halo	Halo	Halo	Halo	Halo	Halo	Halo
Num. Rev.'s	1	1	1	1	1	1	1
Num. Seg.'s/Rev.	10	10	10	10	10	10	10
Prop. Time	3.375316	3.392079	3.404949	3.410493	3.415098	3.414972	
$x$	1.175498	1.177863	1.179583	1.180285	1.180847	1.180832	
$y$	0	0	0	0	0	-2.2127E-05	
$z$	-0.069189	-0.053191	-0.035885	-0.024799	-0.007278	0.008271	
$\dot{x}$	0	0	0	0	0	-2.1395E-05	
$\dot{y}$	-0.178574	-0.170341	-0.162896	-0.159323	-0.156163	-0.156252	
$\dot{z}$	0	0	0	0	0	-2.6562E-06	

Table B.7.  
Orbit chain setup data for 9:2 NRHO to northern NRHO exterior type transfer. All quantities are presented in nondimensional units.

	9:2 NRHO		Partial 3:4		Partial 3:4	Partial 4:3	North NRHO
	Res. Orbit	Res. Orbit	Res. Orbit	Res. Orbit	Res. Orbit	Res. Orbit	Res. Orbit
Num. Rev.'s	3	1	1	1	1	1	3
Num. Seg.'s/Rev.	10	20	20	20	20	20	10
Prop. Time	1.509150	8.282712	9.388860	12.838615	1.806417		
$x$	1.021870	1.041370	-1.956454	0.992197	0.925330		
$y$	-7.0043E-04	0.037252	-0.053828	-0.061464	-5.2460E-07		
$z$	-0.181982	0	0	0	0.219090		
$\dot{x}$	-8.9630E-04	0.534650	-0.040667	-0.506176	-8.3998E-07		
$\dot{y}$	-0.102922	-0.016535	1.361147	-0.298936	0.121016		
$\dot{z}$	0.003428	0	0	0	2.0272E-06		

Table B.8.  
 Part 1 of the orbit chain setup data for 9:2 NRHO to northern NRHO interior type transfer. All quantities are presented in nondimensional units.

	9:2 NRHO		$L_2$		$L_2$		$L_2$		$L_2$	
		Halo	Halo	Halo	Halo	Halo	Halo	Halo	Halo	Halo
Num. Rev.'s	2	1	1	1	1	1	1	1	1	1
Num. Seg.'s/Rev.	10	10	10	10	10	10	10	10	10	10
Prop. Time	1.509150	3.041782	3.133468	3.221614	3.283583	3.331601				
$x$	1.021870	1.133081	1.142819	1.153580	1.162062	1.169065				
$y$	-7.0043E-04	0	0	0	0	0				
$z$	-0.181982	-0.172923	-0.159013	-0.139350	-0.119382	-0.097842				
$\dot{x}$	-8.9630E-04	0	0	0	0	0				
$\dot{y}$	-0.102922	-0.225154	-0.222300	-0.215322	-0.206026	-0.194518				
$\dot{z}$	0.003428	0	0	0	0	0				

Table B.9.  
 Part 2 of the orbit chain setup data for 9:2 NRHO to northern NRHO interior type transfer. All quantities are presented in nondimensional units.

	$L_2$		$L_1$		Partial $L_1$		$L_1$		$L_1$		
	Halo		Halo		Halo		Halo		Halo		
Num. Rev.'s	7		6		1		1		1		1
Num. Seg.'s/Rev.	10		10		10		10		10		10
Prop. Time	3.374384		2.763353		1.397055		2.783092		2.783412		2.747953
$x$	1.175364		0.870274		0.870274		0.827097		0.831776		0.836649
$y$	0		0.002979		0.002979		0		0		0
$z$	-0.069958		-0.047432		-0.047432		0.092802		0.124598		0.146869
$\dot{x}$	0		0.001223		0.001223		0		0		0
$\dot{y}$	-0.178991		-0.193586		-0.193586		0.207837		0.238898		0.255633
$\dot{z}$	0		-0.005395		-0.005395		0		0		0

Table B.10.  
 Part 3 of the orbit chain setup data for 9:2 NRHO to northern NRHO interior type transfer. All quantities are presented in nondimensional units.

	$L_1$		$L_1$		North NRHO	
	Halo	Halo	Halo	Halo	Halo	Halo
Num. Rev.'s	1	1	1	1	2	2
Num. Seg.'s/Rev.	10	10	10	10	10	10
Prop. Time	2.681166	2.557192	2.412265	2.412265	1.806417	1.806417
$x$	0.841825	0.849824	0.859159	0.859159	0.925330	0.925330
$y$	0	0	0	0	-5.2460E-07	-5.2460E-07
$z$	0.162058	0.175258	0.183518	0.183518	0.219090	0.219090
$\dot{x}$	0	0	0	0	-8.3998E-07	-8.3998E-07
$\dot{y}$	0.262975	0.262990	0.254931	0.254931	0.121016	0.121016
$\dot{z}$	0	0	0	0	2.0272E-06	2.0272E-06

VITA

## VITA

Robert Pritchett graduated with his Bachelor of Science in Aerospace Engineering from the University of Texas at Austin in May of 2014. In the fall of that same year Robert moved to West Lafayette and began graduate school at Purdue University where he joined the research group of Professor Kathleen Howell. Robert's Masters research focused on comparing indirect shooting and direct collocation techniques for low-thrust trajectory design. This research was aided by the opportunity to spend the summers of 2015 and 2016 as an intern at the Jet Propulsion Laboratory working with Daniel Grebow and Thomas Pavlak to test MColl, a direct collocation tool that was ultimately incorporated into JPL's primary mission design and navigation software MONTE. After receiving his M.S. degree in August of 2016 Robert, began his Ph.D. research, and was supported by a NASA Space Technology Research Fellowship (NSTRF). Robert continued his examination of direct collocation methods for his Ph.D. research, and focused on developing strategies for applying these methods to the planned Gateway and Lunar IceCube missions. As an NSTRF student, Robert also had the opportunity to complete visiting technologist experiences at the Jet Propulsion Laboratory and Goddard Space Flight Center during the summers of 2017 and 2018 as well as the fall of 2019. These experiences offered opportunities to collaborate with and learn from many engineers at these NASA centers. Robert joined the Pathways program at Goddard Space Flight Center in the summer of 2019 and, following graduation, will continue working there full time as a member of the Navigation and Mission Design Branch.